PNNL-11929

Pacific Northwest
National Laboratory

Operated by Battelle for the
U.S. Department of Energy

The Burnup Dependence of Light Water Reactor Spent Fuel Oxidation

B. D. Hanson

July 1998

PNNL-11929

Prepared for the U.S. Department of Energy
under Contract DE-AC06-76RLO 1830

DISCLAIMER

PACIFIC NORTHWEST NATIONAL LABORATORY
operated by
BATTELLE
for the
UNITED STATES DEPARTMENT OF ENERGY
under Contract DE-AC06-76RLO 1830

Printed in the United States of America

Available to DOE and DOE contractors from the Office of Scientific and Technical Information, P.O. Box 62, Oak Ridge, TN 37831; prices available from (615) 576-8401.

Available to the public from the National Technical Information Service, U.S. Department of Commerce, 5285 Port Royal Rd., Springfield, VA 22161


This document was printed on recycled paper.

PNNL-11929

The Burnup Dependence of Light Water Reactor Spent Fuel Oxidation

B.D. Hanson

July 1998

Prepared for
the U.S. Department of Energy
under Contract DE-AC06-76RLO 1830

Pacific Northwest National Laboratory
Richland, Washington 99352

Summary

Studies are underway to characterize and determine the viability of Yucca Mountain as a potential site for a permanent repository for the spent nuclear fuel presently accumulating at nuclear power plants throughout the United States. Failure of the waste package and fuel cladding could expose the fuel to the oxidizing atmosphere expected within the repository. The spent fuel, UO_2 containing fission products and actinides, could then oxidize. If oxidation past an oxygen-to-metal (O/M) ratio of about 2.42 occurs, U_3O_8, a phase about 20% less dense than the UO_2, forms. The increase in volume as spent fuel oxidizes to U_3O_8 causes fuel fragments to deteriorate and places stress on the cladding, which may split as a result. U_3O_8 also has a larger dissolution rate than UO_2 when normalized to the surface area of the particles. The formation of U_3O_8 may, therefore, result in larger releases of radionuclides from the waste package. An accurate understanding of the time-dependent state of the fuel is necessary for assessing the performance of the proposed repository. Experiments have been conducted at Pacific Northwest National Laboratory to determine the mechanism and kinetics of light water reactor (LWR) spent fuel oxidation, concentrating on the formation of U_3O_8.

Thermogravimetric analysis was used to study the air oxidation of fragments of LWR spent fuel with burnups in the range 16 to 42 MWd/kg M. The spent fuel samples were contacted with dry air over the temperature range 255°C to 325°C. The mass increase of the specimens was correlated directly to the O/M ratio. Mass increases were generally followed until the calculated O/M ratio reached about 2.7.

Spent fuel oxidized via the two-step reaction $UO_2 \rightarrow UO_{2.4} \rightarrow U_3O_8$, where the $UO_{2.4}$ phase is similar to cubic U_4O_9, but contains excess, diffuse oxygen. The transition of $UO_2 \rightarrow UO_{2.4}$ depended on the average grain size of the specimen, with smaller-grained fuels oxidizing faster. No correlation with other fuel parameters, such as burnup, was found. The Arrhenius activation energy was calculated as 109 ± 14 kJ mol^{-1}, in agreement with reported values for oxygen diffusion in UO_{2+x}.

The oxidation of $UO_{2.4}$ to U_3O_8 depended strongly on both temperature and burnup. Spent fuel strongly resisted oxidation beyond $UO_{2.4}$ at either low temperature or high burnup. Plateaus with nearly constant mass lasting for as long as 3000 hours were observed. Both the duration of the plateau and the time-rate-of-change in the O/M ratio beyond the plateau exhibited identical burnup dependencies within experimental errors. The activation energy to convert $UO_{2.4}$ to U_3O_8 was modeled as consisting of a temperature-dependent (Arrhenius) term and a term assumed to be linearly dependent on burnup. The

coefficient for the burnup dependence of the activation energy was determined to be 1.2±0.2 kJ mol^{-1} per MWd/kg M. The Arrhenius activation energy was calculated to be in the range 155 to 211 kJ mol^{-1}, which agrees with the value of 146±10 kJ mol^{-1} reported for the oxidation of unirradiated UO_2, when the large uncertainties of the data were considered and well defined states of the fuel were used. At the low temperatures expected in the repository when failures occur, oxidation to U_3O_8 should be minimal. Based on these results, higher-burnup fuels should experience even less oxidation past the plateau.

Burnup strongly correlates with the kinetics of oxidation, but burnup is only a first-order measure of the total impurity (i.e., fission product and higher actinide) concentration. The substitution of fission products and higher actinides into the vacancies in the uranium sublattice of UO_2 that result from fission stabilizes the fluorite structure with respect to oxidation beyond $UO_{2.4}$. Similar effects are observed with unirradiated, doped fuel. A simple model shows that at least one-half of the burnup dependence of the activation energy may be accounted for by the increased lattice energy caused by the lattice contraction produced by impurity substitutions and the requisite oxidation of matrix uranium ions to maintain charge neutrality.

Acknowledgments

This research was performed under appointment to the Office of Civilian Radioactive Waste Management Fellowship Program administered by the Oak Ridge Institute for Science and Education under Contract DE-AC05-76OR00033 between the U.S. Department of Energy and Oak Ridge Associated Universities.

Funding for this work was provided in support of the Yucca Mountain Project (YMP) as part of the Civilian Radioactive Waste Management Program. The YMP is managed by the Yucca Mountain Site Characterization Office of the U.S. Department of Energy, Las Vegas, Nevada. Pacific Northwest National Laboratory (PNNL) is operated by Battelle for the U.S. Department of Energy under Contract DE-AC06-76RLO-1830.

The assistance, review, and technical guidance provided by Dr. Stanley G. Prussin, Dr. Donald Olander, and Dr. Gene Rochlin of the University of California at Berkeley are gratefully acknowledged. The author thanks H. Craig Buchanan and Dr. Steven C. Marschman of PNNL for their contributions and Dr. Robert E. Einziger, presently at Argonne National Laboratory, for his mentoring and direction. The author also thanks Dr. Ray B. Stout of Lawrence Livermore National Laboratory, Dr. J. Kevin McCoy of Framatome Cogema Fuels, and B. Orie Barnes of PNNL for their technical reviews. The editorial reviews by Wayne Cosby and Sue Gano are appreciated.

Finally, I am eternally grateful to my wife Cindee for her years of support while this work was being done. I thank my family, especially Grandpa Edwards, for their support and encouragement and for giving me the confidence to do this.

Quality Assurance

This work was conducted under SNF-70-001, *SNF Quality Assurance Program* as implemented by the latest revision of the project quality assurance (QA) plan WTC-018. This QA program has been evaluated by the Office of Civilian Radioactive Waste Management (OCRWM) and determined to effectively implement the requirements of DOE/RW-0333P, *Quality Assurance Requirements and Description (QARD)*. This work was originally published as the Ph.D. dissertation for the author at the University of California at Berkeley in February 1998. It was subsequently reviewed by QA and technical personnel in compliance with the requirements for Independent Technical Review outlined in the SNF QA program. Comments and suggestions from the review process have been incorporated in this document.

Sample Identification

Each spent fuel sample has been assigned a unique identification number of the form MM-DD-YY-ATM-ID, where MM-DD-YY represents the calendar date that the sample was loaded in the TGAs, ATM identifies the approved testing material (ATM) from which the fuel came, and ID is the sequential identifier for the sample. For example, 6-20-95-105-09 identifies a sample loaded on June 20, 1995, and consisted of the ninth fragment of ATM-105 fuel to be tested during the present series. For convenience, the sample designation is often shortened, omitting the date or the "0" for a sample where the ID is a single digit. Thus, 6-20-95-105-09, 6-20-95-105-9, 105-09, and 105-9 all refer to the same sample. No two samples from the same ATM have the same ID.

Test Documentation

All TGA testing was performed in accordance with the technical procedure SFO-2-1, Rev. 5, *Measurement of Spent Fuel Oxidation Using a TGA System*. Those samples oxidized before the procedure's approval on March 1, 1995, followed this procedure with only minor changes that did not affect data quality. Testing was performed under either the *Test Plan for Thermogravimetric Analyses (TGA) of Spent Fuel Oxidation*, Rev. 0, or the *Addendum to the Test Plan for Thermogravimetric Analyses of Spent Fuel Oxidation*. Both the test plan and addendum are incorporated in Lawrence Livermore National Laboratory Activity Plan D-20-44.

Data Documentation

The data for all TGA samples in this work are contained in Laboratory Record Books (LRBs) BNW 54869, BNW 55854, and BNW 56042. The raw data, recorded at 5-minute intervals, are stored on floppy disks. All calibration records and supporting documentation are contained either in the LRBs listed above or in the Geologic Disposal Support Project (GDSP) files at PNNL.

Glossary

AEM	analytical transmission electron microscopy
AGR	advanced gas-cooled reactors
ASTM	American Society for Testing and Materials
ATM	approved testing material
BWR	boiling water reactor
CANDU™	Canada deuterium uranium (fuel)
EDS	energy-dispersive X-ray spectrometry
EPMA	electron probe microanalysis
FBR	fast breeder reactor
fcc	face-centered-cubic
FIMA	fission initial metal atoms
JCPDS	Joint Committee for Powder Diffraction Standards
LHGR	linear heat generation rates
LWR	light water reactor
LRB	laboratory record book
MCC	Materials Characterization Center
NIST	National Institute of Standards and Technology
OCRWM	Office of Civilian Radioactive Waste Management
O/M	oxygen to metal
O/U	oxygen to uranium
ORIGEN2	Oak Ridge Isotope Generation and Depletion code
PDF	powder diffraction file
PID	proportional-integral-differential
PNNL	Pacific Northwest National Laboratory
PWR	pressurized water reactor
QA	quality assurance
QARD	Quality Assurance Requirements and Description
REE	rare earth elements
SEM	scanning electron microscopy
SIMFUEL	simulated high-burnup fuel
TEM	transmission electron microscopy
TGA	Thermogravimetric Analysis

U-O	uranium-oxygen (chemical bonding)
XRD	X-ray diffractometry
YMP	Yucca Mountain Project

Contents

Summary iii

Acknowledgments v

Quality Assurance vii

Glossary ix

1.0 INTRODUCTION 1.1

2.0 BACKGROUND 2.1
2.1 Phase Properties 2.1
2.2 Review of Previous Oxidation Work 2.3
2.2.1 Oxidation of Unirradiated UO_2 ..... 2.3
2.2.2 Oxidation of Spent Fuel 2.4
2.2.3 Oxidation of Doped UO_2 ..... 2.8
2.2.4 Burnup-Dependent Oxidation 2.11
2.2.5 Summary of Previous Oxidation Work 2.12
2.3 Spent Fuel Chemistry 2.13
2.3.1 Chemical State of Impurities in Spent Fuel 2.13
2.3.2 Radial Variation in Spent Fuel Chemistry 2.16
2.4 Oxygen Potential 2.17
2.4.1 Oxygen Potential of UO_2 and UO_{2+x} 2.21
2.4.2 Oxygen Potential of Doped UO_2 ..... 2.23
2.4.3 Oxygen Potential in Spent Fuel 2.28
2.5 Theoretical Basis for Matrix Stabilization 2.31
2.5.1 Lattice Energy 2.31
2.5.2 Valence State of Substitutional Ions 2.32
2.5.3 Effect of Substitutional Cations on Lattice Parameter 2.34

3.0 EXPERIMENTAL 3.1
3.1 Fuel Characterization 3.1
3.2 Testing Methodology 3.4
3.2.1 Thermogravimetric Analysis (TGA) 3.4
3.2.2 Dry-Bath Systems 3.6
3.2.3 Burnup Determination 3.8
3.2.3.1 ^{148}Nd Isotope Dilution Method 3.8
3.2.3.2 Gamma Spectrum Analysis 3.9
3.2.4 X-Ray Powder Diffractometry 3.10
3.2.5 Scanning Electron Microscopy 3.11

4.0 EXPERIMENTAL RESULTS 4.1
4.1 TGA Oxidation Results 4.1
4.1.1 Doped Fuel 4.1
4.1.2 ATM-105 Tests 4.3
4.1.2.1 Scoping Tests 4.3
4.1.2.2 283°C Tests 4.6
4.1.2.3 305°C Tests 4.8
4.1.3 ATM-104 Tests 4.12
4.1.4 ATM-108 Tests 4.14

4.2 Burnup Analyses 4.15
4.2.1 ^{148}Nd Isotope Dilution Method 4.15
4.2.2 Gamma Spectrum Analysis 4.16
4.3 Dry-Bath Oxidation Results 4.18
4.3.1 175°C Tests 4.18
4.3.2 195°C Tests 4.19
4.3.3 255°C Test 4.20
4.4 Quantitative XRD Results 4.24
5.0 DISCUSSION OF RESULTS 5.1
5.1 The First Transition ($UO_2 \rightarrow UO_{2.4}$) 5.2
5.1.1 Grain Size Dependence 5.2
5.1.2 Activation Energy 5.4
5.1.3 Burnup Dependence 5.6
5.2 The Second Transition ($UO_{2.4} \rightarrow U_3O_8$) 5.8
5.2.1 Mechanism of U_3O_8 Formation 5.8
5.2.2 Plateau Behavior 5.11
5.2.3 Burnup and Temperature Dependence 5.13
5.2.4 Time-Rate-of-Change in O/M Ratio 5.24
5.2.5 Sensitivity to Impurity Concentration 5.30
5.3 Analysis of Dry-Bath Data 5.35
5.4 Change in Lattice Energy with Burnup 5.37
6.0 CONCLUSIONS 6.1
7.0 REFERENCES 7.1

Tables

Table 2.1. Characteristics of Phases of Interest 2.3
Table 2.2. Typical Composition of PWR Spent Fuel from ORIGEN2 Calculation 2.14
Table 2.3. Chemical State of the Main Fission and Transmutation Products 2.15
Table 2.4. Cumulative Elemental Yields (%) for Thermal Fission 2.20
Table 2.5. Ionic Radii 2.35
Table 2.6. Lattice Parameter Contraction of $U_{1-y}M_yO_2$ 2.37
Table 3.1. Fuel Characteristics 3.2
Table 3.2. XRD Peak Positions for UO_2, U_4O_9, U_3O_7, and U_3O_8 in 2θ (°) 3.11
Table 4.1. Summary of Experimental Conditions and Measured Parameters 4.2
Table 4.2. Atom Densities Found by Mass Spectrometry Normalized to Sample Mass 4.17
Table 4.3. Burnup as a Function of ^{137}Cs Specific Activity 4.17
Table 5.1. Calculated Oxidation Parameters from TGA Tests 5.6
Table 5.2. Summary of Burnup Analyses to Estimate Total Impurity Concentrations 5.34

Figures

Figure 2.1. Oxidation Front at Various O/M Ratios for ATM-105 Fuel Oxidized at 195°C 2.6
Figure 2.2. Schematic Curve Representing the O/M Ratio of LWR Spent Fuel as a Function of Oxidation Time 2.8
Figure 2.4. Radial Profile of Plutonium in ATM-104 Fuel Measured by EPMA 2.17
Figure 2.5. Radial Burnup Profile in ATM-104 Fuel with a Pellet Average Burnup of 44.3 MWd/kg M Measured by EPMA 2.18
Figure 2.6. Cumulative Yields for Thermal Fission of ^{235}U, ^{239}Pu, and ^{241}Pu 2.19
Figure 2.7. Free Energy of Formation as a Function of Temperature for High-Yield Fission Products 2.21
Figure 2.8. Oxygen Potential for $UO_{2.00}$ as a Function of Temperature 2.22
Figure 2.9. Oxygen Potential of Hyperstoichiometric UO_2 as a Function of O/M 2.24
Figure 2.10. Blackburn Model Predictions for the Oxygen Potential in Hyperstoichiometric UO_2 ..... 2.25
Figure 2.11. Oxygen Potential at 1200°C as a Function of O/M for UO_2 Doped with Y or La 2.26
Figure 2.12. Oxygen Potential of $U_{0.75}Pu_{0.25}O_{2+x}$ as a Function of Oxygen-to-Metal Ratio 2.27
Figure 2.13. Burnup Dependence of the Oxygen Potential at 750°C for Different Irradiated Oxide Fuels 2.30
Figure 3.1. Schematic of the Thermogravimetric Analysis Systems 3.5
Figure 3.2. Photograph of the Dry-Bath Oxidation Systems 3.7
Figure 4.1. Oxygen-to-Metal Ratio as a Function of Time for ATM-105 Fragments Oxidized at Various Temperatures 4.4
Figure 4.2. Oxidation Behavior of ATM-105 Fragments in a TGA and Dry-Bath at 255°C 4.5
Figure 4.3. Oxidation Behavior of ATM-105 Fragments Oxidized at 283°C 4.7
Figure 4.4. Oxidation Behavior of ATM-105 Fragments Oxidized at 305°C 4.9
Figure 4.5. Oxidation Behavior of Four Samples Broken from the Same Larger Fragment of ATM-105 Fuel Oxidized at 305°C 4.10
Figure 4.6. Oxidation Behavior of Low-Burnup ATM-105 Fragments Oxidized at 305°C 4.12
Figure 4.7. Oxidation Behavior of ATM-104 Fragments at 305°C 4.13
Figure 4.8. Oxidation Behavior of ATM-108 Fragments at 305°C 4.15
Figure 4.9. Oxidation Behavior of LWR Spent Fuel Fragments Oxidized in a 175°C Dry Bath 4.20
Figure 4.10. Oxidation Behavior of Crushed LWR Spent Fuel Fragments in a 195°C Dry Bath 4.21
Figure 4.11. Oxidation Behavior of As-Irradiated LWR Spent Fuel Fragments in a 255°C Dry Bath 4.22
Figure 4.12. Oxidation Behavior of As-Irradiated and Pre-Oxidized (Open Symbols) LWR Spent Fuel Fragments in a 255°C Dry Bath 4.23
Figure 4.13. Oxidation Behavior of Turkey Point Fuel in a 255°C Dry Bath 4.24
Figure 4.14. Quantitative XRD Analysis of Oxidized LWR Spent Fuel 4.25
Figure 5.1. Time-to-Plateau as a Function of Inverse Temperature for ATM-105 Fragments 5.6
Figure 5.2. Time to Oxidize ATM-105 Fragments from $UO_{2.30}$ to $UO_{2.35}$ as a Function of Inverse Temperature 5.7
Figure 5.3. Time-to-Plateau as a Function of Burnup for LWR Fragments Oxidized at 305°C 5.9
Figure 5.4. Time to Oxidize LWR Fragments from $UO_{2.30}$ to $UO_{2.35}$ at 305°C as a Function of Burnup 5.10
Figure 5.5. Oxidation Behavior of ATM-105 Fragments of Different Burnup Oxidized at 305°C 5.14
Figure 5.6. Duration of the Plateau for LWR Spent Fuel Fragments Oxidized at 305°C (Burnup from ^{137}Cs Analysis) 5.15
Figure 5.7. Duration of the Plateau for ATM-105 Fragments Oxidized at 305°C (Burnup from ^{148}Nd Analysis) 5.17
Figure 5.8. Oxidation Behavior of ATM-105 Fragments of Similar Burnup (~28 MWd/kg M) Oxidized at Different Temperatures 5.19

Figure 5.9. Duration of the Plateau for ATM-105 Fragments of Similar Burnup (~28 MWd/kg M) as a Function of Inverse Temperature 5.20
Figure 5.10. Duration of the Plateau for Moderate Burnup ATM-105 Fragments as a Function of Inverse Temperature 5.21
Figure 5.11. Time to Oxidize LWR Fragments from $UO_{2.45}$ to $UO_{2.50}$ at 305°C as a Function of Burnup (Burnup from ^{137}Cs Analysis) 5.22
Figure 5.12. Time to Oxidize ATM-105 Fragments from $UO_{2.45}$ to $UO_{2.50}$ at 305°C (Burnup from ^{148}Nd Analysis) 5.23
Figure 5.13. Time to Oxidize ATM-105 Fragments of Similar Burnup (~28MWd/kg M) from $UO_{2.45}$ to $UO_{2.50}$ as a Function of Inverse Temperature 5.24
Figure 5.14. Time to Oxidize Moderate Burnup ATM-105 Fragments from $UO_{2.45}$ to $UO_{2.50}$ as a Function of Inverse Temperature 5.25
Figure 5.15. Time-Rate-of-Change of O/M Ratio as a Function of O/M for ATM-105 Fragments of Similar Burnup (~28 MWd/kg M) Oxidized at Different Temperatures 5.26
Figure 5.16. Time-Rate-of-Change of O/M Ratio as a Function of O/M for LWR Spent Fuel Fragments of Different Burnups Oxidized at 305°C 5.27
Figure 5.17. Average d(O/M)/dt After the Plateau as a Function of Burnup and Inverse Temperature 5.28
Figure 5.18. Average d(O/M)/dt After the Plateau as a Function of Burnup for ATM-105 Fragments Oxidized at 305°C (Burnup from ^{137}Cs Analysis) 5.30
Figure 5.19. Average d(O/M)/dt After the Plateau as a Function of Burnup for ATM-105 Fragments Oxidized at 305°C (Burnup from ^{148}Nd Analysis) 5.31
Figure 5.20. Average d(O/M)/dt After the Plateau as a Function of Inverse Temperature for Moderate Burnup ATM-105 Fragments 5.32
Figure A.1. Sample of Unirradiated UO_2 with 8 wt% Gd_2O_3 Oxidized at 283°C A.1
Figure A.2. Sample 105-01 Oxidized at 283°C A.2
Figure A.3. Sample 105-02 Oxidized at 325°C A.3
Figure A.4. Sample 105-03 Oxidized at 305°C A.4
Figure A.5. Sample 105-04 Oxidized at 270°C A.5
Figure A.6. Sample 105-05 Oxidized at 255°C A.6
Figure A.7. Sample 105-06 Oxidized at 283°C A.7
Figure A.8. Sample 105-07 Oxidized at 283°C A.8
Figure A.9. Sample 105-08 Oxidized at 283°C A.9
Figure A.10. Sample 105-09 Oxidized at 305°C A.10
Figure A.11. Sample 105-10 Oxidized at 305°C A.11
Figure A.12. Sample 105-11 Oxidized at 305°C A.12
Figure A.13. Sample 105-12 Oxidized at 305°C A.13
Figure A.14. Sample 105-13 Oxidized at 305°C A.14
Figure A.15. Sample 105-14 Oxidized at 305°C A.15
Figure A.16. Sample 105-15 Oxidized at 305°C A.16
Figure A.17. Sample 105-16 Oxidized at 305°C A.17
Figure A.18. Sample 105-17 Oxidized at 305°C A.18
Figure A.19. Sample 105-18 Oxidized at 305°C A.19
Figure A.20. Sample 104-01 Oxidized at 305°C A.20
Figure A.21. Sample 104-02 Oxidized at 305°C A.21
Figure A.22. Sample 108-01 Oxidized at 305°C A.22
Figure A.23. Sample 108-02 Oxidized at 305°C A.23

1.0 INTRODUCTION

Studies are underway to characterize and determine the viability of Yucca Mountain as a potential site for a permanent repository for spent nuclear fuel. Typical spent fuels from light water reactors (LWRs) consist of fragmented UO_2 pellets enclosed in a Zircaloy cladding. The cladding provides a barrier to radionuclide release by protecting the UO_2 fuel pellets from contact with air or water and by limiting the subsequent egress of radionuclides. However, approximately 0.01% to 0.1% of LWR fuel rods irradiated before 1978 have incurred cladding breaches, usually in the form of small pinholes, during in-reactor service [1]. Newer fuels have experienced substantially lower failure rates. However, fuel rods may also be breached during storage or during emplacement in a storage canister [2]. Additional cladding breaches are predicted to occur over the lifetime of a repository, such as the one proposed at Yucca Mountain. Breached rods can expose the fuel to the oxidizing atmosphere of the proposed repository.

Over the temperature range of interest for dry storage or for placement of spent fuel in a permanent repository under the conditions now being considered, UO_2 is thermodynamically unstable with respect to oxidation to higher oxides. The multiple valence states of uranium allow for the accommodation of interstitial oxygen atoms in the fuel matrix. A variety of stoichiometric and non-stoichiometric phases is therefore possible as the fuel oxidizes from UO_2 to higher oxides.

Of particular concern is the oxidation of spent fuel to oxides of lower density. For example, U_3O_8 has a density of only about 0.8 of the cubic UO_2 and has a markedly different crystal structure. The increase in volume as spent fuel oxidizes to U_3O_8 causes fuel fragments to deteriorate to powder and places stress on the cladding, which may split as a result [3-6]. U_3O_8 has also been shown [7] to have a dissolution rate that is a factor of 2 to 4 greater than that for UO_2 or U_3O_7 when the rates are normalized to the surface area of the particles. The transformation of the fuel to powder, the splitting of the cladding, and the larger dissolution rates potentially can contribute to a release of radionuclides and may impact the design and performance of dry interim-storage facilities and repository disposition options. Therefore, understanding the rate at which spent fuel can oxidize to U_3O_8 is fundamental to assessing the likelihood and consequences of cladding failure under a variety of conditions.

The oxidation of UO_2 has been studied extensively for over 40 years. It has been shown that spent fuel and unirradiated UO_2 oxidize via different mechanisms and at different rates. The oxidation of LWR spent fuel from UO_2 to $UO_{2.4}$ was studied previously and is reasonably well understood. The study

presented here was initiated to determine the mechanism and rate of oxidation from $UO_{2.4}$ to higher oxides. During the early stages of this work, a large variability in the oxidation behavior of samples oxidized under nearly identical conditions was found. Based on previous work on the effect of dopants on UO_2 oxidation and this initial variability, it was hypothesized that the substitution of fission product and actinide impurities for uranium atoms in the spent fuel matrix was the cause of the variable oxidation behavior. Since the impurity concentration is roughly proportional to the burnup of a specimen, the oxidation behavior of spent fuel was expected to be a function of both temperature and burnup. This report 1) summarizes the previous oxidation work for both unirradiated UO_2 and spent fuel (Section 2.2) and presents the theoretical basis for the burnup (i.e., impurity concentration) dependence of the rate of oxidation (Sections 2.3, 2.4, and 2.5), 2) describes the experimental approach (Section 3) and results (Section 4) for the current oxidation tests on spent fuel, and 3) establishes a simple model to determine the activation energies associated with spent fuel oxidation (Section 5).

As part of this work, the rate of U_3O_8 formation under the conditions expected for dry storage or in a repository were determined to provide data for designing such facilities. Thermogravimetric methods were used to monitor the mass change of LWR spent fuel samples oxidized in a dry-air atmosphere in the temperature range 255°C to 325°C. The oxygen-to-metal (O/M) ratio was calculated based on the mass increase of the specimen. The range in burnup for the individual specimens was 16 to 42 MWd/kg M, as determined by analyzing the γ-ray energy spectrum emitted by ^{137}Cs or by using a ^{148}Nd isotope dilution method. X-ray diffractometry (XRD) and scanning electron microscopy (SEM) were used to determine the phases present. A brief description of the phases expected is presented in Section 2.1.

Since the oxidation of UO_2 to $UO_{2.4}$ has been studied extensively, the major emphasis of this work was the transition of $UO_{2.4}$ to U_3O_8. When the concentration of impurities within the fuel increased, as estimated by the sample burnup, the rate of U_3O_8 formation decreased. The activation energy of the $UO_{2.4}$ to U_3O_8 transition was calculated, and a model of the physical changes in the fuel that may result in its stabilization with respect to oxidation to U_3O_8 is presented. While results show that the delay in the onset of U_3O_8 formation may assist in delaying potential releases of radionuclides from spent fuel in a repository, additional research and modeling are necessary to better understand the processes involved.

2.0 BACKGROUND

This section reviews previous oxidation work and presents evidence for the stabilization effect of dopants in the UO_2 matrix on oxidation from $UO_{2.4}$ to U_3O_8. The fundamental aspects of spent fuel chemistry that support the model developed in this report are also presented.

2.1 Phase Properties

Crystalline UO_2 consists of U^{4+} and O^{2-} ions in the fluorite structure. The uranium ions form a face-centered-cubic (fcc) lattice with a lattice parameter of 547.0 pm [8], while the oxygen ions form a simple cubic sublattice. This corresponds to a theoretical density of 10.96 g cm^{-3} for UO_2. UO_2 is readily oxidized in air, and its multiple valence states allow for incorporation of interstitial oxygen atoms. These interstitial oxygen atoms cause a slight displacement of the lattice oxygen atoms from their ideal positions. For UO_{2+x} over the range $0<x<0.25$, the unit-cell contracts with increasing oxygen concentration. This contraction most likely is due to the smaller ionic radii of U^{5+} and U^{6+}, formed upon oxidation, compared to the U^{4+} ion. Still, the UO_{2+x} retains the cubic fluorite structure with a lattice parameter in the range 544.5 to 547.0 pm [9].

As oxidation of UO_{2+x} approaches $x=0.25$, a new phase, U_4O_9, is formed as a result of the slight but systematic contraction of the uranium atoms from their ideal lattice positions and the now-ordered placement of the unit-cells containing the oxygen interstitial. The U_4O_9 phase of interest to spent fuel oxidation is γ-U_4O_9 [10], which maintains the cubic fluorite structure of UO_2, but lacks the long-range ordering of β-U_4O_9 that is the product of unirradiated UO_2 oxidation [11]. The lack of long-range ordering is readily explained by the disruption of the U_4O_9 superlattice when fission products and heavier actinides are incorporated that differ in size and valence from the uranium atoms they replace. Since the superlattice reflections that accompany long-range ordering of U_4O_9 are not observed in the oxidation of unirradiated, doped (synthetic) fuels, it appears that this lack of ordering is not due to radiation damage. U_4O_9 has a lattice parameter of approximately 544.1 pm and a theoretical density of 11.30 g cm^{-3} [12]. The contraction in the unit-cell from UO_2 results in a slight shift of the X-ray peaks to higher diffraction angles when analyzed via XRD, thus allowing the individual phases to be identified.

The phase diagram for the uranium-oxygen (U-O) system is very complex in the $UO_{2.25}/U_3O_{8-x}$ region, with a number of fluorite phases being reported. The addition of oxygen atoms beyond U_4O_9

leads to a slight distortion of the cubic unit-cell to tetragonal or monoclinic variations. U_3O_7 is the phase reported most often in the oxidation of unirradiated UO_2 to O/M ratios in this region. The deviation from the cubic structure results in splitting the U_4O_9/UO_2 peaks on an X-ray diffractogram, again allowing the phases to be identified via XRD. U_3O_7 is slightly more dense than U_4O_9, with a theoretical density of ~11.40 g cm^{-3}.

Further oxidation results in a new series of phases based on the U_3O_8 structure with stoichiometries ranging from ~$UO_{2.5}$ to UO_3. U_3O_8 no longer maintains the fluorite structure, but is layered. The phase of interest for fuel oxidation in repository or dry storage conditions is α-U_3O_8 [12], which is orthorhombic and has unit-cell dimensions of a=415, b=1197, and c=672 pm [13]. The theoretical density for U_3O_8 is ~8.35 g cm^{-3} [14]. The orthorhombic structure is easily distinguished from the previous cubic or tetragonal phases by the appearance of multiple peaks on an X-ray diffractogram. Although U_3O_8 is thermodynamically unstable (based on the standard free energy changes) with respect to γ-UO_3 in air oxidation below about 700°C [15,16], oxidation beyond U_3O_8 is not usually observed in the absence of moisture or at atmospheric pressure, presumably due to a large energy barrier necessary for the restructuring of U_3O_8 to UO_3. UO_3 is thought to consist of uranyl-like bonds, meaning two collinear oxygens bonded to a uranium ion at much shorter distances than other U-O bonds [16,17]. The restructuring necessary to form the uranyl bond and to arrange the 4 to 6 additional oxygens bound to the uranium ion in a plane perpendicular to the double bond may result in the relative stability of the U_3O_8 with respect to oxidation to UO_3. It is possible, however, that some uranyl-type bonding exists in U_3O_8, but not to the extent it does in UO_3 [17].

The complexity of the phase diagram for the U-O system cannot be overemphasized, and hypo- and hyperstoichiometries are possible for the phases of interest. Each phase also has polymorphs that vary depending on the conditions under which the sample was oxidized. There is also considerable disagreement and contradiction found among various experimenters as to which phases exist and under what conditions (i.e., temperature and pressure). However, the characteristics of the phases reported most often in studies of UO_2 and spent fuel oxidation (UO_2, U_4O_9, U_3O_7, and U_3O_8) are summarized in Table 2.1. Other phases may be present, or may be precursors to those identified, but they have not been present in sufficient quantity to be observed in recent oxidation studies on spent fuel or doped (synthetic) fuel specimens.

Table 2.1. Characteristics of Phases of Interest

Phase	Structure	Crystal Class	Unit cell (pm)	Density (g cm^{-3})
UO_2	Fluorite	Cubic	a=547.0 [8]	10.96
U_4O_9	Fluorite	Cubic	a=544.1 [12]	11.30
U_3O_7	Fluorite	Tetragonal	a=547.2, c=539.7 [18]	11.40
U_3O_8	Layered	Orthorhombic	a=415, b=1197, c=672 [13]	8.35

2.2 Review of Previous Oxidation Work

The oxidation of unirradiated UO_2 and spent fuel has been studied extensively, with a number of parameters, including temperature, moisture, and particle size, found to affect oxidation behavior. McEachern and Taylor [19] have recently presented a critical review of UO_2 and spent fuel oxidation. Since the study presented here focuses on the behavior of spent fuel under dry storage or repository conditions prior to contact with groundwater, the discussion below emphasizes work on oxidation in air at temperatures below about 400°C.

2.2.1 Oxidation of Unirradiated UO_2

The oxidation of unirradiated UO_2 has been shown [14,20] to proceed via the two-step reaction

$$UO_2 \rightarrow U_3O_7 \rightarrow U_3O_8 \qquad (2.1)$$

It is generally agreed [19] that the first transition, $UO_2 \rightarrow U_3O_7$, on UO_2 powders is controlled by the diffusion of oxygen through the discrete layer of U_3O_7 formed on the sample surface. The oxide layer grows thicker with time and follows parabolic reaction kinetics, at least until 65% of the sample is oxidized [21]. For oxidation of unirradiated UO_2 sintered pellets, however, it has been reported [22,23] that surface oxidation proceeds via linear kinetics. Linear kinetics can be expected since oxygen can transport preferentially along grain boundaries. Taylor et al. [22] have shown that initial U_3O_7 formation occurs in a uniform surface layer, but subsequent formation appears at microcracks and grain boundaries. Also, as shown in Table 2.1, there is a slight densification as the fuel oxidizes to U_3O_7. The normal stresses associated with this lattice shrinkage are accommodated by crack formation and the opening of the grain boundaries [10,23]. The inter- and transgranular cracking provides relatively free transport of oxygen to unreacted UO_2 surfaces and may result in the linear kinetics observed. Still, the primary mechanism for oxidation of unirradiated UO_2 is surface formation of U_3O_7 controlled by diffusion of

oxygen through the product layer. It is important to note that there is a sharp interface between the UO_2 and U_3O_7 phases, with no evidence of a UO_{2+x} phase acting as an intermediate [24]. However, Teixeira and Imakuma [25] have reported that at 235°C and at very low oxygen concentrations, U_4O_9 is a precursor to U_3O_7 formation, although the U_3O_7 was not observed until after both the temperature and the oxygen concentration were increased.

Further oxidation to U_3O_8 proceeds while the U_3O_7 surface layer is still only a few micrometers thick. However, below about 200°C, the rate of U_3O_8 formation is extremely slow, leading to the appearance that oxidation beyond U_3O_7 does not occur [26]. Above about 250°C, oxidation to orthorhombic U_3O_8 is readily observed [24,26]. The density of U_3O_8 is appreciably less than that of either UO_2 or U_3O_7 (see Table 2.1), and subsequently the U_3O_8 formed spalls from the sample. The spallation of the oxidized product exposes the underlying U_3O_7 directly to the oxidizing atmosphere. The reaction rate is not controlled by diffusion through the product layer, as it is for the first transition, but by the transformation of U_3O_7 to U_3O_8, resulting in linear kinetics until the reaction slows down as it approaches completion [19]. Taylor et al. [26] have reported that many of the U_3O_8 peaks observed via XRD on oxidized UO_2 are broad, indicating a defective structure and/or small crystallite size. Similarly, Hoekstra et al. [27] have shown that U_3O_8 formed below about 250°C may be poorly crystalline and thus may appear amorphous when analyzed via XRD. Finally, U_3O_8 has been observed to form more rapidly on rough surfaces (as-cut or 400-grit finishes) than on polished surfaces (600-grit or higher) [26], which is consistent with the observation that U_3O_8 first forms at microcracks [23]. It is expected that areas of higher energy states (i.e., grain boundaries, cracks, etc.) would be more chemically reactive since the surface atoms are not bonded to the maximum number of nearest neighbors.

2.2.2 Oxidation of Spent Fuel

Irradiated CANDU™ (Canada deuterium uranium) fuel, with burnups typically in the range of 6 to 12 MWd/kg M, has also been shown to oxidize, first from UO_2 to U_3O_7, followed by spallation of U_3O_8 [6,28]. However, the rate of mass increase for irradiated fuel in defected fuel elements was a factor of 2 to 50 greater than the rate for unirradiated fuel at 230°C and 250°C, depending on the number of defects [6]. Similarly, for oxidation of bare fuel fragments, the rate of mass increase for irradiated fuel was a factor of 5 to 10 greater than for unirradiated fuel at these temperatures [29]. For example, a fragment with an approximate burnup of 7.9 MWd/kg M converted to U_3O_8 within 70 hours at 275°C [29]. Oxidation occurring preferentially along grain boundaries [28] is one reason for the increased oxidation rate of the irradiated fuel.

LWR spent fuels, with typical burnups of 20 to 50 MWd/kg M, however, have been shown [5,10,30-36] to oxidize via the two-step reaction

$$UO_2 \rightarrow U_4O_9 \rightarrow U_3O_8 \quad (2.2)$$

Einziger et al. [30] have extensively studied the oxidation of LWR spent fuel from UO_2 to U_4O_9. LWR spent fuel oxidizes by rapid advance of unordered, non-stoichiometric U_4O_9 (similar to γ-U_4O_9) along the grain boundaries [10,30,36]. Closely spaced fission-gas bubbles (interbubble spacing of about 2 nm) that form on the grain boundaries of spent fuel are believed to facilitate the rapid transport of oxygen through the grain boundaries relative to bulk diffusion [10]. As noted in Table 2.1, the lattice parameter for U_4O_9 is slightly smaller than for UO_2, which results in a slight contraction of the lattice. However, the lattice maintains the cubic fluorite structure. As oxidation of the grain boundaries proceeds, the fuel becomes embrittled, and the boundaries tend to open and thus create an open pathway for oxygen transport to all exposed grains [32]. The U_4O_9 structure formed as LWR spent fuel oxidizes accommodates excess oxygen, resulting in an O/M ratio of ~2.4, rather than the nominal stoichiometry of $UO_{2.25}$ [30]. This $UO_{2.4}$ phase then grows into the UO_2 grains until they are entirely converted, as seen in Figure 2.1. Unlike oxidation of unirradiated UO_2 or irradiated CANDU™ fuel where conversion of U_3O_7 to U_3O_8 occurs simultaneously with the conversion of UO_2 to U_3O_7, no higher oxides have been observed in LWR spent fuel oxidized at temperatures up to 250°C until conversion to $UO_{2.4}$ is complete [30]. Transmission electron microscopy (TEM) analysis has also shown that other than a slight mismatch at the phase interface, the lattices of UO_2 and $UO_{2.4}$ are indistinguishable [10]. Thomas [35,37] used XRD to determine the lattice parameters of the two phases present over the O/M ratio range of 2.0 to 2.6. (U_3O_8 was not observed, even at O/M ratios above 2.4, most likely as a result of the low temperatures of oxidation, i.e., <255°C. At these temperatures, U_3O_8 may be poorly crystalline and may not be detectable by XRD [27].) The analysis yielded a constant lattice parameter for UO_2 and a fairly constant parameter for $UO_{2.4}$ [35,37]. The TEM and XRD analyses, combined with the fairly uniform oxidation-front progression within grains [30,33], show that the oxidation of LWR spent fuel proceeds directly from UO_2 to $UO_{2.4}$ without forming an intermediate phase detectable by any of these methods, and the hyperstoichiometric U_4O_9 phase formed initially is near $UO_{2.4}$ in composition [35].

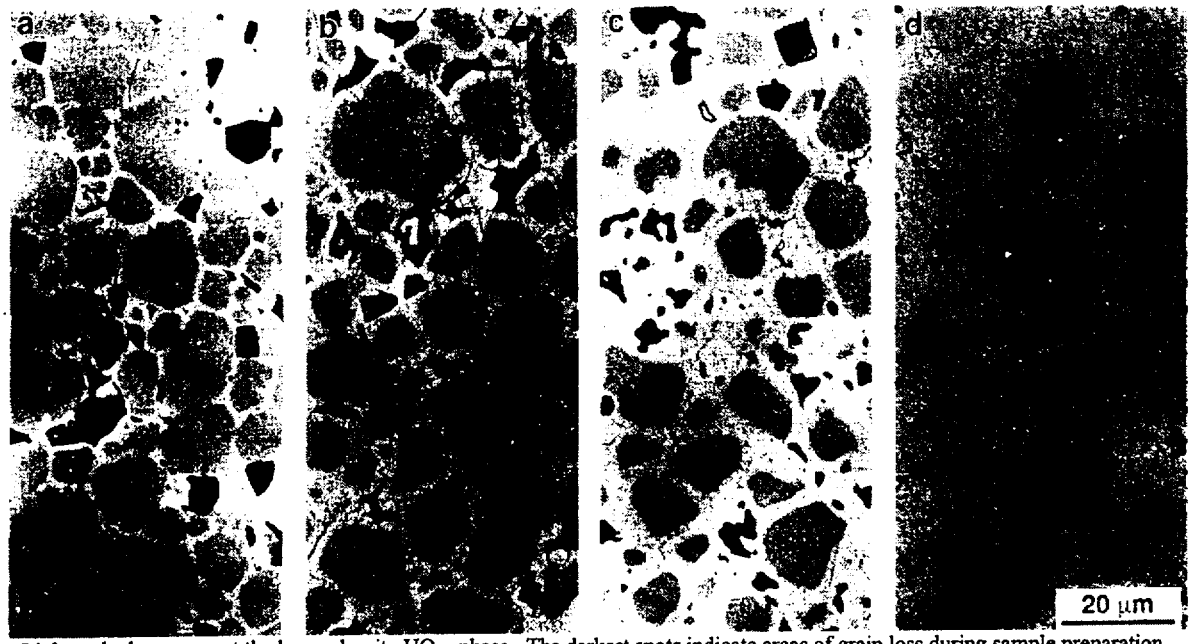

Lighter shades represent the lower density $UO_{2.4}$ phase. The darkest spots indicate areas of grain loss during sample preparation. The progressive bulk average O/M ratios based on mass increase are as follows: a) 2.05, b) 2.17, c) 2.24, and d) 2.31.

Figure 2.1. Oxidation Front at Various O/M Ratios for ATM-105 Fuel Oxidized at 195°C

The study of the first transition, $UO_2 \rightarrow UO_{2.4}$, has shown no apparent correlation of burnup, moisture, or fuel type with the oxidation behavior of spent fuel [30,31,38]. Differences in the initial rate of change in the O/M ratio have been attributed to grain size, with finer-grained fuels oxidizing faster in accordance with the greater surface area per unit grain volume [38]. A similar dependence of initial oxidation rate on grain size has been reported for unirradiated UO_2 [39]. After short times, however, all fuel specimens studied oxidized at essentially the same rate [30]. However, Thomas et al. [32] have reported greatly enhanced oxidation of UO_2 to $UO_{2.4}$ in specimens associated with the fuel pellet rim and the outer one-third of the pellet and slower oxidation in specimens from near the fuel-pellet centers [35]. This enhanced oxidation at the rim may be related to the large-scale porosity present in the as-irradiated fuel [32,40] and the slower oxidation related to the coarsening of the fission-gas bubbles formed at the higher temperatures near the pellet centers [35]. The burnup of this fuel is below the local threshold (60 to 75 MWd/kg M) associated with a high-burnup rim necessary before the fuel undergoes the restructuring to become highly porous as the original fuel grains [41,42] subdivide. Still, it is clear that as-fabricated and fission-induced porosity can influence oxidation behavior. The differences in porosity may explain the findings summarized in McEachern and Taylor [19] that the rate of oxidation both before and after the induction period for U_3O_8 formation decreases with increasing sample density.

After oxidation to a nominal O/M ratio of about 2.4, LWR spent fuel has shown a resistance to further oxidation, exhibited as a plateau on a plot of the O/M ratio as a function of time. Oxidation to U_3O_8 then proceeds to completion at a nominal O/M ratio of about 2.75. Figure 2.2 is a schematic representation of the oxidation behavior, including the plateau. The duration of the plateau, δ, strongly depends on temperature. Virtually no discernible plateau was found at temperatures above 283°C for spent fuel fragments from a pressurized water reactor (PWR) fuel rod with an average measured centerline burnup of about 27 MWd/kg M [4]. However, a plateau persisted for at least 10^4 hours when the same fuel was oxidized at 250°C under the same conditions of ambient atmosphere (see Figure 2.3). A similar plateau behavior has been reported [30] for fuels with burnup in the range 27 to 48 MWd/kg M oxidized at 175°C and 195°C. The time to reach the plateau, $t_{2.4}$, has been shown [30] to have an Arrhenius dependence and can be expressed by the equation

$$t_{2.4}\,(\text{h}) = 2.6 \times 10^{-9} \exp(111 \pm 29\ \text{kJ mol}^{-1}/\text{RT}) \qquad (2.3)$$

where R is the ideal gas constant (8.314 J mol^{-1} K^{-1}), and T is the temperature (K). Given enough time or temperatures greater than 250°C, oxidation continues past the plateau to higher O/M ratios. It is clear that before the plateau is reached, i.e., O/M ratio < 2.4, the fuel consists of a mixture of UO_2 and $UO_{2.4}$,

with no indication of U_3O_8 formation [10,30]. The present study was initiated to determine the mechanism and kinetics of LWR spent fuel oxidation on and after the plateau.

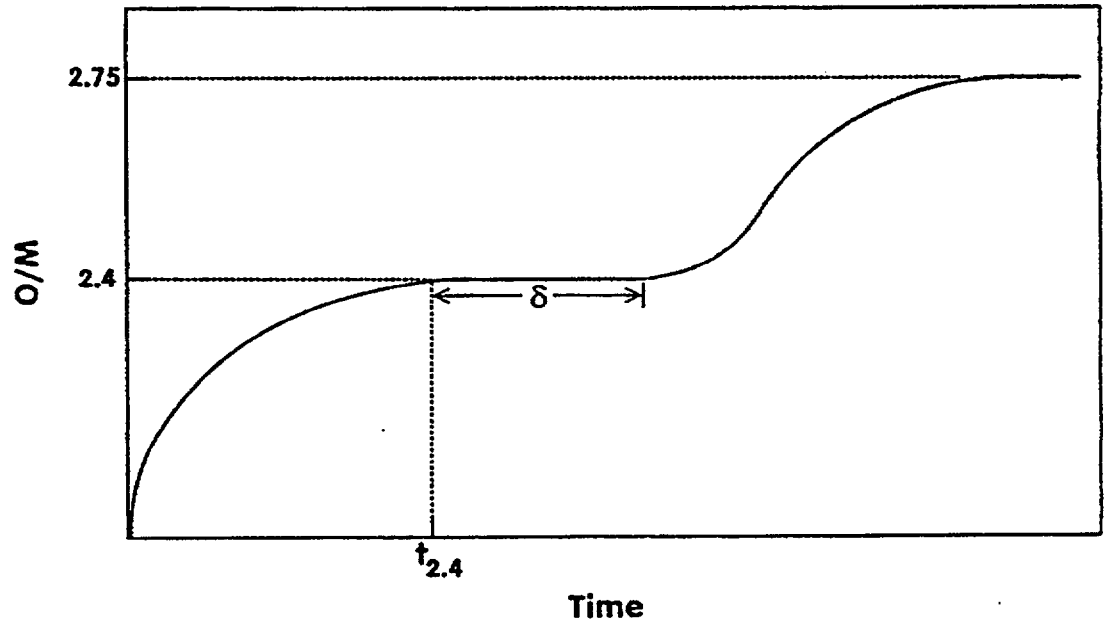

Figure 2.2. Schematic Curve Representing the O/M Ratio of LWR Spent Fuel as a Function of Oxidation Time

2.2.3 Oxidation of Doped UO_2

It has long been known that added impurities stabilize the fluorite structure in UO_2 [43-45]. Spent fuel has three main categories of impurities: fission products, other actinides (e.g., thorium or plutonium), and dopants added for reactivity control or to decrease the fuel volatility. Wilson et al. [43] oxidized mixtures containing up to 60 mole% La_2O_3 or Y_2O_3 with UO_2 at 1375°C and 1750°C. The oxidation rates decreased with increasing impurity additions, and the fluorite structure was stabilized with respect to oxidation to orthorhombic phases of higher O/M ratios at impurity concentrations above about 35 mole%. Roberts et al. [44] have also reported the stabilization of the cubic phase for doping urania with Y_2O_3, ThO_2, ZrO_2, PuO_2, and NpO_2. Adding La_2O_3 to uranium dioxide also has shown the cubic fluorite phase to be stable over a considerable portion of the uranium oxide-lanthanum oxide system; U_3O_8 was observed for specimens oxidized in oxygen at 1000°C only when the La_2O_3 concentration was less than about 20 mole% [45].

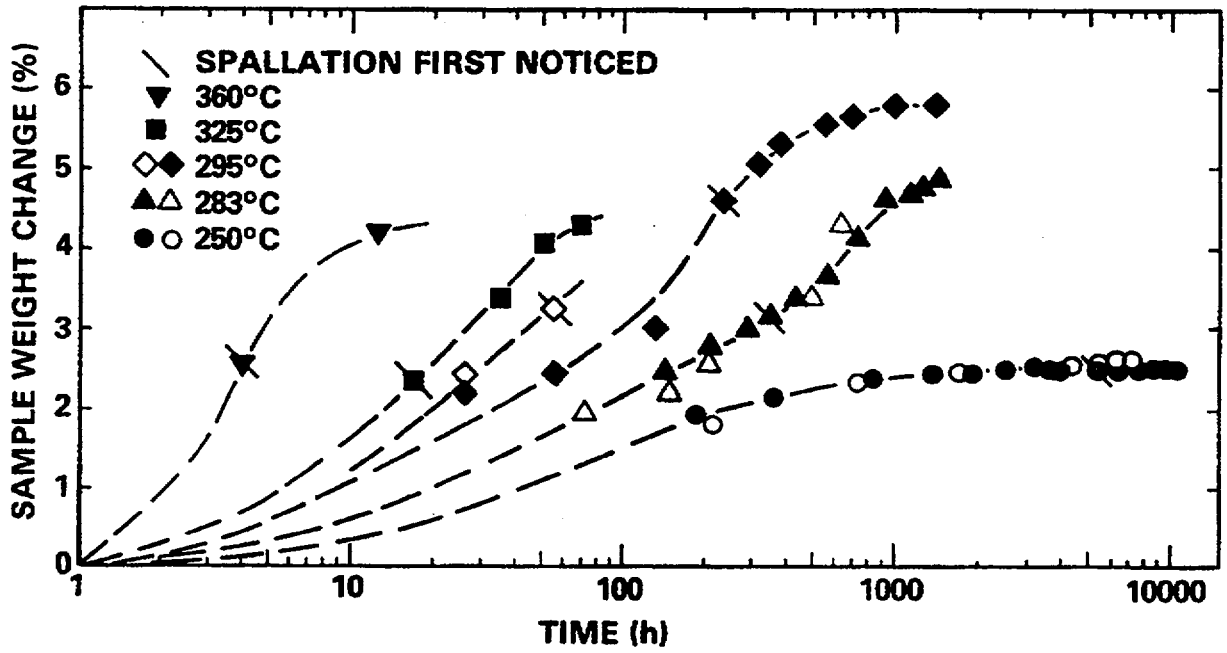

Figure 2.3. Oxidation Behavior of LWR Spent Fuel Fragments at Various Temperatures [4]

Oxidation studies of mixed oxide fuels containing uranium, plutonium, and/or thorium have also been conducted because of their importance as potential reactor fuels. Roberts et al. [44] reported that for air oxidation at 500°C, only cubic phases were formed in $(U,Pu)O_2$ mixtures with Pu concentrations of greater than 20 mole%. Brett and Fox [46] studied the oxidation of $(U,Pu)O_2$ mixtures at 750°C. For mixtures with 1 to 40 mole% PuO_2, the oxidation resulted in a mixture of an orthorhombic and cubic phase, whereas only a cubic phase was observed for the mixed oxides with 60 or 80 mole% PuO_2. There is evidence that the Pu and U cations migrate since the oxidation of a $(U,Pu)O_2$ powder containing 39.9 mole% Pu produced roughly equal amounts of the cubic and orthorhombic phases. However, the cubic phase consisted of ~80 mole% Pu, while the orthorhombic phase contained only ~4 mole% Pu. Similar results led Leme and Matzke [47] to study the self-diffusion of U in U_3O_8. Although they found the diffusion of U in orthorhombic U_3O_8 to be much faster than diffusion in UO_2, it was not fast enough to explain the observed segregation of the metal atoms during oxidation below 800°C. The apparent migration, however, may actually be a result of the inhomogeneity of $(U,Pu)O_2$ [48] or the mechanical and chemical processes that occur during oxidation to higher oxides that might enhance metal atom diffusion [47]. Tennery and Godfrey [49] oxidized $(U,Pu)O_2$ solid solutions with 20 and 25 mole% Pu. They found that M_3O_7 (M=U,Pu) was formed for the lower Pu content fuel, and cubic M_4O_9 was formed for the 25 mole% Pu fuel. Although the rates of oxidation were found to be strongly influenced by the

method of oxide fabrication (coprecipitation, sol-gel, mechanical blending), all samples oxidized in the temperature range 480°C to 750°C exhibited a plateau behavior similar to that observed in spent fuel oxidation at lower temperatures. Similarly, Roberts et al. [44] reported that mixed oxides of UO_2 and ThO_2 containing more than 22 mole% ThO_2 are stable in air at any temperature. Mixtures containing more than 50 mole% ThO_2 are stable, meaning the fluorite structure remains intact, even under very strongly oxidizing conditions.

Thomas et al. [35] conducted oxidation experiments on unirradiated fuel pellets with 4 and 8 wt% Gd_2O_3 and 0.4 wt% NbO_2, as well as on undoped fuel. All samples were oxidized at a heating rate of 5°C min^{-1}. The formation of M_3O_8 (M=U, Gd) shifted to higher onset temperatures with increasing Gd content. The undoped and Nb-doped material oxidized first to U_3O_7 and then to U_3O_8 whereas both Gd-doped specimens oxidized to U_4O_9 and then to U_3O_8. Campbell et al. [39] also found that the presence of Gd (as 5 or 10 wt% Gd_2O_3) in UO_2 inhibited the formation of U_3O_8 relative to undoped material when oxidized at 200°C. However, they reported that the initial rate of oxidation was greater for the doped material. Natural uraninite and pitchblend, which contain large amounts of impurities such as Th, Si, Pb, or Ca, have also been heated at temperatures up to 300°C and oxidized to cubic U_4O_9-like structures [50].

A recent study [51] using simulated high-burnup fuel (SIMFUEL), UO_2 doped with various non-radioactive impurities in quantities that correspond to those found in spent fuel of specific burnup, has also shown the stabilization of UO_2 with respect to air oxidation to U_3O_8. SIMFUEL samples with simulated burnups of 1.5, 3.0, 4.0, 6.0, and 8.0 atom% were oxidized in the temperature range 150°C to 320°C. Quantitative XRD analysis was used to determine the amount of each phase present at various stages of oxidation. Oxidation of the 6% and 8% SIMFUEL yielded a cubic phase similar to that obtained in the oxidation of spent fuel. Lower burnup specimens yielded U_3O_7-type phases when oxidized. The results of Choi et al. [51] also clearly show that a positive correlation exists between simulated burnup and the time required for U_3O_8 powder formation at 250°C. The time for powder formation, t_p, was assumed to be the time required for 8% surface oxidation to U_3O_8. For undoped UO_2, t_p was about 1.3 to 3.3 days; for 3% SIMFUEL, t_p was about 6.6 days; and for 8% SIMFUEL, t_p>317 days. The authors reported that the time for powder formation can be calculated using the expression

$$\ln(t_p) = (0.469 \pm 0.040) \times B + 0.875 \qquad (2.4)$$

where B is the simulated burnup in atom%, and t_p is in days.

2.2.4 Burnup-Dependent Oxidation

Low-burnup (6 to 12 MWd/kg M) CANDU™ fuel oxidizes by surface formation of U_3O_7 followed by formation and spallation of U_3O_8, the same process as unirradiated UO_2. There is some evidence that LWR fuel with burnups in this low range also form U_3O_7 upon oxidation in air [12]. Some samples with burnups ≤8 MWd/kg M oxidized at temperatures ranging from 135°C to 230°C displayed U_3O_7 when analyzed by XRD, whereas other samples displayed U_4O_9. There is some question concerning the validity of these data since the samples were subjected to an unknown quantity of fluorine during the testing [52]. The presence of this stronger oxidizing agent may have facilitated formation of U_3O_7, although no U_3O_7 was observed for samples with higher burnup oxidized to similar O/M ratios under identical conditions. Typical LWR spent fuel oxidizes to $UO_{2.4}$, a phase that maintains the cubic structure of UO_2 and is similar to U_4O_9, before oxidizing to U_3O_8. Einziger et al. [30] previously showed that fuels having burnup in the range 27 to 48 MWd/kg M apparently have no correlation of burnup with the oxidation kinetics of the UO_2 to $UO_{2.4}$ transition. The slight differences observed in the initial rate of change in O/M for the various LWR spent fuels examined have been attributed to grain size [38]. After a short transitory period, however, all fuels tested oxidized at essentially the same rate [30]. Bennett and coworkers [53,54] studied the oxidation of a number of irradiated UO_2 fuel specimens from advanced gas-cooled reactors (AGR) in air at 175°C to 400°C and also found no correlation between burnup (11.7 to 26.7 MWd/kg M) and the time required for formation of U_3O_8 powder. However, they did note that the induction period for the production of particulate U_3O_8 was shorter on irradiated fuel than on unirradiated UO_2. You et al. [55] oxidized fragments of PWR fuel with reported burnups of 13.9 and 39.2 MWd/kg M at 350°C. They reported no burnup dependence of oxidation behavior, but did note that irradiated fuel initially oxidizes faster than unirradiated UO_2.

In contrast, Harrison et al. [56] oxidized spheres (approximately 120 μm diameter) of natural and 93% enriched UO_2 irradiated to burnups in the range 0 to 9 atom% at temperatures in the range 320°C to 380°C. The authors reported activation energies for two different stages of oxidation that correspond to the two sections observed in a plot of $(1-\alpha)^{-1}$ as a function of time, where α is the fraction of the specimen oxidized. However, they state that the second stage does not necessarily correspond to the $U_3O_7 \rightarrow U_3O_8$ transition. Still, in that report, there is no observed dependence of oxidation behavior on kinetics for the first stage, but the activation energy for the second stage increases from 63 kJ mol^{-1} at low burnup to 105 kJ mol^{-1} at a burnup of 9 atom%.

Einziger and Strain [4] reported an increase in the time required for spallation to be observed, a possible measure of U_3O_8 formation, with increased burnup at 295°C for PWR fragments (22.1 to 26.7 MWd/kg M). Further, propagation of cladding cracks in breached PWR rod segments was observed to begin earlier in segments from the low-burnup end of a fuel rod than in segments from the higher-burnup center of the rod. This result was consistent with earlier tests on defected whole rods [5], where U_3O_8 formed at the low-burnup end within 2235 hours at 229°C and split the cladding. The higher-burnup center of the rod displayed only minor U_3O_8 formation after as long as 5962 hours. It is important to note that the formation of U_3O_8 in quantities large enough to be detected by XRD precedes visible powdering in both unirradiated UO_2 [26] and spent fuel [12], and thus visible powdering is not a precise method of determining the extent of U_3O_8 formation. Campbell et al. [57] have also reported that increasing burnup retards U_3O_8 formation, but some of their data are questionable because of the presence of fluorine in the experiments [52].

Nakamura et al. [36] observed that fuel near the center of pellets in defected-rod tests oxidized to U_3O_8 faster than fuel near the pellet surface. While the authors attributed this to a larger specific surface area of the grains near the center, it may instead be caused by the known radial variation in burnup that is a result of the intense resonance absorption in ^{238}U. The radial distribution in fission rate leads to burnup at the fuel surface at a factor of 1.2 to 2.8 larger than at the centerline of the fuel, depending on the final bulk average burnup and the detailed irradiation conditions [41,58]. This radial distribution is further discussed in Section 2.3.2.

2.2.5 Summary of Previous Oxidation Work

- Unirradiated UO_2 and low-burnup spent fuel oxidize via the two-step process $UO_2 \rightarrow U_3O_7 \rightarrow U_3O_8$, where the oxidation proceeds mainly as formation of a product layer on the surface of a specimen, and the transitions occur concurrently at temperatures ≥250°C.
- Typical LWR spent fuel oxidizes via the two-step process $UO_2 \rightarrow U_4O_9 \rightarrow U_3O_8$, where no U_3O_8 formation has been observed until conversion of the entire grain to U_4O_9 is complete, at least at temperatures <250°C.
- The U_4O_9 phase in spent fuel accommodates excess oxygen beyond the nominal stoichiometry of $UO_{2.25}$ and typically forms $UO_{2.4}$.
- Initial rates of oxidation of irradiated fuel are greater by a factor of 5 to 10 as compared to unirradiated fuel. The presence of fission gas bubbles on the grain boundaries is thought to be the main reason for this increase and results in the rapid grain boundary oxidation observed in spent

fuel. However, similar rate increases have been observed with doped UO_2, which does not contain such gas bubbles.

- LWR spent fuels exhibit an apparent resistance to oxidation beyond $UO_{2.4}$, as exhibited by the plateau behavior observed in plots of O/M as a function of time.
- Unirradiated UO_2 doped with rare earths, higher actinides, and fission product simulants has also exhibited an apparent resistance to U_3O_8 formation at large dopant concentrations.
- Some evidence exists that the stabilization of the cubic $UO_{2.4}$ phase with respect to oxidation to the orthorhombic U_3O_8 occurs over the range of burnup found within a typical spent fuel element.

2.3 Spent Fuel Chemistry

Fission of a single U or Pu nucleus produces two fission-product atoms. Thus, for every 1 atom% burnup, there are very nearly 2 atom% (neglecting oxygen) fission products produced. Since 1 atom% burnup corresponds roughly to 10 MWd/kg M (9.6±0.3 [59]), fuels with typical burnups in the range 30 to 50 MWd/kg M will contain approximately 6 to 10 atom% fission products. However, only about one-half of these fission products may occupy the vacancies created in the metallic sublattice by fission. Other dopants, e.g., Gd, which will substitute for U ions in the metallic sublattice, are often added to the UO_2 to serve as burnable poisons for reactivity control in the reactor. In addition, neutron absorption in ^{238}U leads to significant production of heavier actinides, especially Pu and to a lesser extent Am. Table 2.2 lists the typical elemental composition as predicted by the Oak Ridge Isotope Generation and Depletion code (ORIGEN2) [60] using the PWR-US [61] cross section library for PWR spent fuel irradiated to 33 MWd/kg M and allowing for a 10-year decay.

2.3.1 Chemical State of Impurities in Spent Fuel

The chemical state of the fission products and higher actinides determines what effect, if any, they will have on oxidation. Table 2.3 groups the elements listed in Table 2.2 by their chemical states. The fission gases (Xe and Kr) are significant in their role of forming gas bubbles within the UO_2 grains and, more importantly, along grain boundaries. Iodine and bromine are volatile fission products that are chemically active and may react with other elements, or, along with other possible volatiles such as Cs, Rb, and Te, may form gas bubbles similar to Xe and Kr [62]. The metallic elements Mo, Ru, Pd, Tc, and Rh are known to form a metallic precipitate, referred to as ε-Ru, whose composition is approximately in proportion to the fission yields [10,34] of these five metals. This five-metal phase is the only precipitate commonly found in LWR spent fuel [34], although the tendency to precipitate other fission products increases slightly at the higher fuel temperatures found near the pellet centerline. Thomas et al. [10]

examined spent fuel oxidized to a final O/M ratio of 2.13 and determined that the ε-Ru was unaffected by oxidation of the UO_2 to U_4O_9. Other fission products thought to form metallic precipitates include Ag, Cd, In, Sn, Sb, and Te [63,64]. Minor amounts of Cd, Sn, and Ag were found with α-Pd particles at the high-temperature center (estimated at 1700°C) of an LWR fuel rod that had experienced high fission gas release [34].

Table 2.2. Typical Composition of PWR Spent Fuel from ORIGEN2 Calculation[a]

Element	Z	Weight %[b]	Atom %[b]
U	92	95.62	92.36
Pu	94	0.87	0.82
Xe	54	0.53	0.93
Nd	60	0.40	0.64
Zr	40	0.36	0.91
Mo	42	0.33	0.79
Cs	55	0.24	0.42
Ce	58	0.24	0.39
Ru	44	0.22	0.50
Ba	56	0.17	0.28
Pd	46	0.14	0.30
La	57	0.12	0.20
Pr	59	0.11	0.18
Sm	62	0.09	0.14
Tc	43	0.08	0.19
Sr	38	0.08	0.21
Am	95	0.06	0.06
Te	52	0.05	0.09
Np	93	0.05	0.05
Y	39	0.05	0.13
Rh	45	0.05	0.11
Kr	36	0.04	0.11
Rb	37	0.04	0.11
I	53	0.02	0.04
Eu	63	0.01	0.02
Cd	48	0.01	0.02
Gd	64	0.01	0.01
Cm	96	0.002	0.002

(a) 33 MWd/kg M burnup, 10-year decay period, 3.2% initial ^{235}U enrichment.

(b) On a per gram initial uranium basis, neglecting oxygen.

It has been reported [63-65] that the elements Rb, Cs, Ba, Zr, Nb, Mo, Te, and even Sr form complex oxide (i.e., zirconates, uranates, molybdates) precipitates that are known as the "gray phases" because of their appearance under electro-optical examination. Although the gray phases have been reported widely for fast breeder reactor (FBR) fuels [63,64], in SIMFUEL that simulates fuel operated at high temperature (1650°C) [66], and in LWR fuels subjected to higher-than-normal operating temperatures, such as exist under transient conditions [65,67], they have not been observed in typical LWR fuels operated at low temperature [34,68-70]. Even in the LWR fuel that had experienced a peak centerline temperature of 1700°C, no precipitates containing Ce, Nd, Ba, Sr, Zr, or Cs were found in the UO_2 [34]; however, the detection limit for the TEM/EDS (energy-dispersive X-ray spectrometry) analysis is approximately 10 nm, and precipitates smaller than this limit would not be observed.

Table 2.3. Chemical State of the Main Fission and Transmutation Products[(a)]

Elements	Chemical State
Xe, Kr	Fission Gas Bubbles
I, Br, (Cs, Rb, Te)	Volatiles
(Mo), Ru, Pd, Tc, Rh, [(Ag, Cd, In, Sn, Sb, Te)][(b)]	Metallic Precipitates
[Nb, (Rb, Ba, Cs, Te, Zr, Mo, Sr)][(b)]	Oxide Precipitates
Np, Pu, Am, Cm, La, Ce, Pr, Nd, Pm, Sm, Eu, Gd, Y, (Sr, Zr, Ba, Te, Mo)	Soluble in Fuel Matrix

(a) Elements in ( ) exhibit the possibility of an alternative chemical state.

(b) Not observed in LWR spent fuels at normal operating temperatures.

For the purpose of this study, the most important elements are those that form oxides in solid solution with the UO_2; that is, they may act as substitutional ions in the fuel matrix. These substitutional elements include the actinides Np, Pu, Am, and Cm; the rare earth elements (REE) La, Ce, Pr, Nd, Pm, Sm, Eu, Gd; Y; and Sr, Zr, Ba, Te, and Nb to the limits of their solubility and to the extent that they have not precipitated as metallic particles or as complex oxides [63-65]. However, Thomas et al. [34,68] observed neither the oxides of Ba, Zr, or Cs nor any of the gray phases in LWR spent fuels, suggesting that the elements classified as oxide precipitates may be at least partly soluble in the UO_2 matrix for fuels with peak average burnups ≤48 MWd/kg M. In fact, Schleifer et al. [71] have shown that in the temperature range of 1270 to 1670 K, ZrO_2 is significantly more soluble in ternary (U,Zr,Ln where Ln=La,Ce,Nd) oxides than in UO_2 (0.4 atom% ZrO_2 in UO_2 below 1200°C [72]). The solubility is

sufficiently high that in mixtures simulating a burnup of 20% to 40% fission initial metal atoms (FIMA), only a single phase was found. Those elements that can exist in more than one chemical state will transition between states, depending on the oxygen potential and burnup of the fuel [63] (see Section 2.4).

2.3.2 Radial Variation in Spent Fuel Chemistry

The intense resonance absorption in ^{238}U results in a significant gradient in the radial concentration distribution of Pu near the surface of UO_2 pellets, as well as a corresponding gradient in both fission rates and the concentration of fission products and heavier actinides. The outer 5% of the fuel volume can easily contain about 10% of the total radioactivity of the fuel [41]. Similarly, the concentration of plutonium near the fuel surface is almost a factor of 3 greater than that found in the central regions of the fuel pellet for LWR spent fuels of moderate burnup. Figure 2.4 is a plot of the radial distribution, as measured by electron probe microanalysis (EPMA), of Pu in a PWR spent fuel pellet with a pellet-average burnup of 44.3 MWd/kg M. Figure 2.5 is a plot of the corresponding radial burnup profile for the same fuel pellet, as found by comparing EPMA results for Nd with concentrations predicted by ORIGEN2. It is clear that the burnup varies from ~42 MWd/kg M at the pellet center to ~70 MWd/kg M at the fuel pellet surface [69]. Similar burnup distributions, with burnup at the fuel surface a factor of 1.2 to 2.8 larger than at the centerline, have been previously reported [41,58]. The total concentration of fission and transmutation product impurities, including impurities that can substitute for U in the UO_2 lattice, will thus vary with radial location. Although the thickness of the fission product- and actinide-rich region is typically on the order of 100 to 200 μm, it corresponds to 4% to 8% of the total fuel volume.

The total fission product concentration is directly proportional to burnup, which is known to vary as a function of both radial and axial position within the fuel rod. The elemental fission product concentrations depend, in turn, on the isotope fissioned, as seen in Figure 2.6. Overall, fission of Pu results in yields of the noble metals Ru and Rh nearly a factor of 2 greater than their yield by fission of U; the cumulative yield of Pd from fission of Pu is approximately a factor of 10 greater than for fission of U (see Table 2.4). However, the cumulative elemental yields for Y, Zr, and Mo are significantly less for Pu than for U; fission of Pu also yields generally smaller amounts of the REEs than does U. The cumulative elemental yields for the major fission products that may remain in solid solution are listed in Table 2.4. (If the half life of an isotope is less than 5 years, then it was assumed that decay of that isotope to its daughter is complete; if the half life is greater than 50 years, it was assumed that no decay has occurred and thus no daughter had been formed. For those isotopes with a half life $5<t_{½}<50$ years, the yield was counted for both the parent and daughter. For example, the yield for ^{137}Cs with a half life of 30 years was

counted both for ^{137}Cs and ^{137}Ba.) Thus, the chemical properties of any segment of spent fuel will depend more-or-less strongly on its specific radial and axial location within the fuel rod.

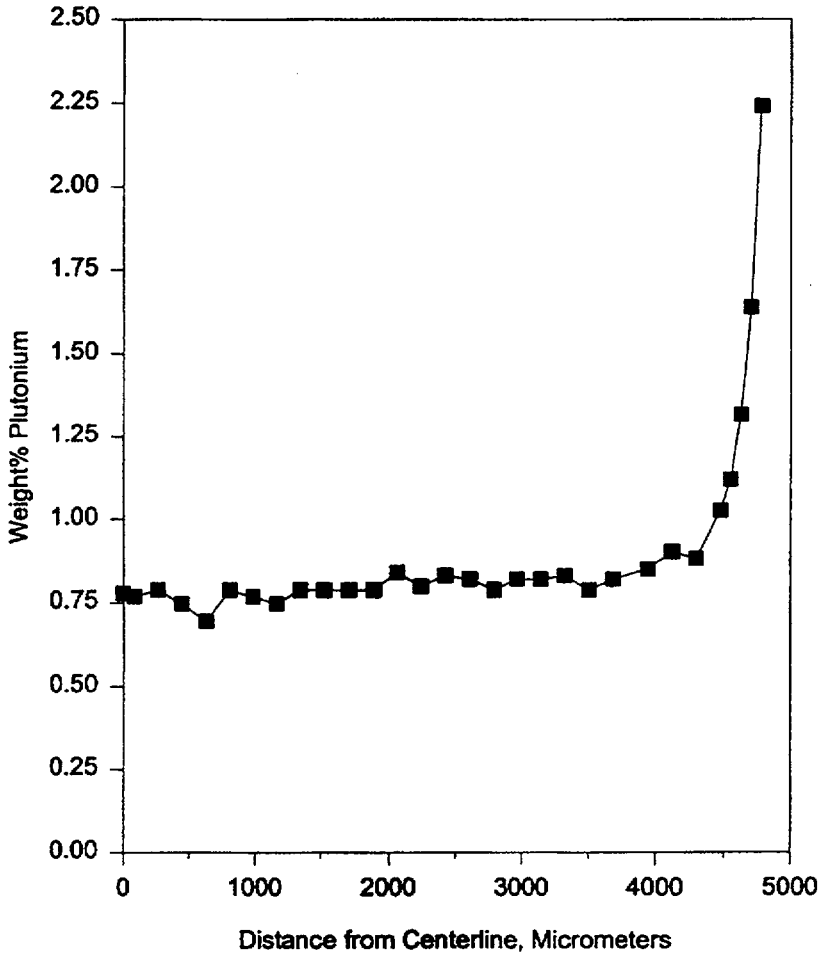

Figure 2.4. Radial Profile of Plutonium in ATM-104 Fuel Measured by EPMA [69]

2.4 Oxygen Potential

The factor that determines whether a particular fission product is stable as an element or as an oxide in the fuel matrix is the difference between the free energy of formation of the fission product oxide and the oxygen potential of the fuel. The oxygen potential is defined in terms of the equilibrium partial pressure of oxygen over the mixture as

$$\Delta\bar{G}_{O_2} = RT \ln p_{O_2} \tag{2.5}$$

If the free energy of formation of the fission product oxide is less (more negative) than the oxygen potential of the fuel, the oxide will be formed; otherwise, the fission product is expected to be present as the element at chemical equilibrium. Figure 2.7 is a plot of the free energies of formation for the high-yield fission products as a function of temperature. The ability to transform from element to stable oxide is especially important for Mo, which can act as a buffer to fuel oxidation [75-77].

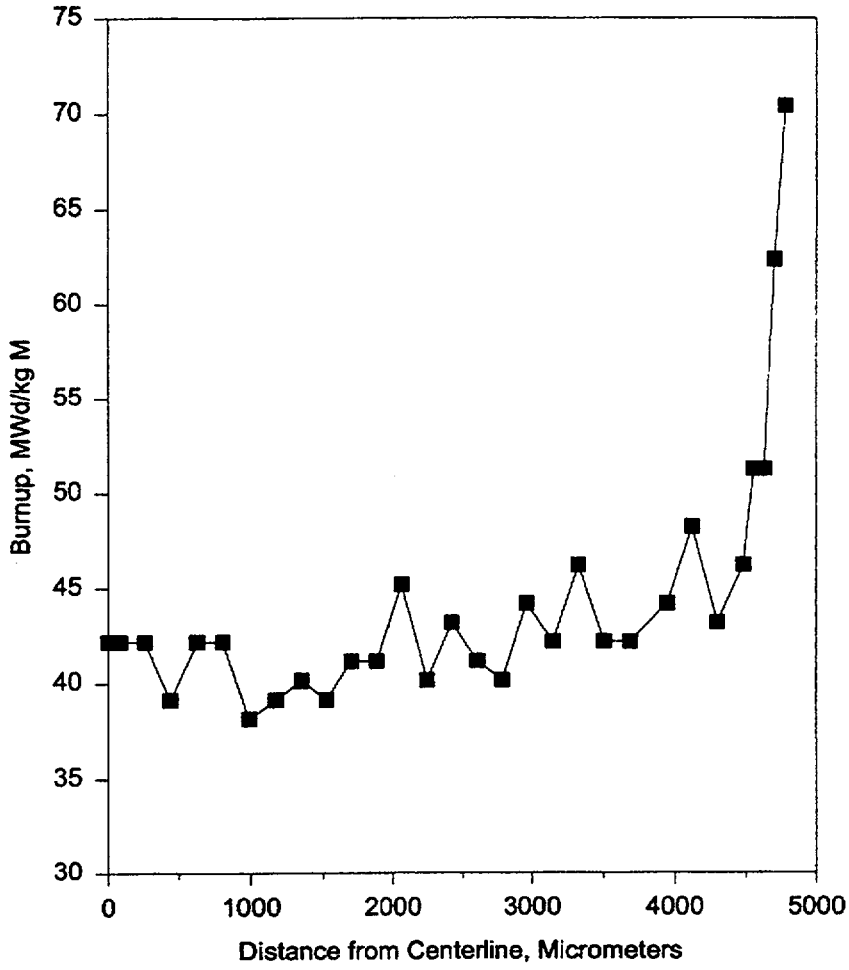

Figure 2.5. Radial Burnup Profile in ATM-104 Fuel with a Pellet Average Burnup of 44.3 MWd/kg M Measured by EPMA [69]

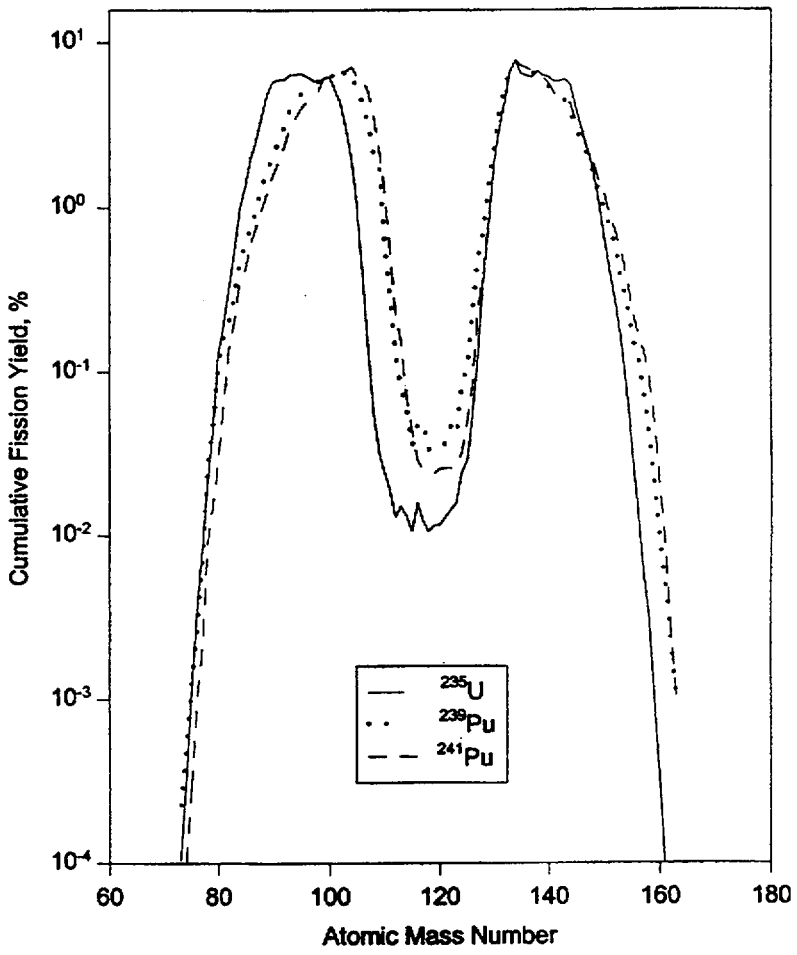

Figure 2.6. Cumulative Yields for Thermal Fission of ^{235}U, ^{239}Pu, and ^{241}Pu [73]

The oxygen potential is both a measure of the stability of an element with respect to oxidation and the stability of the oxide with respect to reduction to the free element. Therefore, it is reasonable to conclude that anything that affects the binding of an atom in the chemical form of the free element being considered or affects the potential function of the oxide lattice can affect the magnitude of the oxygen potential. Thus, impurities, either free element or oxide, within the lattice of a substance could have an impact on the oxygen potential relative to the pure oxide and pure element, to the extent that the impurities affect the mean binding of an atom. The oxygen potential of the fuel will be shown to be a function of temperature, impurity concentration, and the O/M ratio. As the oxygen potential of the fuel changes, those fission products with free energies of formation close to that of the fuel may experience a change in chemical state. It is important to note, however, that the reaction kinetics can also be affected even if the oxygen potential is not changed significantly since it is possible to change the potential barrier

over which the reaction must proceed without changing the initial and final states significantly. The kinetics of a reaction can be affected even if the difference in energies between the initial and final states does not change.

Table 2.4. Cumulative Elemental Yields (%) for Thermal Fission [73]

Z	Element	^{235}U	^{239}Pu	^{241}Pu
37	Rb	3.88	1.60	1.16
38	Sr	9.35	3.45	2.52
39	Y	4.82	1.69	1.22
40	Zr	36.76	21.03	16.58
42	Mo	24.47	22.96	19.92
43	Tc	6.07	6.16	6.08
44	Ru	11.44	17.83	20.04
45	Rh	3.03	6.94	6.73
46	Pd	1.60	15.79	22.44
52	Te	2.24	3.37	2.33
55	Cs	19.41	21.26	20.67
56	Ba	12.90	12.86	13.31
57	La	6.36	5.54	6.22
58	Ce	12.05	10.31	10.48
59	Pr	5.79	5.29	4.91
60	Nd	20.72	16.22	18.03
62	Sm	4.17	4.84	5.77
63	Eu	0.16	0.36	0.54
64	Gd	0.06	0.41	0.66

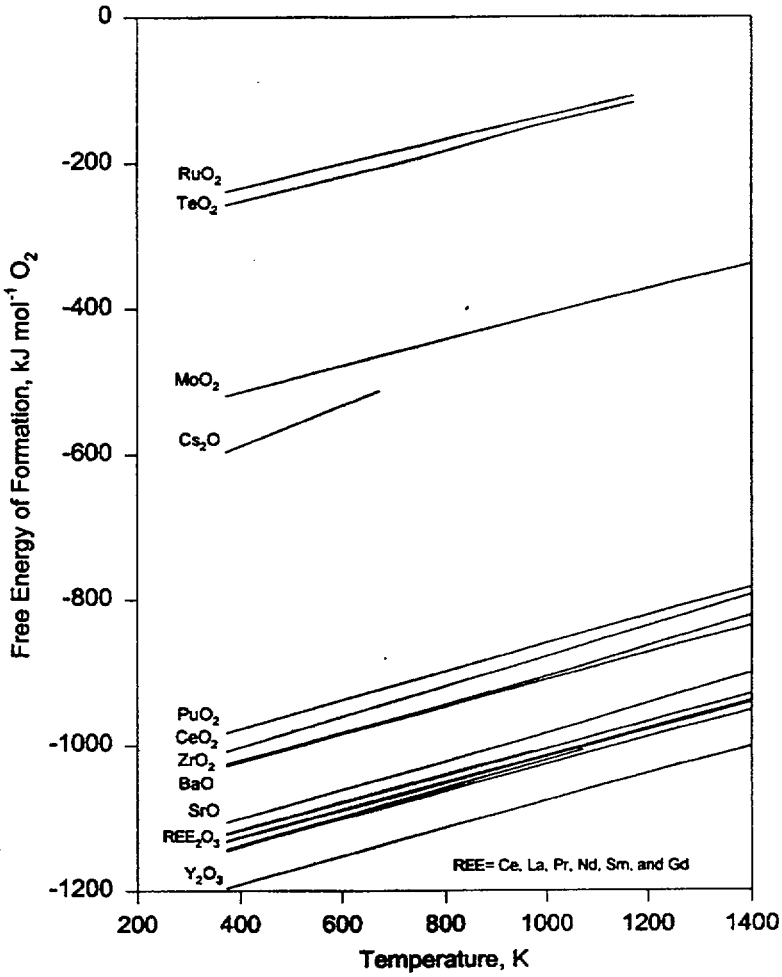

Figure 2.7. Free Energy of Formation as a Function of Temperature for High-Yield Fission Products [74]

2.4.1 Oxygen Potential of UO_2 and UO_{2+x}

The existing database for oxygen potential measurements on UO_2 and UO_{2+x} is extensive; however, very little work has been performed at temperatures below 900°C. Lindemer and Besmann [78] have summarized this database. Two general trends are observed and widely reported: 1) the oxygen potential for a fixed stoichiometry becomes more positive with increasing temperature (see, for example, Figure 2.8), and 2) for a fixed temperature, the oxygen potential becomes more positive as the oxygen-to-uranium (O/U) ratio increases (see, for example, Figure 2.9). In particular, the oxygen potential increases sharply as the fuel changes from being slightly hypostoichiometric to slightly hyperstoichiometric. This large increase in the oxygen potential is due to the change in the predominant oxygen defect from anion

vacancies to interstitial anions [79]. Again, most of the data were taken at temperatures above 900°C, and extrapolation to lower temperatures is not necessarily valid.

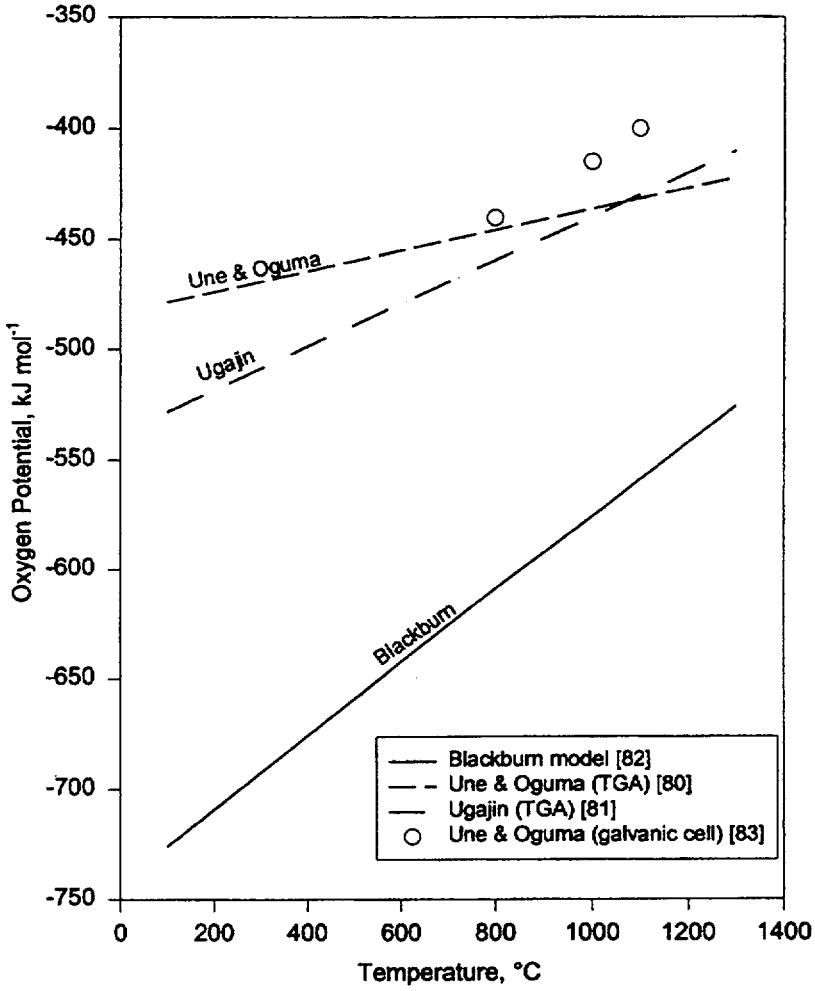

Figure 2.8. Oxygen Potential for $UO_{2.00}$ as a Function of Temperature

Figure 2.8 is a plot of the oxygen potential of stoichiometric UO_2 as a function of temperature as reported by Une and Oguma [80], Ugajin [81], and for the Blackburn model [82], which has been shown to predict the oxygen potential of $UO_{2\pm x}$ with reasonable accuracy. The experimental data were taken in the temperature range 1000°C to 1300°C, and the validity of the extrapolations at lower temperatures is questionable. However, it is clear that the oxygen potentials measured at the higher temperatures using thermogravimetric analysis (TGA) and galvanic cell methods are more positive than the Blackburn model predictions by ~90 to 140 kJ mol^{-1} [80]. When extrapolated to the lower temperatures of interest for this study, the TGA data of Une and Oguma have even larger deviations from the Blackburn values. However, Une and Oguma [80] have suggested that their data, as shown in Figure 2.8, may not represent

$UO_{2.00}$, but rather UO_{2+x} where x is in the range 10^{-6} to 10^{-5}, exhibiting the sensitivity of the oxygen potential near exact stoichiometry. Still, the trend of increasing oxygen potential with increasing temperature for a fixed stoichiometry is evident in all cases.

Figure 2.9 is a plot of the oxygen potential of UO_{2+x} at 750°C, 1000°C, and 1200°C as a function of O/U ratio. As UO_{2+x} becomes more hyperstoichiometric, and thus the valence of U increases, the oxygen potential becomes more positive. Figure 2.10 is a plot of the predicted values of the oxygen potential from the Blackburn model at various temperatures and O/U ratios. Also included is the provisional oxygen potential reported by Rand et al. [85] for the diphasic region U_4O_9/U_3O_{8-z}. Again, it is clear that as UO_2 oxidizes, the oxygen potential becomes more positive. Also, the data in Figure 2.9 correlate excellently with the Blackburn model predictions in Figure 2.10.

2.4.2 Oxygen Potential of Doped UO_2

In an effort to improve the performance of UO_2 as a reactor fuel, the effect of dopants on the thermochemical properties of UO_2 has been studied. For most dopants, the general trend observed is that after a very rapid increase in the oxygen potential around exact stoichiometry, a gradual increase in oxygen potential is observed with increasing O/M ratio, where M includes U and the dopant. The oxygen potential of Gd-doped fuel has been studied extensively [80,83,86] because of its widespread use for reactivity control as a burnable poison. For a fixed temperature and O/M ratio, as the Gd content increases, the oxygen potential also increases. At 1000°C, for example, Une and Oguma [83] report that for exact stoichiometry (i.e., x=0) in $U_{1-y}Gd_yO_{2+x}$, the oxygen potential for y=0 was -415 kJ mol^{-1}, -331 kJ mol^{-1} for y=0.04 (3 wt% Gd_2O_3), -222 kJ mol^{-1} for y=0.14 (10 wt%), and -151 kJ mol^{-1} for y=0.27 (20 wt%). For x>0, the increase in oxygen potential is ~3.0 kJ mol^{-1} per mole% Gd addition [83]. The implication of these data for oxidation of Gd-doped fuels is that when UO_2 and UO_2-Gd_2O_3 fuels are placed in an atmosphere with a fixed oxygen partial pressure, the doped fuel will be at a lower O/M ratio than the UO_2.

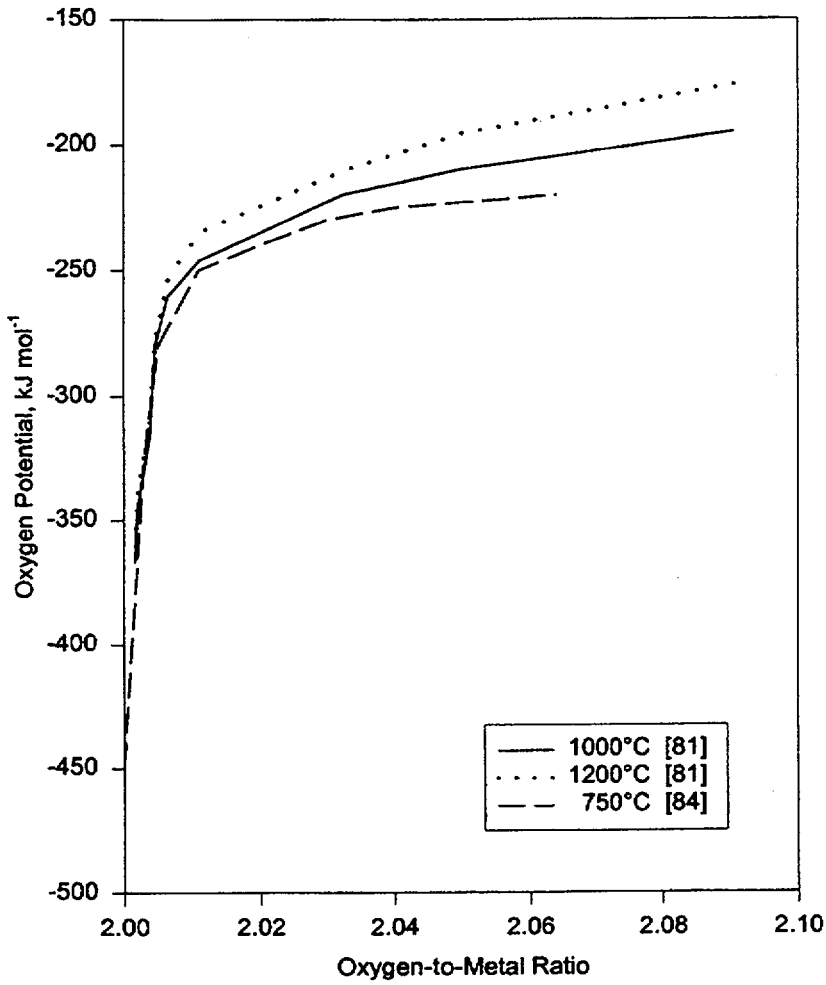

Figure 2.9. Oxygen Potential of Hyperstoichiometric UO_2 as a Function of O/M

Similar behavior has been reported for doping with Y and La [87]. Figure 2.11 is a plot of the oxygen potential as a function of O/M ratio at 1200°C for fuels doped with 2.5% Y, 4.8% Y, 2.5% La, and 5% La, respectively. Again, the oxygen potential of $(U_{1-y}M_y)O_{2+x}$, where M is Y or La, is larger (more positive) than that of UO_{2+x} for the same value of x and increases with increasing dopant content (y). Other authors [88,89] report similar findings for La doping, but with oxygen potentials about 26 kJ mol^{-1} larger than those plotted. UO_2 doped with Nd, one of the highest yield fission products, has been shown to behave similarly to the Gd-doped fuels, with oxygen potentials about 8 to 12 kJ mol^{-1} more negative than those listed above for similar values of x and y [90].

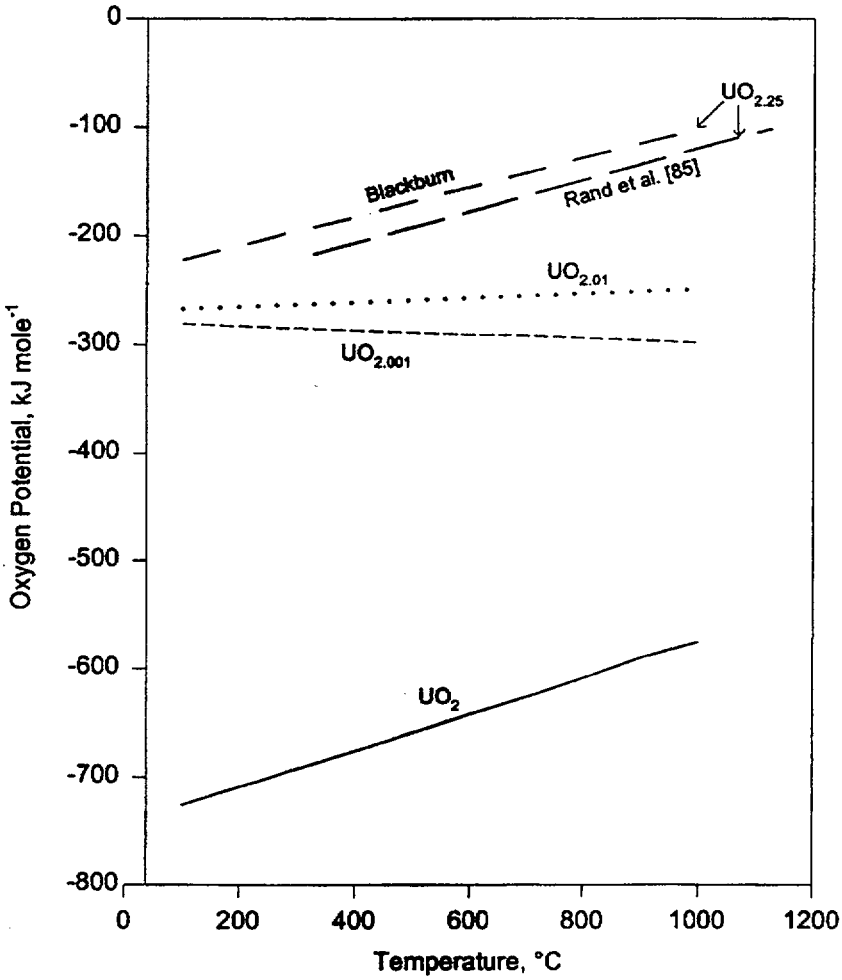

Figure 2.10. Blackburn Model Predictions for the Oxygen Potential in Hyperstoichiometric UO_2 [82]

UO_2 with Eu as a dopant also follows a similar trend in that the oxygen potential for $U_{1-y}Eu_yO_{2+x}$ is more positive at a given temperature and value of x than for UO_{2+x}. However, the oxygen potentials found for the Eu-doped fuels are higher than those of the other REEs [91]. At 1000°C, x=0.01, and y=0.3, the oxygen potential for the Eu-doped fuel is about -90 kJ mol^{-1}, while that for the Gd solid solution is about -150 kJ mol^{-1} [83]. Another important difference between the Eu doping and the other REEs is the steep change in the oxygen potential that occurs at exact stoichiometry (x=0) for the other REEs occurs when x<0 for Eu [91]. Park and Olander [92] explain this behavior by adding stable Eu-anion vacancy clusters to their defect model [93].

Woodley and Adamson [94] reported the oxygen potential of $U_{0.75}Pu_{0.25}O_{2\pm x}$ as a function of O/M at 800°C, 900°C, and 1000°C. These data are plotted in Figure 2.12, along with the data of Ugajin [81]

for UO_{2+x} at 1000°C. Other than near the exact stoichiometric composition (x=0), the mixed oxide again has a larger (more positive) oxygen potential that increases with increasing temperature and O/M ratio. Studies in the hypostoichiometric region, $U_{1-y}M_yO_{2-x}$, where M is either Pu or Ce [95,96], have also shown that the oxygen potential increases with increasing y. Since similar trends exist for hypostoichiometric Gd, Y, La, and Nd, it is assumed that both Pu and Ce will have increasing oxygen potentials with increasing dopant content in the hyperstoichiometric region as well.

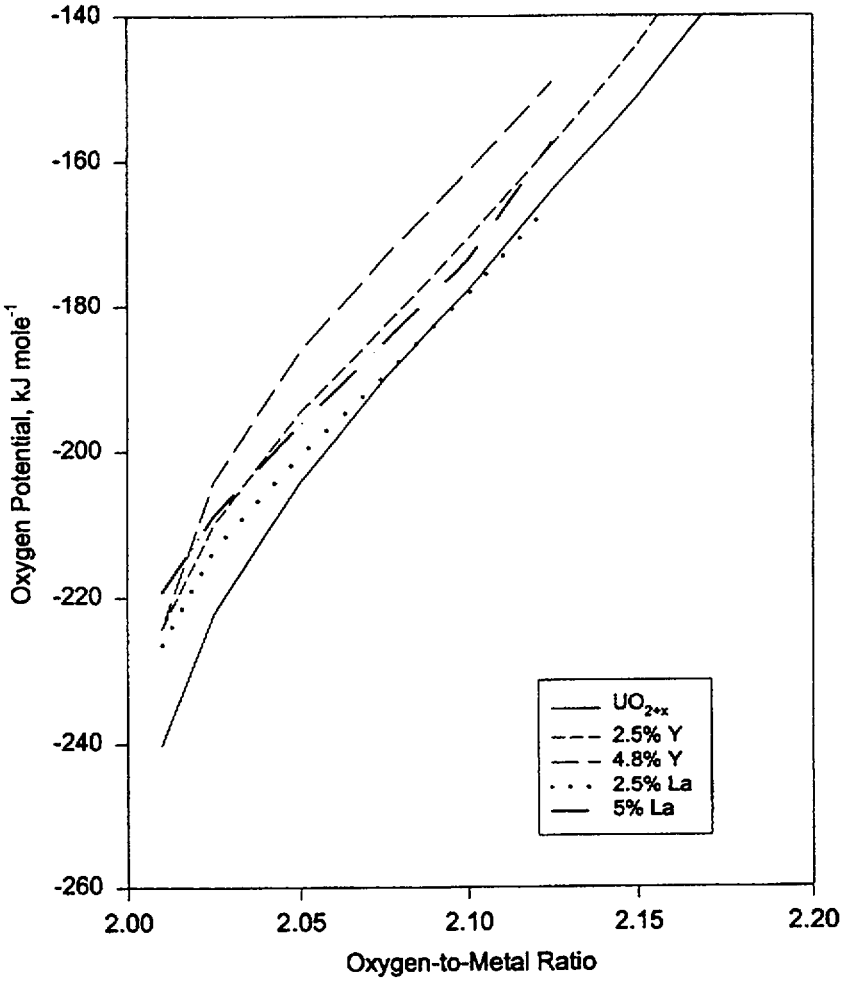

Figure 2.11. Oxygen Potential at 1200°C as a Function of O/M for UO_2 Doped with Y or La [87]

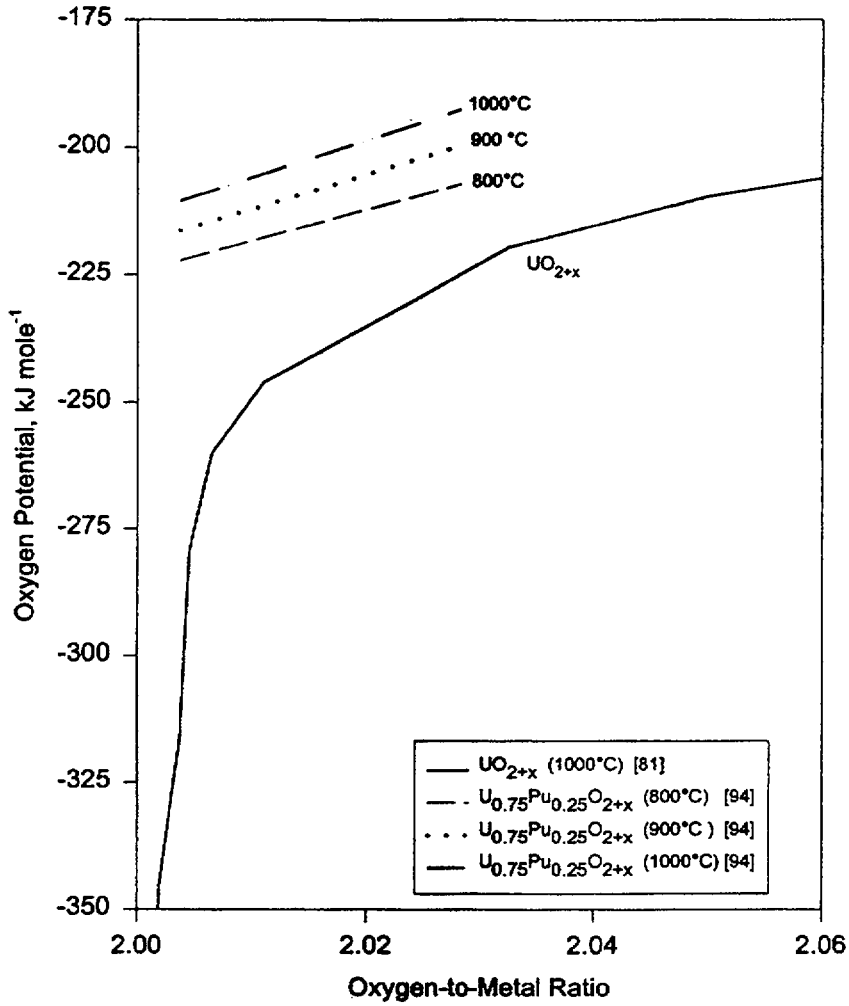

Figure 2.12. Oxygen Potential of $U_{0.75}Pu_{0.25}O_{2+x}$ as a Function of Oxygen-to-Metal Ratio

In addition to the REEs and Pu, Th-doped UO_2 [97] also has oxygen potentials that increase with increasing Th content. Addition of Zr, on the other hand, has been shown to lower the oxygen potential. Une and Oguma [98] have shown that the oxygen potential for $U_{0.85}Zr_{0.15}O_{2+x}$ (~7.5 wt% ZrO_2) is lower than that of pure UO_{2+x} by 12 to 20 kJ mol^{-1} at the same temperature and value of x.

Finally, the oxygen potential has been measured for simulated burnup fuels, UO_2 [99] and $U_{0.75}Pu_{0.25}O_{2-x}$ [79], where Zr, Ce, Pr, Nd, and Y have been added in quantities to simulate 2, 5, and 10 atom% burnup. The quantities of Zr and Y are significantly less for the mixed oxide simulant as a result of the small yield of these elements in Pu fission. For the mixed oxide simulant, the concentration of Zr was reduced by the amount assumed to combine with Ba and Sr, while the concentration of Nd was increased to include the contributions from La, Sm, and Pm. The mixed oxide was tested at 900°C,

1000°C, and 1100°C; at a fixed O/M ratio, the oxygen potential was larger than for UO_{2+x} and increased linearly with burnup, the largest increases occurring at 900°C [79]. As opposed to the simulant for the mixed oxide, the simulant for UO_2 did not have a reduced Zr concentration, but the Nd concentration was increased to account for La and Sm. Nevertheless, the experimental measurements with this material [99] are qualitatively similar to those of the mixed oxide simulant, with the oxygen potential of the simulated burnup fuel as much as 21 kJ mol^{-1} larger than for pure UO_2 and again displaying an increase with increasing burnup. However, the difference between the oxygen potential of the simulant and pure UO_2 decreased with increasing O/M ratio such that at an O/M of 2.006 and a temperature of 1000°C, the difference was only about 4.2 kJ mol^{-1} [99].

SIMFUEL [66], which contains Mo, Ba, La, Sr, Rh, Pd, and Ru in addition to the dopants in the previous simulated burnup fuels, also has slightly higher oxygen potentials than pure UO_{2+x} [76] for a given O/M. For a constant oxygen potential of -246 kJ mol^{-1} at 1000°C, the O/M ratios for UO_2, 3 and 6 atom% SIMFUEL were 2.0025, 2.001, and 2.0005, respectively [76]. It is clear that adding soluble impurities in spent fuel usually increases the oxygen potential relative to unirradiated UO_2, and the solid solutions have considerably higher oxygen potentials for lower values of the impurity valence [100].

2.4.3 Oxygen Potential in Spent Fuel

Since a large fraction of the fission products consists of the rare gases (Xe, Kr) and metallic inclusions (Mo, Tc, Ru, Rh, Pd) that do not combine with oxygen, or the trivalent REEs that combine with less oxygen than the original tetravalent U, it has long been assumed that the fuel would oxidize with increasing burnup as more oxygen is liberated by fission of U. The effect should be even more pronounced for fission of Pu, which has larger yields of the metals. The oxygen potential of spent fuel has been measured to verify this assumption [76,77,84,101,102].

Une et al. [84] measured the oxygen potential at 750°C of UO_2 and UO_2-2 wt% Gd_2O_3 irradiated in commercial boiling water reactors (BWRs) using a solid electrolyte galvanic cell. The oxygen potential of the irradiated UO_2 with burnups of 18 and 30 MWd/kg M ranged from -420 to about -480 kJ mol^{-1}. At 750°C, the oxygen potential of unirradiated $UO_{2.000}$ was predicted by Blackburn [82] to be about -650 kJ mol^{-1}, while that measured for unirradiated $UO_{2.001}$ [84] was about -390 kJ mol^{-1}. For both burnups, the measured oxygen potential decreased (more negative) from the fuel rim to the center [84]. Adamson et al. [101] reported a similar trend with an oxygen potential of -460 kJ mol^{-1} at the fuel rim and -550 kJ mol^{-1} at the center. Similarly, two fuels doped with 2 wt% Gd_2O_3 with burnups of 13 and

27 MWd/kg M had oxygen potentials ranging from -460 kJ mol^{-1} at the rim to -540 kJ mol^{-1} at the center [84], about 40 to 60 kJ mol^{-1} more negative than the undoped fuel. In all cases, the higher burnup fuel had a larger (more positive) oxygen potential at the same radial location than did the lower burnup fuel. This trend is also evident since the burnup at the rim is larger than the bulk average burnup of the pellet, and the oxygen potentials are larger at the rim.

Matzke et al. [102] measured the oxygen potential of unirradiated and irradiated $(U_{0.8}Pu_{0.2})O_{1.982}$ in the temperature range 700°C to 1100°C. Again, the oxygen potential was observed to increase with increasing temperature and also with increasing burnup. Matzke then measured the oxygen potential of low enrichment (1.46% ^{235}U) UO_2 irradiated in a heavy water reactor [76]. The burnup of this fuel ranged from >200 MWd/kg M at the rim to 75 MWd/kg M at the pellet centerline, and thus most fissions were due to Pu. Although the oxygen potential was shown to increase with increasing temperature, in these experiments, the higher burnup rim samples were found to have a smaller (more negative by ~50 kJ mol^{-1}) oxygen potential than the lower burnup specimens from near the centerline of the fuel. Matzke [77] also measured the oxygen potential on spent fuels from the same reactor, but with initial enrichments of ^{235}U of 6.85%, 5.0%, and 8.25% and corresponding burnups of 28.9, 34.5, and 58 MWd/kg M. The oxygen potential was smallest (more negative) for the higher burnup fuel; however, there is no indication of the radial location of these fuel specimens, nor were any uncertainties assigned to the burnups. It is important to note that the rim of the high burnup fuel experienced the typical division of grains (~10 μm diameter) into subgrains (~0.15 to 0.30 μm). Also, no intragranular fission gas bubbles were observed, and the density of precipitates was much lower than in the rim of lower burnup fuels [103]. The center of the specimen, however, contained the typical dislocations, gas bubbles, and five-metal particles.

Both Matzke [76,77] and Une et al. [84] compared their results with unirradiated UO_2 and determined that not only does spent fuel not oxidize with burnup, it may actually be slightly hypostoichiometric. All of the oxygen potentials presented above are plotted as a function of burnup in Figure 2.13. Two trends are clear: 1) the oxygen potential of spent fuel increases with increasing burnup at low to moderate burnup, and 2) at burnups ≥about 30 MWd/kg M, the oxygen potential of the fuel is buffered by the fission product Mo. EDS analysis of the metal precipitates in the rim zone has indicated the presence of Mo, but some Mo oxidation may have occurred [76], especially since Mo has been shown to oxidize in SIMFUEL before the UO_2 matrix oxidizes [77]. The cladding of the high burnup fuels tested by Matzke was found to have formed an oxidized surface layer of <10 μm for the 58 MWd/kg M fuel and of 15 to 20 μm for the 75 MWd/kg M fuel [77]. This suggests, as shown previously by

Kleykamp [63], that at the high temperatures known to have existed in these fuels, oxygen will diffuse toward the cladding, and the Zircaloy can act as an oxygen getter. A similar trend for oxygen to diffuse from the hot fuel center to the cool rim region was suggested by Une et al. [84].

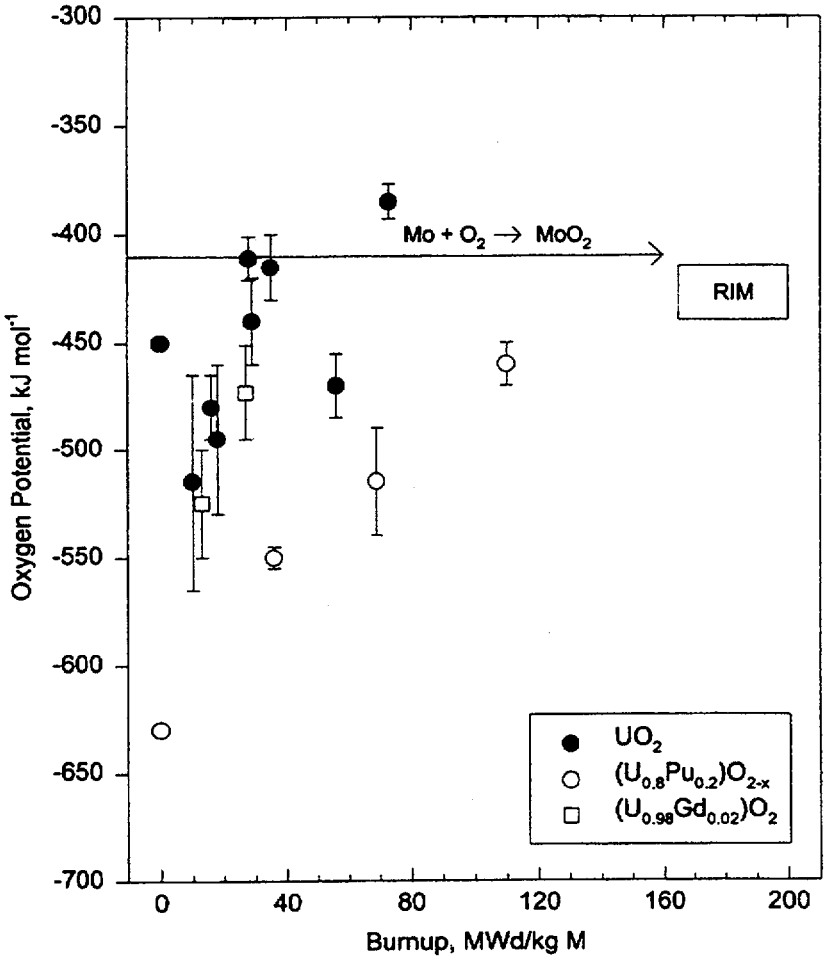

Figure 2.13. Burnup Dependence of the Oxygen Potential at 750°C for Different Irradiated Oxide Fuels [77]

2.5 Theoretical Basis for Matrix Stabilization

It is clear from the previous section that the oxygen potential of UO_2 changes with the addition of impurity ions, either in the form of dopants or fission products. The relative stability of an ionic crystal will be determined by the difference in the lattice energies of the reactant and product phases. It is also important to note that, based on the information presented in Section 2.4, it may be possible for the oxygen potential to be ≥ 0 at high impurity levels and at high O/M ratios, and, depending on the oxygen potential of the ambient atmosphere, thermodynamic control would preclude formation of higher oxides. In most cases, however, the reaction to higher oxides is still thermodynamically favored, but may exhibit slow reaction kinetics. The thermodynamics and kinetics are related because

$$\Delta G^0 = RT \ln K \tag{2.6}$$

where K is the equilibrium constant and ΔG^0 is the standard Gibbs free energy. For a simple homogeneous reaction of the form

$$aA + bB = cC \tag{2.7}$$

that can be broken down into multiple mechanistic steps where a rate-limiting-step approximation holds, the rate expressions for the forward and reverse reactions will be of the form

$$r_f = k_f [A]^{\alpha f} [B]^{\beta f} [C]^{\gamma f} \tag{2.8}$$

$$r_b = k_b [A]^{\alpha b} [B]^{\beta b} [C]^{\gamma b} \tag{2.9}$$

respectively, where r is the rate of reaction and k is the rate constant. At equilibrium, the two rates of reaction are equal and $K = k_f/k_b$. For inhomogeneous reactions, additional complications with respect to transport of oxygen may arise if factors such as the oxygen supply or surface barriers become the rate-limiting step.

2.5.1 Lattice Energy

An ionic crystal is an array of positive and negative ions held together by the Coulomb attraction between the oppositely charged ions. The coordination number for the ion is the number of nearest-neighbor ions. Thus, in the fluorite structure of UO_2, the coordination number for U^{4+} or a substitutional cation is 8, while the coordination number for the oxygen anions O^{2-} is 4. The cohesive energy of the ionic crystal is the molar enthalpy change ΔH^0 for the isothermal conversion of the crystal into isolated ions and can be found using the Born-Haber cycle (see, for example, Cotton and Wilkinson [104]). The cohesive energy can also be estimated by summing the interionic Coulomb attractions and repulsions and accounting for the Pauli repulsion that results from the overlap of the electron clouds of neighboring ions.

The electrostatic energy of attraction for an ion pair $\{M^{a+}, X^{b-}\}$ separated by a distance r is given by the equation

$$E = \frac{Z^+ Z^- e^2}{r} \tag{2.10}$$

where $Z^+ = +a$, $Z^- = -b$, and e is the electronic charge. In a crystal lattice, there will be more interactions than just the simple one of a singular ion pair. For example, each U^{4+} is attracted by 8 O^{2-} nearest-neighbor ions, repelled by the 12 next-nearest-neighbor U ions, attracted by the third-nearest-neighbor O ions, etc. The result is an infinite series of terms in Equation (2.10) that can be manipulated to converge rapidly. The summation of all of the geometric factors representing the interactions from all orders of removal from the central ion is referred to as the Madelung constant, *A*. It is shown in standard inorganic chemistry texts (e.g. [104]) that the lattice energy of a crystal can be written in the form (Born-Landé equation)

$$U = -\frac{A N Z^+ Z^- e^2}{r_0}\left(1 - \frac{1}{n}\right) \tag{2.11}$$

where

U = the equilibrium lattice energy

N = Avogadro's number

r_0 = the equilibrium distance between ions

n = the Born exponent for ionic repulsion.

Clearly, any change or distortion in the lattice parameter will change the distance r_0 between ions and will thus impact the total lattice energy. A decrease in the lattice parameter would result in a more stable lattice. The addition of interstitials can affect the number of nearest neighbors at a given distance and thus alter the Madelung constant and change the lattice energy. The addition of substitutional ions can result in both changes in lattice parameters and the oxidation states of ions on the metal sublattice.

2.5.2 Valence State of Substitutional Ions

For the purpose of this study, it is assumed that the presence of oxide or metallic precipitates, fission gases, and other volatiles will not affect the energy of the fluorite lattice of irradiated fuel. The only elements of interest are those that will exist as substitutional ions in the fluorite matrix. These ions include (see Table 2.3) the actinides, REEs, Y, and possibly Sr, Zr, Ba, Mo, and Te. With the exception of Ce and possibly Pr, all of the REEs and Y are most stable in the +3 valence state. Ce is thought to exist in the +4 state, as CeO_2, in the hyperstoichiometric regime [100,105]. Similarly, Pr is likely to be

found as a +4 ion under oxidizing conditions. Pu oxidizes more readily than U and will thus be in the +4 state in hyperstoichiometric mixtures [100]. Since no oxide of higher oxidation state than PuO_2 is found at temperatures below 2000°C [75], it is assumed that under the conditions of interest for this study, Pu will remain in the +4 state. The actinides of higher atomic number than Pu, namely Am and Cm, will remain in the +3 state. The high-yield fission products Zr and Mo will exhibit a +4 valence, while Cs and Rb will exhibit +1, and Ba and Sr will exhibit +2 valence states.

Grimes and Catlow [65] have used the electronic potentials of the matrix and impurity ions to calculate solution energies. The lattice site with the smallest solution energy for a particular impurity is determined to be the most stable. For each of the ions tested, the most stable site in hyperstoichiometric UO_{2+x} is the uranium vacancy. Their calculations also predict that ZrO_2 and CeO_2 are insoluble, but BaO and SrO are soluble in UO_{2+x}. Finally, the elements Xe, I, and Br are predicted to exist as +1 ions in uranium vacancy sites in UO_{2+x}, whereas Te is predicted to be most stable as a +2 ion. Thus, the actinides and a large fraction of the fission products are predicted to be soluble in the fuel matrix at higher O/M ratios and will essentially dissolve in the fluorite structure as substitutional ions.

The substitution of a fission product with a valence <+4 requires the loss of an oxygen ion and formation of an oxygen vacancy or the oxidation of one or more U ions to maintain electrical neutrality. Matzke [76,77] determined that spent fuel did not oxidize with burnup and was at most only slightly hypostoichiometric. Thus, the role of oxygen interstitials and vacancies in maintaining electrical neutrality for an intact fuel element is assumed to be negligible. The REEs and the higher actinides are produced in significant quantities in the fuel and exhibit, for the most part, a very stable +3 valence state. The substitution of a pair of trivalent ions into the lattice requires, in the absence of oxygen vacancies, that the valence of one remaining U ion increase from +4 to +6 or the valence of two U ions must increase to +5. While early models, such as Blackburn's [82], assumed the primary charge-defect states of U to be U^{2+} and U^{6+}, recent models [93,106] indicate U^{3+} and U^{5+} are the main charge-defect cations. Thus, for every trivalent substitution, one U lattice ion must change valence to +5 as well. In the case of a divalent substitution, two U ions would be oxidized. The substitution of Pu, Ce, Zr, and Mo as +4 ions does not result in oxidation of remaining U ions.

Again, in the absence of oxygen vacancies, the condition of charge neutrality requires that the oxidation of matrix U ions compensate for lower valence cation substitutions. However, the neutrality requirement also dictates there be no change in the potential energy of the lattice for a constant lattice parameter. Instead of plotting the oxygen potential of the fuel as a function of O/M, the potential is often

plotted as a function of the mean U valence (or mean Pu valence for hypostoichiometric $U_{1-y}Pu_yO_{2-x}$) of the solid solution. At a fixed temperature and fixed mean U valence, the oxygen potential for doped or spent fuel should be the same as for pure UO_{2+x} if there is no change in the total lattice energy. The mean valence theory works reasonably well when applied to $U_{1-y}Gd_yO_{2+x}$ [83] and $U_{1-y}Pu_yO_{2-x}$ [95]. A good approximation is observed for the simulated high-burnup fuel of Une and Oguma [99] for a mean U valence >4.06. This theory does not apply well, however, to solid solutions with Zr [98] or to Th [107] where the oxygen potential is a function of both the U valence and the U/(U+Th) ratio. The best agreement of the mean valence theory with experimental data is achieved with ions of ionic radii similar to U^{4+}; the worst agreement is for solid solution with Zr^{4+}, which has a markedly smaller radius than U^{4+}.

As long as the lattice parameter remains constant, it seems that the substitution of cations of lesser valence and the requisite oxidation of U matrix ions does not directly affect the lattice energy or oxygen potential. However, Park and Olander [92] have shown that the effective negative charge of a substitutional Gd ion (Gd^{3+} as compared to U^{4+}) repels neighboring interstitial oxygen ions that have an oxidation state of 2–, effectively eliminating these sites from occupancy by oxygen. Such occupancy restrictions increase the activity of the oxygen interstitials and hence the oxygen partial pressure with which the solid is in equilibrium. Park and Olander explain that the site-blocking caused by lower valence cation substitution can explain the difference between the oxygen potentials of doped and pure urania, but not necessarily the absolute magnitude of the doped-fuel oxygen potential [92]. Still, at higher burnup and higher O/M ratios, the number of sites available for oxygen interstitials could be greatly limited and result in stabilization of the matrix.

2.5.3 Effect of Substitutional Cations on Lattice Parameter

Because of the dependence of the lattice energy on the equilibrium spacing of the ions (see Equation 2.11), it is clear that changes in the lattice parameter will have an impact on the stability of the lattice with respect to oxidation. In fact, differentiation of the lattice energy with respect to the equilibrium distance between the cations and anions reveals the relationship

$$(\Delta U/U) = (-\Delta r_0/r_0) \tag{2.12}$$

Since the change in valence due to substitutional cations does not affect the lattice energy (as demonstrated in the previous section), the stability of the lattice before adding oxygen interstitials will be determined solely by changes in the lattice parameter. In a classical sense, the lattice parameter is a simple function of the ionic radii and depends on the crystal structure. For an fcc lattice such as exists for U in the UO_2 matrix, the lattice parameter, a, is determined as a function of the ionic radius, R, by the equation

$$a = 8^{½} R \tag{2.13}$$

Shannon [108] calculated the ionic radii listed in Table 2.5. Except where noted in parentheses, the radii listed are for a coordination number of 8. The large differences in atomic radii for Ba, Cs, Mo, Rb, Sr, and Zr from those of the host U result in the reported insolubility of these elements in the UO_2 matrix.

Table 2.5. Ionic Radii [108]

Ion	Ionic Radius (pm)	Ion	Ionic Radius (pm)
Am^{3+}	109	O^{2-} (IV)	138
Ba^{2+}	142	Pr^{4+}	96
Ce^{4+}	97	Pu^{4+}	96
Cm^{3+} (VI)	97	Rb^{1+}	161
Cs^{1+}	174	Sr^{2+}	126
Eu^{3+}	106.6	U^{4+}	100
Gd^{3+}	105.3	U^{5+} (VII)	84
La^{3+}	116.0	U^{6+}	86
Mo^{4+} (VI)	65.0	Y^{3+}	101.9
Nd^{3+}	110.9	Zr^{4+}	84
Np^{4+}	98	Sm^{3+}	107.9

Clearly, the lattice parameter (547 pm [8]) of UO_2 is not adequately described by Equation (2.13) if the radius of U^{4+} is used and the effect of the oxygen anions is ignored. Instead, assuming that the cation-anion distance is the sum of the radii of the two, the lattice parameter of a solid solution with the fluorite structure is expressed as

$$a = \frac{4}{\sqrt{3}}(r_c + r_a) \tag{2.14}$$

where r_c and r_a are the radii of the cation and anion, respectively [109]. When the ionic radii listed in Table 2.5 for U^{4+} and O^{2-} are used in Equation (2.14), a lattice parameter of 549.6 pm is obtained as compared to the empirical value of 547.02 pm. Ohmichi et al. [109] demonstrate that the ionic radius of the O^{2-} in four coordination must be equal to or less than one-quarter the lattice parameter of UO_2. The maximum radius for the oxygen anion is thus 136.9 pm. Schleifer et al. [71] argue similarly that the

lattice parameter of UO_2 can only be explained by assuming deviations from the spherical shape of O^{2-} ions. All of the substitutional cations of interest with a valence of 4+ have a smaller radius than the original U^{4+}, and thus the lattice parameter is expected to decrease; the smaller lattice parameter in turn results in a smaller lattice energy or a more stable phase. Those cations with a valence of 3+, on the other hand, all have larger radii, by at most 11 pm (Nd^{3+}). However, for every 3+ cation, one U^{4+} must be oxidized to U^{5+}, which has a smaller radius by about 12 to 16 pm, and so the net effect is a contraction of the lattice.

Studies on doped UO_2 have indeed shown that the lattice parameter of $U_{1-y}M_yO_{2.00}$ decreases with increasing cation impurity. In most cases, the Vegard law, which states that a linear relation exists between the lattice parameter and the composition of a solid solution expressed as mole%, is closely followed. Several of the calculated lattice parameter contractions are expressed in Table 2.6, where C_d is the mole% of the dopant listed. The lattice has also been found to contract for the simulated high-burnup fuel of Une and Oguma [99]. They report that the lattice parameter of $(U,M)O_{2.00}$ decreased linearly with increasing simulated burnup according to the equation

$$a(pm) = 547.02 - 0.122 \times B \qquad (2.15)$$

where B is the burnup in atom%. Very similar results were obtained on the simulated fuel of Schleifer et al. [71], which contained Zr, Y, La, Ce, Nd, Sm, and Eu dopants. The lattice also contracts with increasing O/M ratio, at least for phases maintaining the cubic structure, as is evident by the densification and contraction of the grains upon oxidation [32]. The lattice parameter decreases from 547.02 pm for UO_2 to 544.13 pm for $UO_{2.25}$ [110]. For spent fuel, the lattice parameter of $UO_{2.4}$ has been reported to be in the range ~544.5 to 545.5 pm [37].

Unlike unirradiated UO_2, however, the lattice parameter for unoxidized spent fuel has been shown to increase with burnup [84,113,114]. Still, for fuels irradiated to 18 [84], 23 [114], and 35 MWd/kg M [84], the largest lattice parameter observed was 547.51 pm compared to 547.02 pm for unirradiated UO_2. The lattice dilation is attributed to the accumulation of point defects. The degree of lattice parameter dilation for spent fuel decreases toward the center of the pellet, close to the value for UO_2 [84]. This decrease is due to the lower burnup experienced at the fuel center, in addition to the higher temperatures which allow annealing to occur [84]. It has been shown [115] that the lattice damage (and increase in lattice parameter) associated with α-particles and α-decay is particularly large, and thus will be more important at the fuel rim, which contains appreciably more actinides (i.e., α emitters) than the fuel center. The lattice dilation is also slightly higher in standard fuel with a typical grain size of 16

μm (547.51 pm) than in large-grained fuel of 43 μm (547.25 pm), which is unexpected since the diffusion pathway of point defects to the grain boundaries is longer for larger grains [114].

Table 2.6. Lattice Parameter Contraction of $U_{1-y}M_yO_2$

Dopant	Lattice Parameter Expression
CeO_2	$a = 547 - (0.062 \times C_d)$ [105]
Zr	$a = 547 - (0.27 \times C_d)$ [98]
Gd_2O_3	$a = 547 - (0.2 \times C_d)$ [111]
Nd	$a = 547 - (0.067 \times C_d)$ [90]
Eu	$a = 547 - (0.14 \times C_d)$ [109]
Y	$a = 547 - (0.25 \times C_d)$ [109]
Pu	$a = 547 - (0.075 \times C_d)$ [112]

Une et al. [84] have shown that the lattice parameter of as-irradiated UO_2 near the fuel rim can be calculated using the equation

$$a(pm) = 547.02 + 0.017 \times B \qquad (2.16)$$

It appears, however, that the increase in lattice parameter saturates at burnups above about 50 MWd/kg M [116]. (The saturation of lattice dilation coincides roughly with the threshold burnup necessary to form the porous rim structure [116].) When the spent fuel samples were annealed under reducing conditions, the lattice parameters decreased [84,113,114]. Thermal recovery of the lattice parameter occurred after 5 hours at ~650°C to 850°C, and was complete, meaning the spent fuel had the same lattice parameter as UO_2 with the corresponding simulated burnup, after 5 hours at temperatures >850°C [114]. There is some indication, however, that the degree of recovery of the lattice dilation brought about by annealing is more difficult with increasing burnup [84].

3.0 EXPERIMENTAL

Several methods were used in the present study to determine the mechanism and kinetics of oxidation of LWR spent fuel from $UO_{2.4}$ to U_3O_8. Two TGA systems were used to measure the mass increase of specimens when heated in a controlled atmosphere. To minimize the influence of factors associated with fuel variability, fuel specimens from the same fuel rod were used for most of the tests. All fuel specimens used in the TGA tests were taken from fuel rods that had been extensively characterized by the Materials Characterization Center (MCC) [69,70,117]. Initial TGA results revealed a large variability in both the duration of the plateau at an O/M ratio of about 2.4 and the time-rate-of-change in O/M ratio after the plateau for samples oxidized under seemingly identical conditions. The focus of the study then turned to the burnup dependence of the oxidation behavior. In addition to the TGA tests, this study used data from similar lower-temperature experiments conducted over the past 10 years at Pacific Northwest National Laboratory (PNNL) in support of the Yucca Mountain Project. Some of the oxidized fuel specimens were examined with XRD and SEM to determine the phases present and to determine the extent of intra- and transgranular cracking. Finally, the burnup of selected specimens was determined by either a ^{148}Nd isotope dilution method or by analysis of the γ-ray spectrum emitted by the specimen.

3.1 Fuel Characterization

Most of the fuel specimens oxidized in the TGA systems were taken from a single 56-cm axial segment of a General Electric 7×7 fuel rod discharged in May 1982 from the Cooper Nuclear Power Plant, a BWR. This fuel is part of ATM-105 (Approved Testing Material) [70] that had been characterized by the MCC at PNNL before the oxidation studies were initiated. Other fuels used in the TGA studies included ATM-108, which is similar to ATM-105, but contains 3 wt% Gd_2O_3 as a burnable poison, and ATM-104, a higher-burnup fuel from a Combustion Engineering 14×14 fuel rod discharged in April 1982 from the Calvert Cliffs No. 1 PWR [69]. Fuel from ATM-104 [69], ATM-105 [70], ATM-106 [117], as well as fuel discharged from the Turkey Point PWR in November 1975 that was characterized by Battelle Columbus Laboratories [118] were used in separate lower-temperature tests [119]. The main characteristics of each fuel are identified in Table 3.1.

Table 3.1. Fuel Characteristics

	ATM-105 [70]	Turkey Point [118]	ATM-104 [69]	ATM-106 [117,120]
Reactor	Cooper	Turkey Point	Calvert Cliffs	Calvert Cliffs
Fuel Type	BWR 7×7	PWR 15×15	PWR 14×14	PWR 14×14
Nominal Burnup (MWd/kg M)	~28	~27	~43	~48
Fission Gas Release (%)	0.6	<0.3	1.1	18
Initial Enrichment (wt% ^{235}U)	2.93	2.56	3.04	2.45
Initial Pellet Density (%)	95	92	94 to 96	92 to 94
Postirradiation Grain Size (μm)	11 to 15	20 to 30	10 to 13	7 to 16[(a)]
Average Nominal LHGR (kW/m)	~17	~18.2	21	~18[(a)]
Discharge Date	May 1982	November 1975	April 1982	October 1980

(a) Measured on a companion rod with only 11% fission gas release.

The first step in the fuel characterization was to perform a full-length gamma scan of each fuel rod using a Ge(Li) γ-ray detector. Once the gamma scanning was completed, each rod was punctured, and a gas sample was taken to analyze the amount and composition of fission gas release. Three to four segments of fuel from different axial locations were then taken and analyzed for burnup using a ^{148}Nd mass spectrometry method. The burnups from these analyses were used to correlate the measured cesium activity from the gamma scan with burnup. Optical ceramography was performed on samples to determine the cracking pattern, porosity, fission gas bubble density, metallic inclusions (ε-Ru phase), and grain-size distributions as a function of axial and radial position. Grain growth was estimated by comparing the grain size at the pellet periphery and the lower-burnup ends of the fuel rod with the grain size at the higher-temperature centerline of specimens from the high-burnup region of the rod. For the fuels used in the TGA studies, maximum grain growth is estimated at 13% and 30% for the high-burnup regions of ATM-105 [70] and ATM-104 [69], respectively. ATM-106, utilized in the lower-temperature experiments [119], experienced both substantial fission gas release (18%) and grain growth (>100%) [120]. The initial ^{235}U enrichments, pellet densities, and nominal linear heat generation rates (LHGR) listed in Table 3.1 were provided by the fuel vendors and reactor operators.

Analytical transmission electron microscopy (AEM) was conducted on samples from the ATM rods to observe fuel microstructures at resolutions approaching 1 nm. AEM analysis revealed a high density of very small fission gas bubbles and five-metal particles (ε-Ru phase) present throughout the UO_2 grains and along grain boundaries in the region near the edge of the fuel pellet. At the mid-radius of the fuel, where operating temperatures were higher, the gas bubbles and metallic inclusions were larger and tended to concentrate at grain boundary triple-points. The metallic particles were even more coarse at the fuel-pellet centerline, but no gas bubbles were detected at the grain boundaries, and few bubbles were within the grains [69,70]. The only fission products detected by EDS (detection limit of about 0.5 wt% [68]) in either the fuel matrix or on grain boundaries were the constituents of the ε-Ru metallic precipitates, Xe, and minor amounts of Kr. The resolution for compositional and phase identification analyses requires a particle size ≥20 nm [69]. No oxide precipitates, or gray phases, have been observed in any of the fuels used in the present oxidation studies. However, at most, one-half of the fission products produced may fill the metallic sublattice sites created by fission of matrix atoms. The remaining fission products form phases, whether on the atomic or macroscopic level, separate from the fuel matrix. The lack of observable oxide precipitates may be due to the lower temperatures experienced by the fuels in this study, which would have limited their growth. Preliminary analyses of the as-irradiated Turkey Point and ATM-105 fuels equilibrated in a CO/CO_2 gas mixture at 1000°C indicated that the fuels had a postirradiation O/M ratio of 2.01±0.01 [30]. These findings are consistent with those of Matzke [76,77]

and Une et al. [84], who determined that spent fuel does not oxidize with burnup and may actually be slightly hypostoichiometric. For the purposes of this study, all fuel was assumed to have an initial O/M ratio of 2.00.

3.2 Testing Methodology

Two different means of oxidizing the spent fuel, TGA and lower-temperature dry-bath systems, have been used for this study. The TGA systems provided for continuous weighing of the fuel specimen, making them ideal for studying the rate of mass increase at moderate to high temperatures. However, radiologic dose constraints limited the sample size to ~200 mg. The lower-temperature experiments used dry-bath ovens, hot-plate type heaters located in a hot cell. Only interim weighing and sample examinations were possible with the dry-bath systems, making these tests more suitable for multiple, large (~10 g) samples oxidized at low temperatures for long periods. The burnup of most specimens selected for TGA testing was determined either by analyzing the γ-ray spectrum emitted by the fuel fragment or by destructive analysis using a ^{148}Nd isotope dilution method. Post-oxidation analyses, including XRD and SEM, determined the phases present and the extent of fuel cracking.

3.2.1 Thermogravimetric Analysis (TGA)

Two TGA systems were used to perform the oxidation experiments. Both consisted of a recording microbalance from which the fuel sample was suspended, a furnace and proportional-integral-differential (PID) feedback controller to regulate the sample temperature, a closed gas-circulating system, and a computerized data acquisition system (see Figure 3.1). The microbalances allowed the sample mass to be determined to within ±10 μg, but convective currents within the system at operating temperature produced fluctuations in the mass reading of ±0.3 mg. To compensate for these fluctuations, a mass reading was taken every 10 seconds, and the average over a 5-minute interval was recorded as the sample mass. With this procedure, fluctuations were reduced to less than ±0.1 mg, which is equivalent to an O/M change of 0.008 with a sample mass of 200 mg. The sample temperatures were measured with a calibrated Chromel-Alumel thermocouple positioned immediately below a quartz crucible that served as the sample container.

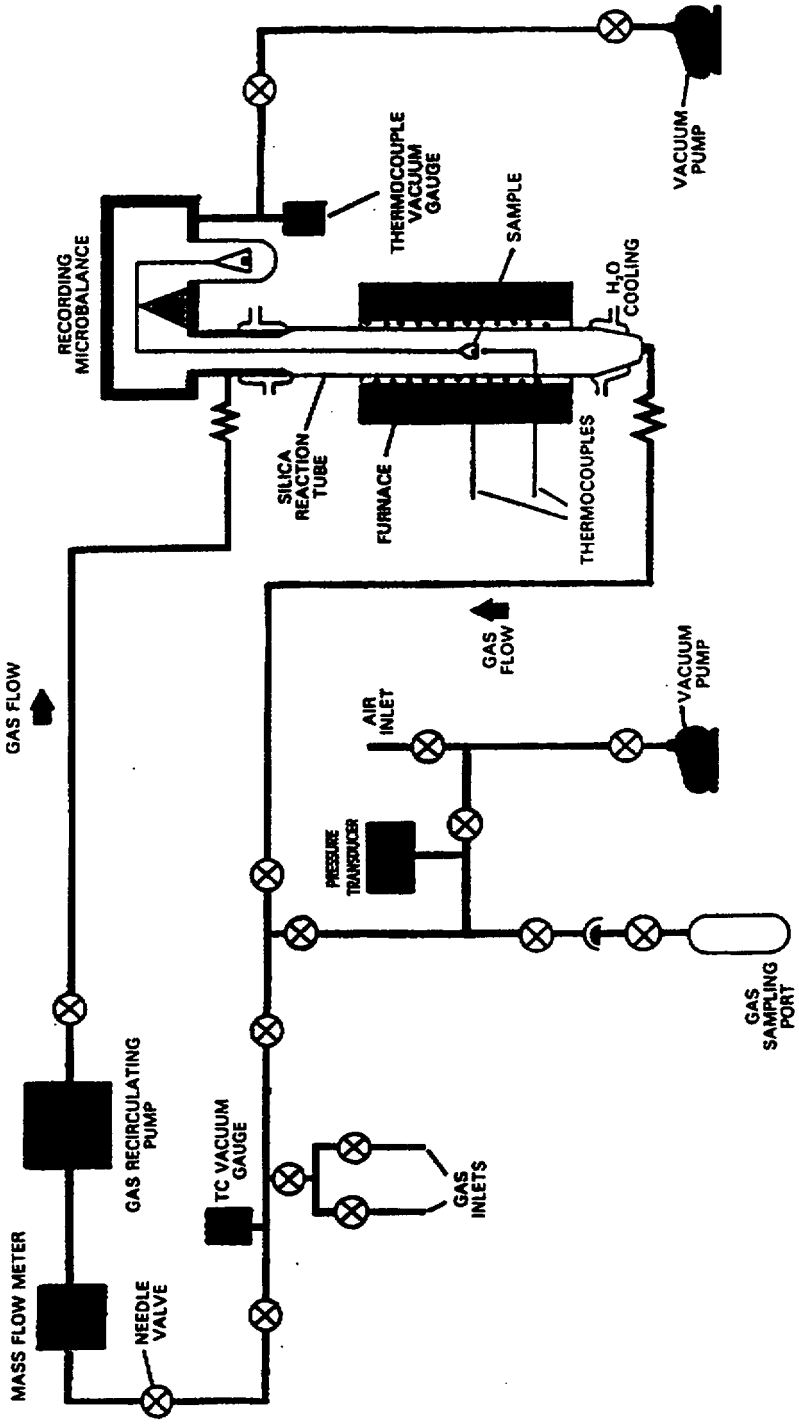

Figure 3.1. Schematic of the Thermogravimetric Analysis Systems

A single fuel fragment was placed in the quartz crucible and suspended on a platinum chain from the microbalance. The system was evacuated to a pressure less than 7 Pa for at least 12 hours. Commercial dry air containing 21% oxygen and 2.4 ppm H_2O was then admitted to the system at a pressure of approximately 95 kPa. A gas circulation pump directed airflow downward onto the sample at a total flow rate of 100 cc/min. Heating was begun, and the fuel sample reached an operating temperature of 283°C (305°C) within 1.25 hours (1.5 hours), at which time the operating pressure was approximately 101 kPa. Because oxidation is relatively slow at temperatures below about 275°C, it was assumed that no oxidation occurred as the sample was heated to operating temperatures, an assumption that is verified by examining the mass increase of the samples during the initial heating. The sample mass and temperature, system pressure, and gas recirculation rate were recorded every 5 minutes. The oxidation continued until a desired O/M ratio was reached as calculated from the mass increase of the specimen using the equation

$$\Delta(O/M) = (270/16) \times (\Delta M/M_0) \tag{3.1}$$

where

270 = the atomic mass of UO_2 (the mass difference due to fission of U and substitution of fission products and higher actinides is ignored)

16 = the atomic mass of the oxygen taken up by the sample (i.e., assumes that the only mechanism for mass increase is oxygen uptake)

ΔM = the increase in mass

M_0 = the original mass of the specimen.

The sample was then cooled to room temperature and removed from the system, and subsamples were taken for post-oxidation analyses.

3.2.2 Dry-Bath Systems

Each dry-bath system consists of three anodized aluminum blocks sitting on a bottom-heating element, as seen in Figure 3.2. Each specimen consisted of 8 to 10 grams of spent fuel placed in a preweighed Inconel 600 crucible with a Chromel bail. The mass increase of an empty crucible was monitored throughout the duration of the tests to act as a control. The fuel samples consisted of either multiple fragments or powders obtained by crushing and sieving fragments to -10/+24 or -24/+60 Tyler mesh size. Once the mass of the crucible with the fuel had been recorded on a balance sensitive to ±0.1 mg, the crucible was placed in its designated hole in the aluminum block and covered with a Ni/Cr alloy mesh screen to prevent cross-contamination between samples and still allow an adequate supply of

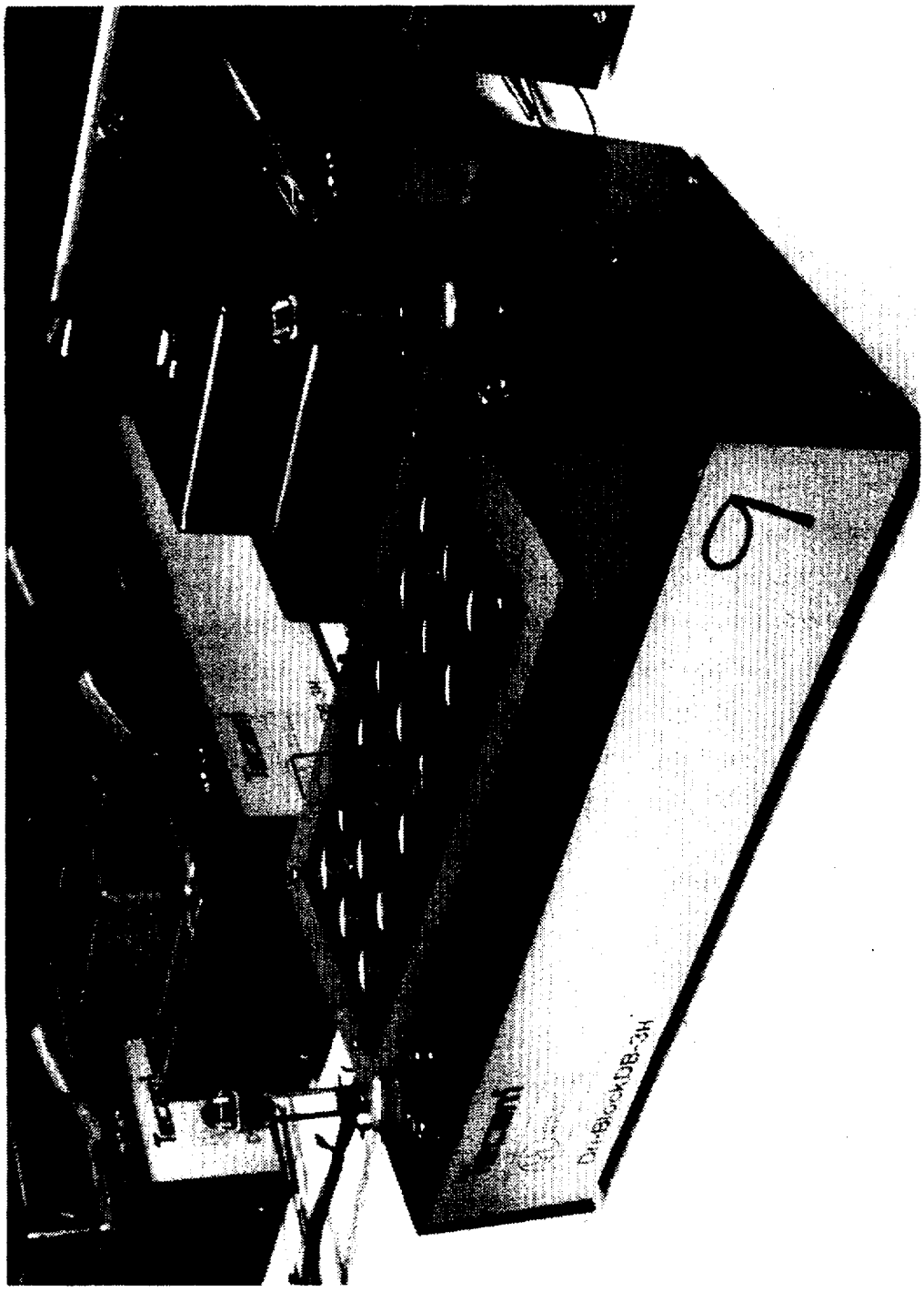

Figure 3.2. Photograph of the Dry-Bath Oxidation Systems

air to reach the samples. A lid was then placed on each dry-bath to minimize convective currents. The temperature of each block within a dry-bath was measured with a calibrated Chromel-Alumel thermocouple (seen in Figure 3.2), and a PID controller was used to regulate the temperature of the dry-bath. The temperature difference between blocks was usually less than 3°C to 4°C.

Oxidant was admitted through the tube curving upwards, as seen in Figure 3.2. Most of the dry-baths used certified commercial dry air as the oxidant. However, some of the baths used building air humidified to dew points up to 80°C. The flow admitted to each bath was enough to create a positive pressure differential between the bath and the hot cell atmosphere. It is still likely, however, that the "dry" samples could have been affected by the residual humidity in the hot cell, especially since all samples were exposed to the hot cell ambient atmosphere during periods of shutdown and weighing.

When the dry-bath tests were operating, the temperature of each block and the dew point of the moist air were closely monitored and recorded. At designated intervals, the baths were cooled to ambient temperature, the crucibles were weighed individually, and the mass increase was recorded. The change in O/M ratio was then calculated using Equation (3.1). Often, oxidized subsamples were examined with XRD or SEM. The crucibles were weighed again and returned to the designated location in the blocks, and the baths were reheated to operating temperature. Further details on dry-bath operations are found in a report by Einziger and Buchanan [119].

3.2.3 Burnup Determination

Ten spent fuel samples were oxidized in the present TGA study before it was clear that the observed differences in oxidation behavior resulted from sample-to-sample variability. Consequently, the burnup of all subsequent samples was determined before oxidation by analyzing the γ-ray spectrum emitted by the sample. Other selected specimens were destructively analyzed for burnup using a ^{148}Nd mass spectrometry isotope dilution method.

3.2.3.1 ^{148}Nd Isotope Dilution Method

A ^{148}Nd method essentially equivalent to American Society for Testing and Materials (ASTM) procedure E321 [59] was used to determine the burnup of selected specimens. The oxidized fuel samples were dissolved in nitric acid and diluted to a final volume of 25 mL. One-tenth mL aliquots were individually mixed with a spike solution containing known quantities of ^{150}Nd, ^{233}U, and ^{242}Pu. The U, Pu, and Nd were then chemically isolated using anion exchange chromatography. The isolated elements from samples with and without the added isotopic tracers were then subjected to thermal ionization mass

spectrometry. After correction for natural contamination, the atom ratios were used to calculate the number of fissions per sample and the fraction of total heavy element that had undergone fission. The estimated uncertainty ($\pm 1\sigma$) for the calculated burnup (MWd/kg M) is about ±4%.

3.2.3.2 Gamma Spectrum Analysis

An attempt was made to characterize the burnup of selected samples before oxidation by analyzing the γ-ray spectrum emitted by the fuel fragments. Each fragment was counted at about 3 meters from an intrinsic germanium detector for 10 to 15 minutes, and the specific activity (μCi/mg fuel) of several isotopes was calculated from the intensity of the γ-rays characteristic of these isotopes. The detector deadtimes were on the order of 20% to 30%, but were corrected automatically by the system hardware. For most specimens, the isotopes ^{134}Cs, ^{137}Cs, ^{154}Eu, ^{155}Eu, and ^{241}Am were readily identified. However, because of the high atomic number, Z, of U and the irregular shapes of the fragments, it is very difficult to make accurate corrections for photon attenuation within the fuel except for photons of sufficiently high energy. A spreadsheet was used to determine the absorption corrections for different γ-rays by varying the sample radii to obtain the best fit to the data for γ-rays from ^{134}Cs and ^{154}Eu. This radius was then used to determine the correction for the other gamma emitters. The uncertainties are large (i.e., 15% to 20% for ^{241}Am) for the isotopes with low-energy characteristic γ-rays.

In addition to the problem of photon attenuation, it is important to note that both ^{134}Cs and ^{154}Eu are shielded nuclei with low fission yields. Neutron capture will thus be a significant source of their production, and their atom densities will be quite sensitive to the shape of the local neutron spectrum, making them unreliable as good indicators of sample burnup. The fission yield of ^{155}Eu is very sensitive to the isotope fissioned, again making it difficult to accurately determine burnup from its specific activity. As a result, the specific activity of ^{137}Cs was used to correlate the measured activity with burnup since attenuation of its 661.6 keV photon is small. Further, the fission yield of ^{137}Cs is large, and its yield in the fission of ^{235}U, ^{239}Pu, and ^{241}Pu differs by no more than 10%. This reduces the impact of the radial burnup distribution and neutron capture on the final concentration of ^{137}Cs in an individual sample. Since both fuels had only small fission gas release [69,70], it is not expected that the fuel temperatures were high enough for any Cs to have migrated significantly.

The ORIGEN2 code [60], using the BWR-US and PWR-US reactor models [61], was run for multiple burnups for both the BWR (ATM-105) and PWR (ATM-104) fuels. The power histories and fuel compositions used as input to ORIGEN2 were taken from the ATM characterization reports [69,70] for each fuel, and the decay times were chosen to correspond to the dates of the γ-ray energy analyses. A

third-order polynomial with the intercept set equal to zero was fit to the results from these computations to correlate the ^{137}Cs specific activity with burnup. The resultant polynomial was then used to estimate the burnup of each sample. Uncertainties in the specific activity of ^{137}Cs, based on the correction for self-absorption as well as counting and calibration uncertainties, are on the order of 2% to 10%. In addition, radiochemical analyses of both ATM-104 [69] and ATM-105 [70] have shown that the specific activities of ^{137}Cs predicted by ORIGEN2 over the burnup range of interest for these two fuels may differ from experimental data by 0 to 10%. Thus, the total uncertainty in calculated burnup using the γ-ray spectroscopy method is approximately $\pm$(2% to 15%).

3.2.4 X-Ray Powder Diffractometry

After oxidation, samples for XRD were prepared by grinding approximately 5 mg of fuel (powder or piece chipped from oxidized fragment) in a 5% collodion/amyl acetate solution. The slurry containing the fuel was spread on a glass mounting slide and allowed to dry. Since the dried sample was slightly above the specimen slide, the measured peaks are shifted slightly from their ideal positions. Small amounts of either CeO_2 or Al_2O_3 were often added to allow for proper correction for this shift in peak location. In other cases, known quantities of fuel and Al_2O_3 were mixed together so that an accurate quantitative analysis of the phases present could be performed.

A Scintag automated diffractometer system with a copper X-ray source (45 kV, 40 mA) and a Si(Li) solid-state X-ray detector was used for phase identification. The phases present in a sample were identified through diffractometer scans from 5 to 60° 2θ (the angle between the X-ray source and the detector where θ is the angle of reflection) at 0.02° per step, with a count time of 20 to 25 seconds per step. This process produces a spectrum of X-ray intensity as a function of diffraction angle. Once the background was removed, the spectra (peak positions and relative peak intensities) were compared to those found in the reference spectra of known phases published by the Joint Committee for Powder Diffraction Standards (JCPDS) using the computer program JADE™. Table 3.2 is a listing of the 2θ peak positions for the phases of interest in this study. (Note that the 2θ positions are readily obtained using Bragg's Law and the known d-spacing between planes of atoms within a sample.) The shift in peak position due to the contraction of the lattice from UO_2 to U_4O_9 is easily observed, as is the splitting of the UO_2/U_4O_9 peaks for the tetragonal U_3O_7. The additional peaks formed due to the different lattice type readily identify U_3O_8; many low-intensity peaks are formed in addition to those listed in Table 3.2. JADE can be used to calculate the integrated intensity of peaks to assist in quantitative analysis of the phases present.

Table 3.2. XRD Peak Positions for UO_2, U_4O_9, U_3O_7, and U_3O_8 in 2θ (°)

Reflection #	UO_2 (05-0550)[a]	U_4O_9 (20-1344)[a]	U_3O_7 (15-0005)[a]	U_3O_8 (31-1425)[a]
1	28.244	28.401	28.540	21.435
2	32.717	32.890	32.328	26.149
3	46.942	47.201	33.368	34.048
4	55.695	55.990	47.151	43.670
5	58.400	58.726	47.971	46.121
6	68.537	68.997	55.439	51.398
7			56.709	51.607
8			59.057	53.787
9			67.692	58.559
10				65.395

(a) Numbers in parentheses represent the identifying powder diffraction file (PDF) card number of this phase as published by the JCPDS.

3.2.5 Scanning Electron Microscopy

The first five oxidized samples were analyzed via SEM to determine the topography and gross microstructure of the fuel surfaces, e.g., particle or grain size and shape, and the extent of cracking. Due to radiologic dose constraints, the sample size for SEM was limited to only about 1 mg. The fuel particle was mounted on an aluminum sample holder using double-sided carbon adhesive tape. The entire mount was then coated with a fine layer of carbon to prevent charging during examination. A focused 15 to 35 keV electron beam scanned the surface of the sample, and an image was formed from either backscattered or secondary electrons. Local changes in the sample surface orientation, texture, and differences in average atomic number created contrast. Resolutions down to much less than 1 μm were achieved with this SEM unit, allowing observation of single grains of fuel.

4.0 EXPERIMENTAL RESULTS

This section details the results of the oxidation studies, including the burnup and post-oxidation analyses. Discussion, interpretation, and analyses of the experimental results are presented in Section 5. Detailed oxidation curves (O/M ratio as a function of time at operating temperature) for individual samples are presented in Appendix A.

4.1 TGA Oxidation Results

A summary of the experimental conditions and measured parameters for the TGA tests is presented in Table 4.1. All O/M ratios were calculated using Equation (3.1). The O/M ratios were calculated directly from the mass increase of a sample with neglect of any effects due to substitution of two fission products for each fission in the specimen or replacement of a uranium atom by a higher actinide. Further, it was assumed that all specimens had an initial O/M ratio of 2.00. The uncertainty in the calculated O/M ratios using the 5-minute averaging discussed in Section 3.2.1 is estimated as ±0.01. One-hour averaging of the mass increase data results in an estimated uncertainty of about ±0.002.

4.1.1 Doped Fuel

The TGA systems had not been used for a period of 2 to 3 years prior to the present tests. New, calibrated pressure transducers were installed, and the sample temperature thermocouples were checked by comparing them with a calibrated thermocouple. The balances and data acquisition systems were calibrated as well. All calibrated standards are traceable to National Institute of Standards and Technology (NIST) standards.

One of the TGA systems was tested with a 268.50 mg disk of UO_2 cut from an unirradiated pellet that was doped with 8 wt% Gd_2O_3. The specimen was oxidized in TGA#2 for 454 hours at 283°C. As seen in Figure A.1, the sample reached a plateau at an O/M ratio of about 2.35 within about 250 hours. Upon unloading, the disk broke apart into smaller pieces, which were found to be quite friable. A subsample was taken and analyzed via XRD, which revealed that the sample was entirely converted to a phase that most closely matched U_4O_9, even though the O/M ratio was significantly higher than the nominal value of 2.25 for U_4O_9. No other analyses were performed, and the systems were deemed ready for experimental use.

Table 4.1. Summary of Experimental Conditions and Measured Parameters

Sample ID#	Oxidation Temperature (°C)	Final O/M Ratio	XRD results	Sample Burnup (MWd/kg M)	
				^{137}Cs[a]	^{148}Nd[b]
105-01	283	2.78	U_3O_8	(c)	(c)
105-02	325	2.73	U_3O_8	(c)	(c)
105-03	305	2.75	U_3O_8	(c)	28.1
105-04	270	2.59	(c)	(c)	27.5
105-05	255	2.41	U_4O_9	(c)	29.2
105-06	283	2.49	U_3O_8/ U_4O_9	(c)	31.5
105-07	283	2.62	U_3O_8/ U_4O_9	(c)	27.6
105-08	283	2.47	U_3O_8/ U_4O_9	(c)	32.5
105-09	305	2.43	(c)	(c)	(c)
105-10	305	2.65≤	(c)	(c)	29.8
105-11	305	2.70	(c)	25.9	29.6
105-12	305	2.73	(c)	27.9	(c)
105-13	305	2.71	(c)	28.3	(c)
105-14	305	2.73	(c)	28.1	(c)
105-15	305	2.73	(c)	19.1	18.6
105-16	305	2.71	(c)	18.3	(c)
105-17	305	2.70	(c)	16.7	(c)
105-18	305	2.69	(c)	16.8	(c)
104-01	305	2.51	(c)	42.3	(c)
104-02	305	2.42	(c)	42.4	(c)
108-01	305	2.48	(c)	17.6	(c)
108-02	305	2.45	(c)	34.8	(c)

(a) Measured by γ-ray energy analysis before oxidation.

(b) Measured by destructive analysis after oxidation.

(c) Measurement/analysis not performed.

4.1.2 ATM-105 Tests

To minimize the possible influence of factors associated with fuel variability, all fuel specimens, except where noted for samples 105-15 through 105-18, consisted of a single fragment of ATM-105 fuel which came from a 56-cm axial segment from the high-burnup region of the characterized rod ADD2974 [70]. The bulk average burnup of this segment, as calculated by correlating the measured ^{137}Cs γ-ray activity with ^{148}Nd analyses [70], ranged from 28.5 to 31.5 MWd/kg M. A radial distribution in burnup similar to that shown in Figure 2.5 was also expected. The fuel had been removed from the cladding and fragments taken for earlier TGA studies, as well as for the dry-bath tests. The remaining fragments (approximately 90 g from the original 687 g of fuel in this segment) had been placed in a capped storage tube and kept in the hot cell where the dry-baths are located. When a fragment was needed for a test, the tube was opened and fragments poured into a petri dish. Once a fragment of ~200 mg was found, it was placed in a glass vial and transported to the TGA laboratory. The remaining fragments were returned to the storage tube. Thus, the exact radial and axial location of these specimens within the irradiated rod was not known.

4.1.2.1 Scoping Tests

The first five oxidation tests were run as scoping tests to help determine the time required to oxidize the spent fuel samples to U_3O_8 (i.e., a second plateau at an O/M ratio of approximately 2.75) as a function of temperature. These results, plotted as the O/M ratio as a function of time (Figure 4.1), were to be used to establish the test matrix to determine the oxidation kinetics and assist in developing the mechanism of oxidation of spent fuel to U_3O_8. The temperatures were chosen to compare the data from the present studies with the previous oxidation data of Einziger and Strain [4], as plotted in Figure 2.3.

Sample 105-01 (i.e., ATM-105 sample #1) consisted of a 184.63 mg fragment and was oxidized for 793 hours at 283°C. The first plateau at an O/M ratio of about 2.4 was reached after about 55 hours, and a short plateau, although not of zero slope, was observed before the onset of more rapid mass increase resumed. A final bulk O/M ratio of 2.78 was achieved. XRD analysis revealed that the sample was converted to U_3O_8 with minor amounts of U_4O_9 remaining. SEM revealed that the sample had disintegrated into small clusters of individual grains with substantial inter- and intragranular cracking.

Sample 105-02 was a 193.73 mg fragment oxidized at a temperature of 325°C to a final bulk O/M ratio of about 2.73. An O/M ratio of about 2.4 was reached after only about 8 hours, and no truly identifiable plateau existed, although there is an obvious change in the rate-of-increase in O/M ratio after

this point (see Figure A.3). The only phase detected by XRD was U_3O_8. SEM revealed even more intragranular cracking than the first sample, consistent with the higher stresses experienced due to the rapid oxidation at higher temperatures.

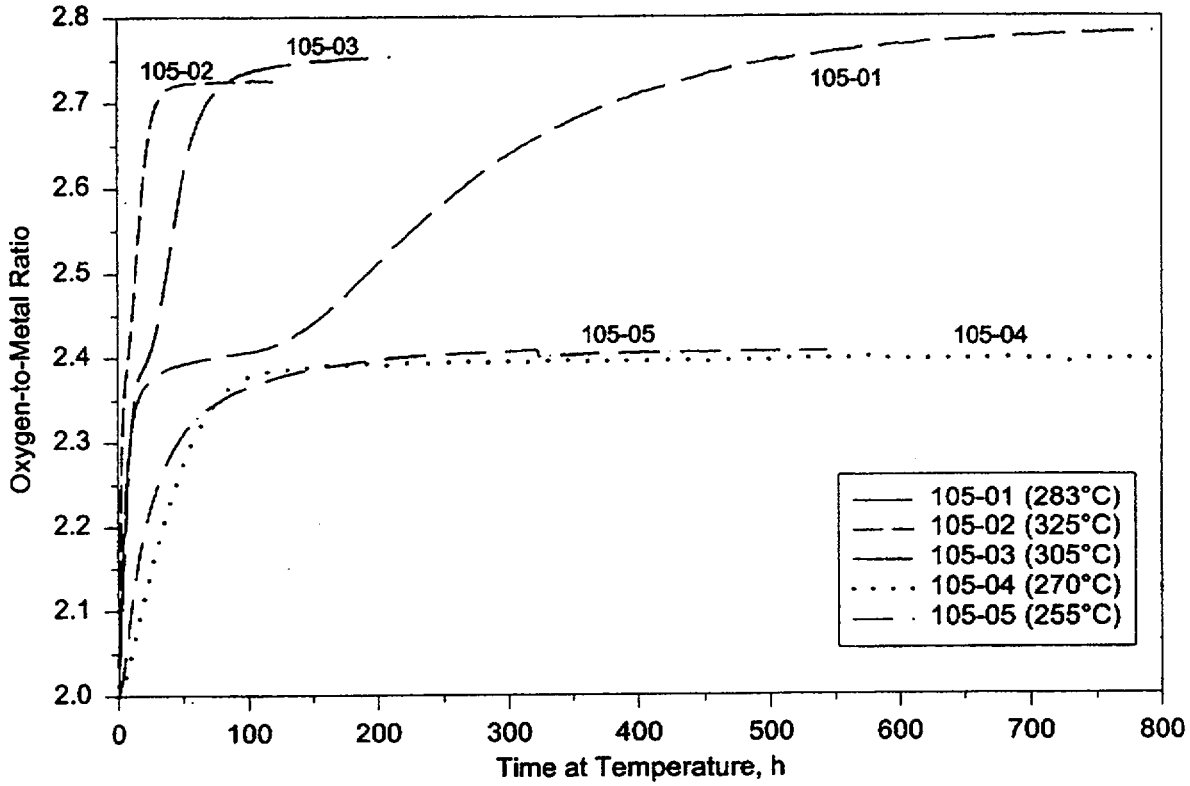

Figure 4.1. Oxygen-to-Metal Ratio as a Function of Time for ATM-105 Fragments Oxidized at Various Temperatures

The third sample, 105-03, consisted of a single 207.11 mg fragment and was oxidized at 305°C to a final bulk O/M of 2.75. An O/M ratio of 2.4 was reached after about 23 hours. Again, a plateau with zero slope did not exist, although there was clearly a different rate-of-change in O/M ratio after a ratio of about 2.39 was reached. XRD of the resultant powder detected only U_3O_8.

Sample 105-04 was oxidized for 2375 hours at 270°C. This 203.39 mg fragment was the first in this series to exhibit a plateau with zero slope, as seen in Figure A.5. The duration of the plateau was between 700 and 800 hours before mass increase began again. An eventual final bulk average O/M of 2.59 was reached before the test was terminated. This sample was converted to powder, but no XRD analysis was performed because of the loss of the subsample taken for this purpose. Twice during oxidation of this sample, at 1076 and 1870 hours, power fluctuations caused relays to the furnace to reset,

and the furnace lost power. Each time, the sample cooled to room temperature before the test was restarted.

Sample 105-05 was oxidized at 255°C to compare with sample 105F-100, which was oxidized in a dry-bath also operating at 255°C. As can be seen in Figure 4.2, the two oxidation curves agree fairly well over the first 400 hours. A computer malfunction after 322 hours at operating temperature caused the sample to cool to room temperature before it was reheated to 255°C. Since the data of Einziger and Strain [4] suggested that the duration of the plateau would be on the order of 10^4 hours, this TGA test was halted after only 544 hours when a bulk O/M ratio of 2.41 had been reached. The sample appeared to be an intact fragment when it was unloaded, and XRD analysis revealed that the only phase present was U_4O_9.

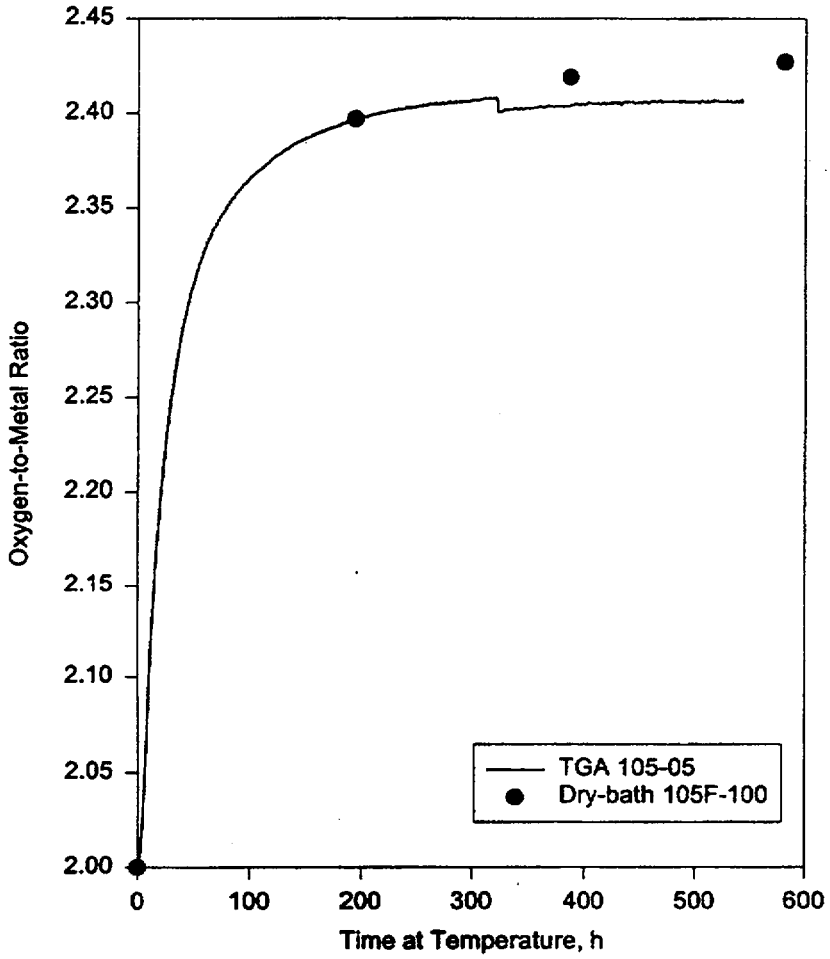

Figure 4.2. Oxidation Behavior of ATM-105 Fragments in a TGA and Dry-Bath at 255°C

Originally, spent fuel fragments were to be oxidized to progressively larger O/M ratios between the plateau (~2.4) and final completion (~2.75) at a fixed temperature. Post-oxidation analyses would then be used to determine the amount of each phase present and to determine the mechanism and kinetics of the $UO_{2.4}$ to U_3O_8 transition. The tests would then be repeated at different temperatures to determine the temperature dependence of oxidation. From the scoping tests, it was clear that for enough tests to be performed to adequately study this transition, the temperatures would need to be in the range 275°C to 305°C. At temperatures below 275°C, the duration of the plateau was expected to be ≥800 hours; at temperatures above 305°C, the plateau was not well defined, and oxidation occurred rapidly. Consequently, a temperature of 283°C was chosen for the first series of tests.

4.1.2.2 283°C Tests

Based on the behavior of sample 105-01 oxidized at 283°C and the earlier samples of Einziger and Strain [4] (see Figure 2.3), it was expected that a short plateau with non-zero slope would exist for each sample at this temperature. Sample 105-06 was then oxidized at 283°C. It is clearly seen in Figure 4.3 that the oxidation behavior of samples 105-01 and 105-06 was quite different. Although the time to reach an O/M ratio of 2.4 was similar, and neither specimen exhibited a plateau of zero slope, the time-rate-of-change in O/M after the plateau for sample 105-06 was much smaller than for sample 105-01. This 214.06 mg fragment was oxidized for 1125 hours to a final bulk O/M ratio of 2.49. This sample consisted of both powder and a remaining fragment when unloaded from the TGA. XRD was performed, and both U_3O_8 and U_4O_9 were detected in the powder, whereas the fragment consisted solely of U_4O_9. The only known difference between sample 105-01 and 105-06 was that the latter sample experienced two intermittent power losses to the furnace, at 21 and 816 hours, where the sample cooled to room temperature before the test was resumed.

Sample 105-07 was then oxidized at 283°C for 743 hours. The oxidation behavior of this 167.37 mg fragment was intermediate to the previous two samples oxidized under identical conditions. The initial rate of O/M increase for this sample was less than that of the other samples (Figure 4.3); however, the time to reach an O/M ratio of 2.4 was about the same for all specimens. This sample then exhibited a plateau with a near-zero slope, and, once mass increase resumed, it was at a rate intermediate to that of the previous samples. The test was halted when a final bulk O/M ratio of 2.62 was reached. The sample consisted of powder only, which XRD identified as a mixture of U_3O_8 and U_4O_9. During oxidation of this specimen, a power outage caused the sample to cool to room temperature after 314 hours at operating temperature. Also, a computer malfunction resulted in the loss of data from 356 to 434 hours, although no other impact on the test was observed.

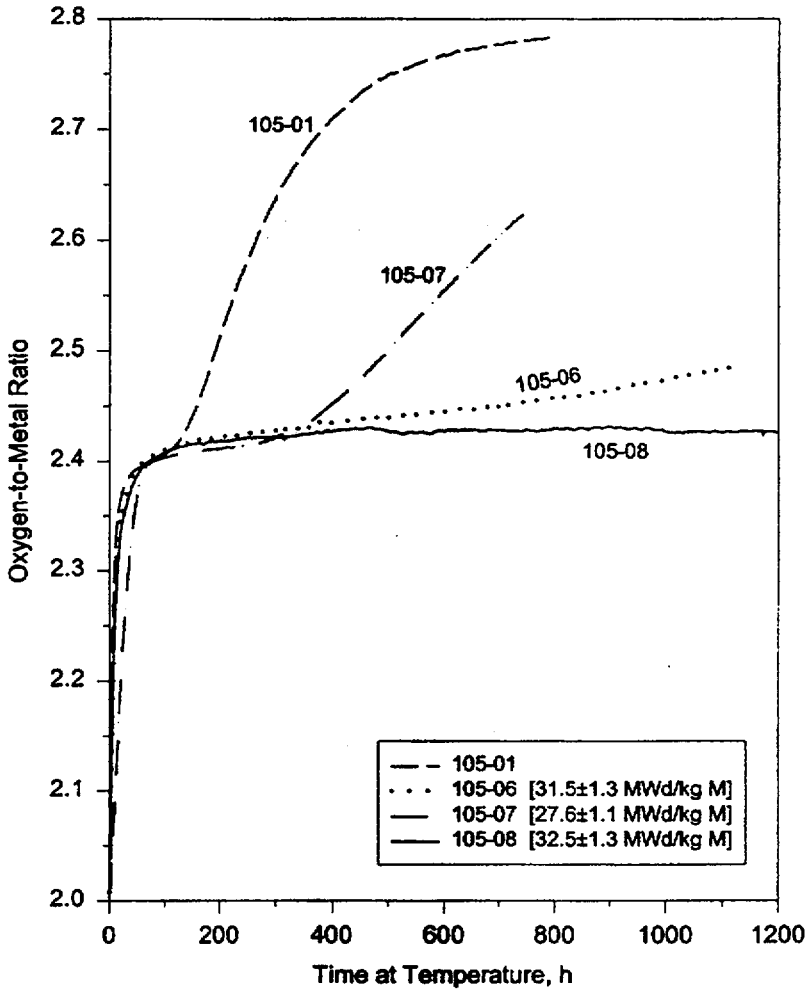

Figure 4.3. Oxidation Behavior of ATM-105 Fragments Oxidized at 283°C

Both TGA systems were then thoroughly checked using NIST traceable standards to ensure their proper calibration. Copper wire was oxidized in each TGA to determine if the tare and/or calibration of the balance drifted as a function of time or temperature. No problems were found with either the balances or with the calibrated data acquisition systems. Thus, the observed difference in oxidation behavior for the first three samples oxidized at 283°C was determined to be real and not due to equipment problems. The furnace control relays were reconfigured so that power fluctuations or power outages lasting less than 2 minutes would not cause the relays to reset.

Sample 105-08 was a 195.63 mg fragment that was oxidized at 283°C. Three weeks after this test was initiated, the building where the TGA laboratory is located was placed under a radiologic work stoppage. No entry was allowed to the laboratory, and the system ran virtually unattended for months.

Although the system appeared to have operated normally, there are large gaps in the data because no data were recorded once the data disk was full. Still, it is clear that a plateau with zero slope persisted for well over 1000 hours and is likely to have been closer to 3000 hours, as observed in Figure A.9. Once mass increase began after this plateau, it was at a very slow rate. This experiment was halted after 5375 hours at constant temperature, and the final bulk average O/M ratio was 2.47. The sample consisted of powder and a remaining fragment. As with earlier samples, XRD detected a mixture of U_3O_8 and U_4O_9 in the powder, whereas only U_4O_9 was detected in the fragment. While the oxidation behavior to an O/M ratio of ~2.4 was generally consistent with earlier observations [30], the duration of the plateau and oxidation behavior to U_3O_8 varied widely among the samples tested.

4.1.2.3 305°C Tests

A second series of samples from the high-burnup region of the ATM-105 fuel rod was oxidized at 305°C to determine if the variable oxidation behavior after reaching an O/M ratio of ~2.4 persisted at higher temperatures. Sample 105-09 (185.42 mg) was oxidized for about 122 hours, at which time the bulk O/M ratio was 2.43. This sample oxidized at a much slower rate than sample 105-03, the scoping test specimen also oxidized at 305°C. Oxidation of sample 105-09 was halted because of this marked difference. The sample consisted of both powder and a remaining fragment when unloaded. XRD of this sample is planned for future work. Sample 105-10 was then oxidized under identical conditions of temperature and ambient atmosphere in the same TGA system that had been used to oxidize sample 105-09. As seen in Figure 4.4, the oxidation behavior of this 181.36 mg fragment was intermediate to those of the samples previously oxidized at 305°C. This sample oxidized for 287 hours; however, a problem with the balance resulted in no mass data being recorded for the last 60 hours. Before this failure, the O/M ratio was calculated as 2.65. It is clear that the variability in oxidation behavior persisted at 305°C.

The only known differences among the first 10 samples oxidized were specimen-to-specimen variations and the intermittent cooling of some specimens to room temperature as a result of power fluctuations or computer failure. To test the effect of these variables, one large fragment from the high-burnup region of the ATM-105 fuel was broken into four smaller fragments. All four, samples 105-11 through 105-14, were oxidized individually at 305°C, and the time dependence of their oxidation is shown in Figure 4.5.

Sample 105-11 (143.37 mg) was oxidized for 843.5 hours to a final bulk O/M ratio of 2.70. Concurrently, sample 105-12 (188.27 mg) was oxidized for 840.5 hours to a final bulk O/M ratio of 2.73.

Although some variability in the oxidation kinetics is evident (see Figure 4.5), it is much less than seen in Figure 4.4 for fragments with random locations within the same fuel segment.

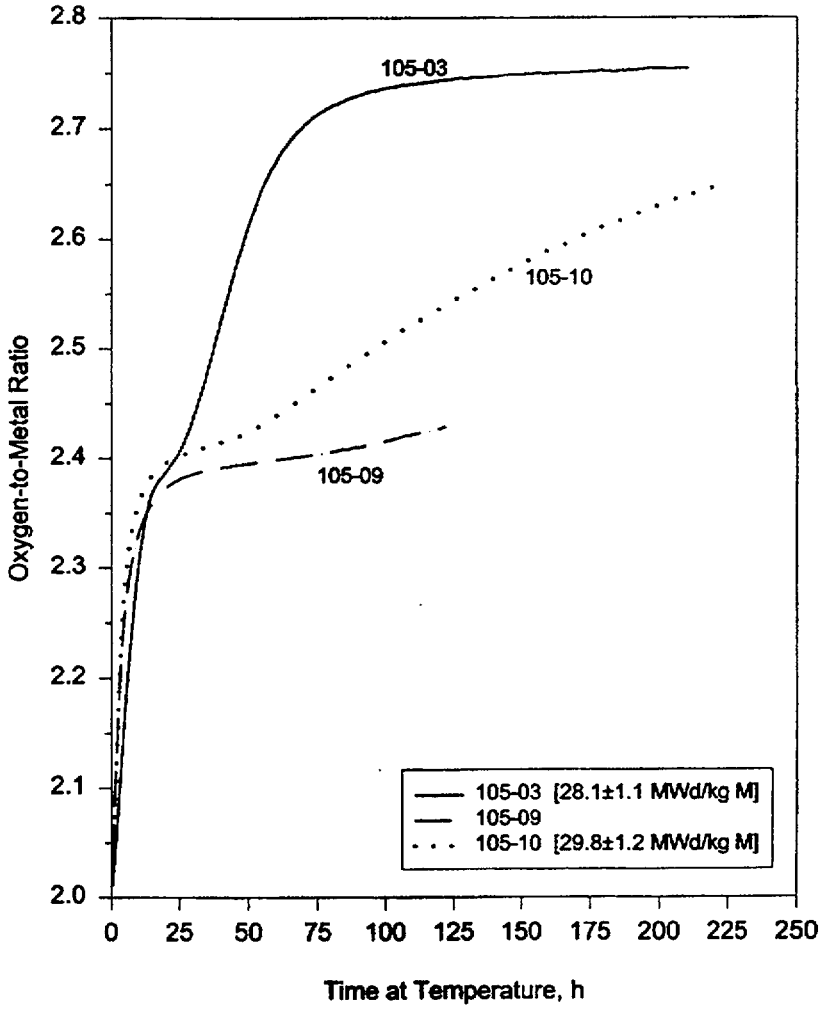

Figure 4.4. Oxidation Behavior of ATM-105 Fragments Oxidized at 305°C

Sample 105-13 (238.26 mg) was then oxidized under identical conditions. The furnace was turned off after 170 hours when the O/M ratio was 2.53. A subsequent problem with the balance required that the sample remain at room temperature for 1 month before testing could be resumed. It was necessary to open the system to temporarily add weight to the tare side of the balance. The system was then sealed, evacuated, and filled with dry air. During this procedure, some of the sample fell from the quartz crucible to the bottom of the reaction tube. This was confirmed by the very high activity measured in this location with a Geiger-Mueller detector. Comparison of the mass before and after this incident indicated that about 22.58 mg of the sample fell from the crucible. Since the entire sample had gained only 7.54 mg, it was assumed that the sample lost included both $UO_{2.4}$ and U_3O_8 and that the remaining

sample had an O/M ratio of 2.53. The test was restarted and continued for a total oxidation time of 819.5 hours when a final bulk average O/M ratio of 2.71 was achieved.

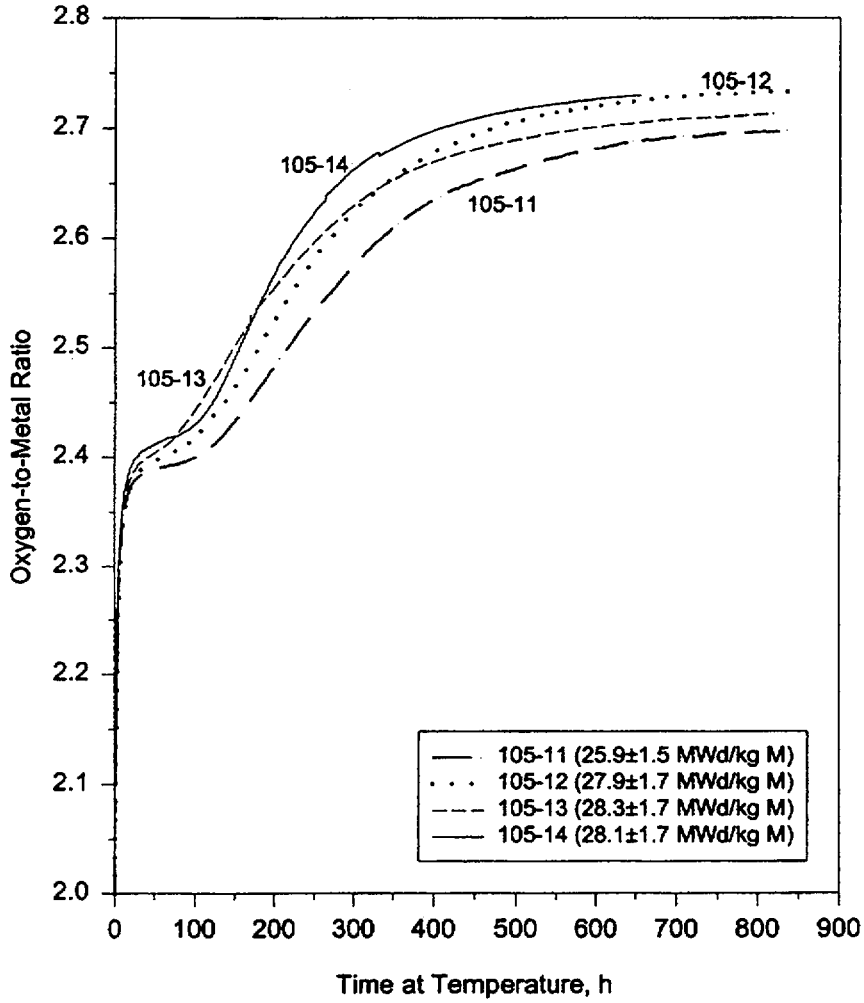

Figure 4.5. Oxidation Behavior of Four Samples Broken from the Same Larger Fragment of ATM-105 Fuel Oxidized at 305°C

Sample 105-14 (241.21 mg) was also oxidized at 305°C. The behavior of this sample was nearly identical to that of sample 105-12 for the first 50 hours. Power to the furnace was turned off after 68 hours when the bulk O/M ratio was 2.42. The sample remained at room temperature for 1 week before being reheated to 305°C. Oxidation continued for a total of 656 hours, when the relay for the temperature controller failed, resulting in a slight rise in the sample temperature, which in turn resulted in an automatic loss of power to the furnace. The final bulk O/M ratio was 2.73. Again, Figure 4.5 clearly illustrates some variability in the oxidation kinetics for these four samples broken from the same, larger fragment; however, the variability is much less than observed previously for fragments that were likely

from random locations within the segment of the fuel rod taken for study. Based on the comparison of the results of the oxidation of samples 105-11 through 105-14, as well as dry-bath data where the samples were intermittently cooled for periodic weighings, it was concluded that temperature cycling had a relatively small, or negligible, effect on the characteristics of the fuel oxidation and was not the cause of the variability observed.

Clearly, specimen-to-specimen variability was the main cause of the different oxidation behaviors observed. The small sample size (~200 mg) mandated by radiologic dose control ensures that an individual specimen is much too small to sample across the entire fuel radius. The small sample size, coupled with the axial and radial burnup variations in the fuel, was suspected to be the cause of the wide variation found in the oxidation kinetics of $UO_{2.4}$ to U_3O_8. To test this hypothesis, two large fragments of ATM-105 fuel from the low-burnup upper-end of the same fuel rod were each broken into two smaller fragments (samples 105-15 through 105-18) and oxidized at 305°C. The bulk average burnup reported [70] for this segment ranges from 13.5 to 17.5 MWd/kg M.

The variation in the O/M ratio dependence on time for samples 105-15 through 105-18 is shown in Figure 4.6. Samples 105-15 (213.20 mg) and 105-16 (138.68 mg) both oxidized rapidly, achieving an O/M ratio of 2.4 within 16 hours. The plateaus at this lower burnup were merely an inflection in the O/M curve. Sample 105-15 reached an O/M of 2.73 in 78.5 hours and remained at this O/M until the test was terminated after 121 hours of operation. Similarly, sample 105-16 obtained an O/M ratio of 2.71 within about 100 hours and remained there until the test was terminated after 142 hours. Samples 105-17 (210.49 mg) and 105-18 (161.97 mg) oxidized even faster and reached bulk O/M ratios of 2.70 and 2.69, respectively, within 50 hours. Clearly, the transformation from $UO_{2.4}$ to U_3O_8 occurred much earlier than for the fragments from the high-burnup region.

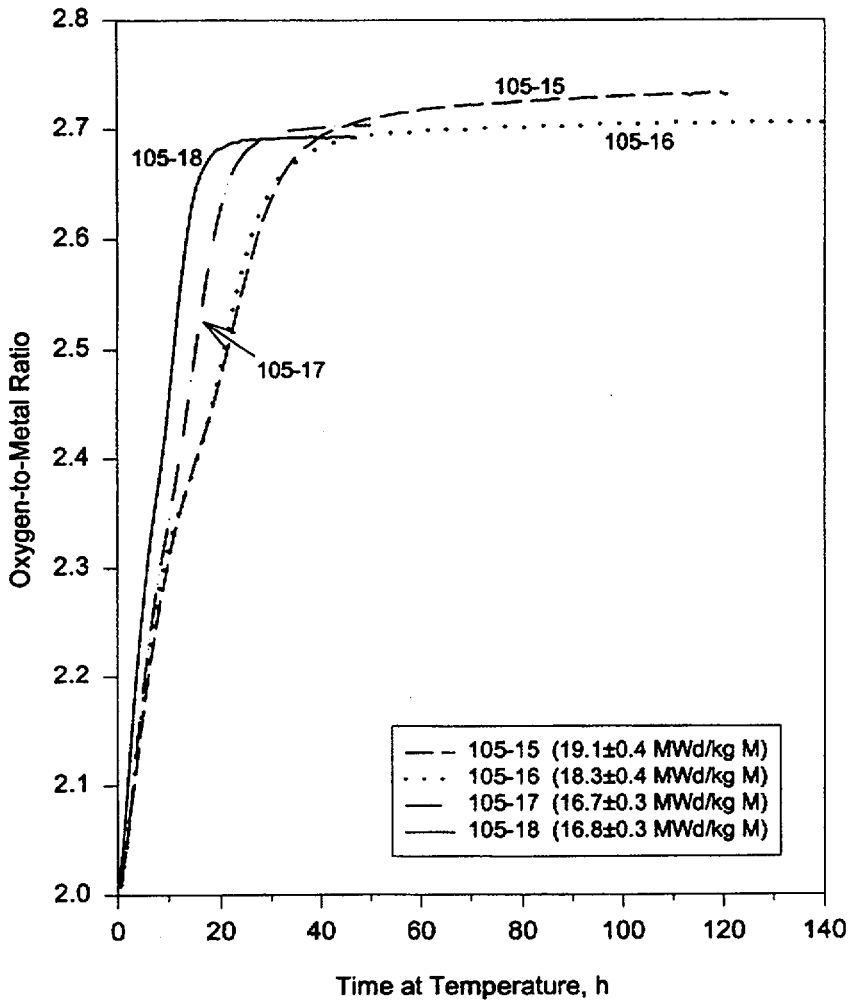

Figure 4.6. Oxidation Behavior of Low-Burnup ATM-105 Fragments Oxidized at 305°C

4.1.3 ATM-104 Tests

Tests were also performed on fuel specimens taken from a specially cut segment of ATM-104 (PWR) fuel in which the fuel had not separated from the cladding. The purpose of these tests was to determine if the burnup dependence on oxidation rate inferred from measurements on fuel fragments that were randomly distributed axially and radially throughout the ATM-105 (BWR) fuel segments studied also existed for higher-burnup specimens. Two fragments were cut with a low-speed saw from near the centerline of a segment from the high-burnup region of the ATM-104 fuel rod (MKP-109). This sampling method reduced the likelihood that the sample contained the large burnup gradients and highly restructured microstructure found near the fuel surface. The fuel in this region had an estimated bulk average burnup of 44 MWd/kg M [69]. These two fragments, 104-01 and 104-02, were oxidized

individually at 305°C (see Figure 4.7). Sample 104-01 (184.53 mg) oxidized to an O/M ratio of about 2.41 within 100 hours and exhibited a plateau with zero slope for approximately 400 hours before mass increase resumed.

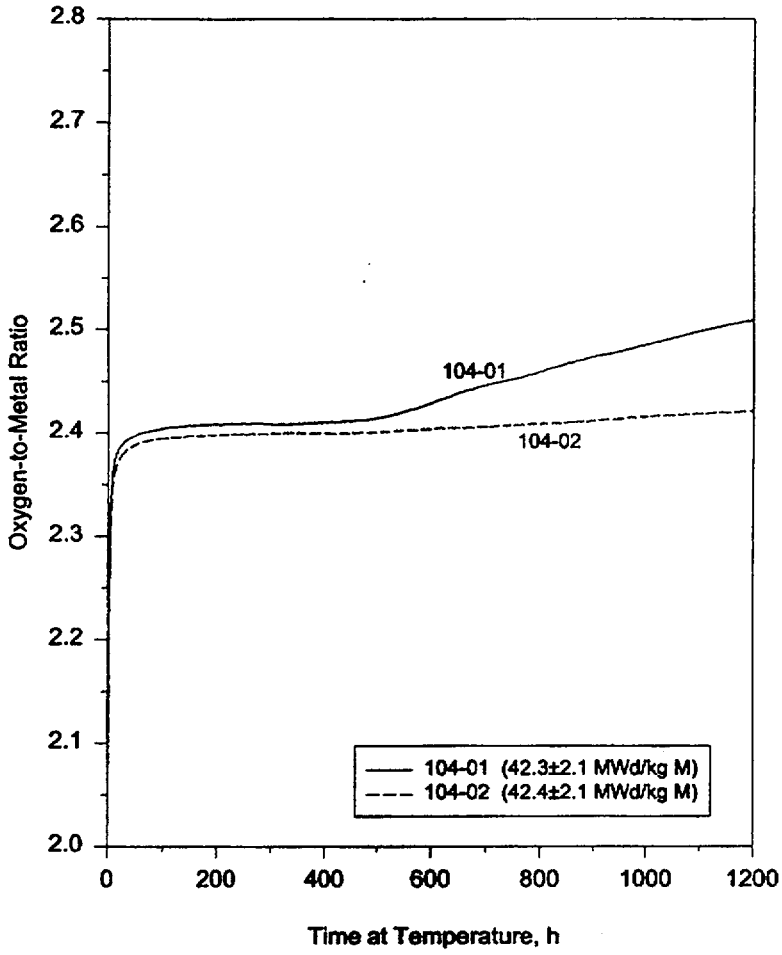

Figure 4.7. Oxidation Behavior of ATM-104 Fragments at 305°C

The test was terminated after 1201 hours of operation with a final O/M ratio of 2.51. Sample 104-02 (213.90 mg) oxidized to an O/M ratio of about 2.40 within 120 hours and remained on this plateau with no mass increase for over 500 hours before mass increase resumed, albeit at a much slower rate than sample 104-01. A final bulk average O/M ratio of 2.42 was reached before the test was terminated after 1200 hours. Oxidation of these PWR fragments clearly demonstrated much longer plateaus than those observed in oxidation of the lower burnup ATM-105 (BWR) fragments at the same temperature and under similar atmosphere. While further testing should be performed to rule out the possible dependence of the stabilization effect (plateau behavior of the $UO_{2.4}$ to U_3O_8 transition) on reactor type, the data

obtained in these measurements strongly suggest similar oxidation behavior dependencies on burnup for BWR and PWR fuels.

4.1.4 ATM-108 Tests

Finally, two fragments of fuel from the high-burnup region of ATM-108 were obtained in a similar fashion as for the ATM-104 samples. One fragment (108-01) was cut from near the centerline of a pellet, and a second fragment (108-02) was cut from the pellet surface. ATM-108 was a group of fuel rods from the same assembly as ATM-105; however, the rods comprising ATM-108 contain an initial doping of Gd_2O_3 to serve as a burnable poison for reactivity control. The rod (ADN0206) from which these samples were cut contain 3 wt% Gd_2O_3 and the same initial enrichment (2.93 wt%) of ^{235}U as the ATM-105 rod from which the previous samples were obtained. The burnup of the ATM-108 fuel in this region was expected to be approximately 26 to 28 MWd/kg M [120], slightly lower than the 28.5 to 31.5 MWd/kg M expected for the ATM-105 high-burnup region [70]. The initial Gd in the fuel undergoes neutron capture during reactor operations and remains as Gd, although of higher atomic mass number. Both the substitution of U with fission products and actinides and the Gd-doping are expected to stabilize the $UO_{2.4}$ with respect to oxidation to U_3O_8. The actual distribution of Gd_2O_3 within the fuel is not known; however, the homogeneity of these early fuels is questionable.

Sample 108-01 (171.01 mg) was oxidized at 305°C for over 2400 hours. As seen in Figure 4.8, this sample did not exhibit a plateau with zero slope, but exhibited a very slow, continuous increase in the O/M ratio. The time required to oxidize this sample from an O/M of about 2.475 to 2.481 was approximately 1000 hours. On the other hand, sample 108-02 (232.23 mg) was taken from the higher burnup fuel pellet surface and exhibited two different plateau behaviors. The first plateau at an O/M ratio of about 2.38 was reached after about 40 hours and had a duration of less than 50 hours before more rapid mass increase resumed. A second plateau at an O/M ratio of 2.45 was reached after about 475 hours, and then a plateau with zero slope was exhibited for over 2000 hours. It is believed that those portions of the specimen with lower burnup or lower Gd content oxidized to U_3O_8, while the portions with higher substitutional impurities remained at $UO_{2.4}$. This would explain the second plateau at such a low O/M ratio. Post-oxidation analyses are planned to determine the quantity of each phase present. These irradiated samples doped with Gd_2O_3 have exhibited much slower overall oxidation behavior than any other specimen oxidized at 305°C.

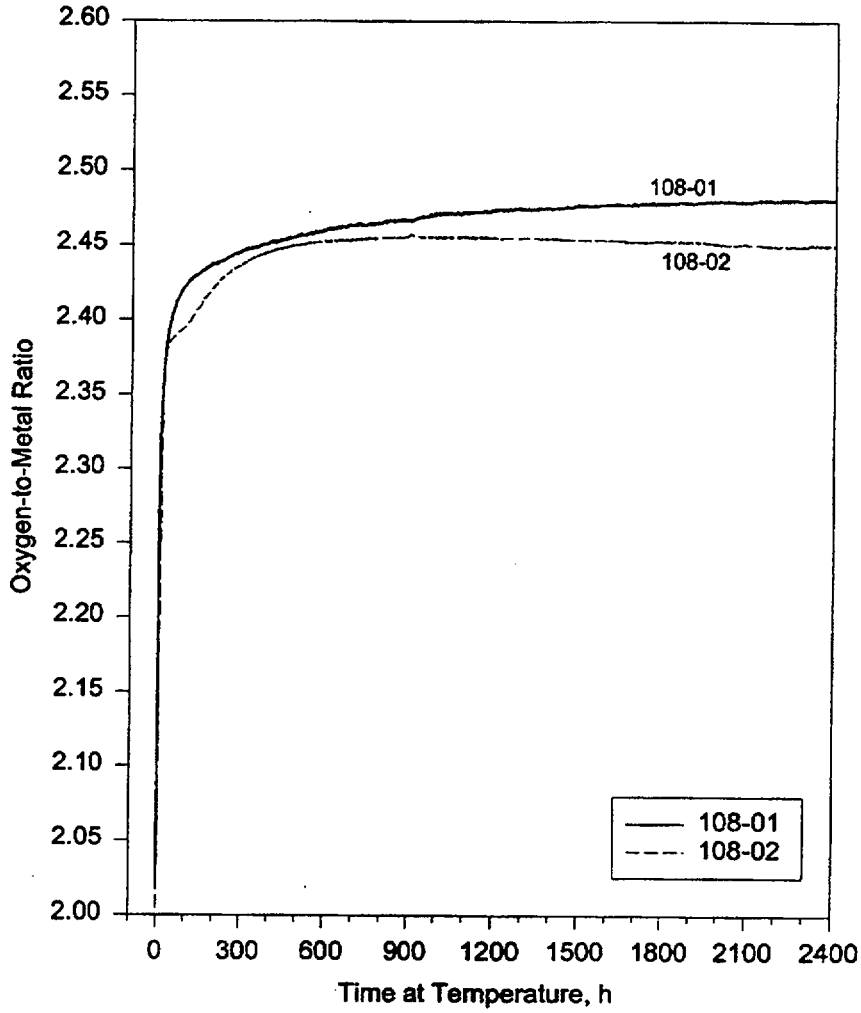

Figure 4.8. Oxidation Behavior of ATM-108 Fragments at 305°C

4.2 Burnup Analyses

In order to quantify the apparent burnup dependence of the oxidation behavior, the burnup for each sample had to be known. The exact radial and axial location for most samples was not known. Thus, the individual burnup of each specimen was measured using either a ^{148}Nd isotope dilution method or by analysis of the γ-ray energy spectrum.

4.2.1 ^{148}Nd Isotope Dilution Method

After it became apparent that the sample-to-sample variability was the cause for the different oxidation behaviors observed, authorization and funding were obtained to perform an analysis of the burnup of some of the individual specimens that had been oxidized earlier in the project. Nine of the first

18 oxidized samples were chosen. Samples 105-01 and 105-02 had been disposed of and were unavailable for any further testing. Three specimens each from the scoping tests (105-03 through 105-05), the 283°C tests (105-6 through 105-08), and the 305°C tests (105-10, 105-11, and 105-15), including one of the known low-burnup specimens, were analyzed using the method described in Section 3.2.3.1. The results of this analysis are found in Table 4.1 and are identified on the appropriate oxidation curves in brackets []. The uncertainty of ±4% accounts for experimental uncertainty, as well as the reported uncertainty in converting atom% burnup to burnup in units of MWd/kg M [59]. Other specimens will be analyzed upon funding approval.

Table 4.2 lists the total number of fissions, as well as the total number of uranium and plutonium atoms normalized to the mass of the specimen in the one-tenth mL aliquots analyzed. The atom% burnup is calculated using Equation (4.1):

$$\text{atom\% burnup} = \text{Fissions}/(\text{U}+\text{Pu}+\text{Fissions}) \tag{4.1}$$

Also included is the fraction of ^{242}Pu in the total Pu, as determined by thermal ionization mass spectrometry. The amount of ^{242}Pu can be used to qualitatively order the samples with respect to possible higher actinide content. The atom densities reported for sample 105-11 appear very low with respect to the other samples; however, additional calculations (comparing the ratios of the atom densities of this sample to samples of similar burnup) seem to indicate that the burnup results are correct. It is suspected that either the reported mass was incorrect (too large) or that not all of the sample dissolved.

4.2.2 Gamma Spectrum Analysis

The burnup of all specimens starting with sample 105-11 was determined before oxidation by correlating the specific activity of ^{137}Cs with ORIGEN2 predictions, as described in Section 3.2.3.2. The specific activity for each sample, the uncertainty associated with the combined effects of the γ-ray self-absorption and statistical and calibration uncertainties, and the corresponding burnup range are listed in Table 4.3. Burnups calculated by comparing the measured ^{137}Cs specific activity with ORIGEN2 predictions are also included in parentheses ( ) in the corresponding oxidation curves. Included in Table 4.3 are the specific activities for ^{241}Am and the rather large uncertainties associated with this isotope. Although the activity of ^{241}Am is not a good measure of burnup, it is the only higher actinide detected by this method and is the only means of qualitatively determining the relative higher actinide content of samples. Samples from near the pellet surface will have not only higher burnup, but larger concentrations of higher actinides due to the resonance absorption in ^{238}U.

Table 4.2. Atom Densities Found by Mass Spectrometry Normalized to Sample Mass

Sample	Atom Density U	Atom Density Pu	Atom Density Fissions	Percent ^{242}Pu
105-03	8.107×10^{18}	5.583×10^{16}	2.458×10^{17}	8.03
105-04	8.247×10^{18}	5.629×10^{16}	2.445×10^{17}	7.56
105-05	8.234×10^{18}	7.209×10^{16}	2.610×10^{17}	7.79
105-06	8.033×10^{18}	7.104×10^{16}	2.753×10^{17}	9.01
105-07	8.109×10^{18}	5.610×10^{16}	2.414×10^{17}	7.84
105-08	8.069×10^{18}	7.206×10^{16}	2.851×10^{17}	10.44
105-10	7.933×10^{18}	6.548×10^{16}	2.559×10^{17}	8.19
105-11	6.386×10^{18}	5.157×10^{16}	2.048×10^{17}	8.46
105-15	8.343×10^{18}	4.169×10^{16}	1.653×10^{17}	3.17

Table 4.3. Burnup as a Function of ^{137}Cs Specific Activity

Sample	Specific Activity of ^{137}Cs (μCi/mg)	Burnup (MWd/kg M)	Specific Activity of ^{241}Am (μCi/mg)
105-11	48.3±2.9	25.9±1.5 (3.9)	1.6±0.5
105-12	52.1±3.1	27.9±1.7 (4.2)	1.9±0.6
105-13	52.8±3.2	28.3±1.7 (4.2)	1.1±0.3
105-14	52.5±3.2	28.1±1.7 (4.2)	2.0±0.6
105-15	34.9±0.7	19.1±0.4 (2.9)	1.4±0.4
105-16	33.3±0.7	18.3±0.4 (2.7)	0.8±0.2
105-17	30.3±0.6	16.7±0.3 (2.5)	0.7±0.2
105-18	30.6±0.6	16.8±0.3 (2.5)	1.1±0.3
104-01	80.8±4.0	42.3±2.1 (6.3)	1.8±0.5
104-02	81.1±4.1	42.4±2.1 (6.4)	2.0±0.6
108-01[a]	31.3±3.1	17.6±1.8 (2.6)	Not detected
108-02[a]	63.0±3.2	34.8±1.9 (5.2)	18.0±6.7

(a) ORIGEN2 runs performed using the same input parameters as for the ATM-105 samples; i.e., Gd_2O_3 doping was ignored.

In the present tests, two samples had burnups determined by both the ^{148}Nd and ^{137}Cs methods. ORIGEN2 was run for the burnups found by the ^{148}Nd method for these two samples, and the specific

activity of ^{137}Cs predicted by ORIGEN2 was compared with the measured value. Sample 105-15 had a burnup of 18.6±0.7 MWd/kg M measured using the isotope dilution method. The ^{137}Cs activity predicted for a BWR sample with this burnup was within 3% of the value measured by the γ-ray energy analysis. Similarly, sample 105-11 had a measured burnup of 29.6±1.2 MWd/kg M. ORIGEN2 predicts a specific activity of 55.5 μCi/mg, which is 13% larger than the experimentally measured value of 48.3 μCi/mg. The deviation of the predicted value from the measured value ranges from 8% (at +1σ of the measured value) to 18% (at -1σ). With the estimated uncertainty of about 4% for the ^{148}Nd analysis and an average difference between the ORIGEN2 burnup prediction for ^{137}Cs activity and experimental values of 13%, it is reasonable to assume an uncertainty in the burnup estimates obtained through γ-ray spectroscopy of approximately ±15%. This 15% uncertainty is expressed in parentheses ( ) for the burnups reported in Table 4.3. The smaller uncertainties are those associated with the uncertainty in the specific activity only. It is important to note the marked difference in ^{137}Cs activity and the corresponding difference in local burnup between sample 108-02, which was taken from the pellet surface, and sample 108-01, which was taken from the pellet centerline.

4.3 Dry-Bath Oxidation Results

During the past 10 years, over 100 different samples have been oxidized at various temperatures in the dry-baths at PNNL. A large fraction of the samples have been oxidized at temperatures less than 150°C, and even though they had operated for about 50,000 hours, the bulk average O/M ratios are less than 2.2. Samples consisting of fragments and fragments crushed to powders were oxidized in the dry-baths, both in dry and moist air. However, to allow direct comparison with the single fragment TGA tests, the primary focus for this study was samples that consisted of fragments oxidized in dry air. As with the TGA tests, the precise axial and radial location of the fuel samples in the fuel rod segments was not known.

4.3.1 175°C Tests

Multiple samples of each of the fuels have been oxidized at 175°C in two separate dry-baths using a dry air atmosphere. Overall agreement of the samples for each ATM has been excellent, with the largest difference in the O/M ratio between samples at any given time being about 0.04. Each sample had an initial mass of approximately 10 grams; however, the number of fragments required to make up this sample varied greatly. For example, the three different ATM-105 samples contained 15, 22, and 28 fragments, respectively. The number of fragments for a 10-g sample of Turkey Point fuel ranged from 31

to 34, while the range was from 15 to 40 and 35 to 101 for ATM-104 and ATM-106, respectively. The corresponding variation in surface area exposed to the oxidant is possibly one reason for the minor differences in the initial mass increase among samples of the same fuel type. Also, fragments from near the pellet surface will have a high concentration of fine fission gas bubbles on the grain boundaries, promoting more rapid oxidation than for the fuel near the center where the bubbles are larger and fewer in number. This hypothesis is substantiated by the fact that the differences between samples decreased with increasing time such that the O/M ratios for samples of each fuel type varied by no more than 0.02 at the end of these experiments. The temperature difference between the two blocks of dry-bath #1 was roughly 7°C, which also contributed to the more rapid mass increase for some of the samples. Figure 4.9 shows the change in the O/M ratio as a function of time for one sample of each of the four fuel types. For each fuel, with the possible exception of ATM-106, it appears that a plateau at an O/M of about 2.4 had been reached, and mass increase was continuing to occur at the end of the measurements.

4.3.2 195°C Tests

One sample of each of the four fuel types was oxidized in a dry-air atmosphere at 195°C. In each case, the sample consisted of fragments that had been crushed and sieved to a Tyler mesh size of –12/+24 (roughly 0.7 to 1.7 mm). Figure 4.10 shows the change in the O/M ratio as a function of time for these four samples. With the exception of the Turkey Point fuel, which had previously been oxidized for 28,868 hours at 110°C to a bulk O/M of 2.009, all of the samples were as-irradiated and assumed to have an O/M of 2.00. The ATM-105 sample was freshly crushed for this test, while the ATM-104 and ATM-106 samples were from powder stored for 3 years before the start of this test. Again, it appears that a plateau in the range of O/M 2.35 to 2.40 had been reached, and mass increase was continuing to occur at the end of the measurements.

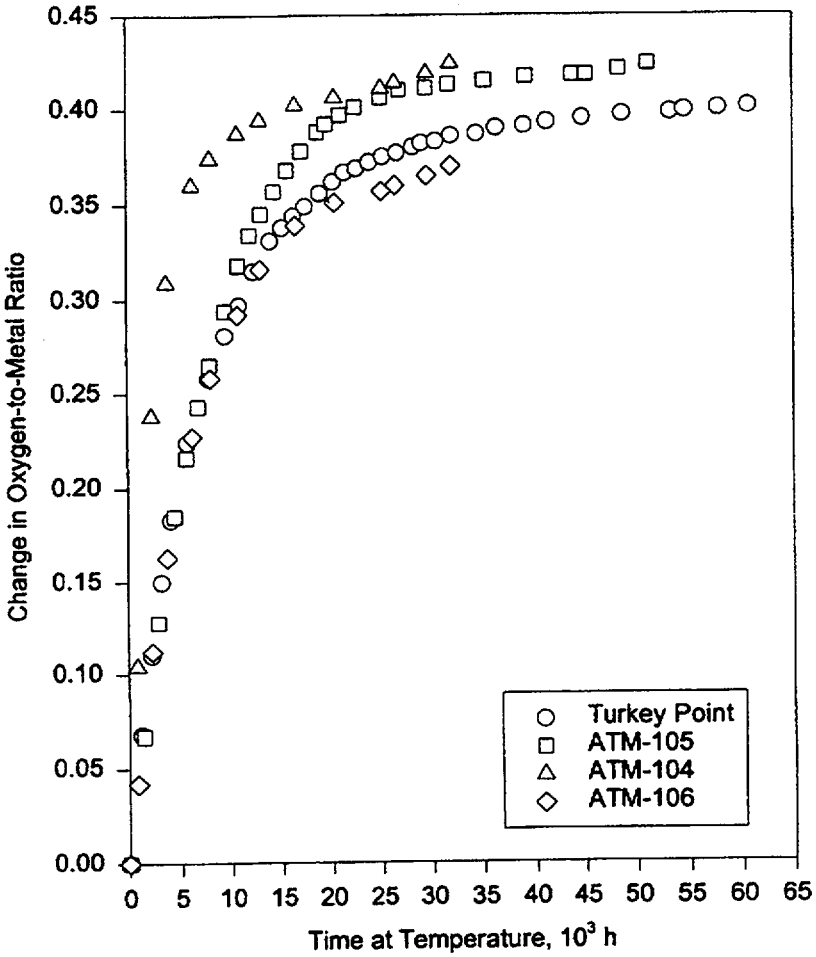

Figure 4.9. Oxidation Behavior of LWR Spent Fuel Fragments Oxidized in a 175°C Dry Bath

4.3.3 255°C Test

A dry-bath test at 255°C was initiated about 2 years after the start of the 175°C and 195°C tests. This test contained 11 samples in which seven each consisted of about 5 g of spent fuel fragments; the remaining four samples consisted of about 5 g each of crushed-fuel fragments, i.e., powder. The seven samples were prepared as follows: 1) one sample each of ATM-104 and ATM-105 from as-irradiated (no prior oxidation) fuel fragments, 2) one each of Turkey Point (110°C for 28,868 hours to O/M ~2.004) and ATM-106 (110°C for 525 hours to O/M ~2.000) that had been very slightly oxidized at low temperature, and 3) one each of Turkey Point (175°C for 43,945 hours to O/M ~2.395), ATM-105 (175°C for 34,420 hours to O/M ~2.422), and ATM-104 (176°C for 15,671 hours to O/M ~2.395) from fragments that had been oxidized to an O/M ratio near the plateau at 175°C. Figure 4.11 is a plot of the oxidation curves for

the as-irradiated and slightly pre-oxidized samples. Unlike the previous data of Einziger and Strain [4] (Figure 2.3) where the plateau at a temperature of 250°C existed for almost 10,000 hours, none of these samples exhibited the typical plateau behavior. The lack of an observable plateau for these samples,

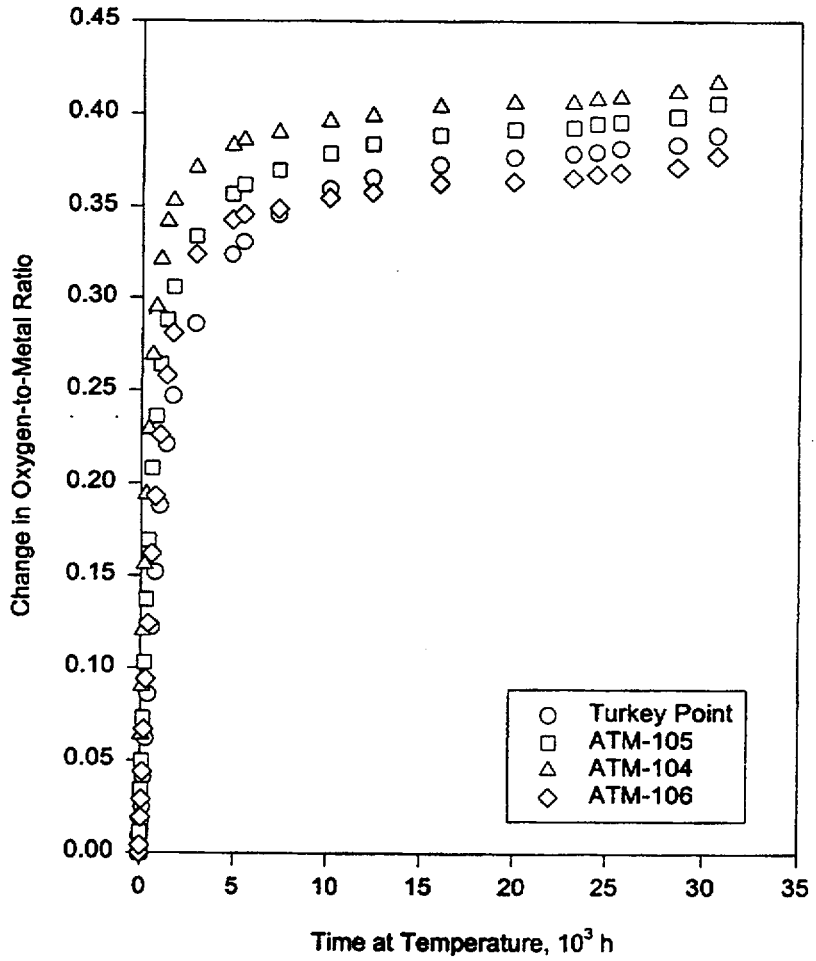

Figure 4.10. Oxidation Behavior of Crushed LWR Spent Fuel Fragments in a 195°C Dry Bath

which started with an O/M <2.005, is in marked contrast to the behavior of the Turkey Point and ATM-105 samples that had been pre-oxidized to an O/M ratio near the plateau at lower temperatures before being oxidized at 255°C. The open symbols in Figure 4.12 represent the pre-oxidized samples. The previously oxidized samples of Turkey Point and ATM-105 fuel clearly exhibited plateau behavior, although the duration is much less than that expected based on the previous Einziger data [4]. The ATM-104 pre-oxidized sample, on the other hand, had no observable plateau. All samples, however, began to oxidize at about the same rate-of-change in O/M ratio after about 4000 hours. (No interim weighings to

determine mass increase were performed between 4095 and 7281 hours.) Figure 4.13 is a plot of the oxidation curves for the four different Turkey Point fuels oxidized in the 255°C dry-bath test. Again, it is clear that the sample oxidized at a lower temperature to an O/M ratio of about 2.4 before oxidation at 255°C exhibited a plateau (open circles), whereas the as-irradiated or only slightly pre-oxidized samples (closed symbols) exhibited no plateau. It is also clear that the crushed fragments increased in mass much faster than the intact fragments because of the much larger surface area exposed. Possible explanations for the different oxidation behaviors observed are presented in Section 5.

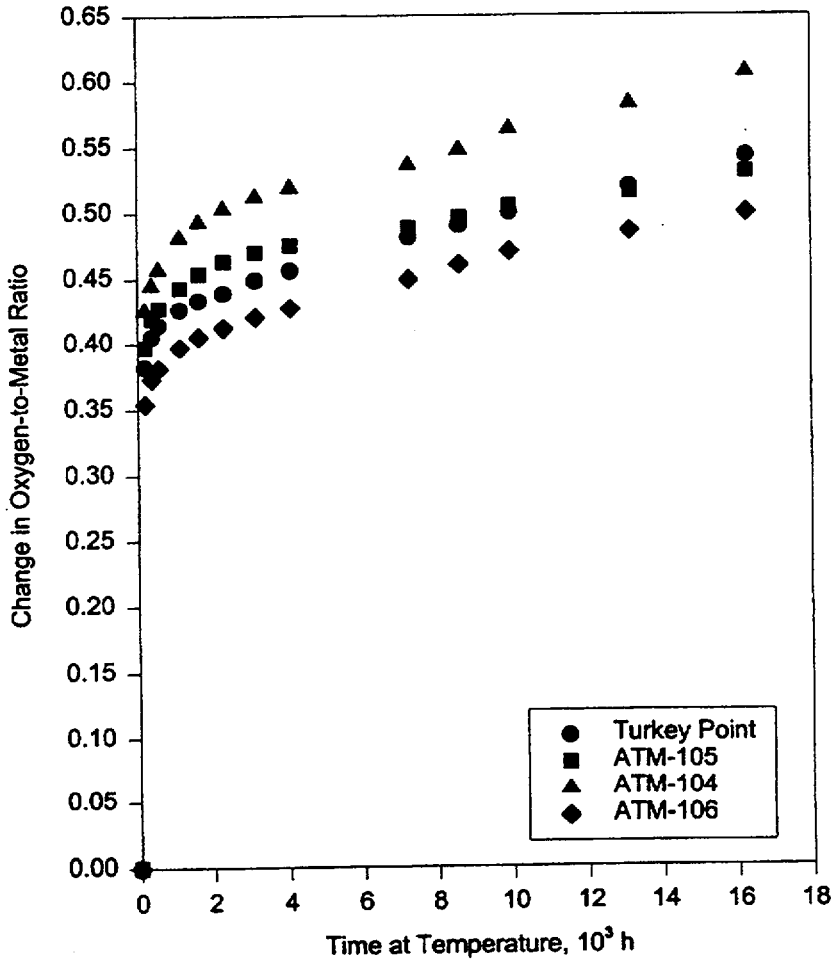

Figure 4.11. Oxidation Behavior of As-Irradiated LWR Spent Fuel Fragments in a 255°C Dry Bath

XRD of the samples oxidized in the 255°C dry-bath with an O/M ratio as high as 2.56 detected U_4O_9 with only minor U_3O_8 formation, even though the two Turkey Point samples and one of the ATM-105 samples had formed significant amounts of powder. A Turkey Point sample of crushed fragments also oxidized at 255°C obtained a bulk O/M ratio of 2.62 and, still, the only phase identified by

XRD was U_4O_9. The lack of observable U_3O_8 at these relatively high O/M ratios is in contrast with the TGA studies where U_3O_8 was identified in samples oxidized at 283°C to an O/M ratio as low as 2.49.

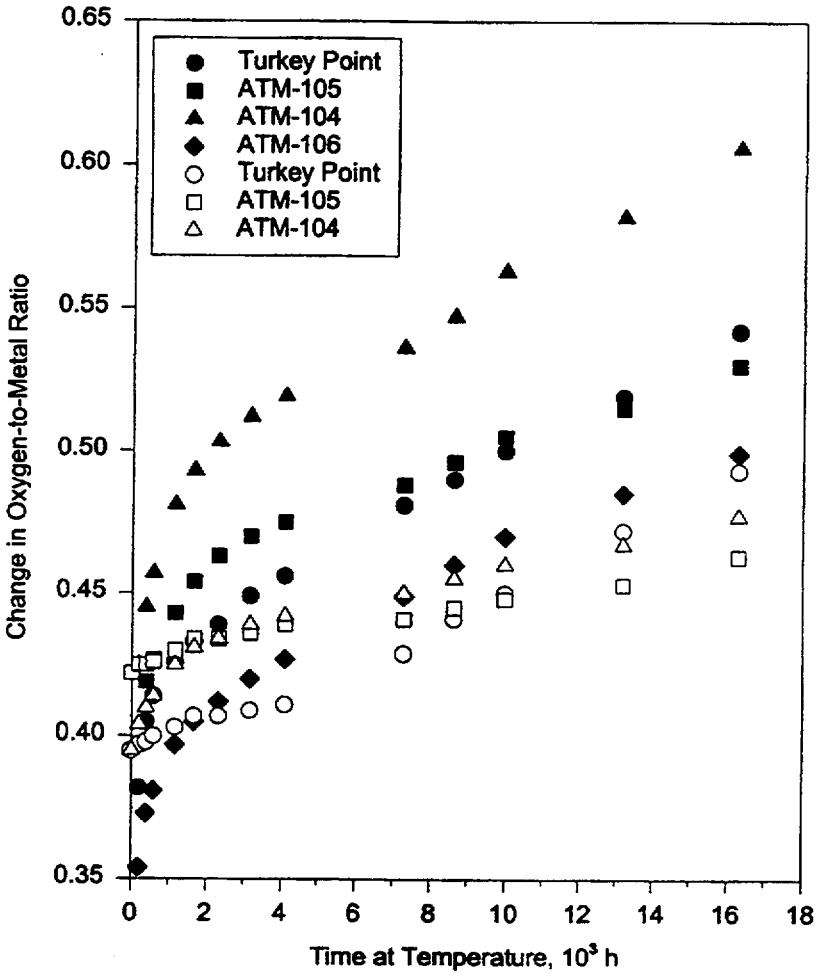

Figure 4.12. Oxidation Behavior of As-Irradiated and Pre-Oxidized (Open Symbols) LWR Spent Fuel Fragments in a 255°C Dry Bath

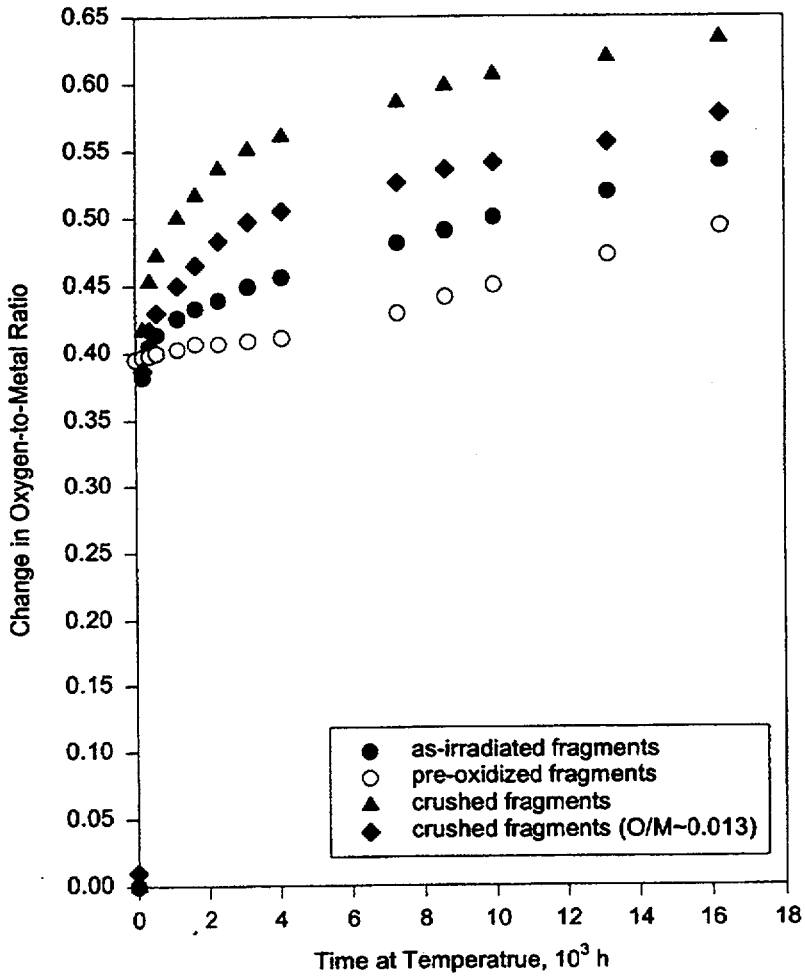

Figure 4.13. Oxidation Behavior of Turkey Point Fuel in a 255°C Dry Bath

4.4 Quantitative XRD Results

Larry Thomas of PNNL [37] used XRD to quantitatively analyze spent fuel samples oxidized in the dry-baths with average O/M ratios ranging from 2.40 to 2.61 by combining known quantities of fuel and a reference material (in this case, Al_2O_3). Using the integrated peak intensities with the knowledge of the amount of material present, it was possible to determine the weight fractions of each phase present. Figure 4.14 is a plot of the peak intensity of the U_4O_9 ($UO_{2.4}$) peak when normalized to the Al_2O_3 standard and corrected for the fuel-to-Al_2O_3 weight ratio of each sample. As seen in the figure, as the O/M ratio increases, the amount of $UO_{2.4}$ present decreases. There is also a corresponding broadening of the X-ray peak. Since no other phases are present, the $UO_{2.4}$ is obviously being transformed into a phase that is amorphous to XRD, meaning it is either a nanocrystalline phase or truly amorphous. Analysis of 10

oxidized samples resulted in an average O/M of 2.70±0.08 for this "amorphous" phase. A truly amorphous phase would not be expected to have such a constant O/M. Since the calculated O/M ratio is very similar to that of U_3O_8, it is believed that oxidation of spent fuel beyond $UO_{2.4}$ at temperatures ≤255°C results in U_3O_8 formation, but in a nanocrystalline state that is not readily detected by XRD. This is in agreement with the findings of Hoekstra et al. [27], who have shown that U_3O_8 formed below about 250°C may be poorly crystalline.

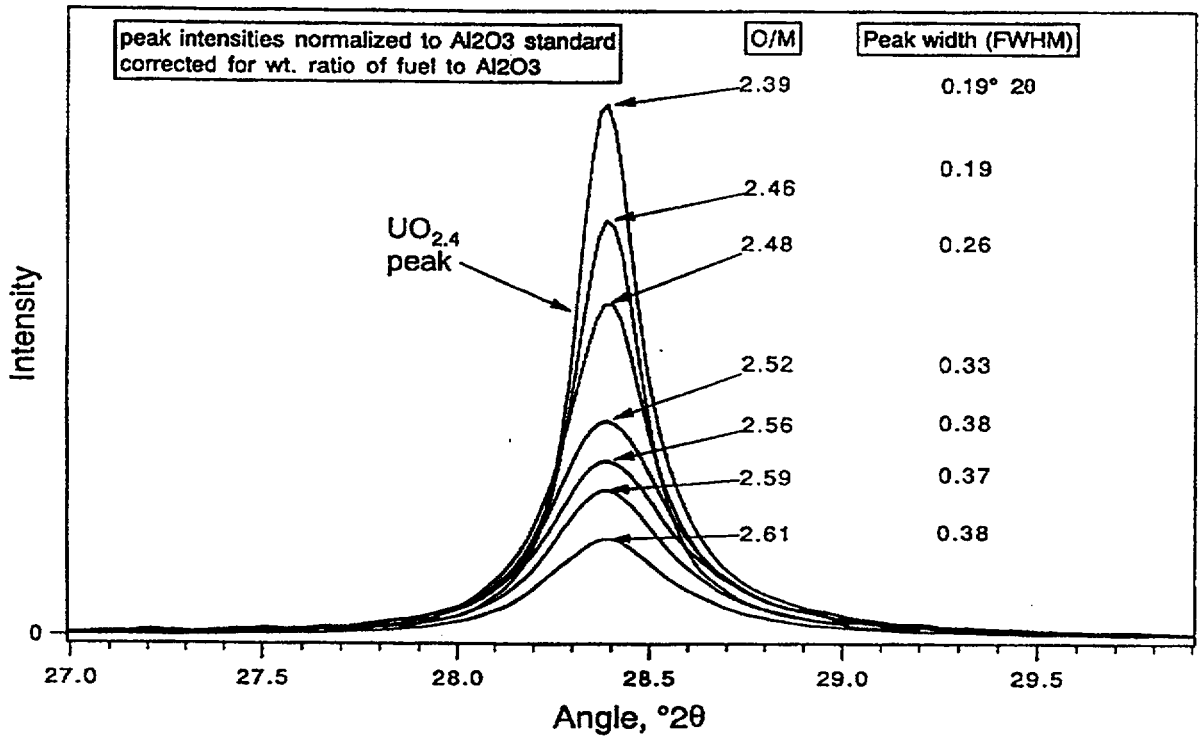

Figure 4.14. Quantitative XRD Analysis of Oxidized LWR Spent Fuel [37]

5.0 DISCUSSION OF RESULTS

Sections 4.1 and 4.3 indicate that a large variability exists in the oxidation behavior of LWR spent fuel. The variable burnup of the individual specimens, presented in Section 4.2, was thought to be the primary factor resulting in the different behaviors observed. In this section, the burnup dependence of spent fuel oxidation will be examined and related to the empirical dependence to changes in the crystal lattice energy that result from fission product and actinide impurities acting as substitutional cations. The primary focus will be the results of the TGA tests, with the results of the dry-bath tests also included in the discussion.

The plateau observed in the oxidation of LWR spent fuel nominally occurs at an O/M ratio of 2.4, but was actually observed to vary in the range 2.35 to 2.43 for the specimens tested in the TGA systems. Some samples (e.g., 105-04, 105-08, 104-01, 104-02, and 108-02) exhibited plateaus with a nearly-zero slope for extended periods; others (e.g., 105-06, 105-11, and 108-01) exhibited plateaus characterized by a very slow, continual increase in the O/M ratio; and other samples (e.g., 105-02, 105-17 and 105-18) had no observable plateau whatsoever. As a way to provide a rational basis to analyze the data, the O/M ratio at which the plateau occurs, $(O/M)_\delta$, was defined as the O/M ratio at which a local minimum in the time-rate-of-change in the O/M ratio was reached. Further, the duration of the plateau, t_δ, was then defined as the time required to oxidize the sample through the range $(O/M)_\delta \pm 0.005$. The time to reach the plateau, $t_{2.4}$, was defined as the time required to oxidize the sample to an O/M ratio of $(O/M)_\delta$-0.005. This methodology can be applied to the TGA data, which were recorded every 5 minutes and then averaged over a 1-hour interval for this analysis. For the dry-bath data, where there are often hundreds to thousands of hours between data points, determining $t_{2.4}$ and t_δ is much more subjective. It is important to stress that $t_{2.4}$ and t_δ do not necessarily correspond to parameters that are quantitative measures of the state of the fuel or characteristics of the underlying oxidation mechanism, but were defined here to provide consistent measures even in cases where the plateau exhibited a non-zero slope or was not observable. Nevertheless, this methodology could not be used, for example, with sample 108-01, which did not exhibit the characteristic local minimum in the time-rate-of-change in O/M ratio because it had a slow, continuous mass increase after an O/M ratio of about 2.4 had been reached (see Figure 4.8). Further observations and comments concerning the shortcomings of this methodology are included in the following sections.

5.1 The First Transition ($UO_2 \rightarrow UO_{2.4}$)

Previous studies by Einziger et al. [10,30-35,38] focused on the oxidation of LWR spent fuel from UO_2 to $UO_{2.4}$. The $UO_{2.4}$ phase is very similar to U_4O_9 in that it maintains the original cubic fluorite structure, albeit with a slightly smaller lattice parameter, but contains excess diffuse oxygen. Oxidation proceeds rapidly along the grain boundaries, presumably because the microscopic fission gas bubbles located on the grain boundaries readily allow transport of oxygen. Growth of the $UO_{2.4}$ phase throughout the individual grains then continues and appears to be controlled by the diffusion of oxygen through the outer $UO_{2.4}$ layer. At temperatures up to 250°C, no U_3O_8 was detected by XRD or TEM until conversion to $UO_{2.4}$ was complete. Once the grain boundaries have completely oxidized, the sample can be approximated as a loose conglomeration of individual grains. The diffusion of oxygen through the grain boundaries (whether in UO_2 or the slightly contracted $UO_{2.4}$), while rapid compared to the diffusion of oxygen through the $UO_{2.4}$ product layer, is not infinitely fast, and thus the grains near the surface of the specimen or near pores and cracks tend to oxidize more rapidly because of the abundant supply of oxygen. Also, oxidation is influenced by the initial grain size, with finer-grained fuels oxidizing faster in accordance with the greater surface area per unit grain volume [38]. Only after an O/M ratio of about 2.05 to 2.1 is achieved do the effects of sample surface area, grain size, and fission product inclusion and gas bubble density on the grain boundaries become less important. From this point, diffusion-controlled kinetics [31] and similar oxidation rates for various fuels [30] become evident. Still, oxidation of individual grains proceeds via a fairly uniform oxidation front.

Unirradiated UO_2 oxidizes via surface formation of U_3O_7 followed by subsequent formation and spallation of U_3O_8. Low-temperature oxidation of spent CANDU™ fuel, which achieves much lower burnup, but has higher LHGR than nominal LWR fuels, appears to exhibit behavior between that of unirradiated UO_2 and LWR spent fuel [121]. The grain boundaries of spent CANDU™ fuel do not contain the high concentration of fission gas bubbles observed in LWR spent fuel; however, the high LHGR in CANDU™ fuel results in more cracking of the fuel pellets, providing additional pathways for oxygen transport to the grains. Recent experiments on the oxidation of spent CANDU™ fuel at 150°C have displayed essentially complete oxidation to U_3O_7 throughout the sample with only minimal conversion to U_3O_8 [121].

5.1.1 Grain Size Dependence

The average grain size of a sample is an important factor in determining the rate of mass increase. As seen in Figure 2.1, oxidation of a large fraction of the grain boundaries is complete once the O/M ratio

reaches about 2.05. As the grains oxidize, the oxidized portion contracts due to the densification of the fuel as either U_4O_9 or U_3O_7, and the grain boundaries open up and offer even less resistance to diffusion of oxygen. Thus, the grains can then be modeled as individual entities, each exhibiting a fairly uniform oxidation front. Oxidation of the smaller grains appears to be complete once a bulk O/M ratio between 2.24 and 2.31 has been reached (see Figure 2.1). If, however, all grains were spherical and of uniform size, a bulk O/M ratio of 2.30 would be achieved when a spherical shell with a thickness of 35% to 40% of the grain radius has been oxidized to $UO_{2.4}$ and the central core remains as UO_2. The thickness of the oxidized shell is 50% to 55% of the grain radius when the bulk O/M ratio is 2.35. Since the rate of mass increase is controlled by diffusion of oxygen through the product layer, the time to oxidize completely to $UO_{2.4}$ increases with increasing grain size, all other factors being equal. The time required to reach a plateau, calculated using the present methodology or through more subjective interpretation of the variation of the O/M ratio as a function of time, is strongly influenced by the mean grain size.

Grain growth near the fuel pellet centerline, especially in the high-burnup region of the fuel rod, has been estimated to be approximately 13% and 30% for ATM-105 [70] and ATM-104 [69], respectively. The ATM-106 [120] samples used in the dry-bath oxidation studies have an estimated grain growth >100%. Examination of the dry-bath data (Figures 4.9, 4.10, and 4.11), where burnup and other sample-to-sample variations were reduced as a result of the much larger sample size (5 to 10 g), shows that at 175°C, 195°C, and 255°C, the larger-grained Turkey Point fuel (mean grain size of 20 to 30 μm) displays smaller rates of O/M increase than the small-grained ATM-105 (11 to 15 μm) and ATM-104 (10 to 13 μm) fuels. The ATM-106 fuel (mean grain size of 7 to 16 μm) displays a lower rate of oxidation than the ATM-104 and ATM-105 fuels, apparently contradicting the previous findings. However, the mean grain size quoted above for ATM-106 was measured on a rod with 11% fission gas release (NBD107) [117], whereas the fuel specimens used in the dry-bath tests came from a rod (NBD131) with 18% fission gas release [120]. It is reasonable to assume that the larger fission gas release is a result of higher operating temperatures in the reactor, which, in turn, would suggest that more grain growth had occurred, and thus the dry-bath specimen might well have had a significantly higher average grain size than assumed above. Specimens from the ends of the fuel rods, which experience lower burnup and temperatures because of the lower neutron flux in these regions, have also been shown [70] to have experienced minimal grain growth. Thus, the axial and radial position of the fuel specimens can affect the oxidation behavior because of variations in both burnup and grain growth.

5.1.2 Activation Energy

The time to reach the plateau for LWR spent fuel has been shown (see Equation 2.3) [30] to follow an Arrhenius temperature dependence with an activation energy of 111±29 kJ mol^{-1}, which compares with the activation energy of 100 kJ mol^{-1} reported by Einziger et al. [30] for the rate at which the width of the $UO_{2.4}$ phase increases with time. Woodley et al. [31] reported an activation energy of 113±17 kJ mol^{-1} for the low-temperature oxidation of UO_2 to $UO_{2.4}$ using Turkey Point [118] spent fuel specimens in the same TGA systems as used for the present tests. A recent review by McEachern [121] reported an activation energy of 96 kJ mol^{-1} for the diffusion-controlled formation of U_3O_7/U_4O_9 on unirradiated UO_2 powders. For data that were best fitted with linear kinetics, such as for unirradiated UO_2 pellets, McEachern [121] reported an activation energy of 99 kJ mol^{-1}. All of these values agree with the reported value of 100 kJ mol^{-1} for the activation energy of oxygen self-diffusion in UO_{2+x} [122], confirming that oxygen diffusion is indeed the rate-limiting step. Since the restructuring of the UO_2 lattice to form either $UO_{2.4}$ (U_4O_9-like) or U_3O_7 is minimal, no large energy barrier would be expected.

Table 5.1 summarizes the calculated oxidation times, including the time-to-plateau ($t_{2.4}$) and the time required to oxidize a sample from an O/M ratio of 2.30 to 2.35, for the present TGA specimens. Because the time-to-plateau is defined as the time required to oxidize a sample from an O/M ratio of 2.00 to $(O/M)_s$-0.005, the effects of variables such as specimen surface area, grain size, etc., are implicitly included in this calculation. Only samples from the same fuel element, 105-01 through 105-18, were used, to minimize the influence of these effects on calculating the temperature dependence of the activation energy. The values of $\log(t_{2.4})$ for these samples are shown as a function of inverse temperature in Figure 5.1. A least-squares fit to the data yields an activation energy of 149±26 kJ mol^{-1} (R^2=0.67). If samples 105-15 through 105-18 are ignored because they are likely to have smaller mean grain sizes compared to the other samples (see Section 5.1.1), then the calculated activation energy is 120±18 kJ mol^{-1} (R^2=0.73), in excellent agreement with the values reported previously. As a means of further verifying the activation energy, an Arrhenius plot of the time to oxidize the samples from an O/M ratio of 2.30 to 2.35 is shown in Figure 5.2. The temperature-dependent activation energy found is 123±18 kJ mol^{-1} (R^2=0.74), or 109±14 kJ mol^{-1} (R^2=0.84) when the four specimens from the low-burnup region are neglected. Again, these values are in excellent agreement with previously published values.

Table 5.1. Calculated Oxidation Parameters from TGA Tests

Sample	Oxidation Temperature (°C)	Time to plateau, $t_{2.4}$ (h)	Time to oxidize $UO_{2.30} \rightarrow UO_{2.35}$ (h)	Duration of the plateau, t_δ (h)	$(O/M)_\delta$	Average d(O/M)/dt after the plateau[a] (h^{-1})
105-01	283	55	6	40	2.40	1.4×10^{-3}
105-02	325	7	1.5	0.5	2.39	1.8×10^{-2}
105-03	305	17	2.5	3.5	2.39	8.8×10^{-3}
105-04	270	152	23	788	2.40	1.4×10^{-4}
105-05	255	212	30	300≤	2.41	N/A
105-06	283	161	7	200	2.43	7.4×10^{-5}
105-07	283	107	10	158	2.41	5.2×10^{-4}
105-08	283	351	17	~3300	2.43	1.7×10^{-5}
105-09	305	46	5	34	2.40	5.7×10^{-4}
105-10	305	27	3	14	2.41	1.5×10^{-3}
105-11	305	34	5	53	2.39	9.2×10^{-4}
105-12	305	43	5	31	2.40	1.1×10^{-3}
105-13	305	32	4.5	22	2.40	1.1×10^{-3}
105-14	305	46	6	35	2.42	1.4×10^{-3}
105-15	305	15	2.5	0.6	2.40	1.7×10^{-2}
105-16	305	14	3	0.8	2.38	2.0×10^{-2}
105-17	305	10	2	0.4	2.35	3.0×10^{-2}
105-18	305	8	1	0.3	2.39	4.0×10^{-2}
104-01	305	103	3	410	2.41	1.3×10^{-4}
104-02	305	96	3.5	610	2.41	3.1×10^{-5}
108-01	305	N/A	7	~2000	2.48	1.4×10^{-3}
108-02	305	30	4	50 (2000)	2.39 (2.45)	N/A

(a) Average taken in the O/M range 2.44-2.60 except for the following samples: 105-06(2.44-2.49), 105-08(2.45-2.47), 105-09(2.412.43), 104-01(2.44-2.51), 104-02(2.41-2.42), and 108-01(2.44-2.48).

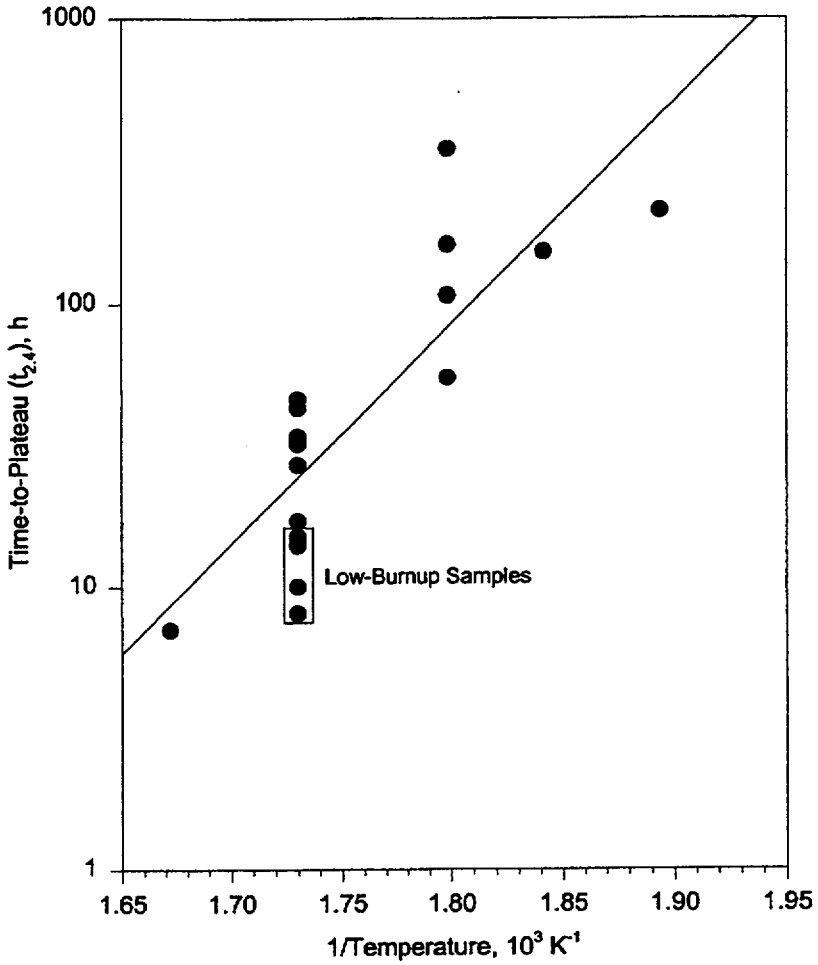

Figure 5.1. Time-to-Plateau as a Function of Inverse Temperature for ATM-105 Fragments

5.1.3 Burnup Dependence

The different mechanisms of oxidation, including the formation of different phases during the oxidation of unirradiated UO_2 and LWR spent fuel, demonstrate that substitutional impurities do indeed affect the $UO_2 \rightarrow UO_{2.4}$ transition. This conclusion is supported by the fact that unirradiated UO_2 doped with sufficient concentrations of substitutional cations, with no effects from either radiation damage or the large temperature gradients experienced in reactor operations, oxidizes in a manner similar to spent fuel. LWR spent fuel with a burnup less than 8 MWd/kg M is oxidized to U_3O_7 [12], similar to the

behavior of spent CANDU™ fuel with typical burnups in the range 6 to 12 MWd/kg M. In the present study, LWR spent fuel fragments with burnups in the range 16 to 20 MWd/kg M (see Figure 4.6) were

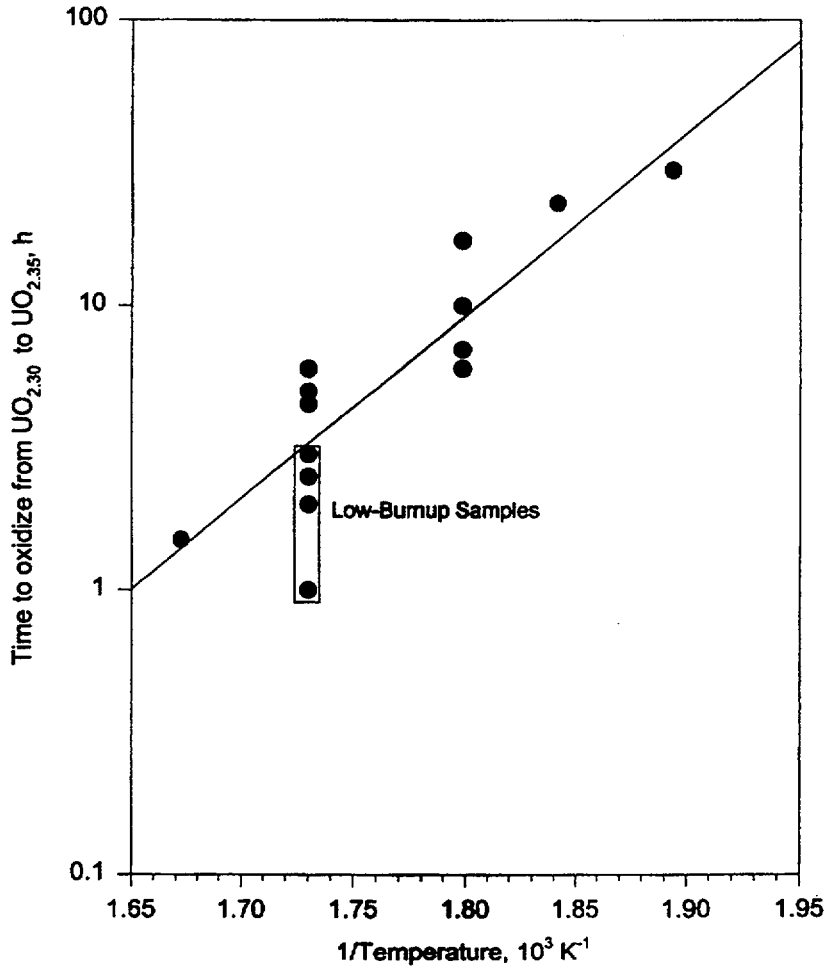

Figure 5.2. Time to Oxidize ATM-105 Fragments from $UO_{2.30}$ to $UO_{2.35}$ as a Function of Inverse Temperature

oxidized at 305°C. The dependence of the O/M ratio on time for two of the samples, 105-17 and 105-18, was nearly linear with almost no inflection at an O/M ratio of 2.4. It is possible that U_3O_8 was forming concurrently with the first transition, although it is not known whether the oxidation resulted in $UO_{2.4}$ or U_3O_7. Further testing of fuels with burnups in this range or of moderately doped fuels is necessary to determine the threshold concentration of impurities necessary to stabilize the cubic $UO_{2.4}$ phase such that no U_3O_7 is formed. However, the type and amount of dopant must truly correspond to what is observed in spent fuel with respect to both fission products and actinides. For example, while SIMFUEL contains a wide variety of dopants, it substitutes U for Pu [66], which is in effect no substitution at all. This may be

one reason that SIMFUEL with simulated burnups of 3.0 and 4.0 atom% oxidized to U_3O_7 [51], while the LWR fuels in the present study oxidized instead to $UO_{2.4}$. Typical Pu concentrations for this range of burnup are on the order of 0.8 to 1.0 atom% (see Table 2.2), as calculated by ORIGEN2, but the Pu composition can increase by a factor of 3 at the surface of the fuel due to resonance absorption in ^{238}U (see Figure 2.4).

Figure 5.3 is a plot of $\log(t_{2.4})$ as a function of burnup for the TGA specimens oxidized at 305°C. The oxidation from UO_2 to $UO_{2.4}$ appears to have a burnup dependence as well as the temperature dependence discussed above. If the apparent burnup dependence were real, it should be evident over all O/M ratios in the range 2.0 to about 2.4 since the oxidation fronts within grains have been shown to be fairly uniform, as is the probable distribution of fission products and higher actinides within a single grain. Figure 5.4 shows the logarithm of the time to oxidize a specimen from $UO_{2.3}$ to $UO_{2.35}$ as a function of burnup. Compared to the data in Figure 5.3, the burnup dependence in these data appears to be much smaller. Instead, it appears that the four specimens from the low-burnup region of the ATM-105 fuel rod, which exhibited no grain growth, oxidized most rapidly in this range. The specimens with a burnup of about 42 MWd/kg M were from ATM-104, which has an average grain size slightly smaller than that of the ATM-105 specimens with burnups in the 25 to 30 MWd/kg M range. Thus, the data in Figures 5.3 and 5.4 support the assertion that grain size has a significant effect on oxidation during the first transition, with finer-grained fuels oxidizing faster in accordance with a larger surface-to-volume ratio as discussed previously [38].

5.2 The Second Transition ($UO_{2.4} \rightarrow U_3O_8$)

This study was initiated to determine the mechanism and kinetics of the $UO_{2.4}$ to U_3O_8 transition. The second transition is more complex than the first transition because of the large structural change that occurs. The plateau behavior and burnup dependence further complicate the analysis.

5.2.1 Mechanism of U_3O_8 Formation

Previous oxidation studies by Einziger et al. [30] found no U_3O_8 formation at temperatures up to 250°C until the spent fuel was first completely converted to $UO_{2.4}$. It is possible, as outlined in Section 4.4, that U_3O_8 formed at low temperatures may be in a nanocrystalline state and thus is not observable via XRD. However, TEM examination of ATM-105 spent fuel oxidized to an O/M ratio of 2.38 at 175°C indicated no submicroscopic U_3O_8 or other oxidation products [35]. XRD on the present TGA samples has identified U_3O_8 in all samples where powder has formed, even with an O/M ratio as low as 2.49. For

those samples that contained both powder and fragments at the end of the experiment, XRD of the remaining fragment identified only $UO_{2.4}$. The lack of U_3O_8 formation until conversion to $UO_{2.4}$ is complete results in the plateau behavior observed on plots of the O/M ratio as a function of time.

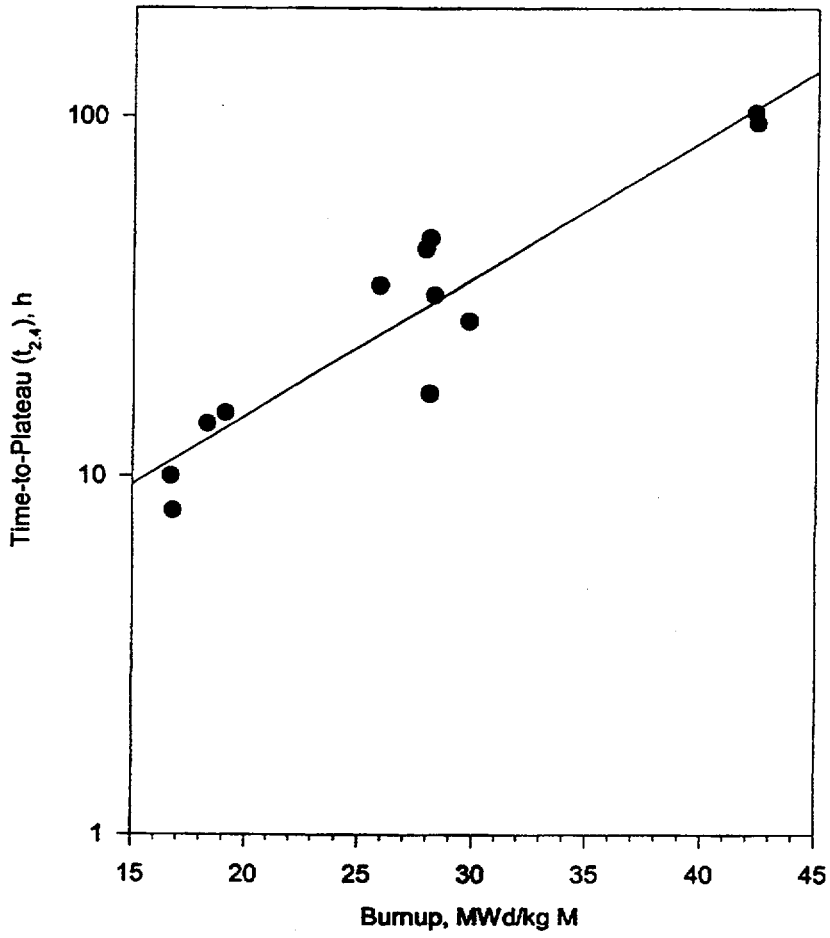

Figure 5.3. Time-to-Plateau as a Function of Burnup for LWR Fragments Oxidized at 305°C

The mechanism for U_3O_8 formation is poorly understood; however, there is general agreement that a nucleation and growth process is involved [19], which is based primarily on fitting of data to reaction kinetic models such as presented by Johnson and Mehl [123]. Nucleation is simply the process by which stable "embryos" of U_3O_8 are formed. Once the embryos have achieved a critical density, the probability that oxygen diffusion through an existing embryo to the $U_3O_8/UO_{2.4}$ interface will react to form additional U_3O_8 is larger than the probability that new embryos will be formed—thus the U_3O_8 phase grows. Such a mechanism for the formation of fission-gas bubbles is presented in numerous texts

(see e.g., Olander [75]). The activation energies for the two processes can differ, depending on the rate-limiting step for each reaction.

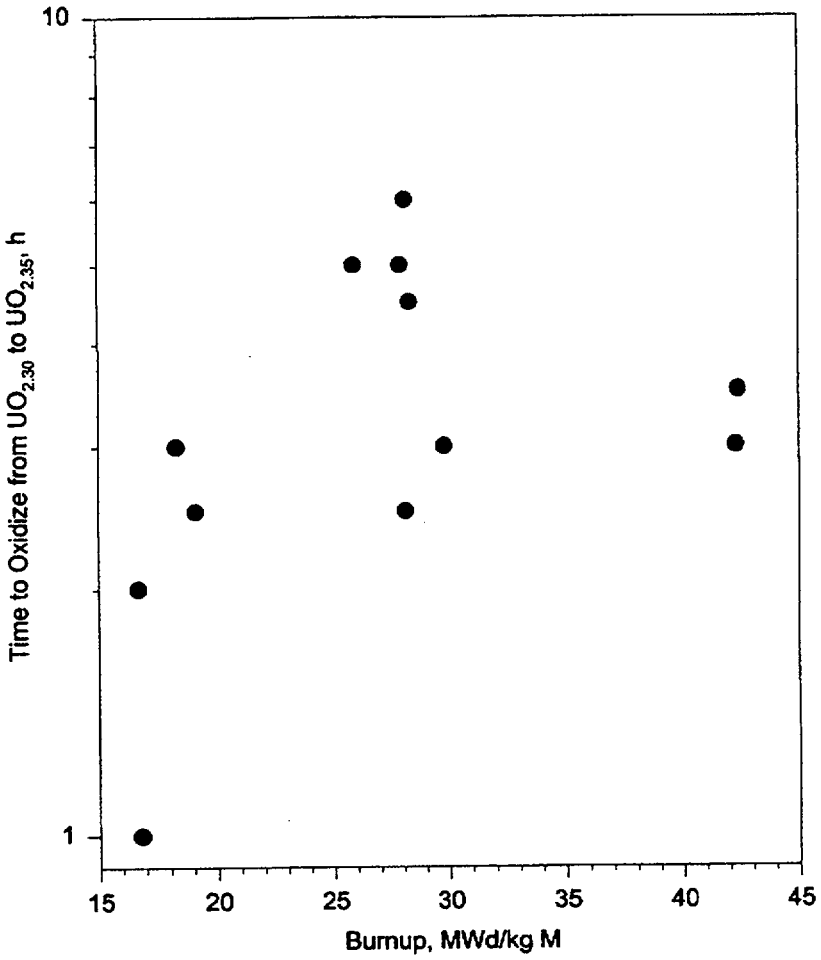

Figure 5.4. Time to Oxidize LWR Fragments from $UO_{2.30}$ to $UO_{2.35}$ at 305°C as a Function of Burnup

Formation of U_3O_8 on unirradiated UO_2 pellets in the temperature range 200°C to 300°C has been shown [26] to take place more rapidly on rough surfaces than on polished surfaces, in agreement with the observation that U_3O_8 first forms at microcracks [23] produced during the lattice contraction as UO_2 oxidizes to U_4O_9/U_3O_7. Further, it is known that the oxidation rate of the (111) face of single crystal UO_2 is greater than those of the (100) and (110) faces [124]. Allen and Holmes [18] have modeled the transformation of UO_2 to U_3O_8 as a displacement of the (111) planes in the fluorite structure, which brings an outer layer of uranium directly over a second layer, thus forming the layered structure of U_3O_8. The outermost layer must then expand away from the surface to give the proper interplanar spacing and to allow for incorporation of oxygen atoms to yield the proper stoichiometry. These displacements are

Weekly Status Report

To: Carolyn Cormier **Project:** Capability Maturity Model

From: Allison Inglett **Week Ending:** 01/18/2002

A. Accomplishments

- Continued major revisions to 6 CMM policy documents. Completed revision to BSC CIO overarching policy to incorporate references to 6 KPAs. Completed revision to draft RM, and PP.

B. Problems & Risks

- Completed DAR on PRO-IM-001. Template for policies in the procedure is not the same as the template provided in the Style Manual.

C. Changes

-

D. Pilot Project Update/Status

- PowerPlay walk-through on documentation

E. Plans for Next Week

- Finalize CBT training for general employee and software professionals

D. Ongoing Work/Metrics

Start Date	Tasks	Budgeted Hours	Hours Spent		Estimated Completion		% Complete	Date Complete
			This Week	To Date	Hours	Date		
	Administrative (email, filing, etc)		2					
	Meetings		2					
	Training							
	Safety		.5					
	Workforce Development							
	Paid Time Off (PTO) & Holiday							
01/02/02	DOE Review of CMM Implementation	40		22				
10/16/01	Project Notebook			20				
10/29/01	CMM Training			73				
01/09/02	CMM Policies and Processes	80		9				
10/11/01	CMM Tools: product research			21				
10/09/01	PowerPlay (assist AIM Proj Mgr)			36				
ongoing	Document review and research			74				

thought to happen stepwise, with the original structure becoming more distorted toward tetragonal U_3O_7 and U_2O_5. No such intermediates have actually been observed in the oxidation of LWR spent fuel, although it may be that these phases are unstable and readily dissociate to $UO_{2.4}$ or U_3O_8. The interstitial oxygen atoms, therefore, are the driving force behind the transformation as oxidation increases the amount of distortion in the fluorite structure until the lattice strain is sufficient to displace the uranium layers [18]. The authors also propose that it is the original matrix oxygen atoms that become the tightly bound uranyl oxygens in U_3O_8, although there is disagreement as to whether uranyl-type binding actually occurs in U_3O_8 [17].

If this model is assumed, substitutional cations, which tend to stabilize the fluorite structure, can act to retard or prevent oxidation to phases such as U_3O_7 that are distortions from the truly cubic lattice structure of UO_2 and $UO_{2.4}$ and thus hinder the formation of U_3O_8. These cations may act as barriers to oxidation by 1) requiring the oxidation of matrix U ions from 4+ to 5+ to maintain stoichiometry if the cations have valences less than 4 (see Section 2.5.2) (this would reduce the number of U ions available for further oxidation and thus limit the number of oxygen interstitials that can be added), 2) contracting the lattice and thereby increasing the energy barrier for oxygen diffusion into the lattice (this arises because many of the fission products and transuranics that act as substitutional cations have smaller radii than the original U^{4+} ions, as do both U^{5+} and U^{6+}), and 3) acting as effective negative charges compared to the U ions, which in turn repel neighboring interstitial oxygen ions, effectively eliminating these sites from occupancy by oxygen as hypothesized by Park and Olander [92]. Unirradiated UO_2 and low-burnup fuels, such as typical CANDU™ fuels, form U_3O_7 directly and thus present a much smaller barrier to U_3O_8 formation.

Finally, it is not known at what point U_3O_8 begins to spall from an oxidized sample. It has been reported [12,26] that U_3O_8 is formed in quantities detectable by XRD before visible powdering. McEachern et al. [125] suggest that much of the variability in reported activation energies for U_3O_8 formation can be traced to inclusion of the energy for spallation. Since the present study uses mass increase as the measure of oxidation, spallation is only important to the extent that transport of oxygen to unreacted $UO_{2.4}$ may be limited by diffusion through the outer U_3O_8 layer.

5.2.2 Plateau Behavior

The duration of the plateau has been defined here as the time required to oxidize a specimen from $(O/M)_\delta$-0.005 to $(O/M)_\delta$+0.005. This time will most likely include some fraction of the time required to complete the oxidation of all grains to $UO_{2.4}$, as well as some time during which U_3O_8 has begun to form.

The average grain size of the specimens will, therefore, have an effect on t_s since the time for complete conversion to $UO_{2.4}$ depends on grain size (see section 5.1.1). Smaller-grained fuels, with a larger surface area per unit grain volume, may also have more (111) planes exposed at grain boundaries and cracks, which in turn may increase the rate of U_3O_8 formation.

As discussed previously, the location of the plateau, $(O/M)_\delta$, occurs at variable O/M ratios in the range 2.35 to 2.43. There is no clear dependence of $(O/M)_\delta$ on burnup, grain size, or oxidation temperature, although the smallest values of $(O/M)_\delta$ were observed for the low-burnup specimens. It is also not known if U_3O_8 formation occurred concurrently with the $UO_{2.4}$ or U_3O_7 phase initially formed for these four specimens. Simultaneous formation of the two phases would result in a smaller than expected value of $(O/M)_\delta$ and would result in no observable plateau. If the four low-burnup samples are ignored, then the range in $(O/M)_\delta$ is only 2.39 to 2.43. It is useful to consider these values in terms of the chemical state of the fuel and the fission products and actinides it contains.

A simple calculation based strictly on the relation between mass increase and the change in the O/M ratio (Equation 3.1) was performed to demonstrate that the $UO_{2.4}$ phase is a result of incorporation of excess diffuse oxygen within a U_4O_9-like phase and not simply due to oxidation of the fission products. If a 200 mg fragment of spent fuel (33 MWd/kg M burnup, 10-year decay period, 3.2% ^{235}U enrichment) were to oxidize to an O/M ratio of 2.4, the corresponding increase in mass would be 4.74 mg. Using the compositions predicted by ORIGEN2 (Table 2.2), the total wt% of the fuel matrix represented by U, the fission products Xe and Kr, which do not oxidize, and the actinides Pu, Am, and Cm that will not oxidize under the conditions studied is 97.12. Oxidation of this fuel matrix to an O/M ratio of 2.25 (U_4O_9) will produce a mass increase of 2.89 mg. If, for example, the remaining 2.88 wt% of the fuel were assumed to be the fission product Zr in the metallic state, complete oxidation to ZrO_2 would produce a mass increase of 1.78 mg and thus a total mass increase of 4.67 mg. At least 0.07 mg of excess oxygen is required to obtain the necessary 4.74 mg mass increase. However, most of the fission products and higher actinides form sesquioxides ($MO_{1.5}$) as opposed to dioxides (MO_2), and if they are substitutional, they are already bound to oxygen in the fuel matrix. Thus, the mass increase necessary for oxidation to the U_4O_9-like phase ($UO_{2.4}$) must be due to the incorporation of additional oxygen beyond the nominal stoichiometric O/M ratio of 2.25 and not due to oxidation of the fission products. However, a change in O/M ratio from 2.40 to 2.43 requires an additional mass increase of only 0.36 mg for the same 200 mg sample. An increase of this magnitude is readily achieved by oxidation of a large fraction of the fission products, such as Mo in the ε-Ru phase, that have remained in the metallic state unbound to oxygen. These calculations

illustrate that the variation in $(O/M)_\delta$ may be due in part to oxidation of fission products. This possibility is also indicated by the observations of Matzke, who showed that Mo in SIMFUEL can oxidize before the UO_2 matrix [77].

Finally, some of the specimens oxidized exhibited plateaus with nearly zero slope; others a continuous, albeit reduced rate of mass increase; and others no plateau whatsoever. No plateau was observed for sample 105-02 oxidized at 325°C, nor were plateaus observed for the four low-burnup samples, 105-15 through 105-18, oxidized at 305°C. Plateaus with near-zero slope were observed for samples oxidized at low temperatures (sample 105-04 at 270°C and 105-05 at 255°C) and for samples with high burnup (greater than about 35 MWd/kg M) at 305°C. Samples that exhibited a creeping or continuous increase in O/M ratio have burnups between these two extremes. It thus appears that the duration of the plateau depends on both temperature and burnup. A detailed examination of these dependencies follows in the next sections.

5.2.3 Burnup and Temperature Dependence

The trends observed in the figures presented in Section 4.1 demonstrate that the duration of the plateau, t_δ, between an O/M ratio of about 2.4 and higher O/M ratios increases by as much as 3 orders of magnitude with increasing impurity concentration. Figure 5.5 illustrates the trend of increasing t_δ with increasing burnup for the ATM-105 fragments oxidized at 305°C in the TGA systems and which had burnups determined by the ^{148}Nd isotope dilution method. These data should be compared with samples oxidized at 283°C (see Figures 4.3 and A.9). Extended plateaus of 158 to 3000 hours were observed for all samples known to have a burnup greater than about 27.6±1.1 MWd/kg M. Oxidation of a sample with similar burnup (105-03), but at 305°C, displayed virtually no plateau, but a plateau was observed for the two samples (Figures 4.4 and 4.5) with a burnup of about 30 MWd/kg M also determined by the ^{148}Nd isotope dilution method. The four samples (see Figure 4.6) with a burnup less than about 20 MWd/kg M that were oxidized at 305°C displayed virtually no plateau at all. It is assumed that sample 105-01, which exhibited a plateau of only 40 hours and oxidized relatively rapidly to U_3O_8, has a burnup less than the other three samples oxidized at 283°C (see Figure 4.3). If this assumption is correct, then at the temperatures tested and within the uncertainties associated with the burnup measurements, a minimum burnup in the range 27 to 30 MWd/kg M may be necessary before an extended plateau is observed. Most of the fuels tested by Bennett and coworkers [53,54] were oxidized at temperatures in the range 250°C to 400°C and had a maximum burnup below 27 MWd/kg M. This may explain the absence of a correlation between burnup and the formation of U_3O_8 powder in these studies.

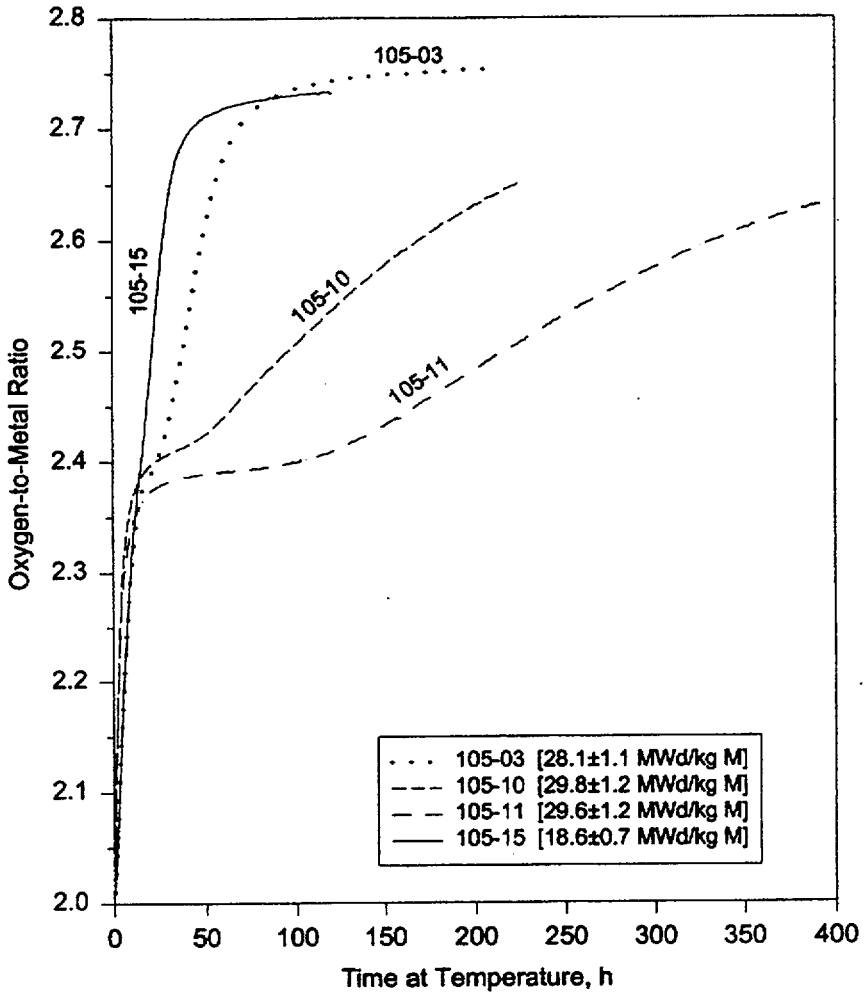

Figure 5.5. Oxidation Behavior of ATM-105 Fragments of Different Burnup Oxidized at 305°C

The logarithm of the duration of the plateau at 305°C is shown as a function of the burnup determined by the ^{137}Cs method in Figure 5.6. The smaller error bars shown in this figure represent the uncertainties due solely to γ-ray self-absorption in a specimen, while the larger error bars represent the total uncertainty (about ±15%), which includes the estimated uncertainties in the burnup as calculated by the ^{137}Cs method with respect to those calculated by the ^{148}Nd method or with the ORIGEN2 code. The duration of the plateau clearly shows a burnup dependence.

A simple model was developed to determine the burnup dependence of the activation energy starting with the basic kinetic equation

$$k = k_0 \exp(-E_A / RT) \quad (5.1)$$

where

k = rate constant

k_0 = pre-exponential factor

E_A = activation energy

R = ideal gas constant (8.314 J mol^{-1} K^{-1})

T = temperature (K).

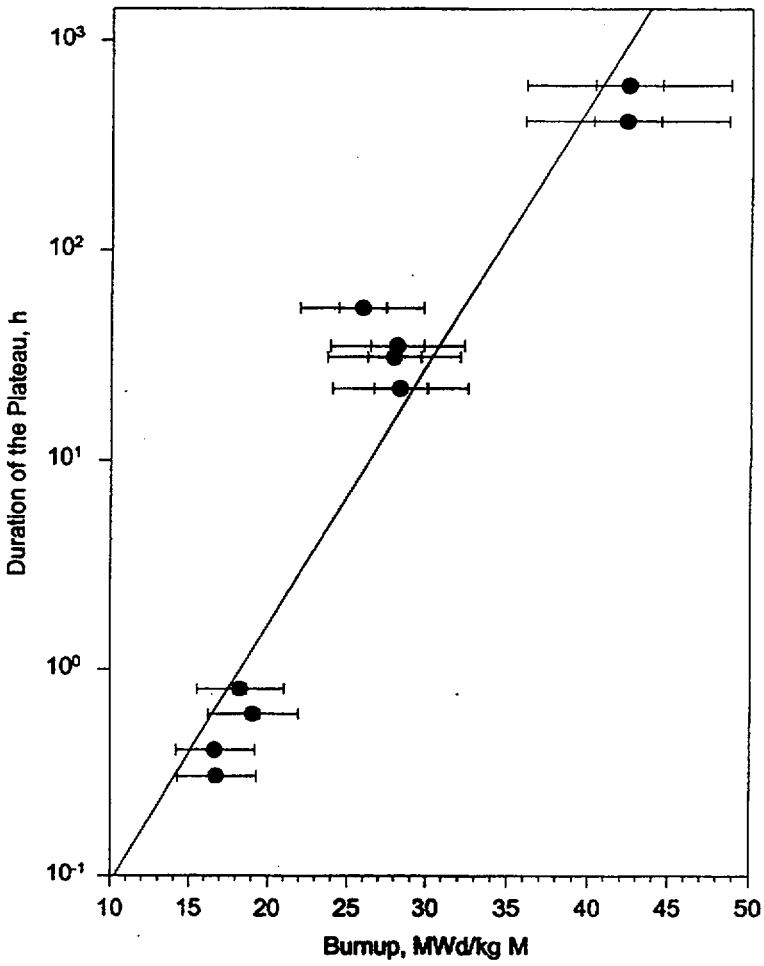

Figure 5.6. Duration of the Plateau for LWR Spent Fuel Fragments Oxidized at 305°C (Burnup from ^{137}Cs Analysis)

It was then assumed that the activation energy could be expressed as

$$E_A = E_{A0} + \alpha B \tag{5.2}$$

where

E_{A0} = the activation energy for the transformation of spent fuel from $UO_{2.4} \rightarrow U_3O_8$ in the limit as the burnup approaches zero

α = the proportionality constant for the activation energy dependence on burnup

B = burnup (MWd/kg M).

It was assumed that α is constant. (This assumption may be an approximation because the matrix undergoes structural changes with increasing burnup, and the chemical state of the fission products may change as well.) The concentration of U_3O_8 was assumed to follow the equation

$$d[U_3O_8]/dt = k\,[UO_{2.4}]\,[O_2] \tag{5.3}$$

where it was assumed that the concentrations of $UO_{2.4}$ and O_2 were constant at the $UO_{2.4}/U_3O_8$ interface. Integration of Equation (5.3) yields

$$[U_3O_8] = k_0 \exp(-(E_{A0} + \alpha B))/RT)\, t \tag{5.4}$$

If it is assumed that no U_3O_8 is formed until after the conversion to $UO_{2.4}$ is complete, that is, until after the plateau has been reached, then the time to reach a concentration of U_3O_8 equal to the concentration at $(O/M)_\delta$+0.005, approximated as t_δ, can be shown to take the form

$$\ln t_\delta = C + (\alpha B)/(RT) \tag{5.5}$$

where C is a constant that includes the contribution from E_{A0}/RT.

The slope of the least squares fit (R^2=0.91) to the data in Figure 5.6 gave the value α=1.4±0.2 kJ mol^{-1} per unit burnup (MWd/kg M) where the uncertainty represents the uncertainty in the fit to the mean values of the data. If the 15% uncertainty in burnup is considered, a qualitative inspection of Figure 5.6 yielded a minimum slope of 1.0 kJ mol^{-1} and a maximum of 2.2 kJ mol^{-1}. A similar least squares fitting (R^2=0.76) of the log(t_δ) vs burnup data for the four ATM-105 samples oxidized at 305°C, which had burnup determined by the ^{148}Nd method, yielded the value of 1.5±0.6 kJ mol^{-1} for α (see Figure 5.7). Although the agreement between these two coefficients is excellent, some caution must be taken because of the scatter in the data and the strong dependence of the slope in Figure 5.7 on the single data point at 18.6 MWd/kg M. (Note: a similar analysis of the three data points at a temperature of 283°C yielded the value of 2.1±2.1 kJ mol^{-1}. Because of the large uncertainty, no further analysis of these data is considered here.) For the data obtained by Harrison et al. [56], a burnup-dependent activation energy for their second oxidation stage was found to be 2.1±0.9 kJ mol^{-1} per unit burnup (MWd/kg M), although these materials

had burnups in the range of only 1.2×10^{-4} to 1.45 atom% and may not be directly applicable to the present study.

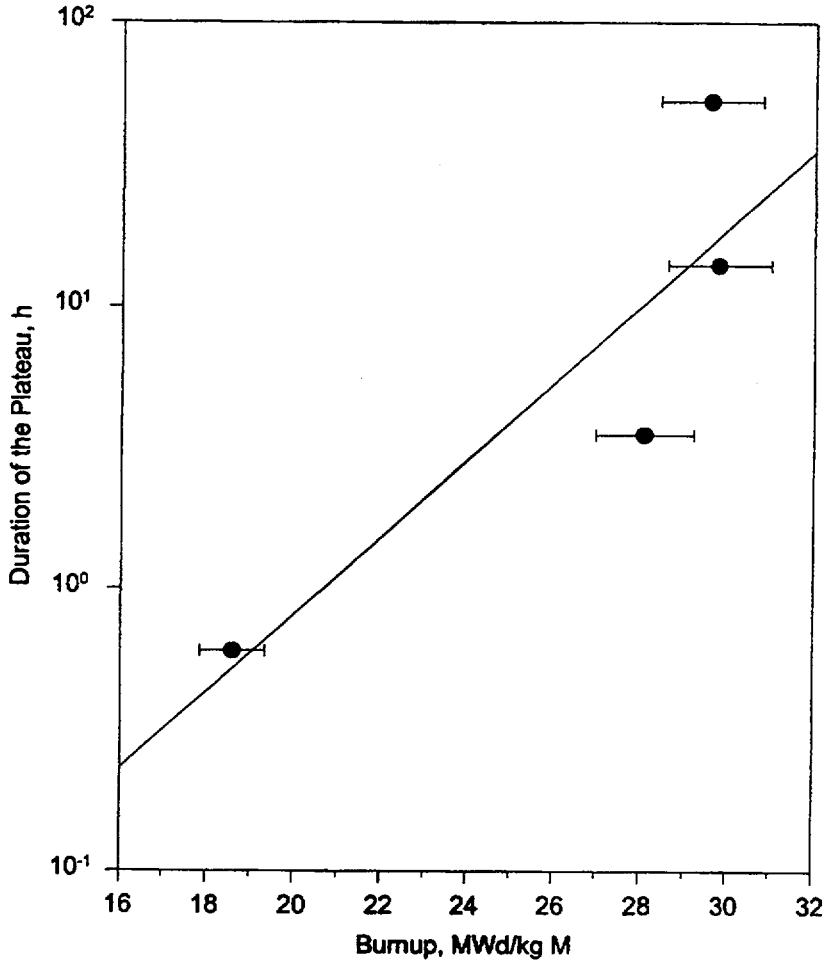

Figure 5.7. Duration of the Plateau for ATM-105 Fragments Oxidized at 305°C (Burnup from ^{148}Nd Analysis)

Despite the reasonable agreement in the activation energies obtained from these data sets, the burnup-dependent coefficient is not a physically well-defined parameter because with respect to the underlying physical chemistry, burnup is not a well-defined parameter. It is important to stress that burnup is being used as a rough estimate of the total substitutional cation concentration, the magnitude and elemental distribution of which are most likely the fundamental physical chemical parameters governing the activation energies. Because the yields of different fission products and transuranic elements vary with burnup, burnup is not a well-defined quantity with respect to the kinetics and mechanism of oxidation. Also, the elemental distribution is time-dependent because most of the isotopes formed are unstable and undergo radioactive decay, and the substitutional character of the daughter

product may differ from that of the parent. In that sense, it is important to emphasize that in the present study, α has been determined from data on fuels with decay times of 11 to 16 years. Further uncertainty results from the transuranic content, which will be larger for a sample from the fuel pellet surface than from the centerline because of the resonance absorption in ^{238}U, even for samples of identical burnup. The sensitivity to such factors is discussed in Section 5.2.5.

The duration of the plateau for fuels of similar burnup is expected to increase with decreasing temperature, as observed in previous work [30]. The oxidation curves for four ATM-105 samples of similar burnup (27.5 to 29.2 MWd/kg M) at different temperatures are plotted in Figure 5.8. The oxidation of sample 105-05 was halted well before the plateau had ended, so no estimate of t_s is available. However, dry-bath data for the ATM-105 fuel oxidized at 255°C suggest a t_s of between 1000 and 2000 hours. In Figure 5.9, the logarithm of t_s as a function of inverse temperature is shown for the remaining three samples along with a least squares fit to the data (R^2=0.99). The slope of the fit is the total activation energy, E_A, found to be 409±41 kJ mol^{-1}. Assuming nominal values of 28 MWd/kg M for the burnup and 1.4 kJ mol^{-1} for α, E_{A0} was calculated to be 370±41 kJ mol^{-1}. This activation energy is much higher than any reported in a recent review by McEachern et al. [125]. These authors determined the activation energy of U_3O_8 formation to be 146±10 kJ mol^{-1} through XRD analysis on unirradiated CANDU™ pellets oxidized in the temperature range 168°C to 300°C [125]. Although the activation energy for unirradiated fuel is not necessarily the same as that determined in the present study, because irradiation results in many other effects besides those caused by substitutional cations, such a large difference was not expected.

The limited data in Figure 5.9 can result in significant bias in the derived E_A, not the least of which may come from differences in the substitutional cation concentration, even for samples of similar burnup. Also, it must be stressed again that t_s does not correspond to a quantitative measure of the state of the fuel, but was defined here to provide a consistent measure among the data. As such, the interpretation of t_s is especially questionable for those samples where t_s is only a few hours because it is not clear whether U_3O_8 formation was occurring concurrently with the transition from UO_2 to $UO_{2.4}$ and because the time to complete conversion to $UO_{2.4}$ depends highly upon grain size. Thus, the activation energy may be heavily biased by sample 105-03 (305°C and t_s=3.5 hours).

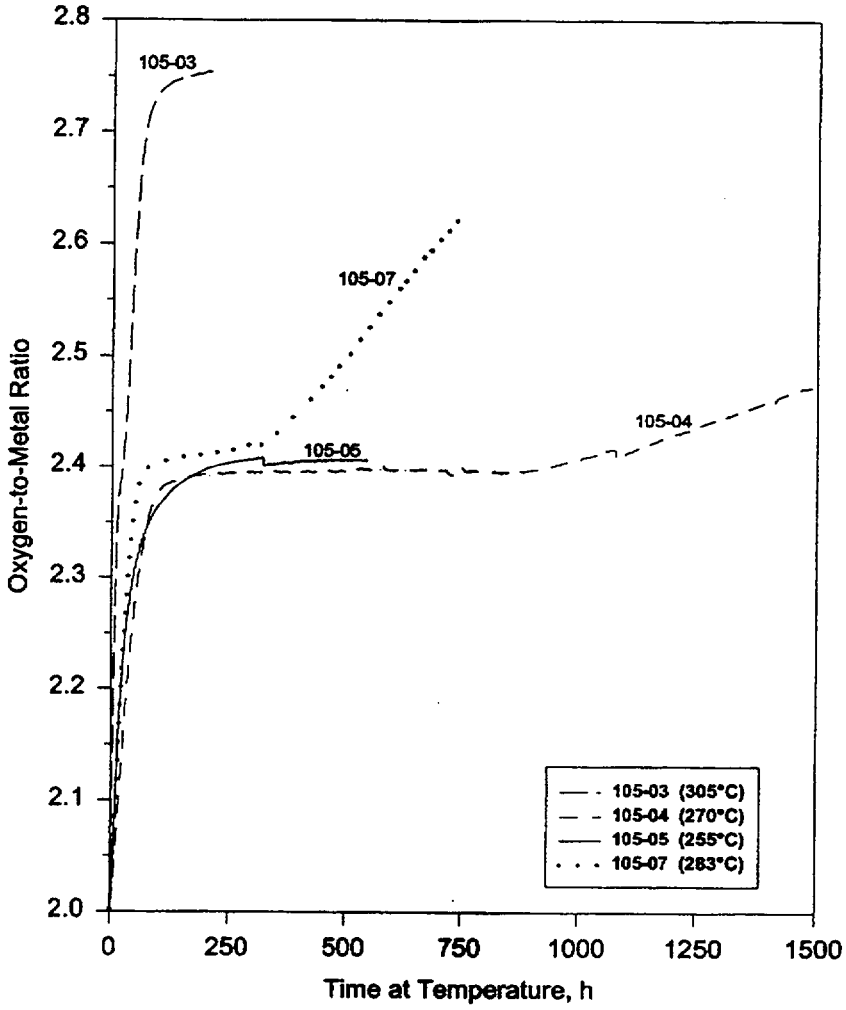

Figure 5.8. Oxidation Behavior of ATM-105 Fragments of Similar Burnup (~28 MWd/kg M) Oxidized at Different Temperatures

For purposes of determining the influence of the effects discussed above, the analysis was repeated using all samples of ATM-105 fuel from the high-burnup region (samples 105-01 through 105-14). The logarithm of t_s as a function of inverse temperature is shown in Figure 5.10, along with a least squares fit (R^2=0.71) of the data that gives a total activation energy of 331±64 kJ mol^{-1}. Assuming an average burnup of 28 MWd/kg M and 1.4 kJ mol^{-1} for the burnup-dependent coefficient α, E_{A0} is then calculated to be 292±67 kJ mol^{-1}. The burnup of these samples is estimated to vary by no more than 10 MWd/kg M; for those samples where burnup was measured, the maximum difference was only 5 MWd/kg M. Thus, the maximum uncertainty in E_{A0} due to burnup variation among the samples is no more than 20 kJ mol^{-1}. When the data were weighted by t_s^{-1} in an attempt to minimize the dependence on data with the most likely hidden bias, E_A and E_{A0} were calculated to be 296±85 and 257±87 kJ mol^{-1},

respectively. Although still large, the latter is in much better agreement with the literature value of 146±10 kJ mol^{-1}, and the heavy bias that may be introduced by the definition of t_s when dealing with samples that display rather short plateaus is quite evident. (Note: You et al. [55] oxidized spent fuel samples with burnups of 13.9 and 39.2 MWd/kg M at 350°C and did not observe any burnup dependence of the oxidation. This result is entirely consistent with the data reported here. The least squares fit in Figure 5.10 predicts a duration of the plateau of only about 0.1 hour at 350°C, which is essentially unobservable.)

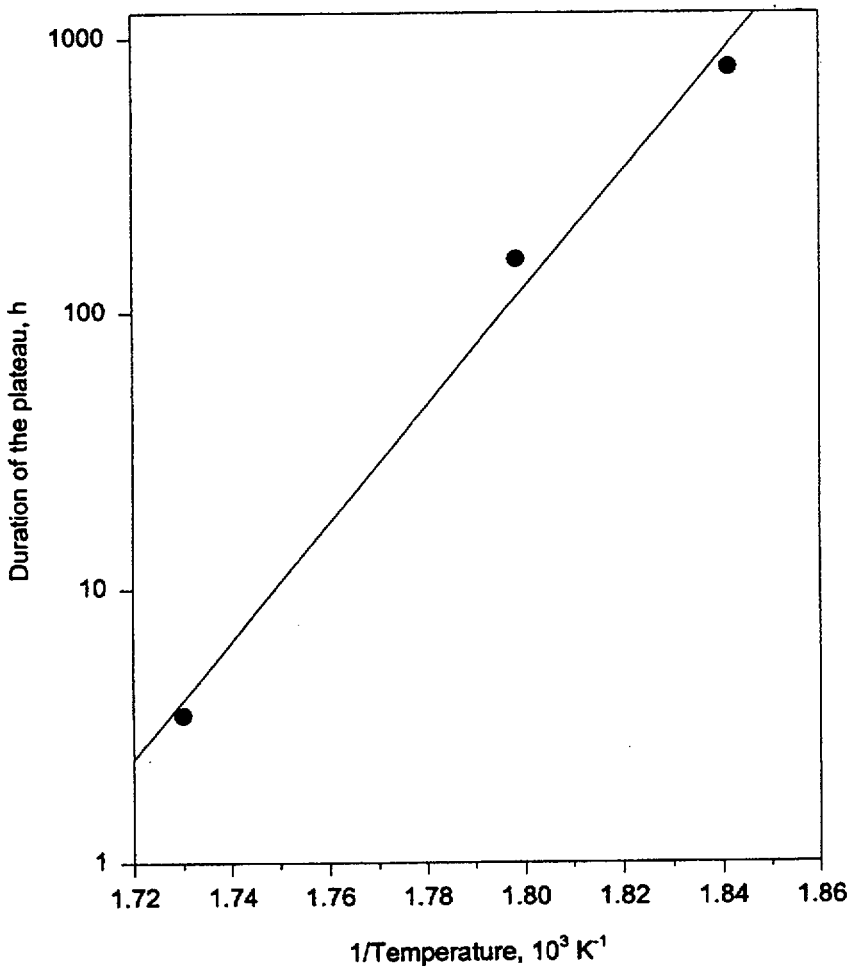

Figure 5.9. Duration of the Plateau for ATM-105 Fragments of Similar Burnup (~28 MWd/kg M) as a Function of Inverse Temperature

The time to oxidize a sample from $UO_{2.45} \rightarrow UO_{2.50}$ was examined to minimize the effect of grain size on α and E_{A0}. The logarithm of this time is shown as a function of burnup for samples oxidized at 305°C in Figures 5.11 and 5.12. The burnups for the samples in these figures were determined using the

^{137}Cs and ^{148}Nd methods, respectively. The burnup-dependent coefficient α was calculated to be 1.1±0.1 (R^2=0.93) and 1.0±0.5 (R^2=0.67) kJ mol^{-1} per unit burnup (MWd/kg M), respectively, in excellent agreement with the values calculated above using the time on plateau. Figure 5.13 shows the logarithm of the time to oxidize a sample through the range in O/M ratio 2.45 to 2.50 as a function of inverse temperature for the three ATM-105 samples of similar burnup (~28 MWd/kg M). The total activation

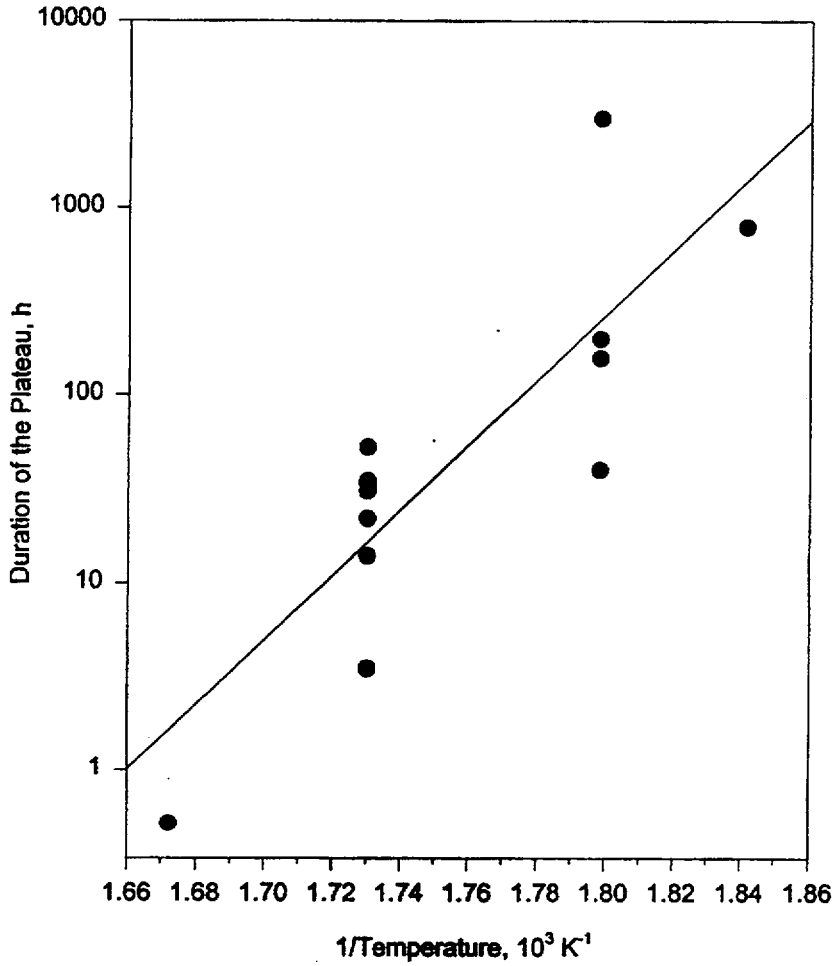

Figure 5.10. Duration of the Plateau for Moderate Burnup ATM-105 Fragments as a Function of Inverse Temperature

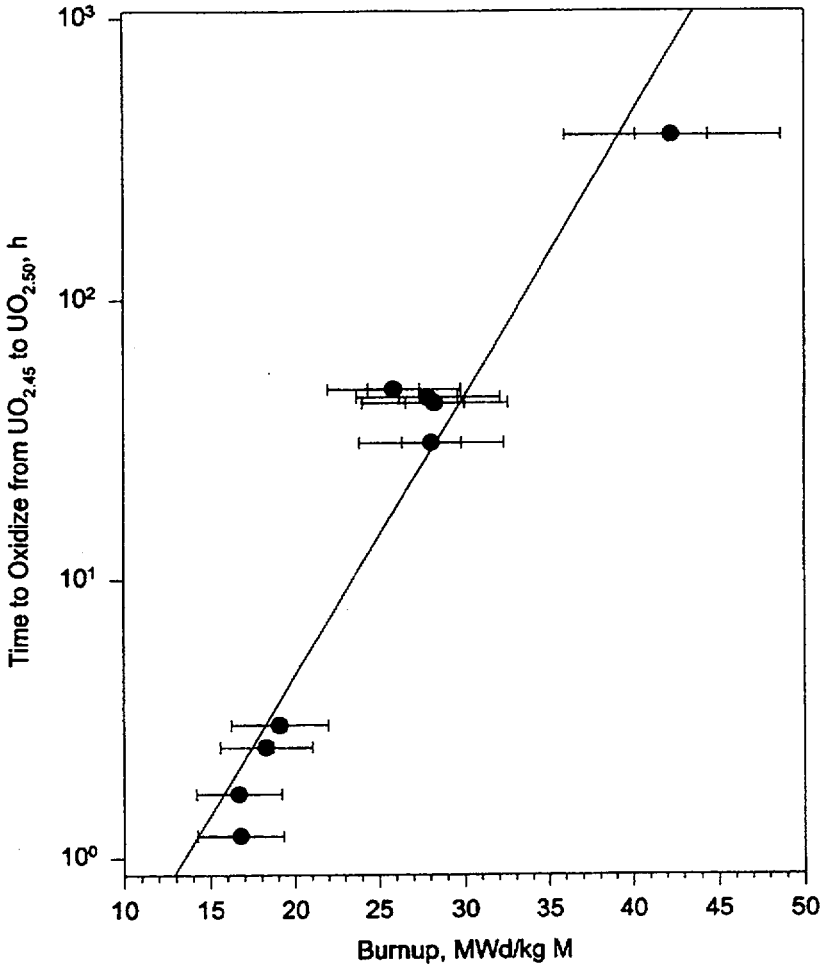

Figure 5.11. Time to Oxidize LWR Fragments from $UO_{2.45}$ to $UO_{2.50}$ at 305°C as a Function of Burnup (Burnup from ^{137}Cs Analysis)

energy, E_A, from the least squares fit (R^2=0.99) shown in the figure is 301±26 kJ mol^{-1}, which in turn corresponds to an E_{A0} of 270±26 kJ mol^{-1} (using α=1.1 kJ mol^{-1}). While these energies are significantly lower than those calculated above using the same three samples, they are still much higher than the literature values. More data using samples of near identical impurity concentration (not simply identical burnup) oxidized at various temperatures are necessary for a more precise determination of the activation energies.

Figure 5.14 illustrates the logarithm of the time to oxidize a sample from an O/M ratio of 2.45 to 2.50 as a function of inverse temperature for the samples from the ATM-105 high-burnup region. Again, the maximum uncertainty introduced in the calculation of the activation energies by the variation in burnup is approximately 20 kJ mol^{-1}, and the effect of grain size differences should still be minimized.

The least squares fit (R^2=0.67) to these data yielded values of 186±47 and 155±51 kJ mol^{-1} for E_A and E_{A0}, respectively. While the close agreement of E_{A0} with the activation energy determined from unirradiated fuel may be fortuitous, the result may be interpreted as indicating that t_5 includes time during which some U_3O_8 is actually forming. Assuming this, the large activation energy determined with the use of t_5 would also reflect the activation energy for formation of U_3O_8. With the limited data set available and the many variables that have not been controlled, it is difficult to interpret these results with certainty, and more definitive experimental data and analysis are warranted. Notwithstanding these uncertainties, it seems certain that the burnup-dependent coefficient for formation of U_3O_8 in LWR spent fuel is 1 to 2 kJ mol^{-1} per unit burnup (MWd/kg M), and it is likely that the temperature-dependent activation energy is on the order of 150 kJ mol^{-1}.

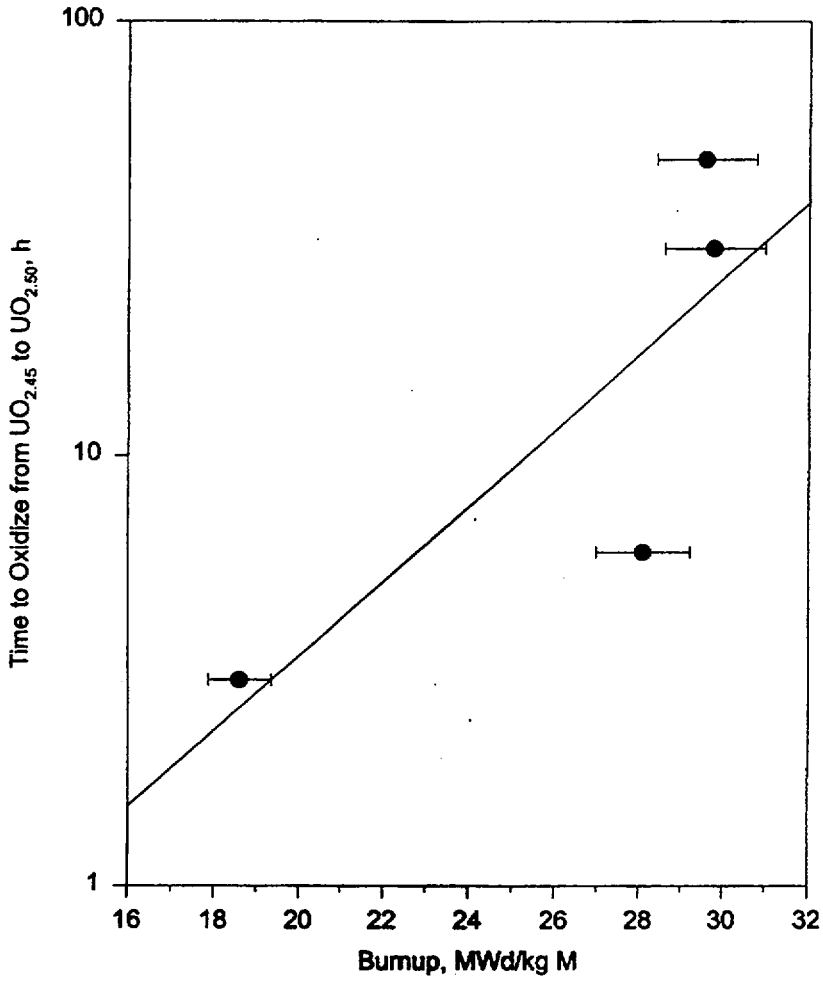

Figure 5.12. Time to Oxidize ATM-105 Fragments from $UO_{2.45}$ to $UO_{2.50}$ at 305°C (Burnup from ^{148}Nd Analysis)

5.2.4 Time-Rate-of-Change in O/M Ratio

For experiments of sufficient duration, oxidation continues past the plateau to higher O/M ratios. Samples that were oxidized for long periods achieved constant masses that correspond to O/M ratios in the range 2.69 to 2.78, indicating that the U_3O_8 phase is non-stoichiometric and capable of accommodating excess oxygen. It was also found that such samples were converted completely to a fine powder. XRD of the powder demonstrated that the material is indeed U_3O_8 with only trace amounts of $UO_{2.4}$ remaining. The typical final O/M ratio is only about 0.06 greater than the nominal O/M ratio.

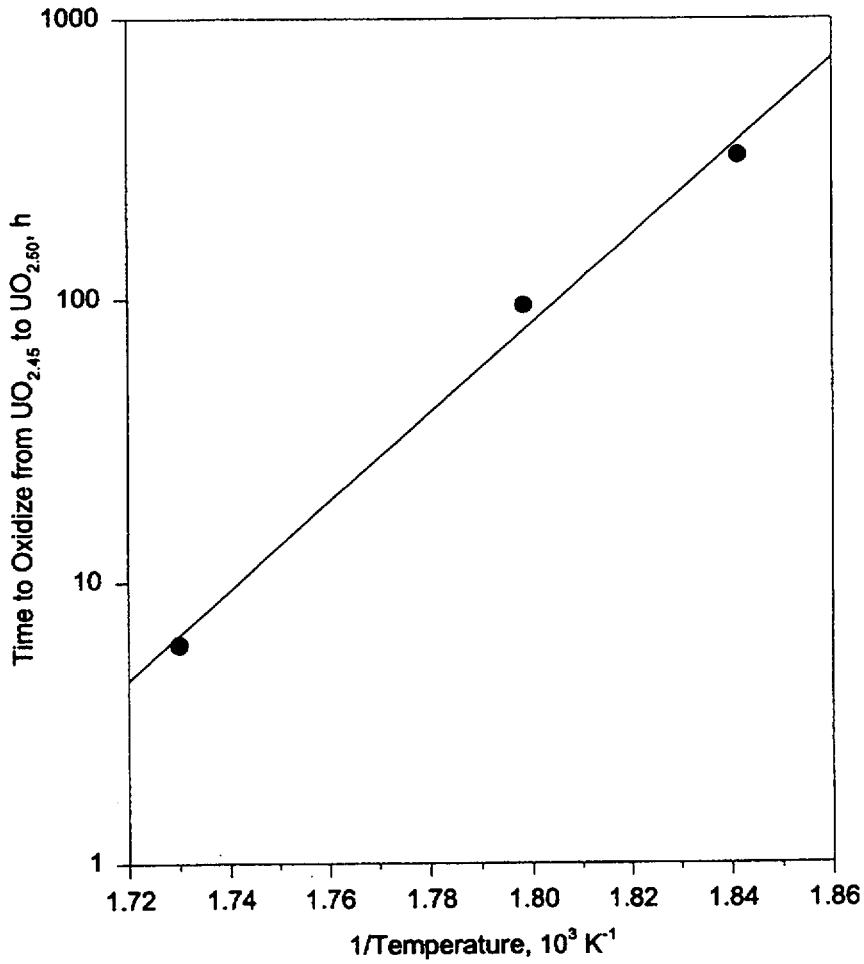

Figure 5.13. Time to Oxidize ATM-105 Fragments of Similar Burnup (~28MWd/kg M) from $UO_{2.45}$ to $UO_{2.50}$ as a Function of Inverse Temperature

The duration of the plateau has been shown to increase with burnup, implying an increasing resistance to further oxidation with increasing impurity level. A similar resistance was shown in Section 2.2.3 for UO_2 containing dopants such as the REEs. Since oxidation past the plateau requires a complete

change from the fluorite structure of UO_2 and $UO_{2.4}$ to the orthorhombic structure of U_3O_8, it is reasonable to conclude that the more stable structure provided by impurity doping will resist oxidation even after U_3O_8 formation has been initiated. Thus, the rate-of-change in the O/M ratio between the plateau and final conversion to U_3O_8 is also expected to be a function of both temperature and burnup. (Note: the time-rate-of-change in the O/M ratio was used in this study because the surface area or surface-to-volume ratio for the specimens was not measured.) Figure 5.15 displays the logarithm of the time-rate-

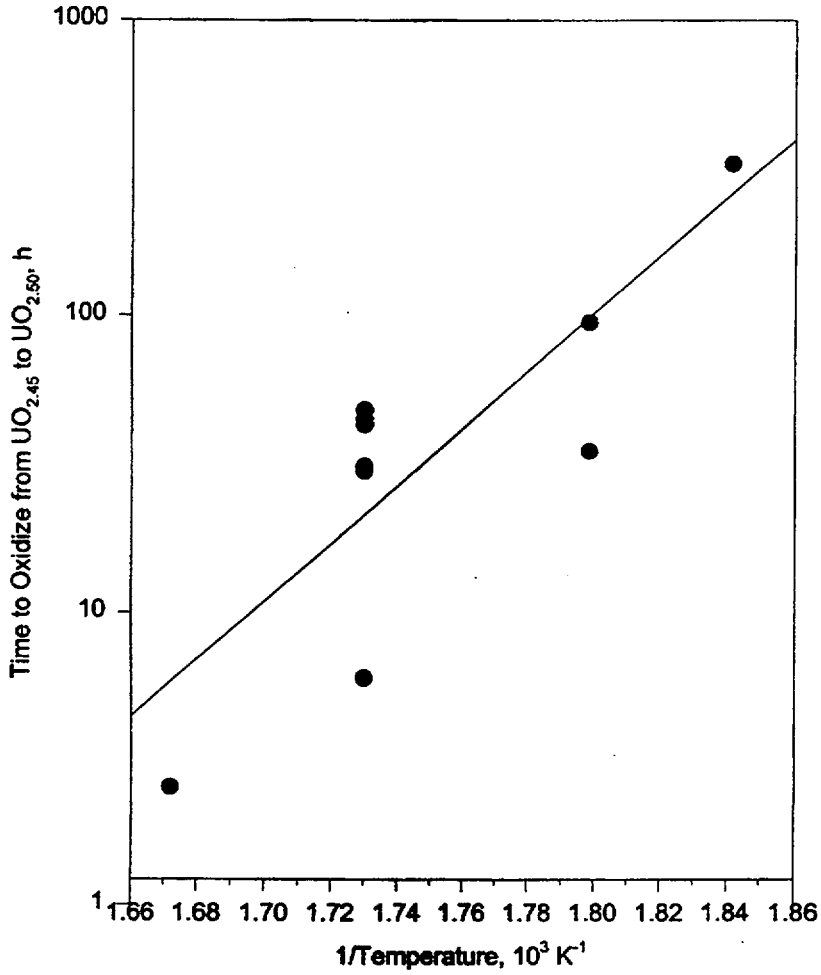

Figure 5.14. Time to Oxidize Moderate Burnup ATM-105 Fragments from $UO_{2.45}$ to $UO_{2.50}$ as a Function of Inverse Temperature

of-change in the O/M ratio as a function of O/M ratio for three ATM-105 specimens of similar burnup that were oxidized at different temperatures. This figure illustrates that the time-rate-of-change in the O/M ratio is temperature dependent, and this dependency is larger for the $UO_{2.4}$ to U_3O_8 transition than it is for the UO_2 to $UO_{2.4}$ transition. The maximum rate-of-change for the second transition is almost two

orders of magnitude larger for the sample oxidized at 305°C than for the sample oxidized at 270°C. When the time-rates-of-change in the O/M ratio for samples oxidized at the same temperature but different burnup are compared (see Figure 5.16), it is apparent that higher-burnup fuels oxidize to U_3O_8 at a much reduced rate than lower-burnup fuels; the fuel specimen with a burnup of about 17 MWd/kg M oxidized at a rate approaching 3 orders of magnitude larger than the specimen with a burnup of about 42 MWd/kg M. This trend is observed at both 283°C and 305°C. From Figure 5.16, a minimal burnup dependence on the UO_2 to $UO_{2.4}$ transition can also be observed.

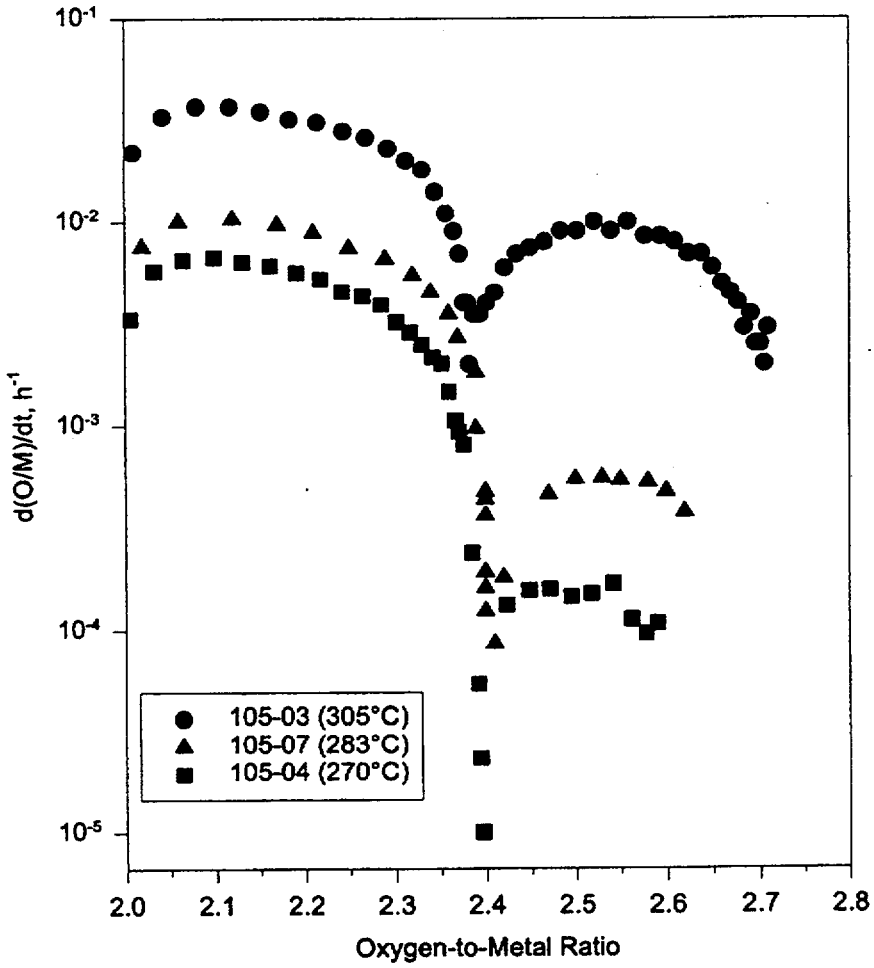

Figure 5.15. Time-Rate-of-Change of O/M Ratio as a Function of O/M for ATM-105 Fragments of Similar Burnup (~28 MWd/kg M) Oxidized at Different Temperatures

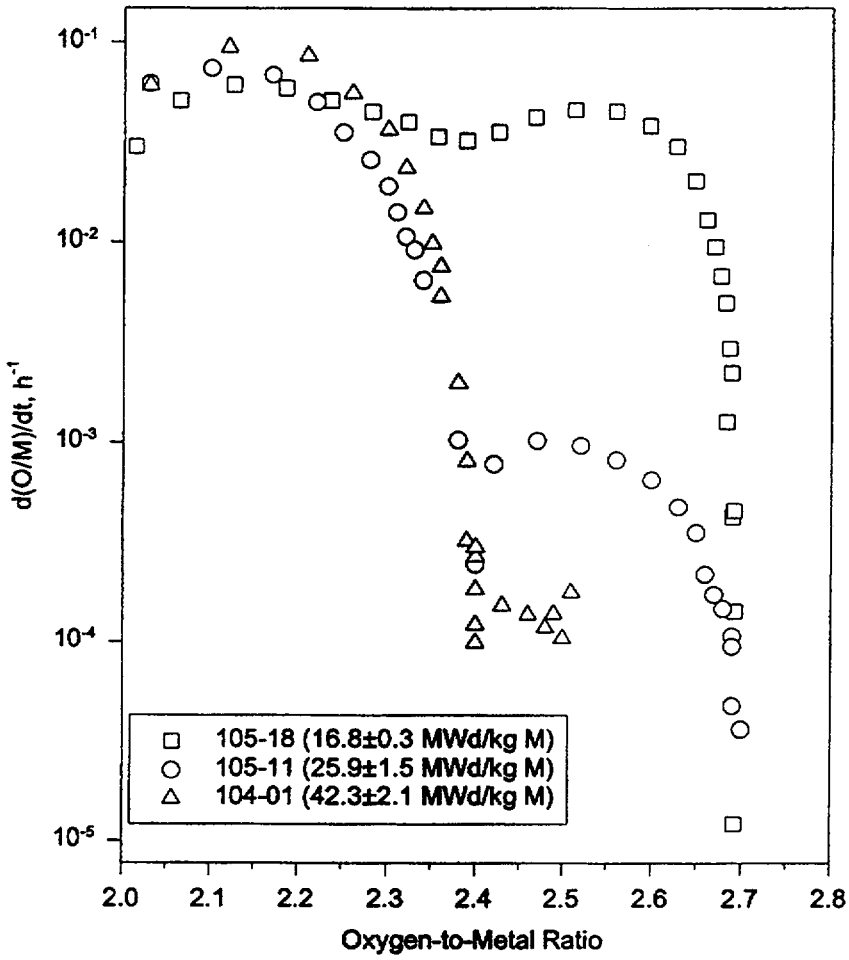

Figure 5.16. Time-Rate-of-Change of O/M Ratio as a Function of O/M for LWR Spent Fuel Fragments of Different Burnups Oxidized at 305°C

The average time-rate-of-change in the O/M ratio after the plateau has been calculated for each sample over the O/M range from 2.44 to 2.60, with a few exceptions noted below. Over this range, the O/M ratio varies almost linearly with time for most of the specimens tested. These average rates are given in Table 5.1 and shown graphically as a function of temperature and burnup in Figure 5.17. The oxidation of samples 105-06, 105-08, 105-09, 104-01, 104-02, and 108-01 was halted not long after the end of the apparent plateau region. For most of these specimens, the rates-of-change in the O/M ratio were estimated with data just beyond the plateau, and therefore they are likely to be biased toward lower rates. Sample 104-01, on the other hand, appeared to have a slightly decreasing time-rate-of-change beginning at an O/M ratio of about 2.50. The reported rate-of-change for this sample may be higher than it would have been had the sample oxidized longer and had the average been calculated over the entire range 2.44 to 2.60. In spite of these biases, the burnup and temperature dependencies of the time-rate-of-

change in the O/M ratio after the plateau are evident in the data of Figure 5.17. Over the burnup range 16 to 44 MWd/kg M, the low-burnup fuel oxidized from $UO_{2.4}$ to U_3O_8 at an average rate 2 to 3 orders of magnitude greater than the high-burnup fuel. This coincides with the observation that the higher-burnup fuels also had plateau durations that were a factor of 2 to 3 orders of magnitude larger than the low-burnup samples.

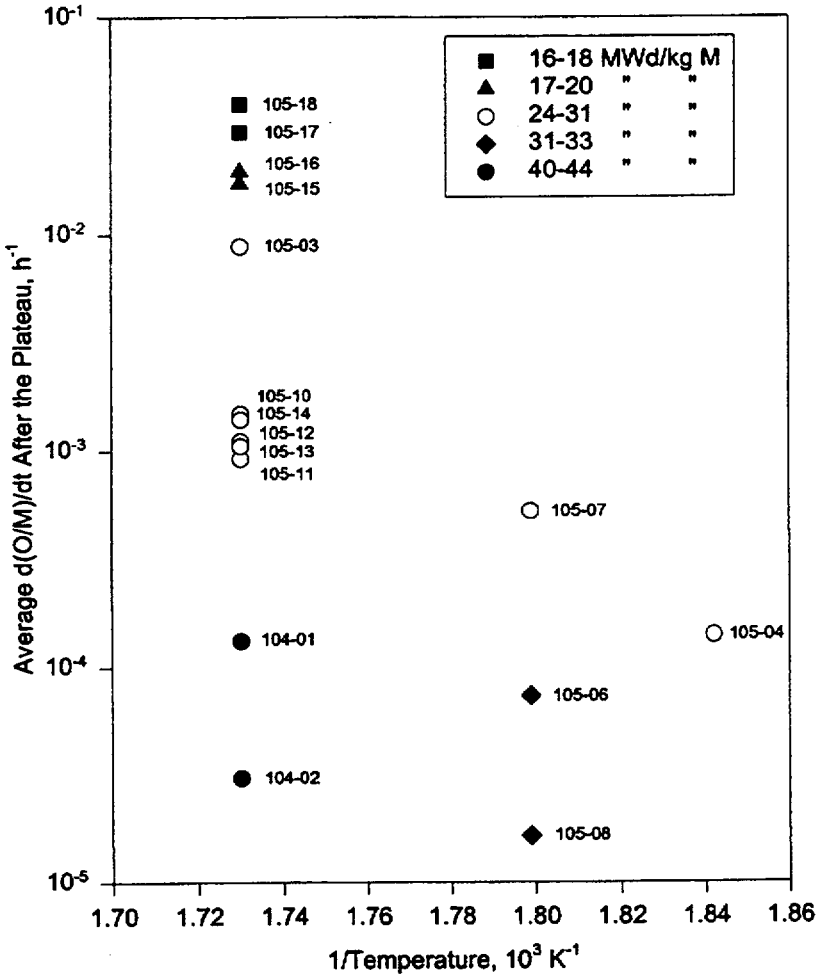

Figure 5.17. Average d(O/M)/dt After the Plateau as a Function of Burnup and Inverse Temperature

The hypothesis that the impurity stabilization of $UO_{2.4}$ directly affects both the duration of the plateau and the rate of U_3O_8 formation after the plateau was further tested by comparing the ratio of the duration of the plateau for samples j and k, $R=t_{\delta j}/t_{\delta k}$, and the ratio of the average time-rates-of-change in the O/M ratio after the plateau, $S=\{d(O/M)/dt\}_k/\{d(O/M)/dt\}_j$. Sample j was chosen as the sample with the longer plateau, and, thus, sample k had the larger rate-of-change. These ratios were calculated for all samples oxidized at a given temperature. The ratio T, chosen either as S/R or R/S to give a value of $T \geq 1$,

could then be used as a measure of how well the time-rate-of-change in the O/M ratio after the plateau compared with the time on the plateau for the two samples. A value of unity for T would indicate that the stabilization of the $UO_{2.4}$ is consistent both on and after the plateau for the samples compared. At 283°C, the value of T varied in the range 1.0 (for samples 105-01 and 105-08) to 5.6 (for samples 105-06 and 105-07). Similarly, at 305°C, the value of T varied in the range 1.0 (for samples 105-17 and 105-18) to 5.2 (for samples 105-15 and 104-01). The largest deviation from unity occurred when the average time-rate-of-change was calculated with data from a limited range in the O/M ratio because of early termination of the experimental measurement. Considering all of the factors that can affect the ratios, it appears that the effect from burnup-dependent stabilization of the $UO_{2.4}$ matrix is rather well correlated to both the duration of the plateau and the average rate of oxidation after the plateau.

To test this correlation more quantitatively, the quantities α, E_A, and E_{A0} were extracted from the data on the average time-rates-of-change in the O/M ratio after the plateau. Figures 5.18 and 5.19 show the logarithm of the average time-rate-of-change in the O/M ratio as a function of burnup for samples oxidized at 305°C, and Figure 5.20 shows an Arrhenius plot for the samples (105-01 through 105-14) from the high-burnup region of the ATM-105 fuel. For those samples where burnup was determined by the ^{137}Cs method (Figure 5.18, R^2=0.92), the burnup-dependent coefficient α was found to be 1.2±0.1 kJ mol^{-1} per unit burnup (MWd/kg M). The corresponding value for samples with burnup determined by the ^{148}Nd isotope dilution method (Figure 5.19, R^2=0.65) is α=1.0±0.5 kJ mol^{-1} per unit burnup. Thus, within experimental errors, the burnup dependence of the $UO_{2.4}$ to U_3O_8 transition is identical on the plateau, shortly after the plateau, and again over the range in O/M ratio of 2.44 to 2.60. A total activation energy of 245±65 kJ mol^{-1} was found from the least squares fit (R^2=0.56) to the data in Figure 5.20. With estimates of 1.2 kJ mol^{-1} per MWd/kg M for α and 28 MWd/kg M for the burnup, the estimate for E_{A0} is 211±68 kJ mol^{-1}. Within experimental limits, this value agrees with the value of 146±10 kJ mol^{-1} for the formation of U_3O_8 on unirradiated UO_2 [125]. Considering the limited data set, the uncertainties associated with the use of burnup as a thermodynamic variable, and the bias that may be introduced by including data from specimens not fully oxidized, this level of agreement is considered quite good.

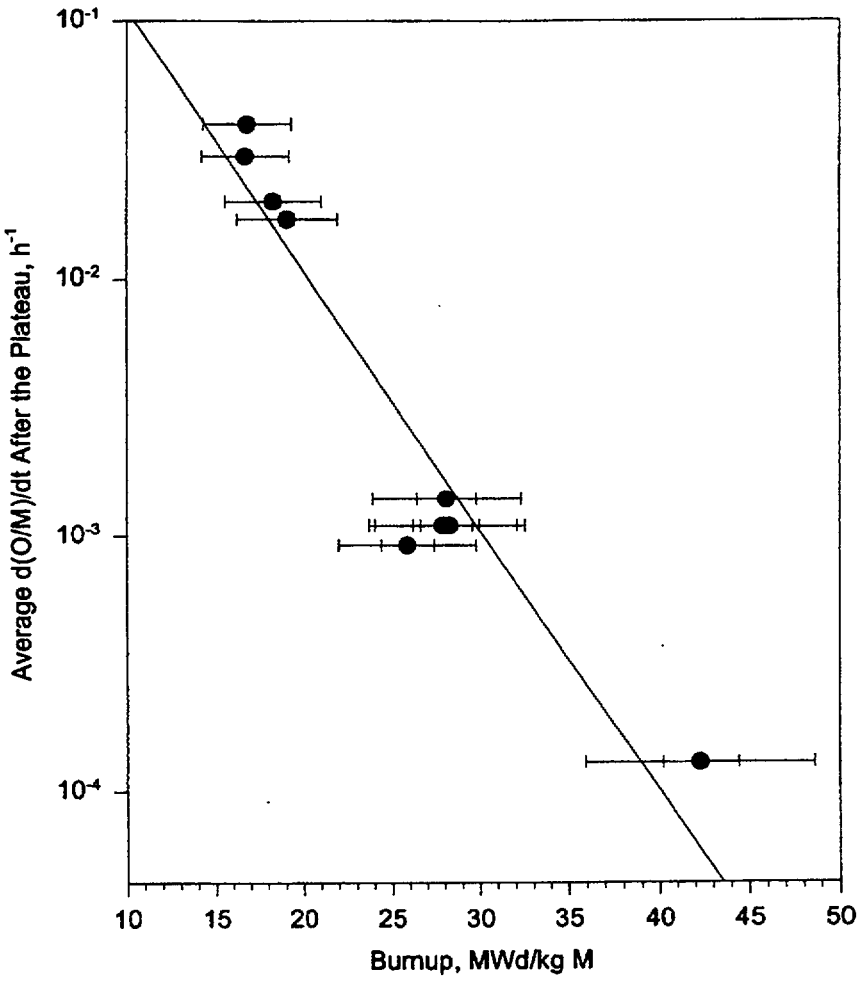

Figure 5.18. Average d(O/M)/dt After the Plateau as a Function of Burnup for ATM-105 Fragments Oxidized at 305°C (Burnup from ^{137}Cs Analysis)

5.2.5 Sensitivity to Impurity Concentration

The experimental data from the oxidation studies conducted with the TGA systems have demonstrated a marked dependence of the rate of oxidation from $UO_{2.4}$ to U_3O_8 on burnup. A number of inconsistencies, however, are worth noting. Although the burnups measured for samples 105-10 and 105-11 are essentially identical (29.8 and 29.6 MWd/kg M, respectively), the duration of the plateaus at 305°C differed by a factor of 4 and the time to oxidize from $UO_{2.45}$ to $UO_{2.50}$, as well as the average time-rate-of-change in the O/M ratio after the plateau, differed by a factor of about 1.6. Similarly, for the sample pairs 105-13 and 105-14 (moderate burnup) and 104-01 and 104-02 (high burnup), where the two members of each pair had essentially identical burnups, the duration of the plateaus differed by a factor of about 1.5.

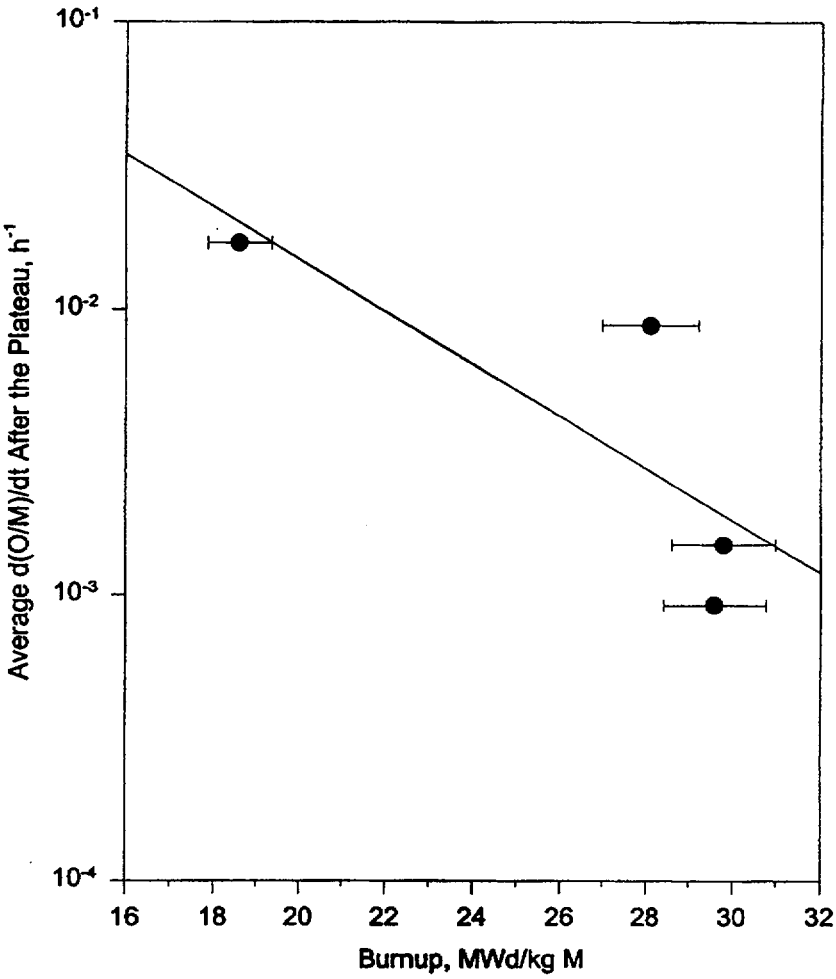

Figure 5.19. Average d(O/M)/dt After the Plateau as a Function of Burnup for ATM-105 Fragments Oxidized at 305°C (Burnup from ^{148}Nd Analysis)

On the other hand, the sample pair 105-06 and 105-07 had plateau durations that differed by a factor of only about 1.3, even though the difference in their respective burnups was much larger than for the previously mentioned sample pairs. Discrepancies of this type have been found for other specimens as well. While these discrepancies may reflect real differences in the materials, it is very clear that the sensitivity to burnup is sufficiently large that uncertainties in the measured burnup may be the source of these discrepancies. However, even if the burnup measurements had negligible error, a number of fundamental factors are not measured by burnup that can be expected to exert influence on the relative stabilities of the phases involved in the oxidation process.

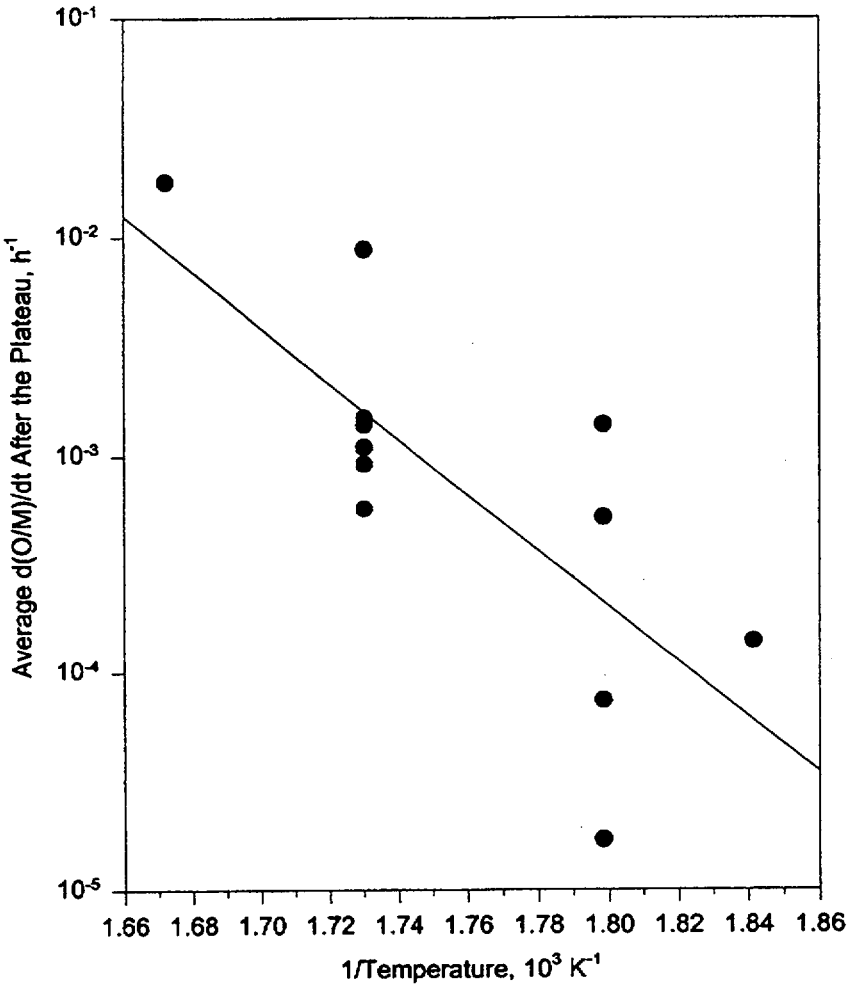

Figure 5.20. Average d(O/M)/dt After the Plateau as a Function of Inverse Temperature for Moderate Burnup ATM-105 Fragments

As a result of the radial dependence of strong resonance absorption in ^{238}U near the surface of a fuel pellet, the composition and concentration of transuranics can vary with both burnup and the neutron spectrum to which the fuel was subjected. Figures 2.4 and 2.5 clearly demonstrate that the surface-to-centerline burnup ratio for the ATM-104 fuel within a fuel pellet is about 1.7, and the corresponding ratio in the plutonium concentration is 2.9. Similar ratios for americium and curium are also expected. Fuels from different axial locations with the same bulk average burnup, and thus similar fission product concentrations, can be predicted to exhibit different oxidation behaviors if one specimen is from the fuel pellet surface and the other from the region near the centerline of the fuel, thereby ensuring markedly different actinide concentration. This is clearly seen with samples 108-01 and 108-02 where ^{241}Am was not detected in the γ-ray spectrum emitted by the fragment from near the centerline of the fuel, but had a

specific activity of 18.0±6.7 μCi/mg for the fragment from the surface (see Table 4.3). Since the fission yields of many of the soluble fission products of interest, namely, those that are expected to act as substitutional cations, vary significantly depending on which isotope undergoes fission (see Table 2.4), the radial location will also influence the amount of soluble fission products in the specimen. For example, the cumulative yields for Y, Zr, and Mo, as well as the REEs are generally smaller for fission of Pu than for U. While fuel fragments from the pellet surface will contain a higher concentration of actinides, the concentration of the lattice-soluble fission products will not be as high as found for the same total burnup in a specimen from the interior of a fuel pellet because the fraction of fissions in Pu will differ in the two locations. While burnup is a good first-order indicator of the impurity concentration in the fuel, it does not necessarily give a comprehensive description of the local fuel composition and thus its chemistry. Again, it should be stressed that the stabilization of the $UO_{2.4}$ phase depends on the total impurity concentration that is not accurately measured by the sample burnup alone. This is very clearly demonstrated by the BWR samples 108-01 and 108-02. Although these samples have burnups of about 18 and 35 MWd/kg M, respectively, the durations of the plateau were at least twice those of the PWR specimens with a burnup of about 42 MWd/kg M because of the initial doping of the fuel with about 3 wt% of Gd_2O_3.

The influence of the radial location of a fuel specimen, and hence its atomic composition, can help explain some of the observed variability in oxidation behavior. For example, as shown in Table 5.2, three of the samples broken from the same larger fragment, 105-12, 105-13, and 105-14, had nearly identical burnup, yet had durations on the plateau of 31, 22, and 35 hours (1.0/0.71/1.1 normalized to sample 105-12), respectively. The concentration of ^{241}Am in each specimen was measured as 1.9, 1.1, and 2.0 μCi/mg (1.0/0.58/1.1) and correlates strongly with the duration of the plateau. This variation in concentration will necessarily imply a variation in both the total actinide and fission product concentrations as well as the elemental compositions. Although errors in the activity measurements and burnups must be considered, the correlation strongly suggests variations in the radial locations of the fuel.

This trend is also found for the two higher-burnup ATM-104 samples of identical burnup. Sample 104-02 has both a higher mean ^{241}Am concentration and a longer plateau than are seen in sample 104-01 (Table 5.2). It is clear that both burnup and the ^{241}Am concentration (i.e., the total impurity concentration) are needed to qualitatively determine the duration of the plateau for an individual specimen. For example, the higher-burnup PWR (ATM-104) samples were taken from near the fuel pellet centerline, so even though their burnup is much higher than the BWR (ATM-105) samples, their Am content is similar.

Table 5.2. Summary of Burnup Analyses to Estimate Total Impurity Concentrations

Sample	Oxidation Temperature (°C)	t_5(h)	Burnup (MWd/kg M)	^{241}Am (μCi/mg)	^{242}Pu (%)
^{137}Cs Analysis:					
105-11	305	53	25.9±1.5	1.6±0.5	N/A
105-12	305	31	27.9±1.7	1.9±0.6	N/A
105-13	305	22	28.3±1.7	1.1±0.3	N/A
105-14	305	35	28.1±1.7	2.0±0.6	N/A
104-01	305	410	42.3±2.1	1.8±0.5	N/A
104-02	305	610	42.4±2.1	2.0±0.6	N/A
^{148}Nd Analysis:					
105-03	305	3.5	28.1±1.1	N/A	8.03
105-06	283	200	31.5±1.3	N/A	9.01
105-07	283	158	27.6±1.1	N/A	7.84
105-08	283	3300	32.5±1.3	N/A	10.44
105-10	305	14	29.8±1.2	N/A	8.19
105-11	305	53	29.6±1.2	N/A	8.49
105-15	305	0.6	18.6±0.7	N/A	3.17

Sample 105-11 had a slightly lower measured burnup than those of samples 105-12 through 105-14, even though it came from the same large fuel fragment. It clearly exhibited both a longer plateau as well as a smaller average rate of oxidation after the plateau, apparently contradicting the trends observed. Because the burnup of sample 105-11 was also measured with the ^{148}Nd method, it can be directly compared with other samples with burnup determined by this method without concern for a possible systematic error in the burnups. Inspection of the data in Table 5.2 indicates that the duration of the plateau correlates with the fraction of ^{242}Pu in the total Pu concentration. An increasing abundance of ^{242}Pu in the total plutonium is indicative of a higher level of neutron capture and correspondingly higher

concentrations of Pu, Am, and Cm. A similar trend exists for the samples oxidized at 283°C. Again, the relative resistance of a sample to oxidize from $UO_{2.4}$ to U_3O_8 can be determined by examining the burnup and fraction of total Pu that is ^{242}Pu. For samples of similar burnup, such as the sample pairs 105-06/105-08 and 105-10/105-11, the sample with the higher ^{242}Pu content had the longer plateau. In fact, the large fraction of ^{242}Pu for sample 105-08 may explain the plateau duration of about 3300 hours, whereas sample 105-06 had only a slightly smaller burnup and a plateau duration of only 200 hours. It would thus seem that the longer plateau for sample 105-11 compared to the other samples from the same large fragment may be explained by a relatively large higher-actinide content for a sample of its burnup. Future testing should better identify the axial and radial location of the fuel specimen or use destructive analysis to accurately characterize the total impurity content to better model the burnup dependence of the $UO_{2.4} \rightarrow U_3O_8$ transition.

5.3 Analysis of Dry-Bath Data

A detailed analysis of the dry-bath data presented in Section 4.3 cannot be accomplished in the same manner as for the TGA data because of the limited nature of the data sets. For example, the data in Figure 4.9 suggest that the oxidation experiments at 175°C were of sufficient length such that the Turkey Point and ATM-105 fuels have been oxidized to a plateau, the ATM-104 fuel has oxidized past a plateau, and the ATM-106 fuel has not yet reached a plateau. These observations apparently contradict those suggested by extrapolating the TGA results to these low temperatures. From the least squares fit of the data in Figure 5.1, the time to oxidize LWR spent fuel to the plateau at an O/M ratio of about 2.4 is calculated to be 2×10^5 hours at 175°C. Similarly, from the data in Figure 5.10, the duration of the plateau was estimated to be 7×10^9 hours. The dry-bath data show that the time to the plateau is on the order of 3×10^4 hours. In the TGA studies, the O/M ratio at which the plateau occurred varied from 2.39 to 2.43 for fuels with moderate or high burnup, but the final O/M ratios for the data in Figure 4.9 vary in the range 2.37 to 2.42. Thus, it is not at all clear that any of these dry-bath samples have yet reached the plateau.

A similar situation exists for the dry-bath samples oxidized at 195°C, as shown in Figure 4.10. Extrapolating the TGA data results in predictions of 4×10^4 and 2×10^8 hours for $t_{2.4}$ and t_5, respectively. However, examining the dry-bath data suggests that the plateau for all four fuel types studied was achieved within 1×10^4 hours and lasted for about 2×10^4 hours, a factor of 10^4 shorter than predicted. Once again, the final O/M ratios are in the range 2.38 to 2.42, so it is not clear that all of the samples have reached the plateau. Finally, it is important to note that the last data point for all of the dry-bath

experiments may be suspect. All of the fuel samples were transferred to new crucibles, and only one set of weighings was performed after this transfer. In every case, the sample appeared to have gained mass during this final oxidation period. For many samples, the mass increase was noticeably larger than for the previous interval. It is likely that as the fuel was transferred, fuel that had been at the bottom of the crucible, where oxygen in the ambient atmosphere may have been depleted, was now located at the top where it was exposed directly to the oxidizing atmosphere. Thus, even if all of these fuel samples had actually been on the plateau, it is not clear that the plateau has ended.

From Figures 4.11 through 4.13, it is evident that all of the dry-bath experiments at 255°C resulted in oxidation past the plateau. Extrapolating the TGA data to 255°C gives values of 400 and 10^4 hours for $t_{2.4}$ and t_8, respectively. Within 387 hours of oxidation, all of the dry-bath samples that had not been previously oxidized had achieved O/M ratios in the range 2.37 to 2.45, in agreement with the TGA data. For each of the four fuel types, the longest plateau was found to be about 2000 hours. From Figure 4.12, it is seen that the Turkey Point and ATM-105 fuels that had been first oxidized at lower temperatures to the plateau remained on the plateau for about 4000 to 6000 hours before gaining mass at approximately the same rate as those samples that had not been pre-oxidized. Thus, for all specimens, the durations of the plateaus are much shorter than predicted by the TGA data. These results also contradict the previous results of Einziger and Strain [4] (see Figure 2.3), who showed that, at 250°C, Turkey Point spent fuel fragments remained on the plateau for at least 10^4 hours before the test was halted.

The reasons for the discrepancies between the results from the TGA experiments, the previous work of Einziger and Strain, and the dry-bath experiments are not known with certainty, but some factors seem most likely to be of importance. It is quite possible that fuel oxidized at low temperatures experiences less cracking as the more dense $UO_{2.4}$ is formed, which might act to produce fewer sites for U_3O_8 nucleation than might be found at higher temperatures. Once the specimens have been heated to higher temperatures and more cracking occurs, the samples can then oxidize at about the same rate as the specimens that had not been pre-oxidized. Support for this hypothesis comes from Ohashi et al. [126], who found that the induction period preceding the U_3O_7 to U_3O_8 transition in unirradiated UO_2 powder was prolonged when the specimen was heated slowly or with prolonged annealing of the U_3O_7 at 200°C.

There are several possible reasons why the dry-bath samples have oxidized faster than expected based on the TGA analysis presented in this study for both the $UO_2 \rightarrow UO_{2.4}$ and $UO_{2.4} \rightarrow U_3O_8$ transitions. First, all of the samples have been exposed to the ambient atmosphere of the hot cell during any period of shutdown or for interim weighings. The exposure to moisture from those tests using humidified air may

have accelerated oxidation, as has been shown in work on CANDU™ fuels [16,28]. However, hydrated phases have not been reported for dry-bath specimens examined using XRD or TEM. Second, the intense radiation field within the hot cell may result in radiolysis of residual moisture or of nitrogen and oxygen in the air, which has been shown by Sunder and Miller [127] to accelerate oxidation. Third, a number of authors [3,53,55] have reported an apparent lower activation energy for the formation of U_3O_8 at temperatures of about 320°C to 350°C and higher. While it is possible that such a difference exists, McEachern et al. [125] found only one activation energy over the temperature range 168°C to 300°C, roughly the same range as for the TGA and dry-bath tests. Finally, no U_3O_8 has been observed via XRD for dry-bath specimens oxidized to O/M ratios up to 2.61, even though significant powder formation had been observed. As discussed in Section 4.4, calculations based on quantitative XRD analyses indicate that U_3O_8 has formed, but in a nanocrystalline state not observable by XRD. It is possible that under the conditions of the dry-bath experiments, the growth of U_3O_8 is limited. However, this would suggest that the activation energy for nucleation of U_3O_8 is significantly less than that for growth, a phenomenon not observed in the TGA study. Further testing is necessary to determine the cause of the discrepancy between the dry-bath data and the present TGA work.

5.4 Change in Lattice Energy with Burnup

The increasing resistance of oxidation of $UO_{2.4}$ to U_3O_8 with increasing burnup and similar results shown in Section 2.2.3 for the oxidation of doped, unirradiated UO_2 strongly point to the increased stability of the UO_2 and $UO_{2.4}$ fluorite phases due to the presence of substitutional impurities. These two phases are very complex owing to the presence of a wide range of elements with varying oxidation states and the fact that they can produce distortions to the lattices in different ways, i.e., from substitution into the metallic sublattice, from their location in interstitial sites, etc. It was hypothesized that the increased stability of the lattice, which is basically a thermodynamic property, affects at least one of the mechanistic steps of the oxidation transformation so as to result in the observed kinetic differences. No specific rate-limiting mechanism is proposed at this time. However, the discussion presented in Sections 2.5.1 through 2.5.3 suggests that a major factor governing the increased stability could be the contraction of the lattice due to incorporating substitutional cations and the resultant change in lattice energy. This is particularly easy to assess because the UO_2 lattice is rather well described by the idealization of a purely ionic crystalline lattice. For example, Olander [128] calculated the cohesive energy of UO_2 as -9791 kJ mol^{-1} by summing the Coulomb, van der Waals (arising from the induced multipole moments of the ions), and repulsive forces. Olander's calculated lattice energy is quite close to the energy of -9858 kJ mol^{-1} estimated by Childs in 1958 [quoted in 128] using the Born-Haber cycle approach and the energy of

-10172 kJ mol^{-1} calculated by Childs (neglecting the dipole-quadrupole and quadrupole-quadrupole forces). These values are slightly larger (less negative) than the value -10644 kJ mol^{-1} reported in the CRC Handbook of Chemistry and Physics [129], which used the assumptions underlying the purely ionic model (Equation 2.11). It is important to note that about 16% of the total cohesive energy calculated by Olander [128] is due to the attractive nature of the van der Waals multipole forces.

Since the purely ionic model does a fairly good job of describing the UO_2 lattice (a 9% increase over Olander's calculations), Equation (2.12) provides a direct route to estimating the effect of substitutional ions on the stability of the lattice. Since $\{(\Delta U/U)=(-\Delta r_0/r_0)\}$, a change in the equilibrium cation-anion distance will change the lattice energy. Thus, the presence of transuranic ions and fission products as substitutional ions in the uranium sublattice must effect a change in the lattice energy if their presence results in a change in the mean radius of ions in this sublattice.

The degree to which this model explains the data obtained in this study can be examined with the assumption that the burnup-dependent coefficient of the activation energy, α, is due solely to the change in the mean radius of the ions in the metal sublattice. If the lattice energy is assumed to be -10644 kJ mol^{-1}, and a nominal value of α is taken as 1.2 kJ mol^{-1} per MWd/kg M, then, for example, a burnup of 33 MWd/kg M and a 10-year decay time implies an increase in the lattice energy of 40 kJ mol^{-1}. Using the ionic radii of 136.9 pm and 100 pm for O^{2-} and U^{4+}, respectively (see Section 2.5.3), the equilibrium cation-anion distance r_0 is 236.9 pm. Equation (2.12) then implies a change in the equilibrium cation-anion distance Δr_0 of 0.89 pm to account for an increase of lattice energy of 40 kJ mol^{-1}. This, in turn, implies (Equation 2.14) that the lattice parameter for the contracted lattice must be 545.04 pm to fully account for the change in lattice energy that results in the stabilization of the $UO_{2.4}$ phase. Within the assumptions inherent in this calculation, the quality of the estimates of the lattice contraction and lattice parameter should be quite reasonable. In summary, the empirical data on the burnup dependence of the activation energy implies that substitutional impurities in the uranium sublattice must result in a net average lattice contraction of about 2 pm if this phenomenon is the principal factor governing the observed stabilization with respect to oxidation to U_3O_8. The choice of the burnup and decay time for the present calculations permits the use of the elemental compositions given in Table 2.2 for estimating the effects of the substitution of cations into the metal sublattice and the subsequent oxidation of matrix uranium ions to U^{5+} that may be necessary to maintain overall charge neutrality.

The chemical form of the solid solution describing spent fuel can be described as

$$U^{4+}_{1-2y-z-3x-4l}\, R^{3+}_{y}\, S^{4+}_{z}\, T^{2+}_{x}\, K^{1+}_{l}\, U^{5+}_{y+2x+3l}\, O^{2-}_{2} \tag{5.6}$$

where y, z, x, and l are the mole fractions of substitutional cations with valence of 3+, 4+, 2+, and 1+, respectively. For every trivalent substitution, one U^{4+} must be oxidized to U^{5+}, whereas two U^{4+} ions must be oxidized to the 5+ state for the substitution of a divalent cation, etc. Substitution of a cation with an ionic charge of 4+ simply replaces one U^{4+} that is lost due to fission or other transformation. The atom fractions for each fission product and actinide element that must be considered are given in Table 2.2, and their ionic radii from the compilation by Shannon [108] are listed in Table 2.5. Modification of Equation (2.14) to account for multiple elements within the lattice yields

$$a = \frac{4}{\sqrt{3}}\left(\sum_i X_{ci} r_{ci} + \sum_i X_{ai} r_{ai}\right) \tag{5.7}$$

where r_c and r_a are the radii of the cations and anions, respectively, X_c and X_a are the mole fractions of the respective cation or anion, and a is the lattice parameter.

It must be stressed that fission of a single U or Pu nucleus produces two fission-product atoms. A burnup of 33 MWd/kg M corresponds to 3.4 atom% burnup, or, in other words, 3.4% of the original U atoms have been fissioned or have been transmuted into Pu atoms that have fissioned. In either event, under normal reactor operating conditions where the spent fuel has been shown to be very nearly stoichiometric or even slightly hypostoichiometric, at most one-half of the fission product atoms (or 3.4 atom%) can substitute into the vacancies created by the fissioned atoms if radiation effects are neglected. It is reasonable to assume that all of the actinides formed by neutron capture will readily remain in the metallic sublattice and act as substitutional cations. Since the lattice will attempt to maintain or at least approach thermodynamic equilibrium, those fission products that will greatly distort the lattice and increase the total energy of the system are assumed to be excluded from the metallic sublattice. These fission products must form other phases, whether on the atomic or macroscopic level. In the presence of sufficient concentrations of oxygen and such ions as Zr^{4+} and Mo^{4+}, for example, simple reference to the relative stabilities of the oxides suggests that such elements as Cs, Te, I, and Br and the rare gases Xe and Kr will not be found as substitutional impurities. Similarly, it is clear that the ε-Ru phase will tend to be stabilized because of the relative instability of the oxides of the elements it comprises: Ru, Rh, Pd, and Tc. Mo, which is also normally found in this metallic precipitate, represents a complex issue because the stability of MoO_2 is very close to that of UO_2 and depends sensitively on the oxygen potential and, as suggested here, the availability of other ions that might substitute into the UO_2 lattice.

Using these considerations, the estimation of the average lattice parameter resulting from cationic substitutions was approached stepwise. Elements with very stable oxides, i.e., those with the most negative free energy of formation in Figure 2.7, were assumed to substitute in the metallic sublattice first. First, the only cations considered were those that are known to substitute for U ions and do not form metallic or oxide precipitates. These cations include the 4+ ions Pu, Ce, Pr, and Np, as well as the 3+ Nd, La, Sm, Am, Y, Gd, Cm, and Eu. With this assumption, the values for x and l in Equation (5.6) are zero, and Equation (5.7) yields an average lattice parameter of 546.8 pm, a contraction of only 0.2 pm from the unperturbed UO_2 lattice (547.0 pm). Next, it was assumed that in addition to the actinides and REEs considered in the first case, all of the fission product Zr acted as a 4+ substitutional ion in the metallic sublattice. Because the Zr ions are randomly dispersed throughout the matrix and because of the presence of the REEs, all Zr is assumed soluble in the matrix. With the addition of the Zr^{4+}, 2.62% of the fission products are now considered in solid solution, and the resulting lattice contraction is 0.5 pm.

For the third step, all of the fission product Sr was incorporated in uranium vacancies for a total of 2.83 atom% of the fission products in solution, and Equation (5.7) yields a lattice parameter of 546.45 pm. Next, all of the Ba and 42% of the Mo were included so that all 3.4 atom% of the uranium vacancies produced by fission would be filled. The lattice contraction was calculated as 0.8 pm. Finally, it was assumed that no Ba acted substitutionally, but 77% of the Mo was in solid solution to fill all metallic vacancies. The resulting average contraction of the lattice was 1.1 pm.

This analysis, of course, oversimplifies a very complex system. It is not clear that thermodynamic equilibrium will be achieved either under reactor conditions or in the oxidation experiments. As such, it is possible that a fraction of the elements that are not stable as oxides under these conditions, such as the metals of the ε-Ru phase, may act as substitutional cations. The small radii of these noble metals would cause the lattice to contract further. However, the analysis clearly demonstrates that the lattice contraction due to incorporation of substitutional cations and the necessary oxidation of uranium ions to maintain charge neutrality can account for about one-half of the change in lattice energy, which in turn results in the burnup dependence of the transition from $UO_{2.4}$ to U_3O_8. It is reasonable to expect that more than one-half of the energy would be accounted for if the additional stability resulting from the interacting van der Waals multipole forces were considered. Also, the chemistry of the actinides and REEs is controlled by the highly non-spherical d and f orbitals in the electron cloud. The possible deformation, and hence smaller ionic radii, of these ions could result in even greater contraction of the lattice. Finally, during oxidation, the oxygen potential of the fuel will increase,

and those elements that were not stable as substitutional cations may now be stable as oxides. The findings of Grimes and Catlow [65] that virtually all elements are predicted to be most stable as cations in uranium vacancy sites in UO_{2+x} support this conclusion.

It is important to note that in this analysis, the dilation of the lattice due to the accumulation of point defects was ignored. From Equation (2.16), a dilation of about 0.06 pm could be expected. However, the effect of low-temperature annealing for long periods (tens to hundreds of hours in the TGA before the plateau is reached, hundreds to thousands of hours in the dry-baths) is not known. The lattice parameter of the unoxidized UO_2, as calculated using XRD data on oxidized specimens reported by Thomas et al. [35], was found to about 546.7 pm; however, the lattice parameter for the $UO_{2.4}$ phase was approximately 544.3 pm, which is about 0.2 pm larger than that for the U_4O_9 phase used for identification. Thus, experimental evidence seems to indicate a contraction of only about 0.3 to 0.5 pm; however, the uncertainties in the methodology used to calculate the lattice parameters were considerable. Equation (2.15), which was determined using simulated high burnup fuel [99], predicts a contraction of only 0.4 pm for a burnup of 33 MWd/kg M (3.44 atom%), although the simulant does not contain all of the fission products or higher actinides.

6.0 CONCLUSIONS

In this study to examine the oxidation of LWR spent fuels, continuous-weighing TGA systems were used to measure the mass increase of specimens oxidized in a dry-air atmosphere over the temperature range 255°C to 325°C. Radiologic dose constraints limited the sample size for TGA analysis to about 200 mg. Analysis of data from long-term oxidation studies conducted by Einziger and others at Pacific Northwest National Laboratory was also included. These studies consisted of large (5 g to 10 g) samples of spent fuel oxidized at temperatures ≤255°C in dry-bath ovens. The samples oxidized in a dry-bath were weighed only intermittently to determine the increase in mass. The mass increase of TGA and dry-bath specimens was correlated directly to the O/M ratio with neglect of any effect due to substitution of fission products or higher actinides for the original uranium atoms. The burnup of individual specimens was determined by either a ^{148}Nd isotope dilution method using mass spectrometry (about ±4% uncertainty) or by analysis of the γ-ray spectrum emitted (about ±15% uncertainty). Some of the samples were examined by XRD and SEM to determine the phases present and to identify grain characteristics, such as the extent of cracking.

Most of the samples used in the TGA tests came from a single 56-cm length from the high-burnup region of a BWR fuel rod. The burnup of these specimens was found to vary in the range 27.5 to 32.5 MWd/kg M, a consequence of both the axial and radial dependence of burnup. Samples from a 3-cm length from the low-burnup end of the same fuel rod were found to have burnups ranging from 16.7 to 18.3 MWd/kg M. Radial distributions in burnup and actinide content that result from resonance absorption in ^{238}U may be significant and should be considered, especially when using specimens that are not large enough to sample across the entire fuel radius. Specimens with a burnup of about 42 MWd/kg M and others with an initial doping of 3 wt% Gd_2O_3 were also tested.

The oxidation of spent fuel was confirmed to proceed via the two-step reaction $UO_2 \rightarrow UO_{2.4} \rightarrow U_3O_8$, where the $UO_{2.4}$ phase is similar to cubic U_4O_9, but contains excess, diffuse oxygen. Calculations verified that the O/M ratio of 2.4 was achieved by incorporation of oxygen into the lattice and not simply due to oxidation of the fission products. The transition of UO_2 to $UO_{2.4}$ was shown to strongly depend on the average grain size of the specimens, with smaller-grained fuels oxidizing faster in accordance with a larger surface area per unit grain volume. No correlation with other fuel parameters, such as burnup, was found. When the variation in grain size from sample-to-sample was minimized, the

Arrhenius activation energy was calculated as 109±14 kJ mol^{-1}, in excellent agreement with previously reported values as well as the reported value of 100 kJ mol^{-1} for diffusion of oxygen in UO_{2+x}.

A plateau on a plot of O/M ratio vs time was observed for most specimens. The duration of the plateau and the average time-rate-of-change in the O/M ratio after the plateau (i.e., the transition of $UO_{2.4}$ to U_3O_8) were found to be strongly temperature and burnup dependent. The activation energy to convert $UO_{2.4}$ to U_3O_8 was modeled as consisting of a temperature-dependent term and a term assumed to be linearly dependent on burnup. The coefficient for burnup-dependence was calculated to be in the range of 1 to 2 kJ mol^{-1} per MWd/kg M, with a nominal value of 1.2 kJ mol^{-1} per MWd/kg M. While the measured burnups and their associated uncertainties may explain most of the observed differences in the oxidation behavior, it is important to stress that burnup was used only as a rough estimate of the total substitutional cation concentration. Because the yields of the fission products and transuranic elements vary with burnup and because it is not clear that thermodynamic equilibrium is achieved either in the reactor or under the conditions studied, burnup is not a well-defined thermodynamic property with respect to the kinetics and mechanism of oxidation.

The temperature-dependent activation energy of the $UO_{2.4}$ to U_3O_8 transition was determined to be in the range 155 to 370 kJ mol^{-1}. The large activation energies were calculated using the dependence of the duration of the plateau as the determining variable. However, this duration, as defined for the purpose of this study, does not correspond to a quantitative measure of the state of the fuel, and the interpretation of the duration is especially questionable for those samples with short (i.e., a few hours or less) plateaus. When a large data set and well defined states of the fuel were used, the temperature-dependent activation energy was calculated to be in the range of 155 to 211 kJ mol^{-1}, in agreement with the literature value of 146±10 kJ mol^{-1} found for oxidation of unirradiated UO_2 when the uncertainties of the data were considered.

A comparison of the average time-rates-of-change in O/M ratio with the durations of the plateau showed excellent agreement. Even in the worst-case, the difference was only about a factor of 5. Thus, it has been shown that the stabilization of the $UO_{2.4}$ phase with respect to further oxidation, or the resistance to U_3O_8 formation, was consistent both on the plateau and after formation of U_3O_8 had begun. A model was presented that suggested that the stabilization of the $UO_{2.4}$ phase is a result of the substitutional fission products and actinides in the metal sublattice. It was shown that one-half of the empirically determined lattice energy of stabilization may be accounted for by the average contraction of the lattice due to incorporation of cations of different ionic radii and valence and the subsequent oxidation of the

uranium ions from 4+ to 5+. More than one-half of the necessary change in lattice energy may be accounted for if the ion multipole interactions are included. Dry-air oxidation of most spent fuels to U_3O_8 at repository temperatures is expected to be sufficiently slow that it will not be a major factor in further cladding degradation or in radionuclide release.

7.0 REFERENCES

1. R.E. Woodley, "The Characteristics of Spent LWR Fuel Relevant to its Storage in Geologic Repositories" Westinghouse Hanford Co. HEDL-TME 83-28 (October 1983).

2. M.A. Mckinnon, T.E. Michener, M.F. Jensen, and G.R. Rodman, "Testing and Analyses of the TN-24P PWR Spent Fuel Dry Storage Cask Loaded with Consolidated Fuel" Electric Power Research Institute EPRI NP-6191 (February 1989).

3. D.G. Boase and T.T. Vandergraaf, "The Canadian Spent Fuel Storage Canister: Some Materials Aspects" Nuclear Technology **32** (1977) 60-71.

4. R.E. Einziger and R.V. Strain, "Behavior of Breached Pressurized Water Reactor Spent-Fuel Rods in an Air Atmosphere Between 250 and 360°C" Nuclear Technology **75** (1986) 82-95.

5. R.E. Einziger and J.A. Cook, "Behavior of Breached Light Water Reactor Spent Fuel Rods in Air and Inert Atmospheres at 229°C" Nuclear Technology **69** (1985) 55-71.

6. J. Novak, I.J. Hastings, E. Mizzan, and R.J. Chenier, "Postirradiation Behavior of UO_2 Fuel I: Elements at 220 to 250°C in Air" Nuclear Technology **63** (1983) 254-265.

7. W.J. Gray, L.E. Thomas, and R.E. Einziger, "Effects of Air Oxidation on the Dissolution Rate of LWR Spent Fuel" Materials Research Society Symposium Proceedings **294** (1993) 47-54.

8. E.H.P. Cordfunke, "The Chemistry of Uranium" Elsevier, Amsterdam (1969).

9. L. Lynds, W.A. Young, J.S. Mohl, and G.G. Libowitz, "Nonstoichiometric Compounds" ed. R.F. Gould, American Chemical Society Advances in Chemistry Series **39** (1962) 58.

10. L.E. Thomas, R.E. Einziger, and R.E. Woodley, "Microstructural Examination of Oxidized Spent PWR Fuel by Transmission Electron Microscopy" Journal of Nuclear Materials **166** (1989) 243-251.

11. H. Blank and C. Ronchi, "Electron Diffraction of U_4O_9" Acta Cryst **A24** (1968) 657.

12. L.E. Thomas, R.W. Knoll, L.A. Charlot, J.E. Coleman, and E.R. Gilbert, "Storage of LWR Spent Fuel in Air, Volume 2-Microstructural Characterization of Low-Temperature Oxidized LWR Spent Fuel" Pacific Northwest Laboratory PNL-6640 Vol.2 (1989).

13. B.O. Loopstra, "Neutron Diffraction Investigation of U_3O_8" Acta Cryst **17** (1964) 651.

14. S.Aronson, ed., "Oxidation and Corrosion of Uranium Dioxide" in "Uranium Dioxide: Properties and Nuclear Applications" J. Belle, ed., ASAEC, Washington, D.C., (1961) 377.

15. H.R. Hoekstra and S. Siegel, "The Uranium-Oxygen System: U_3O_8-UO_3" Journal of Inorganic and Nuclear Chemistry **18** (1961) 154.

16. P. Taylor, R.J. Lemire, and D.D. Wood, "The Influence of Moisture on Air Oxidation of UO_2: Calculations and Observations" Nuclear Technology 104 (1993) 164.

17. J.J. Katz, G.T. Seaborg, and L.R. Morss, ed., "The Chemistry of the Actinide Elements, Second Edition, Vols. I and II" Chapman and Hall, New York, (1986).

18. G.C. Allen and N.R. Holmes, "A Mechanism for the UO_2 to α-U_3O_8 Phase Transformation" Journal of Nuclear Materials **223** (1995) 231-237.

19. R.J. McEachern and P. Taylor, "A Review of the Oxidation of Uranium Dioxide at Temperatures Below 400°C" Atomic Energy of Canada Limited AECL-11335 (1997).

20. S. Aronson, R.B. Roof, Jr., and J. Belle, "Kinetic Study of the Oxidation of Uranium Dioxide" Journal of Chemical Physics **27**, 1 (1957) 137-144.

21. P.E. Blackburn, J. Weissbart, and E.A. Gulbransen, "Oxidation of Uranium Dioxide" Journal of Physical Chemistry **62** (1958) 902-908.

22. P. Taylor, E.A. Burgess, and D.G. Owen, "An X-ray Diffraction Study of the Formation of β-$UO_{2.33}$ on UO_2 Pellet Surfaces in Air at 229 to 275°C" Journal of Nuclear Materials **88** (1980) 153-160.

23. P.A. Tempest, P.M. Tucker, and J.W. Tyler, "Oxidation of UO_2 Fuel Pellets in Air at 503 and 543 K Studied Using S-ray Photoelectron Spectroscopy and X-ray Diffraction" Journal of Nuclear Materials **151** (1988) 251-268.

24. G.C. Allen, P.A. Tempest, and J.W. Tyler, "Characterization of Crystalline UO_2 Oxidised in 1 Torr of Oxygen at 25, 225 and 300°C, Part 2- X-ray Diffraction and Scanning Electron Microscopy" Journal of the Chemical Society, Faraday Transactions I **84** (1988) 4061-4072.

25. S.R. Teixeira and K. Imakuma, "High Temperature X-ray Diffraction Study of the U_4O_9 Formation on UO_2 Sintered Plates" Journal of Nuclear Materials **178** (1991) 33-39.

26. P. Taylor, D.D. Wood, and A.M. Duclos, "The Early Stages of U_3O_8 Formation on Unirradiated CANDU UO_2 Fuel Oxidized in Air at 200-300°C" Journal of Nuclear Materials **189** (1992) 116-123.

27. H.R. Hoekstra, A. Santoro, and S. Siegel, "The Low Temperature Oxidation of UO_2 and U_4O_9" Journal of Inorganic Nuclear Chemistry **18** (1961) 166-178.

28. K.M. Wasywich, W.H. Hocking, D.W. Shoesmith, and P. Taylor, "Differences in Oxidation Behavior of Used CANDU Fuel During Prolonged Storage in Moisture-Saturated Air and Dry Air at 150°C" Nuclear Technology **104** (1993) 309-329.

29. I.J. Hastings, E. Missan, A.M. Ross, J.R. Kelm, R.J. Chenier, D.H. Rose, and J. Novak, " Postirradiation Behavior of UO_2 Fuel II: Fragments at 175 to 275°C in Air" Nuclear Technology **68** (1985) 40-47.

30. R.E. Einziger, L.E. Thomas, H.C. Buchanan, and R.B. Stout, "Oxidation of Spent Fuel in Air at 175 to 195°C" Journal of Nuclear Materials **190** (1992) 53-60.

31. R.E. Woodley, R.E. Einziger, and H.C. Buchanan, "Measurement of the Oxidation of Spent Fuel Between 140 and 225°C" Nuclear Technology **85** (1989) 74-88.

32. L.E. Thomas, O.D. Slagle, and R.E. Einziger, "Nonuniform Oxidation of LWR Spent Fuel" Journal of Nuclear Materials **184** (1991) 117-126.

33. L.E. Thomas and R.E. Einziger, "Grain Boundary Oxidation of Pressurized-Water Reactor Spent Fuel in Air" Materials Characterization **28** (1992) 149-156.

34. L.E. Thomas, C.E. Beyer, and L.A. Charlot, "Microstructural Analysis of LWR Spent Fuels at High Burnup" Journal of Nuclear Materials **188** (1992) 80-89.

35. L.E. Thomas, R.E. Einziger, and H.C. Buchanan, "Effect of Fission Products on Air-Oxidation of LWR Spent Fuel" Journal of Nuclear Materials **201** (1993) 310-319.

36. J. Nakamura, R. Otomo, T. Kikuchi, and S. Kawasaki, "Oxidation of Fuel Rod Under Dry Storage Condition" Journal of Nuclear Science and Technology **32**[4] (1995) 321-332.

37. R.E. Einziger, L.E. Thomas, and B.D. Hanson, "Oxidation of Spent LWR Fuel FY95 Year End Report" Pacific Northwest Laboratory letter report for the Lawrence Livermore National Laboratory and Yucca Mountain Project (1995).

38. R.E. Einziger, S.C. Marschman, and H.C. Buchanan, "Spent-Fuel Dry-Bath Oxidation Testing" Nuclear Technology **94** (1991) 383-393.

39. T.K. Campbell, E.R. Gilbert, G.D. White, G.F. Piepel, and B.J. Wrona, "Oxidation Behavior of Nonirradiated UO_2" Nuclear Technology **85** (1989) 160-171.

40. J.O. Barner, "Characterization of LWR Spent Fuel MCC-Approved Testing Material - ATM-101" Pacific Northwest Laboratory PNL-5109 Rev. 1 (1985).

41. Hj. Matzke, "On the Rim Effect in High Burnup UO_2 LWR Fuels" Journal of Nuclear Materials **189** (1992) 141-148.

42. K. Lassmann, C.T. Walker, J. van de Laar, F. Lindström, "Modelling the High Burnup UO_2 Structure in LWR Fuel" Journal of Nuclear Materials **226** (1995) 1-8.

43. W.B. Wilson, C.A. Alexander, and A.F. Gerds, "Stabilization of UO_2" Journal of Inorganic Nuclear Chemistry **20** (1961) 242-251.

44. L.E.J. Roberts, L.E. Russell, A.G. Adwick, A.J. Walter, and M.H. Rand, "The Actinide Oxides" in Proceedings of the Second United Nations International Conference on the Peaceful Uses of Atomic Energy, Vol. 28 Basic Chemistry in Nuclear Energy, United Nations, Geneva, (1958) 215-222.

45. D.C. Hill, "Phase Relations and Crystal Chemistry in the System Uranium Oxide-Lanthanum Oxide" Journal of the American Ceramic Society **45**[6] (1962) 258-263.

46. N.H. Brett and A.C. Fox, "Oxidation Products of Plutonium Dioxide-Uranium Dioxide Solid Solutions in Air at 750°C" Journal of Inorganic Nuclear Chemistry **28** (1966) 1191-1203.

47. D.G. Leme and Hj. Matzke, "The Diffusion of Uranium in U_3O_8" Journal of Nuclear Materials **115** (1983) 350-353.

48. M. Ishida and Y. Korei, "Modeling and Parametric Studies of the Effect of Pu-mixing Heterogeneity on Fission Gas Release from Mixed Oxide Fuels of LWRs and FBRs" Journal of Nuclear Materials **210** (1994) 203-215.

49. V.J. Tennery and T.G. Godfrey, "Oxidation Properties of $(U,Pu)O_2$ Solid Solutions" Journal of the American Ceramic Society **56**[3] (1973) 129-133.

50. J. Janeczek, R.C. Ewing, L.E. Thomas, "Oxidation of Uraninite: Does Tetragonal U_3O_7 Occur in Nature?" Journal of Nuclear Materials **207** (1993) 177-191.

51. J.W. Choi, R.J. McEachern, P. Taylor, and D.D. Wood, "The Effect of Fission Products on the Rate of U_3O_8 Formation in SIMFUEL Oxidized in Air at 250°C" Journal of Nuclear Materials **230** (1996) 250-258.

52. M.E. Cunningham, "Contamination of BSFS Spent Fuel Oxidation Samples" Journal of Nuclear Materials **187** (1992) 307.

53. M.J. Bennett, J.B. Price, and P. Wood, "Influence of Manufacturing Route and Burn-up on the Oxidation and Fission Gas Release Behaviour of Irradiated Uranium Dioxide in Air at 175-400°C" Nuclear Energy **27**[1] (1988) 49-54.

54. P. Wood, M.J. Bennett, M.R. Houlton, and J.B. Price, "Oxidation and Fission Gas Release Behaviour of Irradiated Uranium Dioxide in Air Below 400°C" in Proceedings of BNES Conference, Stratford-Upon-Avon, UK, March 1985, Vol. 2, (1985) 116-118.

55. G.S. You, K.S. Kim, D.K. Min, S.G. Ro, and E.K. Kim, "Oxidation Behavior of UO_2 in Air" Journal of the Korean Nuclear Society **27**[1] (1995) 67-73.

56. K.T. Harrison, C. Padgett, and K.T. Scott, "The Kinetics of the Oxidation of Irradiated Uranium Dioxide Spheres in Dry Air" Journal of Nuclear Materials **23** (1967) 121-138.

57. T.K. Campbell, E.R. Gilbert, C.K. Thornhill, and B.J. Wrona, "Oxidation Behavior of UO_2 Spent Fuel" Nuclear Technology **84** (1989) 182-195.

58. C.T. Walker, T. Kameyama, S. Kitajima, and M. Kinoshita, "Concerning the Microstructure Changes That Occur at the Surface of UO_2 Pellets on Irradiation to High Burnup" Journal of Nuclear Materials **188** (1992) 73-79.

59. American Society for Testing and Materials, Standard E 321, "Standard Test Method for Atom Percent Fission in Uranium and Plutonium Fuel (Neodymium-148 Method)" in Annual Book of ASTM Standards Vol. 12.02, Philadelphia.

60. A.G. Croff, "ORIGEN2- A Revised and Updated Version of the Oak Ridge Isotope Generation and Depletion Code" Oak Ridge National Laboratory ORNL-5621 (1980).

61. S.B. Ludwig and J.P. Renier, "Standard- and Extended-Burnup PWR and BWR Reactor Models for the ORIGEN2 Computer Code" Oak Ridge National Laboratory ORNL/TM-11018 (1989).

62. Hj. Matzke, "Fission Gases in Nuclear Fuels" Ann. Chim. Fr. **14** (1989) 133-147.

63. H. Kleykamp, "The Chemical State of the Fission Products in Oxide Fuels" Journal of Nuclear Materials **131** (1985) 221-246.

64. H. Kleykamp, "The Chemical State of Fission Products in Oxide Fuels at Different Stages of the Nuclear Fuel Cycle" Nuclear Technology **80** (1988) 412-422.

65. R.W. Grimes and C.R.A. Catlow, "The Stability of Fission Products in Uranium Dioxide" Phil. Trans. R. Soc. Lond. A, **335** (1991) 609-634.

66. P.G. Lucuta, R.A. Verall, Hj. Matzke, and B.J. Palmer, "Microstructural Features of SIMFUEL-Simulated High-Burnup UO_2-based Nuclear Fuel" Journal of Nuclear Materials **178** (1991) 48-60.

67. I.L.F. Ray, H. Thiele, and Hj. Matzke, "Transmission Electron Microscopy Study of Fission Product Behaviour in High Burnup UO_2" Journal of Nuclear Materials **188** (1992) 90-95.

68. L.E. Thomas and R.J. Guenther, "Characterization of Low-Gas-Release LWR Fuels by Transmission Electron Microscopy" Mat. Res. Soc. Symp. Proc. **127** (1989) 293-300.

69. R.J. Guenther, D.E. Blahnik, U.P. Jenquin, J.E. Mendel, L.E. Thomas, and C.K. Thornhill, "Characterization of Spent Fuel Approved Testing Material- ATM-104" Pacific Northwest National Laboratory PNL-5109-104, (1991).

70. R.J. Guenther, D.E. Blahnik, T.K. Campbell, U.P. Jenquin, J.E. Mendel, L.E. Thomas, and C.K. Thornhill, "Characterization of Spent Fuel Approved Testing Material- ATM-105" Pacific Northwest National Laboratory PNL-5109-105, (1991).

71. F. Schleifer, A. Naoumidis, and H. Nickel, "Solid Solutions and Phase Equilibria in (U,Zr,Ln) Oxides in the Temperature Range 1270-1670 K" Journal of Nuclear Materials **101** (1981) 150-161.

72. K.A. Romberger, C.F. Baes, and H.H. Stone, "Phase Equilibrium Studies in the UO_2-ZrO_2 System" Journal of Inorganic Nuclear Chemistry **29** (1967) 1619-1630.

73. B.F. Rider, "Compilation of Fission Product Yields" Vallecitos Nuclear Center report NEDO-12154-3(B) (1980).

74. L.B. Pankratz, "Thermodynamic Properties of Elements and Oxides" United States Bureau of Mines Bulletin 672 (1982).

75. D.R. Olander, "Fundamental Aspects of Nuclear Fuel Elements" TID-26711-P1, Energy Research and Development Administration (1976).

76. Hj. Matzke, "Oxygen Potential in the Rim Region of High Burnup UO_2 Fuel" Journal of Nuclear Materials **208** (1994) 18-26.

77. Hj. Matzke, "Oxygen Potential Measurements High Burnup LWR Fuel" Journal of Nuclear Materials **223** (1995) 1-5.

78. T.B. Lindemer and T.M. Besmann, "Chemical Thermodynamic Representation of $UO_{2\pm x}$" Journal of Nuclear Materials **130** (1985) 473-488.

79. R.E. Woodley, "Variation in the Oxygen Potential of a Mixed-Oxide Fuel with Simulated Burnup" Journal of Nuclear Materials **74** (1978) 290-296.

80. K. Une and M. Oguma, "Oxygen Potential of $U_{0.96}Gd_{0.04}O_2$ (UO_2-3wt% Gd_2O_3) Solid Solution" Journal of Nuclear Materials **131** (1985) 88-91.

81. M. Ugajin, "Measurements of O/U Ratio and Oxygen Potential for UO_{2+x} ($0 \leq x \leq 0.1$)" Journal of Nuclear Science and Technology **20**[3] (1983) 228-236.

82. P.E. Blackburn, "Oxygen Pressures Over Fast Breeder Reactor Fuel, (I) A Model for $UO_{2\pm x}$" Journal of Nuclear Materials **46** (1973) 244-252.

83. K. Une and M. Oguma, "Thermodynamic Properties of Nonstoichiometric Urania-Gadolinia Solid Solutions in the Temperature Range 700-1100°C" Journal of Nuclear Materials **110** (1982) 215-222.

84. K. Une, Y. Tominaga, and S. Kashibe, "Oxygen Potentials and Lattice Parameter of Irradiated BWR Fuels" Journal of Nuclear Science and Technology **28**[5] (1991) 409-417.

85. M.H. Rand, R.J. Ackermann, F. Gronvold, F.L. Oetting, and A. Pattoret, "The Thermodynamic Properties of the Urania Phase" Rev. int. hautes Tempér. Réfract. Fr. **15** (1978) 355-365.

86. K. Une and M. Oguma, "Oxygen Potentials of $(U,Gd)O_{2\pm x}$ Solid Solutions in the Temperature Range 1000-1500°C" Journal of Nuclear Materials **115** (1983) 84-90.

87. K. Hagemark and M. Broli, "Equilibrium Oxygen Pressures Over Solid Solutions of Urania-Yttria and Urania-Lanthana at 1100° to 1400°C" Journal of the American Ceramic Society **50**[11] (1967) 563-567.

88. E. Stadlbauer, U. Wichmann, U. Lott, and C. Keller, "Thermodynamics and Phase Relationships of the Ternary Lanthanum-Uranium-Oxygen System" Journal of Solid State Chemistry **10** (1974) 341-350.

89. T. Matsui and K. Naito, "Electrical Conductivity Measurement and Thermogravimetric Study of Lanthanum-Doped Uranium Dioxide" Journal of Nuclear Materials **138** (1986) 19-26.

90. K. Une and M. Oguma, "Oxygen Potentials of $(U,Nd)O_{2\pm x}$ Solid Solutions in the Temperature Range 1000-1500°C" Journal of Nuclear Materials **118** (1983) 189-194.

91. T. Fujino, K. Ouchi, Y. Mozumi, R. Ueda, and H. Tagawa, "Composition and Oxygen Potential of Cubic Fluorite-type Solid Solution $Eu_yU_{1-y}O_{2+x}$ and rhombohedral Eu_6UO_{12+x}" Journal of Nuclear Materials **174** (1990) 92-101.

92. K. Park and D.R. Olander, "Defect Models for the Oxygen Potentials of Gadolinium- and Europium-doped Urania" Journal of Nuclear Materials **187** (1992) 89-96.

93. K. Park and D.R. Olander, "A Defect Model for the Oxygen Potential of Urania" High Temperature Science **29** (1990) 203-222.

94. R.E. Woodley and M.G. Adamson, "The Oxygen Potential of Near- and Non-stoichiometric Urania-25 mol% Plutonia Solid Solutions: A Comparison of Thermogravimetric and Galvanic Cell Measurements" Journal of Nuclear Materials **82** (1979) 65-75.

95. R.E. Woodley, "Oxygen Potentials of Plutonia and Urania-Plutonia Solid Solutions" Journal of Nuclear Materials **96** (1981) 5-14.

96. T.L. Markin and E.C. Crouch, "Thermodynamic Data for U-Ce-Oxides" Journal of Inorganic Nuclear Chemistry **32** (1970) 77-82.

97. M. Ugajin, "Oxygen Potentials of $(Th,U)O_{2+x}$ Solid Solutions" Journal of Nuclear Materials **110** (1982) 140-146.

98. K. Une and M. Oguma, "Oxygen Potential of $U_{0.85}Zr_{0.15}O_{2+x}$ Solid Solutions at 1500°C" Journal of the American Ceramic Society **66** (1983) C-179 - C-180.

99. K. Une and M. Oguma, "Oxygen Potentials of UO_2 Fuel Simulating High Burnup" Journal of Nuclear Science and Technology **20**[10] (1983) 844-851.

100. T. Fujino, N. Sato, K. Yamada, "Characteristic Thermodynamic Properties of $M_yU_{1-y}O_{2+x}$ ($M=M^{4+}$, M^{3+}, and M^{2+}) Solid Solutions and the Phase Behavior of Mg Solid Solution in Low Oxygen Pressures" Journal of Nuclear Materials **247** (1997) 265-272.

101. M.G. Adamson, E.A. Aitken, S.K. Evans, and J.H. Davies, "Oxygen Redistribution and its Measurement in Irradiated Oxide Fuels" in Thermodynamics of Nuclear Materials Vol. I, International Atomic Energy Agency, Vienna, (1975) 59-72.

102. Hj. Matzke, J. Ottaviani, D. Pellottiero, and J. Rouault, "Oxygen Potential of High Burn-up Fast Breeder Oxide Fuel" Journal of Nuclear Materials **160** (1988) 142-146.

103. I.L.F. Ray, Hj. Matzke, H.A. Thiele, and M. Kinoshita, "An Electron Microscopy Study of the RIM Structure of a UO_2 Fuel with a High Burnup of 7.9% FIMA" Journal of Nuclear Materials **245** (1997) 115-123.

104. F.A. Cotton and G. Wilkinson, "Basic Inorganic Chemistry" John Wiley & Sons, Inc., New York, 1976.

105. K. Yamada, S. Yamanaka, T. Nakagawa, M. Uno, and M. Katsura, "Study of the Thermodynamic Properties of $(U,Ce)O_2$" Journal of Nuclear Materials **247** (1997) 289-292.

106. T. Fujino and N. Sato, "Analyses of the Oxygen Potential of the Solid Solutions $M_yU_{1-y}O_{2+x}$ (M= M^{3+} and M^{2+}) by Statistics of Defects and Defect Complexes" Journal of Nuclear Materials **189** (1992) 103-115.

107. S. Anthonysamy, K. Nagarajan, and P.R. Vasudeva Rao, "Studies on the Oxygen Potentials of $(U_yTh_{1-y})O_{2+x}$ Solid Solutions" Journal of Nuclear Materials **247** (1997) 273-276.

108. R.D. Shannon, "Revised Effective Ionic Radii and Systematic Studies of Interatomic Distances in Halides and Chalcogenides" Acta Cryst. A32 (1976) 751-767.

109. T. Ohmichi, S. Fukushima, A. Maeda, and H. Watanabe, "On the Relation Between Lattice Parameter and O/M Ratio for Uranium Dioxide-Trivalent Rare Earth Oxide Solid Solutions" Journal of Nuclear Materials **102** (1981) 40-46.

110. K. Une, M. Imamura, M. Amaya, and Y. Korei, "Fuel Oxidation and Irradiation Behaviors of Defective BWR Fuel Rods" Journal of Nuclear Materials **223** (1995) 40-50.

111. International Atomic Energy Agency, "Characteristics and Use of Urania-Gadolinia Fuels" IAEA-TECDOC-844, Vienna.

112. T.L. Markin and R.S. Street, "The Uranium-Plutonium-Oxygen Ternary Phase Diagram" Journal of Inorganic Nuclear Chemistry **29** (1967) 2265-2280.

113. J.H. Davies and F.T. Ewart, "The Chemical Effects of Composition Changes in Irradiated Oxide Fuel Materials" Journal of Nuclear Materials **41** (1971) 143-155.

114. K. Nogita and K. Une, "Effect of Grain Size on Microstructural Change and Damage Recovery in UO_2 Fuels Irradiated to 23 GWd/t" Journal of Nuclear Science and Technology **31**[9] (1994) 929-936.

115. Hj. Matzke, "Radiation Damage in Nuclear Materials" Nuclear Instruments and Methods in Physics Research **B65** (1992) 30-39.

116. K. Une, K. Nogita, S. Kashibe, and M. Imamura, "Microstructural Change and its Influence on Fission Gas Release in High Burnup UO_2 Fuel" Journal of Nuclear Materials **188** (1992) 65-72.

117. R.J. Guenther, D.E. Blahnik, T.K. Campbell, U.P. Jenquin, J.E. Mendel, and C.K. Thornhill, "Characterization of Spent Fuel Approved Testing Material- ATM-106" Pacific Northwest National Laboratory report PNL-5109-106 (1988).

118. R.B. Davis and V. Pasupathi, "Data Summary Report for the Destructive Examination of Rods G7, G9, J8, I9, and H6 from Turkey Point Fuel Assembly B17" Westinghouse Hanford Co. HEDL-TME 80-85 (1981).

119. R.E. Einziger and H.C. Buchanan, "Long-Term, Low-Temperature Oxidation of PWR Spent Fuel- Interim Transition Report" Westinghouse Hanford Company WHC-EP-0070 (1988).

120. R.J. Guenther, D.E. Blahnik, and N.J. Wildung, "Radiochemical Analyses of Several Spent Fuel Approved Testing Materials" Pacific Northwest Laboratory PNL-10113 (1994).

121. R.J. McEachern, "A Review of Kinetic Data on the Rate of U_3O_7 Formation of UO_2" Journal of Nuclear Materials **245** (1997) 238-247.

122. W. Breitung, "Oxygen Self and Chemical Diffusion Coefficients in $UO_{2\pm x}$" Journal of Nuclear Materials **74** (1978) 10-18.

123. W.A. Johnson and R.F. Mehl, "Reaction Kinetics in Processes of Nucleation and Growth" Transactions of the American Institute of Mining and Metallurgical Engineers **135** (1939) 416-458.

124. G.C. Allen, P.A. Tempest, and J.W. Tyler, "Oxidation of Crystalline UO_2 Studied Using X-ray Photoelectron Spectroscopy and X-ray Diffraction" Journal of the Chemical Society, Faraday Transactions I **83** (1987) 925-935.

125. R.J. McEachern, J.W. Choi, M. Kolar, W. Long, P. Taylor, and D.D. Wood, "Determination of the Activation Energy for the Formation of U_3O_8 on UO_2" Journal of Nuclear Materials **249** (1997) 58-69.

126. H. Ohashi, E. Noda, and T. Morozumi, "Oxidation of Uranium Dioxide" Journal of Nuclear Science and Technology **11**[10] (1974) 445-451.

127. S. Sunder and N.H. Miller, "Oxidation of CANDU Uranium Oxide Fuel by Air in Gamma Radiation at 150°C" Journal of Nuclear Materials **231** (1996) 121-131.

128. D.R. Olander, "Theory of Helium Dissolution in Uranium Dioxide. I. Interatomic Forces in Uranium Dioxide" Journal of Chemical Physics **43**[3] (1965) 779-784.

129. D.R. Lide, ed., "CRC Handbook of Chemistry and Physics" CRC Press, New York (1997).

APPENDIX A

Oxidation Curves for Individual Specimens

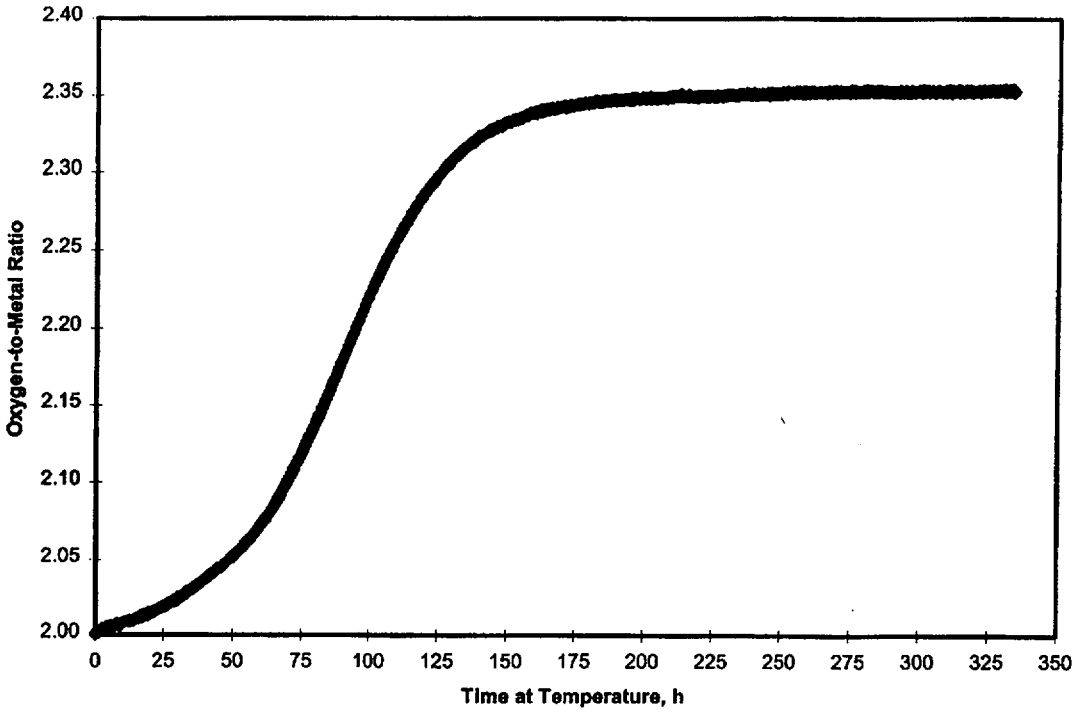

Figure A.1. Sample of Unirradiated UO_2 with 8 wt% Gd_2O_3 Oxidized at 283°C

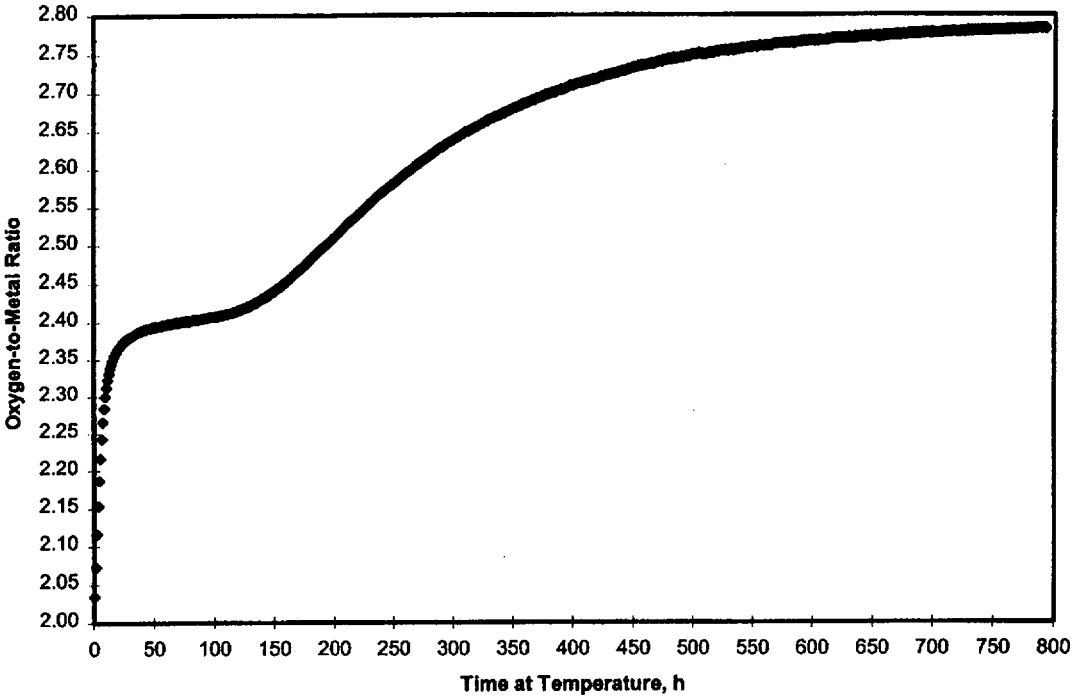

Figure A.2. Sample 105-01 Oxidized at 283°C

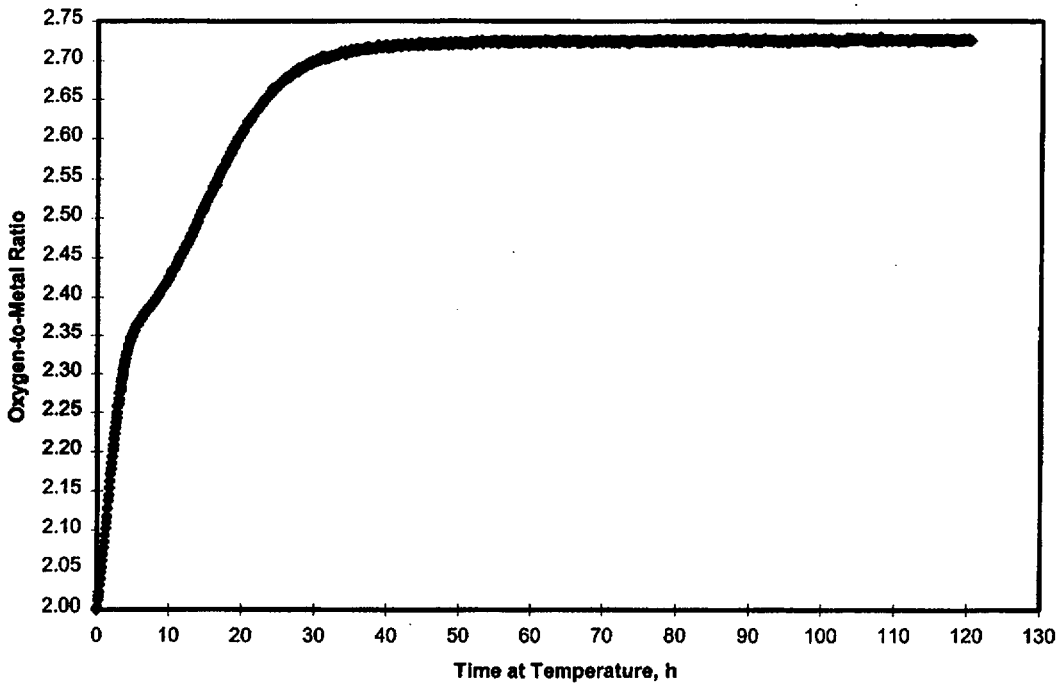

Figure A.3. Sample 105-02 Oxidized at 325°C

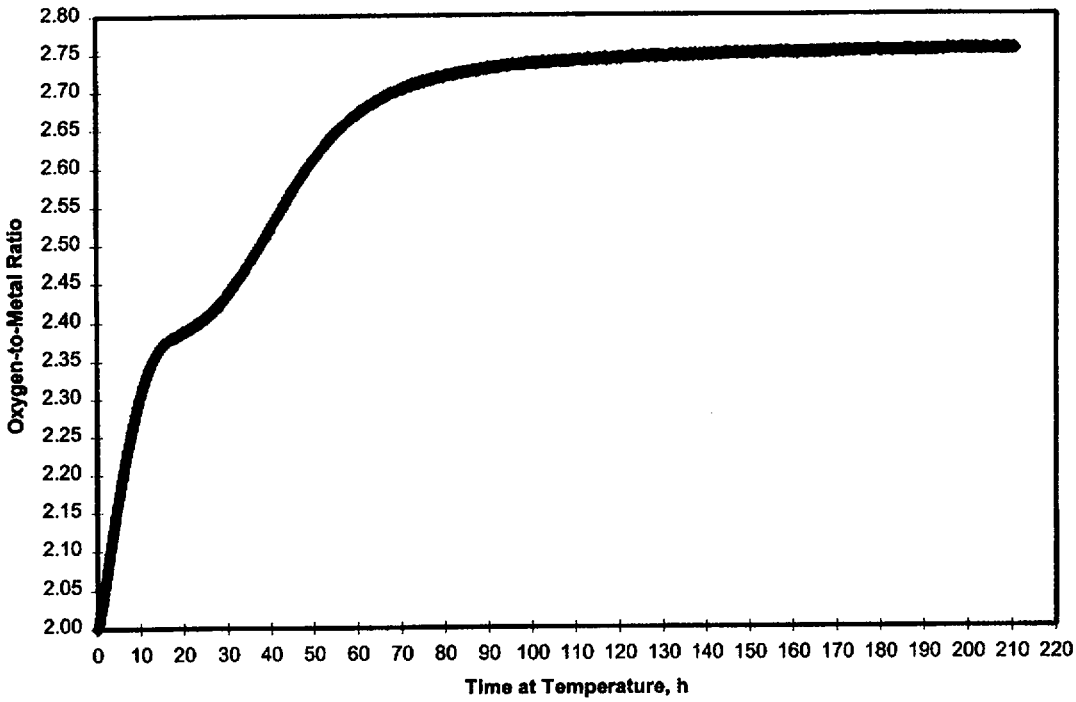

Figure A.4. Sample 105-03 Oxidized at 305°C

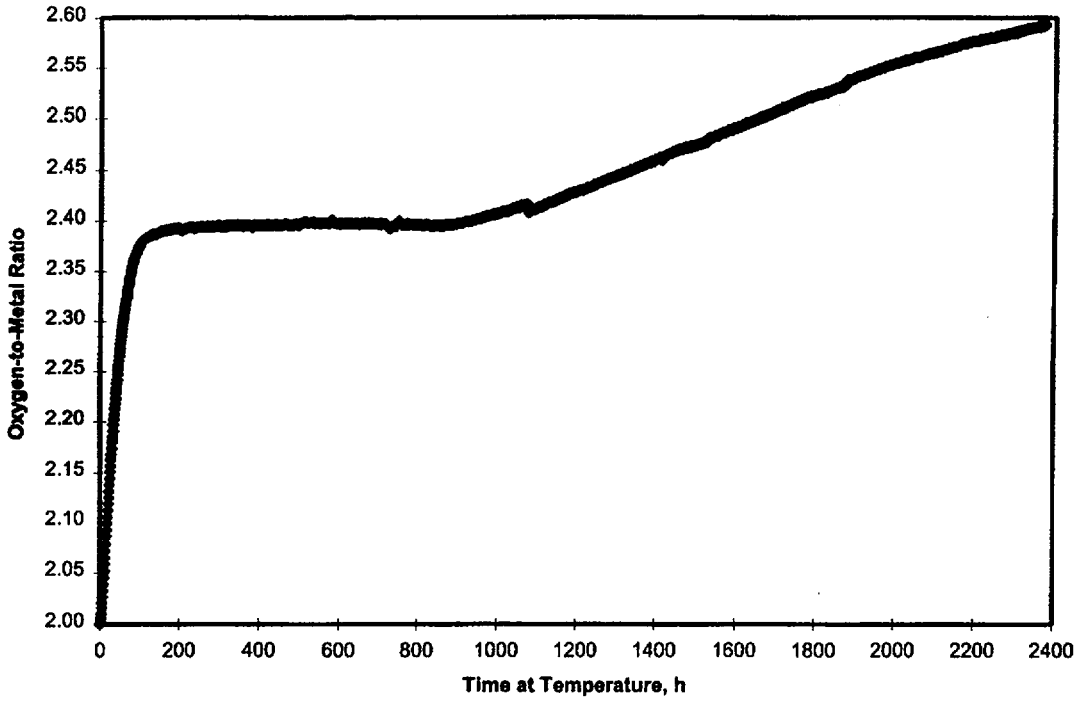

Figure A.5. Sample 105-04 Oxidized at 270°C

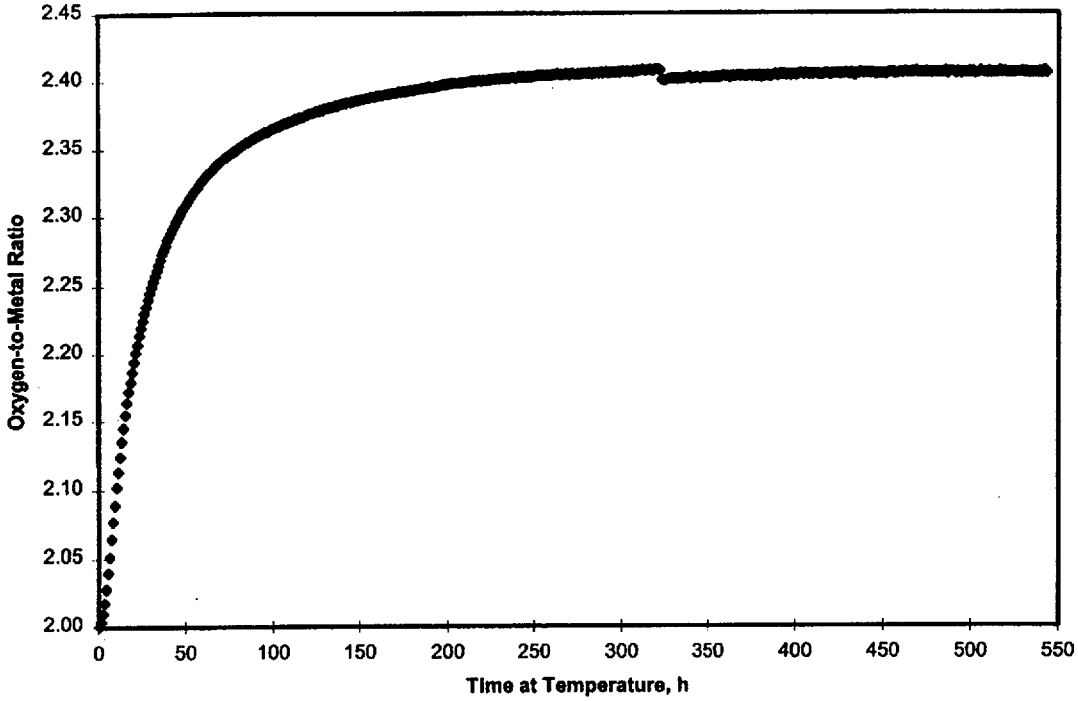

Figure A.6. Sample 105-05 Oxidized at 255°C

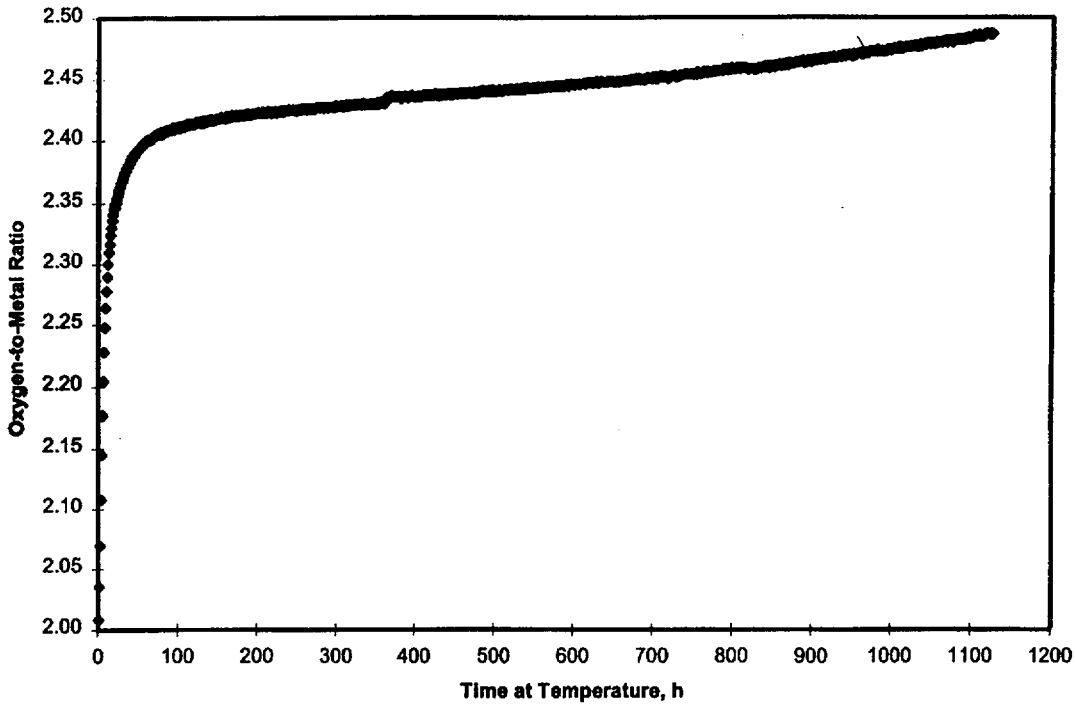

Figure A.7. Sample 105-06 Oxidized at 283°C

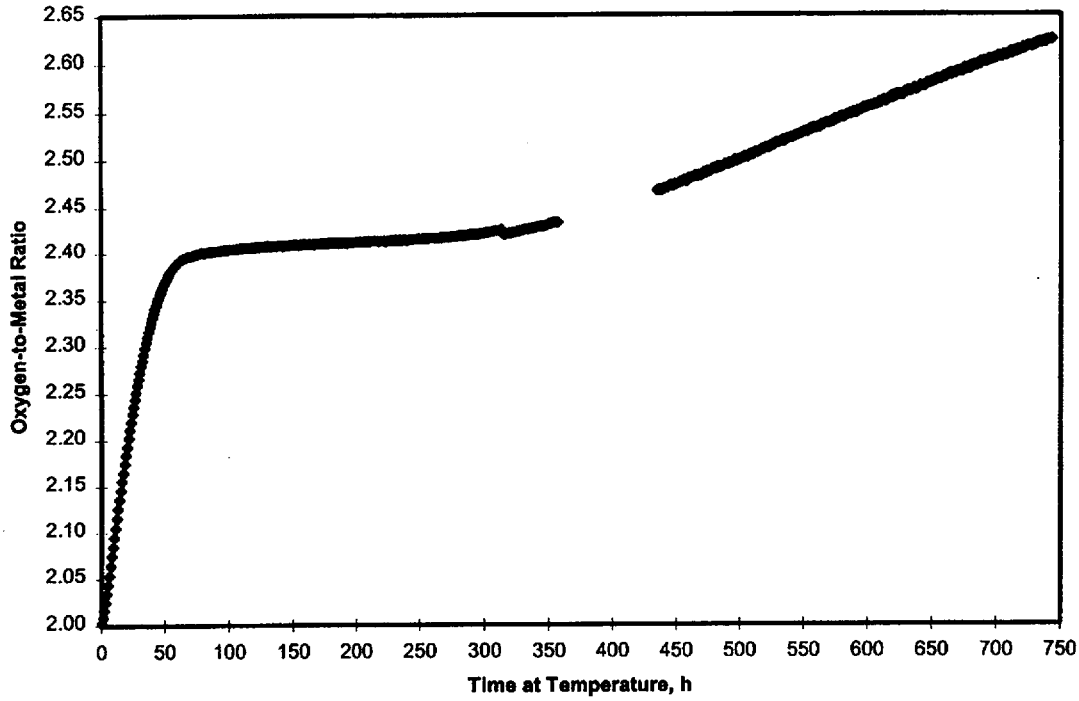

Figure A.8. Sample 105-07 Oxidized at 283°C

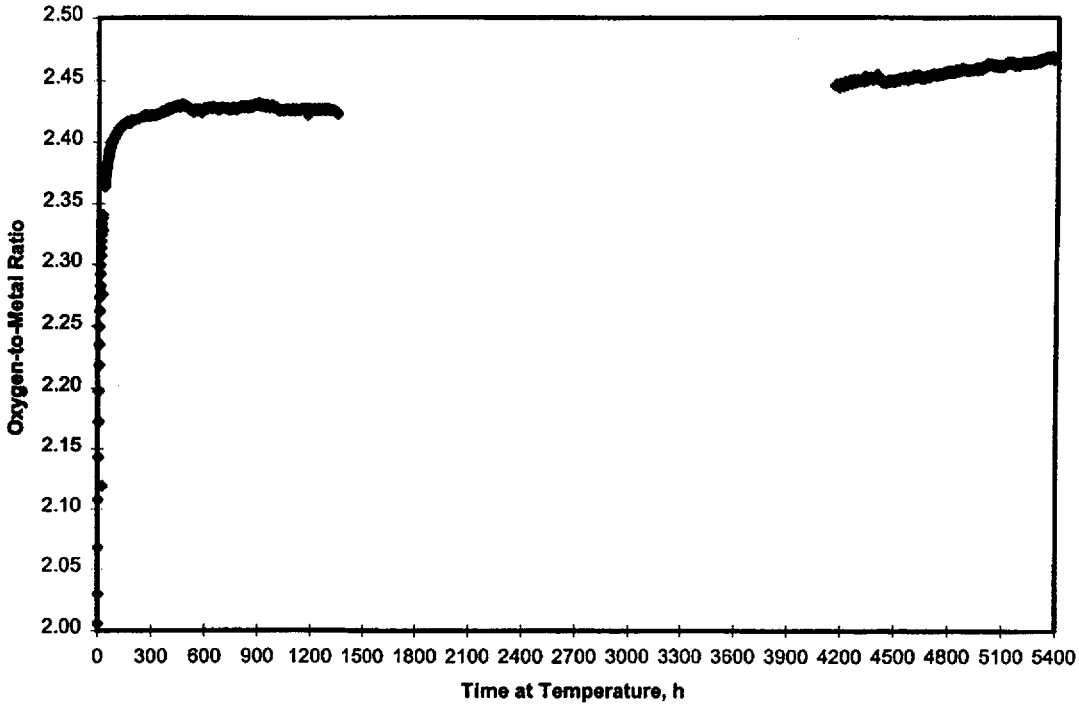

Figure A.9. Sample 105-08 Oxidized at 283°C

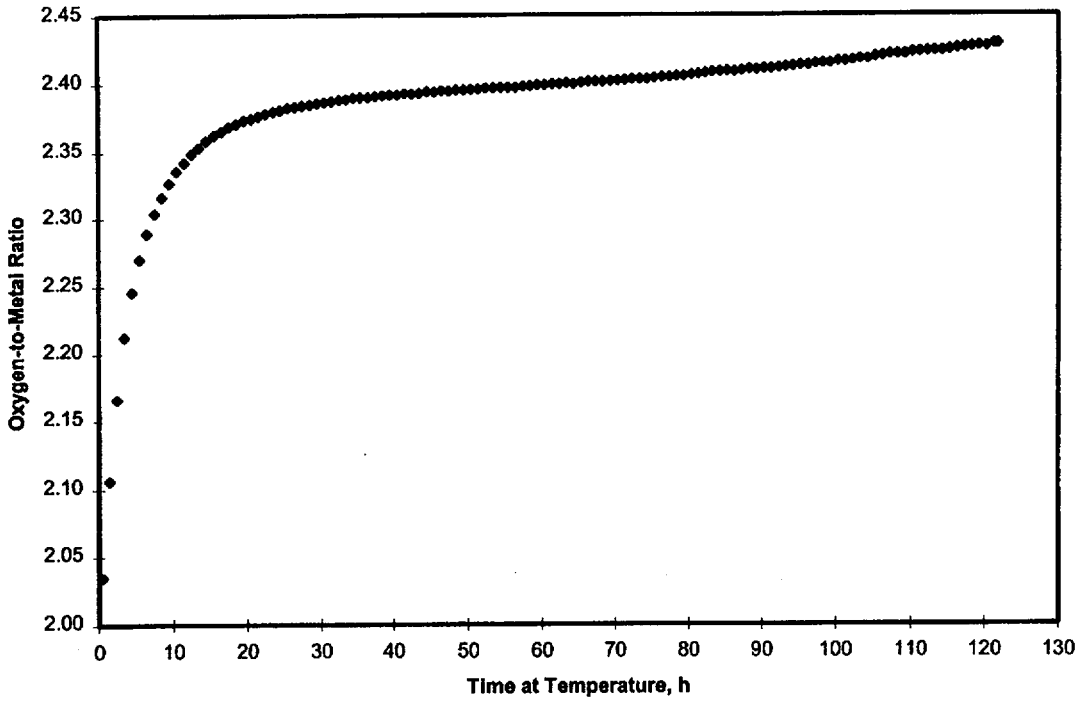

Figure A.10. Sample 105-09 Oxidized at 305°C

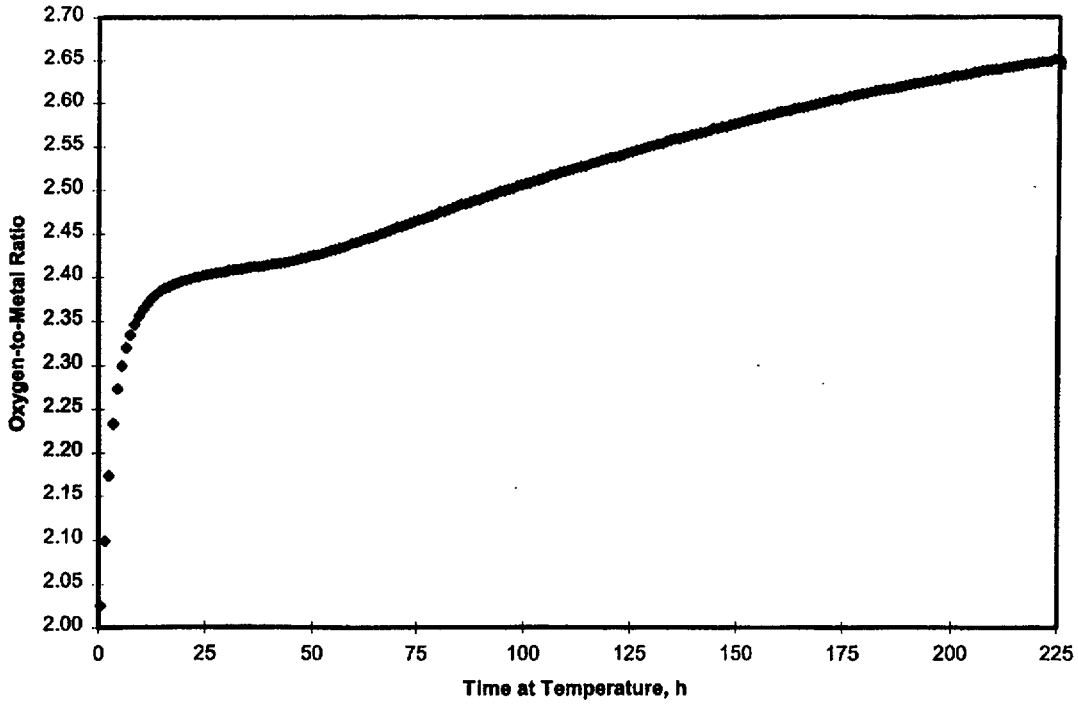

Figure A.11. Sample 105-10 Oxidized at 305°C

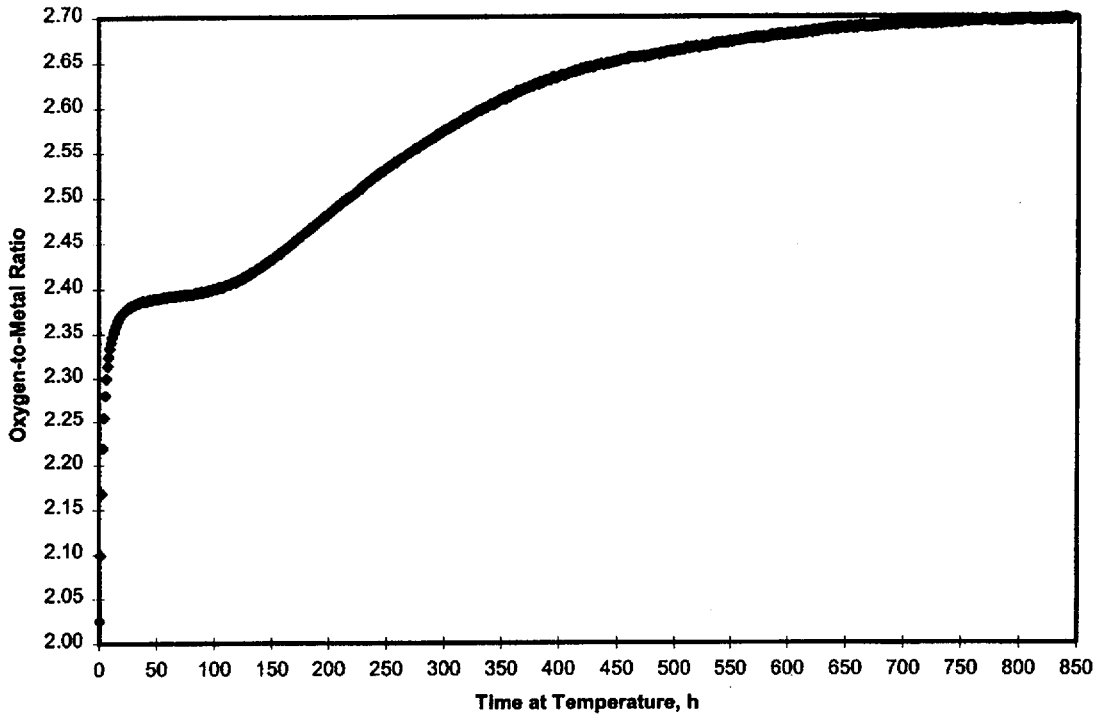

Figure A.12. Sample 105-11 Oxidized at 305°C

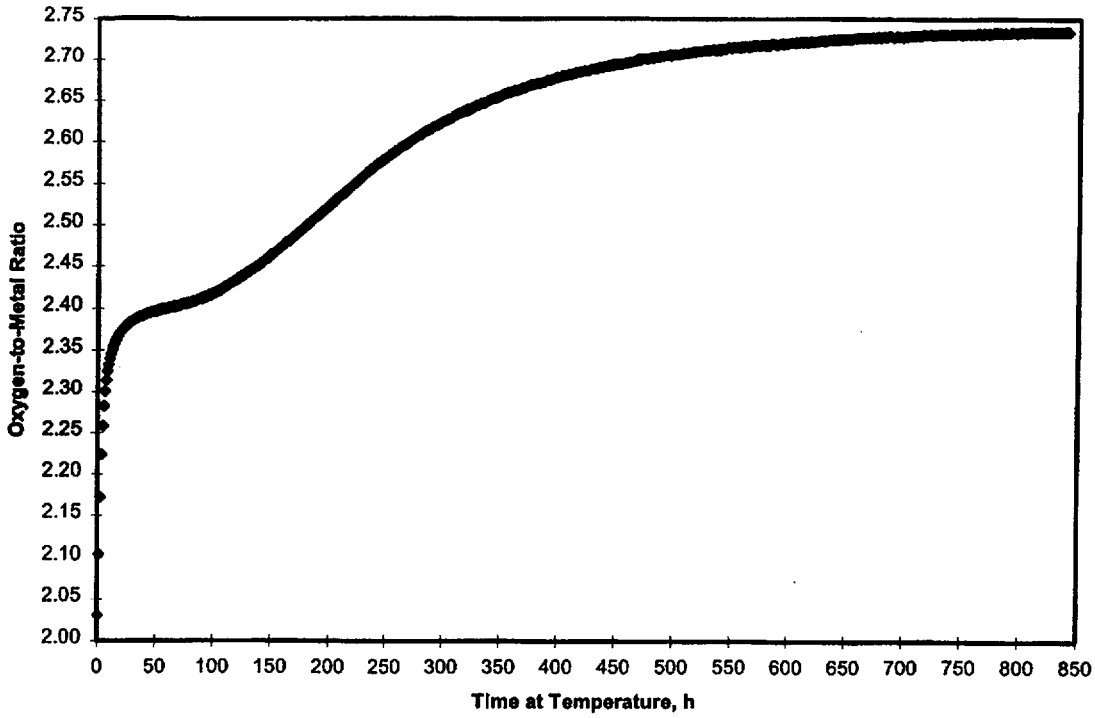

Figure A.13. Sample 105-12 Oxidized at 305°C

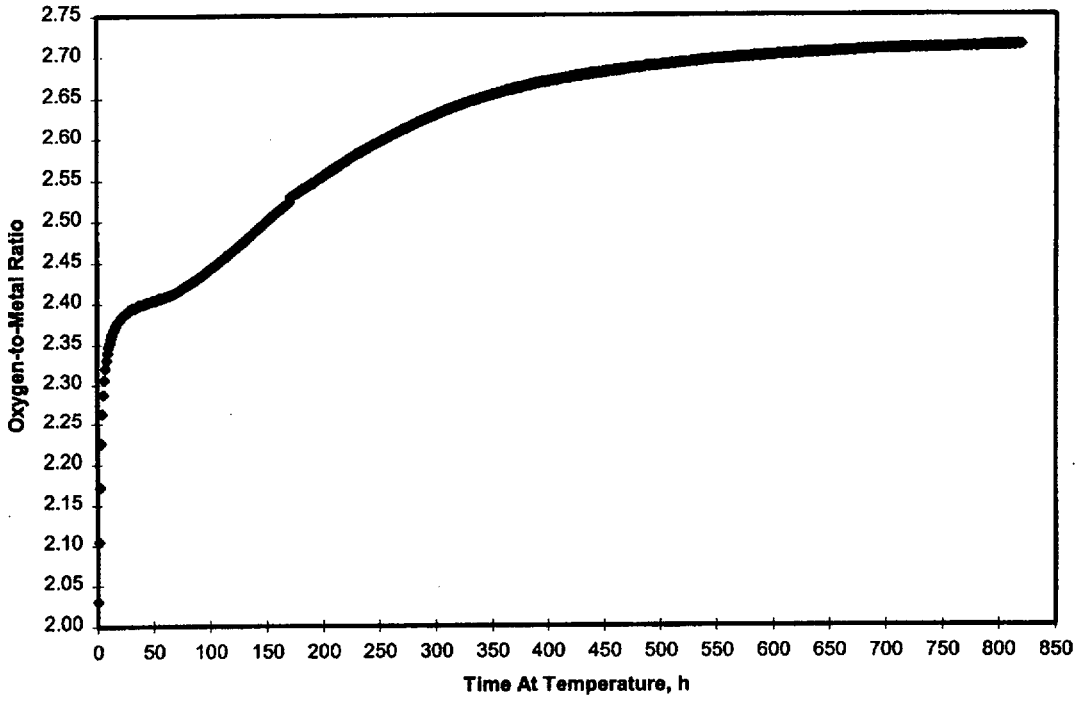

Figure A.14. Sample 105-13 Oxidized at 305°C

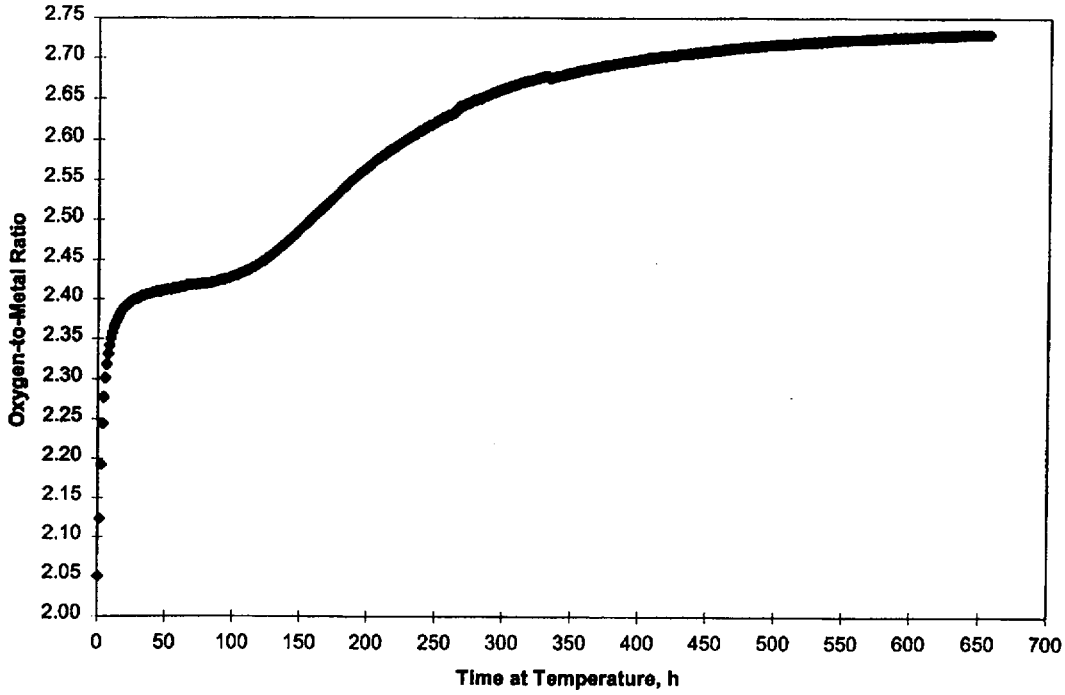

Figure A.15. Sample 105-14 Oxidized at 305°C

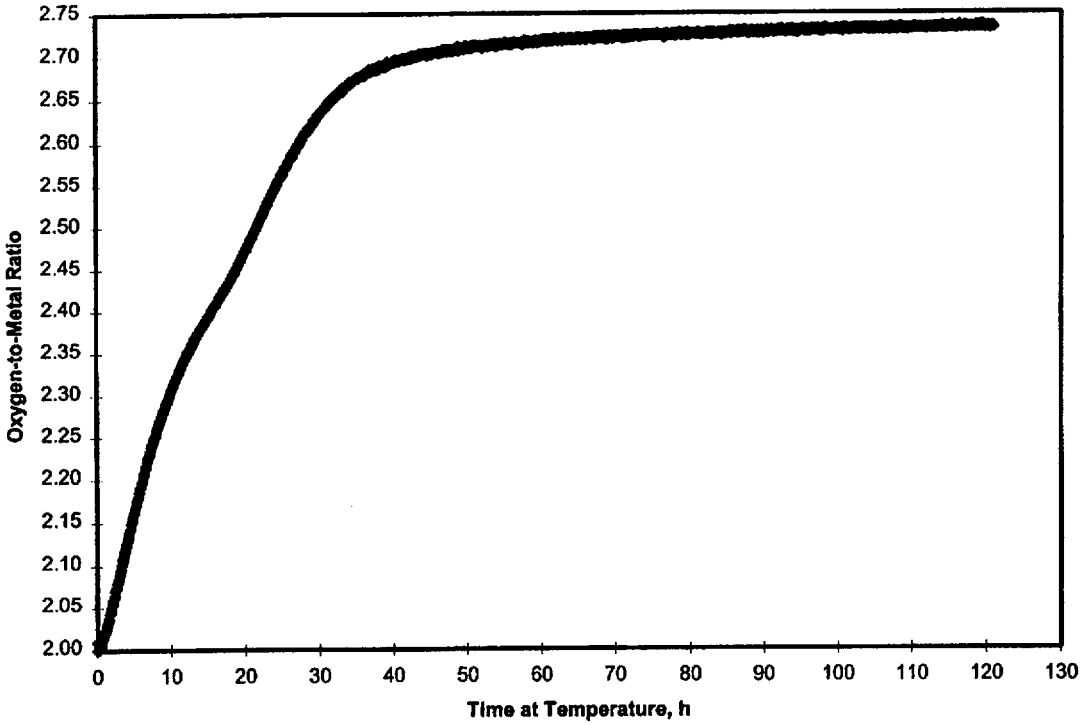

Figure A.16. Sample 105-15 Oxidized at 305°C

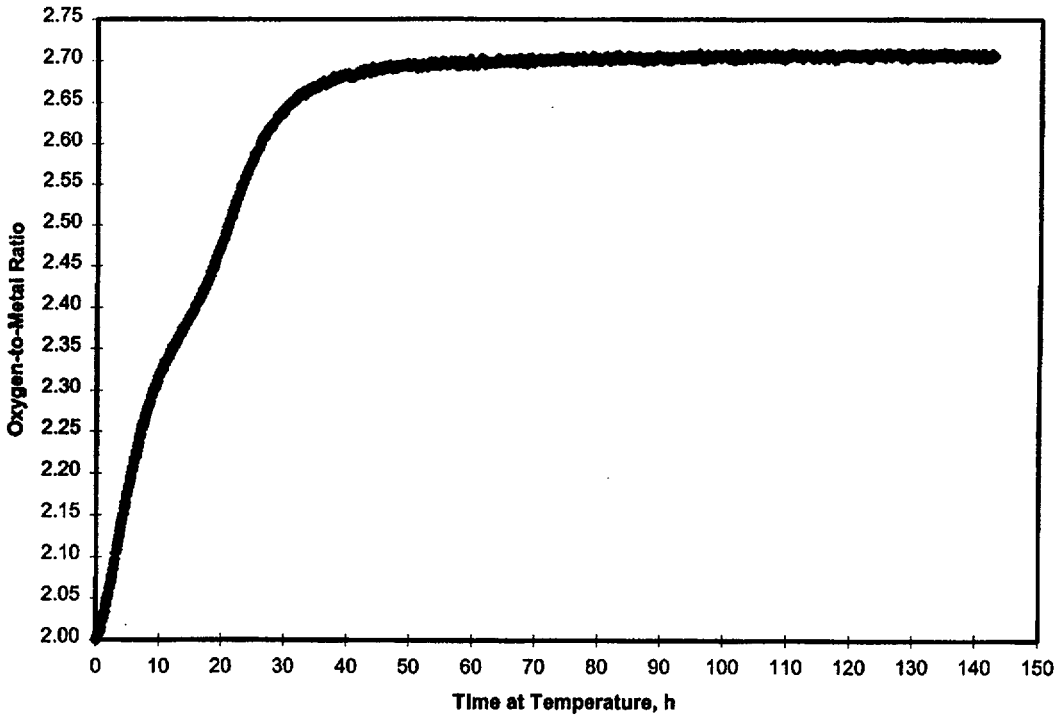

Figure A.17. Sample 105-16 Oxidized at 305°C

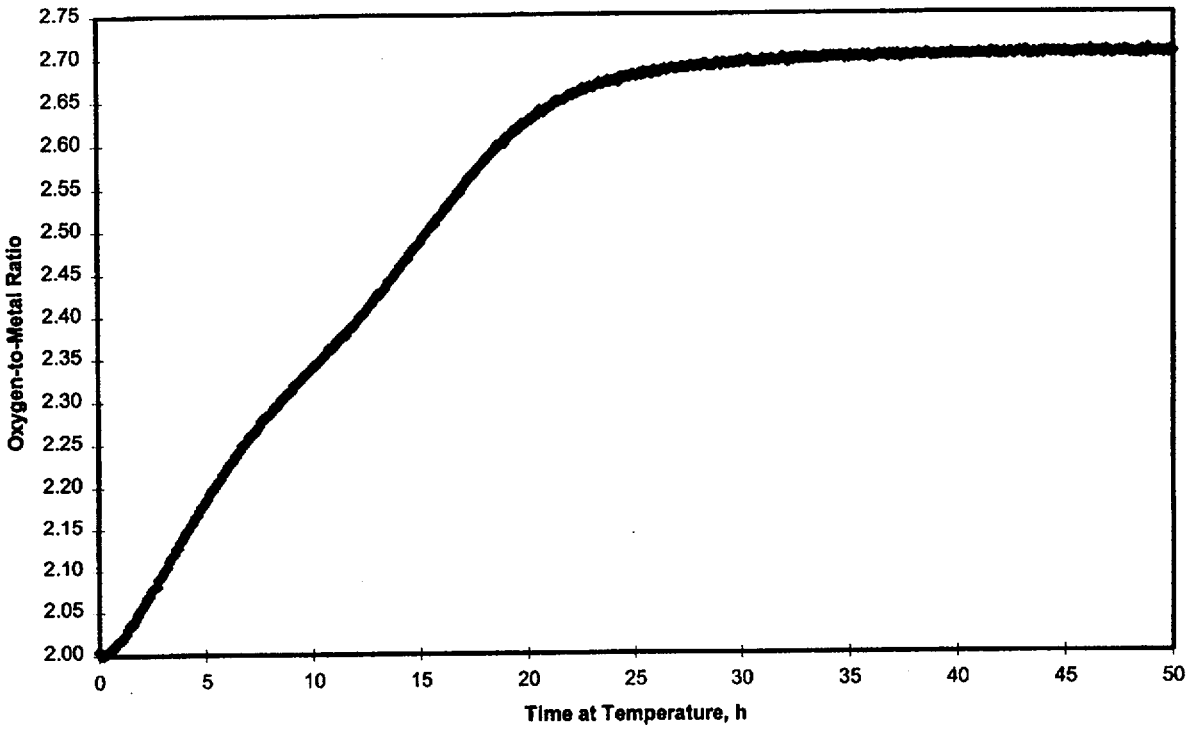

Figure A.18. Sample 105-17 Oxidized at 305°C

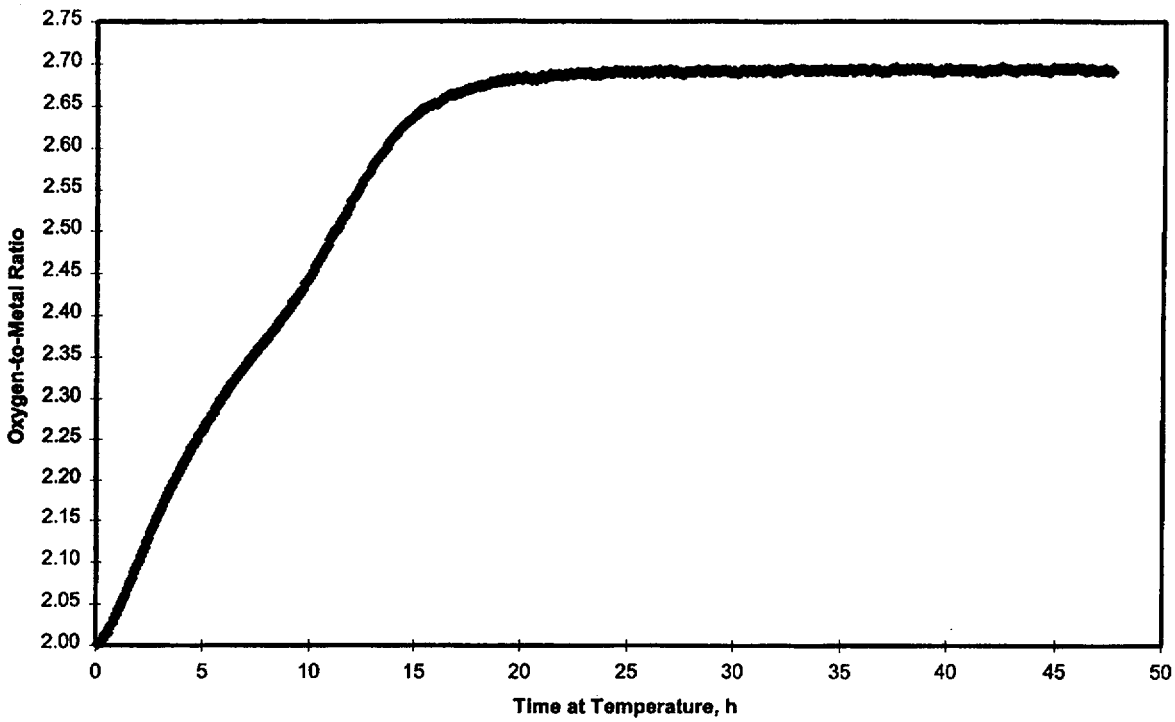

Figure A.19. Sample 105-18 Oxidized at 305°C

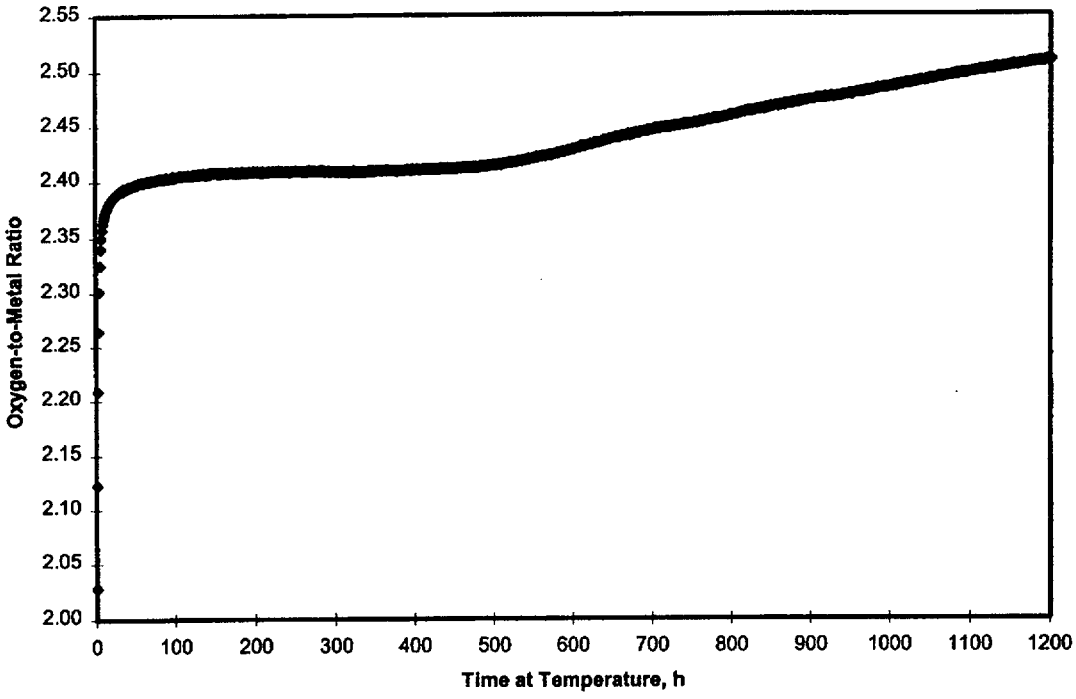

Figure A.20. Sample 104-01 Oxidized at 305°C

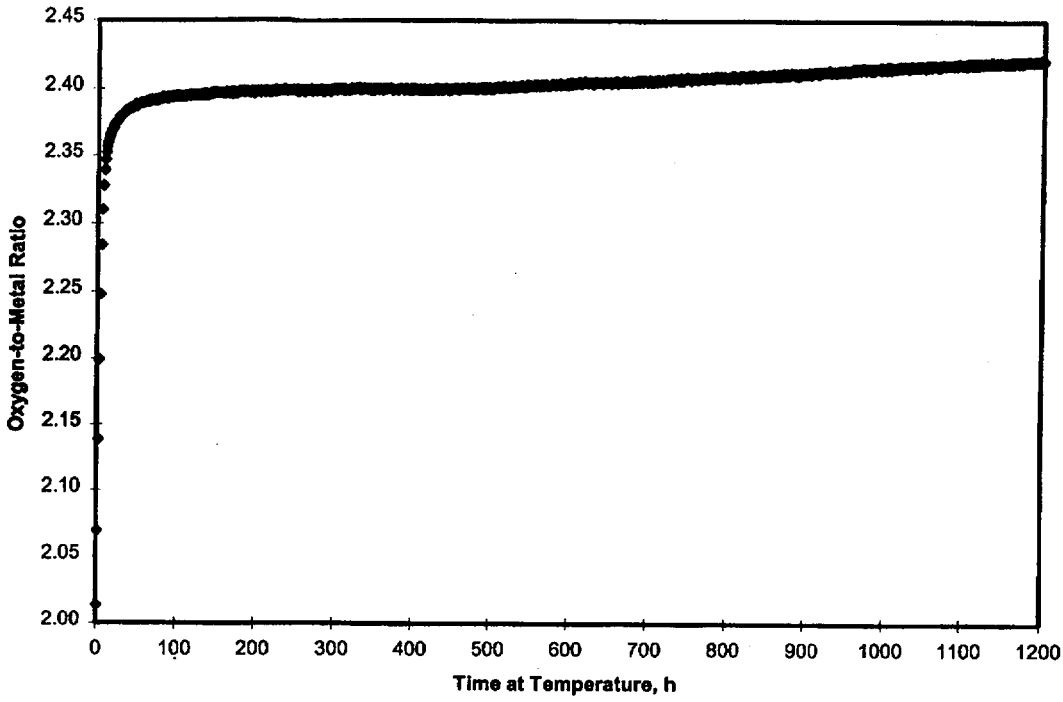

Figure A.21. Sample 104-02 Oxidized at 305°C

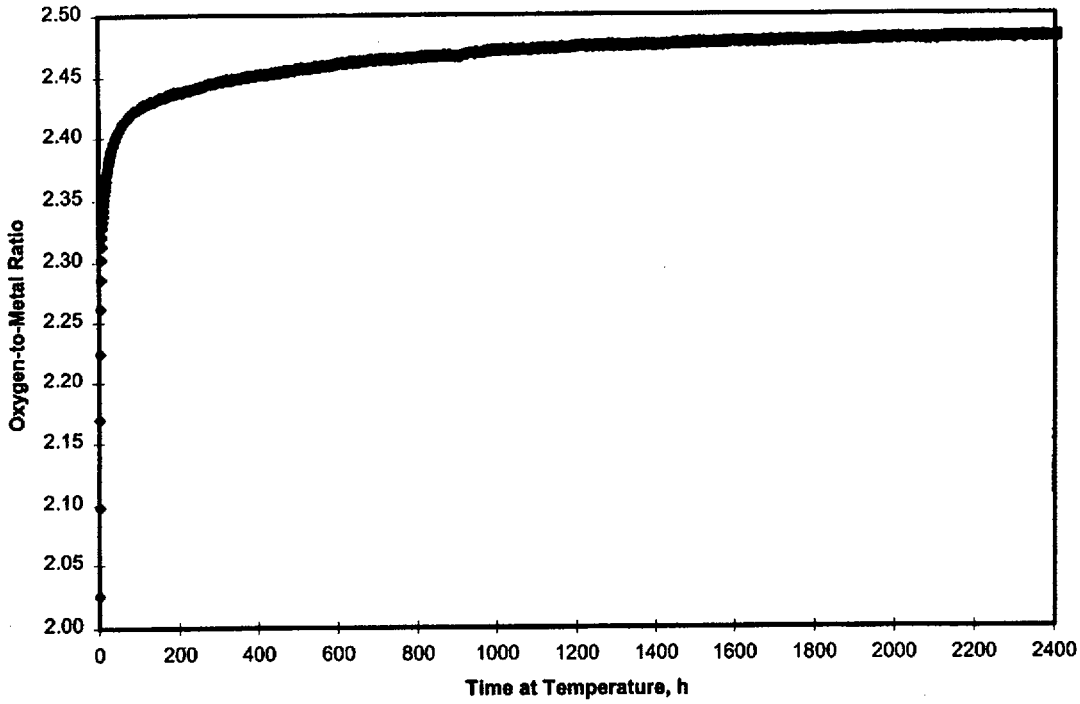

Figure A.22. Sample 108-01 Oxidized at 305°C

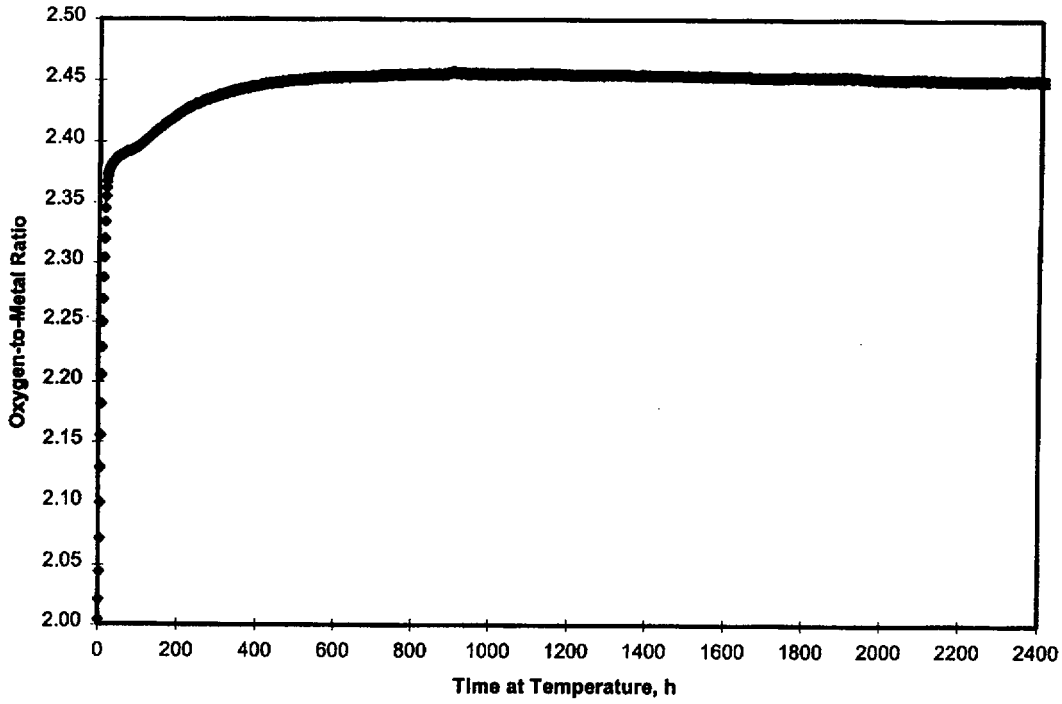

Figure A.23. Sample 108-02 Oxidized at 305°C

Distribution

No. of Copies

OFFSITE

2 DOE/Office of Scientific and Technical Information

2 Engineering and Material Section
Office of Nuclear Material Safety and Safeguards
U.S. Nuclear Regulatory Commission
Washington, DC 20555
Attn: T. Ahn
R. Weller

2 C.G. Interrante
Spent Fuel Project Office
U.S. Nuclear Regulatory Commission
Washington, DC 20555

14 Lawrence Livermore National Laboratory
University of California
P.O. Box 808
Livermore, California 94550
Attn: J.C. Farmer, L-352
W. Halsey, L-204
E. Kansa (2), L-200
D. McCright, L-369
W.J. O'Connell, L-195
R.B. Stout (6), L-217
S.A. Steward, L-092
R.A. Vankonynenburg, L-369

3 Argonne National Laboratory
9700 S. Cass Ave.
Argonne, Illinois 60439
Attn: J.C. Cunnane
R.E. Einziger (2)

No. of Copies

OFFSITE

2 Oak Ridge Institute for Science and Education
P.O. Box 117
Oak Ridge, Tennessee 37831
Attn: S.L. Johnson
C. Williams

3 Oak Ridge National Laboratory
P.O. Box 2008
Oak Ridge, Tennessee 37831
Attn: C.W. Forsberg, MS-6180
S.B. Ludwig, MS-6495
G.E. Michaels, MS-8063

6 University of California at Berkeley
Berkeley, California 94720
Attn: D.R. Olander (2), Dept. of Nuclear Eng.
S.G. Prussin (3), Dept. of Nuclear Eng.
G.I. Rochlin, Energy and Resources

5 Yucca Mountain Site Characterization Office
P.O. Box 371315
Las Vegas, Nevada 89137-1315
Attn: P.R. Daniel/MTS
R.L. Fish/MTS
D.C. Haught/DOE
M. Mansouri/MTS
R.E. Spence/DOE

No. of Copies

OFFSITE

9 Yucca Mountain Project M&O Contractor
SUM1/423
1261 Town Center Drive
Las Vegas, Nevada 89134
Attn: R.W. Andrews
J.A. Blink
J.K. McCoy (2)
J.A. McNeish
D. Stahl
C. Stockman
T.A. Thornton
E.R. Siegmann

FOREIGN

3 AECL Research
Whiteshell Laboratories
Pinawa, Manitoba R0E 1L0
Canada
Attn: L. Johnson
R.J. McEachern
D. Shoesmith

J. Bruno
QuantiSci
Parc Tecnologic del Valles
E-08290 Barcelona
Spain

2 R. Forsyth
Forsyth Consulting
Stenbrinken 7
S-61134 Nykoping
Sweden

B. Grambow
KFK/INE
Postfach 3640
D-76021 Karlsruhe
Germany

No. of Copies

FOREIGN

2 European Institute for Transuranic Elements
Postfach 2340
D-76125 Karlsruhe
Germany
Attn: J. Cabos
H. Matzke

K. Spahiu
SKB
PO Box 5864
S-10240 Stockholm
Sweden

ONSITE

24 Pacific Northwest National Laboratory

J. Abrefah	P7-27
W.J. Gray	P7-27
B.D. Hanson (15)	P7-27
J.M. Latkovich	K9-44
S.C. Marschman	P7-27
Technical Report Files (5)	